

Electronic Thesis and Dissertation Repository

5-31-2023 12:30 PM

Controls on organic matter preservation and distribution, Upper Cretaceous Colorado Group

Jessica Flynn, *Western University*

Supervisor: Tsujita, Cameron, *The University of Western Ontario*

A thesis submitted in partial fulfillment of the requirements for the Doctor of Philosophy degree in Geology

© Jessica Flynn 2023

Follow this and additional works at: <https://ir.lib.uwo.ca/etd>

Recommended Citation

Flynn, Jessica, "Controls on organic matter preservation and distribution, Upper Cretaceous Colorado Group" (2023). *Electronic Thesis and Dissertation Repository*. 9338.
<https://ir.lib.uwo.ca/etd/9338>

This Dissertation/Thesis is brought to you for free and open access by Scholarship@Western. It has been accepted for inclusion in Electronic Thesis and Dissertation Repository by an authorized administrator of Scholarship@Western. For more information, please contact wlsadmin@uwo.ca.

Abstract

Inconsistencies in production performance in self-sourcing, tight-oil reservoirs have been related to lithologic heterogeneities. Applying traditional methods to characterize and model tight-oil petroleum systems presents a challenge as there is an assumption that organic-rich mudstone units are homogeneous with minimal stratal discontinuities. Relating depositional processes that promote organic matter preservation to stratal packaging in a basin evolution context provides the basis for predicting stratigraphic and geographic limits of discrete self-sourcing shale reservoirs. This study uses the regionally extensive organic-rich Blackstone Alloformation, comprising the Fish Scales, Belle Fourche, and Second White Specks formations of the Western Canada Foreland Basin, as a test case to examine the complex relationships between sedimentary facies, basin evolution, and organic matter preservation, with the purpose to determine if organic matter distribution can be predicted by extrapolating sedimentary lithofacies to basin scale.

Correlation of thirteen regionally traceable allostratigraphic surfaces across Alberta and Saskatchewan, covering the majority of the Canadian portion of the Western Interior Seaway, defines the Blackstone Alloformation. The resulting framework features wedge-shaped and tabular stratigraphic geometries that provide evidence for active tectonic loading in the fold and thrust belt and tectonic quiescence on the stable craton, and in the distal basin. Minor, isolated thinning and thickening of allomembers is a response to movement on basement structures. Five primary lithofacies are identified in core and correspond to four lithology categories used for percent lithology mapping: silty argillaceous mudstone, calcareous mudstone, heterolithic sandstone and mudstone, and sandstone. Percent lithology distribution maps show that the Greenhorn marine transgression led to the basinwide deposition of calcareous mudstone and that minor fluctuations in relative sea level from tectonic uplift or eustatic sea level fall meant sedimentation on the low gradient ramp was prone to the reworking of material on the sea floor by storm waves.

Programmed pyrolysis data reveal that the Blackstone Alloformation strata is rich in type II and type II-III kerogen and has high hydrocarbon generation potential. Calcareous mudstone and silty argillaceous mudstone contain the highest wt.% TOC (total organic carbon),

followed by heterolithic sandstone and mudstone. Integration of TOC with upscaled sedimentary lithofacies/lithology mapping at the allomember scale confirms that lateral and vertical variations of organic matter preservation and distribution are controlled by factors contributing to the transport and deposition of fine-grained sediments. Enhanced organic matter preservation corresponds to depositional conditions that favour the development of organo-mineralic aggregates and limit organic matter dilution from siliciclastic sediment input or high carbonate production rates.

Keywords

Allostratigraphy, lithofacies evaluation, organic geochemistry, basin evolution, Colorado Group, Cenomanian-Turonian, organic matter preservation

Summary for Lay Audience

Despite advances in drilling technology that have improved oil and gas extraction from tight, self-sourcing shale-based resources, inconsistencies in production performance have persisted. Recent studies suggest that this variability is related to the heterogeneity of shale and other fine-grained rocks in terms of mineralogy, texture and structure, and its influence on organic matter preservation. The accumulation of organic matter is dependent on the formation of organic-based aggregate particles in the water column and the sedimentary processes responsible for their transport and deposition.

In this thesis, a regionally extensive organic-rich succession of rock spanning Alberta and Saskatchewan is examined to determine the complex relationships existing between sedimentation, basin evolution, and organic matter preservation. The purpose of this work is to determine if organic matter distribution can be predicted by extrapolating distinct physical, chemical, biological attributes of rock units, as observed on vertical scales of centimetres to metres, that show controls on organic matter preservation basinwide. The methodology consisted of creating a time-constrained stratigraphic framework using packages of coeval strata rock packages bounded by key surfaces (discontinuities) and integrating sedimentological and organic geochemistry data into this framework.

Results of this study show that sedimentary processes required to distribute and preserve organic matter are linked to subtle changes in relative sea level. Isopach maps showing thickness variations in rock packages suggest that changes in the thickness of these packages were controlled by the shifting positions of flexural loads in the fold and thrust belt in western Alberta and eastern British Columbia. A rise in relative sea level that accompanied the northward inundation of waters into the Western Interior Seaway from the proto-Gulf of Mexico during the Upper Cretaceous Greenhorn transgression is recorded by the basinwide deposition of calcareous mudstone. Minor fluctuations in relative sea resulting from tectonic movements meant sediment on the sea floor was prone to reworking by storm waves. Integration of organic geochemical data with observations on the sedimentary characteristics of the studied strata revealed that organic matter preservation was enhanced when the environmental conditions in the seaway: 1) promoted development of organic-based aggregates, and 2) limited the input of siliciclastic (silt and sand) and biologically produced

(e.g., coccolith and foraminiferal) sedimentary components. These findings contribute to the current understanding of spatial and temporal controls on organic matter distribution and may assist with better predicting the geographic extent of self-sourcing shale-based oil and gas reservoirs.

Acknowledgments

This has been quite a journey. I never thought that I would get to the point of writing this section of my thesis, but here I am. I would not have achieved this without the following village supporting me along the way.

Firstly, I would like to thank Husky Energy, Devon Canada Corporation, and Tuzo Energy for funding this research. I also thank geologic systems, Divestco, and IHS Canada for donating the software packages and data utilized in this research.

As for my village, I would like to start with Dr. Burns Cheadle. Thank you for giving me the opportunity to work on this project. This experience has been fundamental in getting me to where I am today in my career. I also thank your lovely wife, Sherri, for graciously hosting me and my little Bea when we stayed in London.

Dr. Guy Plint, thank you for always taking the time to (very quickly) respond and send me articles I've asked about, and answering my sedimentology and stratigraphy questions, even when those emails arrive late on a Friday night.

A very big thank you to Dr. Cam Tsujita for agreeing to take me on when Burns retired. I greatly appreciated the constructive feedback you provided and your encouragement along the way.

Dr. Bruce Hart, we crossed paths later in this thesis journey and I am very grateful. You provided me with the final perspective I needed to 'see' the value in my work and cross the finish line.

A massive thank you to my manager, mentor, and friend, Melinda Yurkowski. I seriously doubt that this thesis could have been completed without your support. You empathized with my struggles of balancing it all: work, family, and thesis. I am beyond grateful to you.

My lab crew: Mailying, Kienan, Beth, and Karen. Thank you for the friendship and being there to answer random texts, emails, and voicemails about my research conundrums. We don't get to see each other very often these days, but I truly see you as lifelong friends.

The largest village contributors would be my family. Amy and Caroline: you both have the patience of a saint. Thank you so much for taking care of my babies, and fur baby, so that I could work long hours. I owe you both so much. To my in-laws, Thea and Werner, thank you for coming to spend time with your grandbabies and building wonderful memories as their mommy ignored them while working at a computer. To my mom and sister, thank you for coming to help me with all the things and listening as I vented my frustrations and loving me anyway. Thank you to my dad for signing me up for soccer when I was a little girl – the confidence I gained from playing a competitive sport for over 25 years taught me to believe in myself and that dedication and hard work will pay off.

Dominic, we can finally stop paying tuition and use the money to go on a well-deserved vacation. Oh, I meant me go on a vacation and you stay home with the kids. Kidding. Kind of. I love you and thank you for all you do for our little family.

To my babies, I hope that when you're old enough to see this 'boring book', you will understand why you have so many memories of a 'grumpy' mommy that worked all the time when you were young. Your cuddles got me through the longest days. Love you forever.

Table of Contents

Abstract	ii
Summary for Lay Audience.....	iv
Acknowledgments.....	vi
Table of Contents	viii
List of Tables	xiii
List of Figures	xv
Chapter 1	1
1 Introduction	1
1.1 Problem	1
1.2 Aim and Objectives.....	6
1.3 Database	6
1.4 Significance.....	9
Chapter 2.....	10
2 Geological setting, development of the Western Canada Foreland Basin, and evolution of the Upper Cretaceous Colorado Group.....	10
2.1 Geological history of the Western Canada Sedimentary Basin	10
2.2 Foreland basin development	13
2.2.1 Subsidence history of the Western Canada Foreland Basin	19
2.3 Foreland basin depozones	21
2.4 Paleogeography of the Western Interior Basin during the Upper Cretaceous	23
2.5 Sedimentology and stratigraphy of the Colorado Group	27
2.5.1 Biostratigraphy of the Colorado Group	27
2.5.2 Lithostratigraphy of the Colorado Group	31
2.5.3 Allostratigraphy of the Colorado Group.....	38
Chapter 3.....	51

3	Sedimentary lithofacies of the Upper Colorado Group.....	51
3.1	Shallow marine setting and processes.....	54
3.1.1	Sedimentological evidence of a storm-influenced system.....	57
3.2	Mud aggregate grains.....	59
3.3	Mud transport and sedimentation.....	60
3.3.1	Mud transport on an ancient storm-dominated shelf	62
3.4	Facies model to link proximal shoreface to the distal offshore	63
3.5	Sedimentary lithofacies of the Upper Colorado Group	65
3.5.1	Bentonite.....	68
3.5.2	Lithofacies 1 – Fine-grained sandstone with thinly bedded and weakly bioturbated mudstone.....	69
3.5.3	Lithofacies 2 - Thinly bedded, heterolithic sandstone and mudstone.....	71
3.5.4	Lithofacies 3 – Very thinly bedded, carbonaceous, calcareous-argillaceous mudstone.....	77
3.5.5	Lithofacies 4 – Foraminifera- and coccolith-rich packstone-grainstone ..	82
3.5.6	Lithofacies 5 – Thinly bedded silty argillaceous mudstone.....	85
3.6	Lithofacies successions.....	88
	Chapter 4.....	92
4	Sequence stratigraphy and mapping methods	92
4.1	Sequence stratigraphy	92
4.1.1	Eustasy	94
4.1.2	Systems tracts.....	96
4.2	Allostratigraphic cross-sections	99
4.3	Geophysical well log database.....	105
4.3.1	Gamma Ray	105
4.3.2	Bulk-Density	107
4.3.3	Photoelectric Effect (PEF)	109

4.3.4	Neutron Porosity	110
4.3.5	Resistivity/Conductivity	112
4.4	Isopach and lithology mapping.....	116
4.4.1	Isopach mapping.....	117
4.4.2	Lithology mapping.....	117
Chapter 5	123
5	Allostratigraphy and stratigraphic geometries of the Blackstone Alloformation	123
5.1	Bounding discontinuities of the Blackstone Alloformation.....	123
5.1.1	Allomember I (Fish Scales Alloformation) – BFSM and FSU surfaces	127
5.1.2	Allomember II – X Bentonite	127
5.1.3	Allomember III – “Dunvegan A” equivalent.....	129
5.1.4	Allomember IV – X transgressive surface.....	130
5.1.5	Allomember V – K1 surface	133
5.1.6	Allomember VI – Bighorn River bentonite	137
5.1.7	Allomember VII – Regional flooding surface	138
5.1.8	Allomember VIII- ‘Blue’ bentonite	138
5.1.9	Allomember XI – “Green” bentonite.....	139
5.2	Allostratigraphic cross-sections and stratal geometries.....	139
5.2.1	Approximately strike-oriented correlation lines (North-South trending)	139
5.2.2	Approximately dip-oriented correlation lines (West-East trending)	148
5.3	Precambrian basement structures in the Western Canada Sedimentary Basin ...	161
5.3.1	Subsidence patterns and Precambrian basement influence.....	165
Chapter 6	183
6	Sediment distribution and paleogeographic history of the Upper Cretaceous Colorado Group	183
6.1	Albian-Cenomanian	183

6.1.1	Allomember I.....	183
6.2	Cenomanian	186
6.2.1	Allomember II.....	186
6.2.2	Allomember III	189
6.2.3	Allomember IV	192
6.2.4	Allomember V	195
6.2.5	Allomember VI.....	198
6.3	Turonian.....	202
6.3.1	Allomember VII.....	202
6.3.2	Allomember VIII	206
6.3.3	Allomember IX.....	210
6.3.4	Allomember X	210
6.3.5	Allomember XI.....	215
Chapter 7	219
7	Organic geochemistry data collection and evaluation methods.....	219
7.1	Origin of organic matter in marine mudstones	219
7.2	Geochemical database.....	225
7.2.1	Sample collection.....	226
7.2.2	Sample preparation	227
7.3	Rock-Eval pyrolysis.....	227
7.3.1	Rock-Eval 6 pyrolysis.....	229
7.3.2	232	
7.3.3	Rock-Eval limitations	234
7.4	LECO analysis	234
7.4.1	LECO limitations	236
7.5	Organic geochemistry characterization.....	236

7.5.1	Reconstruction of original total organic content.....	237
Chapter 8	245
8	Organic matter distribution in the Upper Cretaceous Colorado Group	245
8.1	Kerogen type.....	245
8.2	Thermal maturity	248
8.3	Kerogen quality.....	252
8.3.1	S ₂ vs TOC.....	255
8.4	Total organic content	255
8.4.1	Variation of total organic content in lithofacies	258
8.5	Organic matter distribution in the Blackstone Alloformation	264
Chapter 9	271
9	Conclusions	271
9.1	Objectives and results	271
9.1.1	Objective 1: Constructing a basinwide allostratigraphic framework.....	271
9.1.2	Objective 2: Map lithology distribution across the basin	273
9.1.3	Objective 3: Link programmed pyrolysis data to basin lithology distribution	275
9.2	Acknowledgement of limitations of this study	276
9.3	Future work.....	276
References	278
Curriculum Vitae	303

List of Tables

Table 3.1: List of cored wells logged for this study. Wells located in Alberta were logged and sampled at the Alberta Energy Regulator Core Research Centre in Calgary, Alberta. Saskatchewan-based wells were logged at the Saskatchewan Subsurface Geological Laboratory in Regina, Saskatchewan. *Data provided on the graphic log for 100/07-19-045-06W5 was collected by K. Greff in 2011 and shared with the author. This information was supplemented by lithofacies interpretations presented by Marion (2019)..... 67

Table 3.2: Summary of lithofacies recorded in this study. 68

Table 4.1: List of wells and the core intervals used in this study. An ‘X’ indicates the allomember was observed in core at that well location. Grey shaded boxes indicate missing core interval. Yellow shaded boxes indicate the allomember was not preserved (i.e., lapped out) at that well location. 102

Table 4.2: Photoelectric effect measured values for different matrix materials. (From Ellis and Singer, 2008). 110

Table 4.3: Summary of lithofacies equivalent for the lithology maps shown in this study. Lithofacies descriptions are found in Chapter 3. 118

Table 4.4: Geophysical log data cut-off criteria used to classify mudstone, heterolithic, sandstone, and carbonate rich lithofacies in the lithology distribution maps. GR = Gamma ray. PE = photoelectric..... 121

Table 5.1: List of surfaces observed in cores. B = Bentonite. FS = Flooding surface. *DF* = Discrete flooding. CS = Condensed section. L = Lag. DL = Discrete lag. GF = Gradual flooding. LP = Geophysical log pick. *Not sampled. **Rubbled core. 125

Table 7.1: List of cores examined in this study, number of samples collected and the organic matter analysis type..... 228

Table 7.2: Estimated HI_0 values for lithofacies classifications..... 239

Table 8.1: Geochemical parameters indicating source rock quality. Modified from Peters and Casa (1994). 252

Table 8.2: Average total organic content per allomember and meridian to illustrate data variation stratigraphically and spatially. The bolded average values include all TOC data with the initial filter added (TOC values <0.5, Tmax <400, and S2< 0). The mean restored TOC data shown in italics have been filtered to remove TOC<1.5, as per Chen and Jiang (2015). HI₀ = estimated hydrogen index value used to estimate TOC₀..... 257

Table 8.3: Average total organic content per lithofacies. The lithofacies classification is sourced from core and geophysical log. 258

List of Figures

Figure 1:1: Regional map showing shale gas plays within North America. (United States Information and Administration, 2011). 2

Figure 1:2: Location of recent sedimentological (Tyagi, 2009; Mohebati, 2016; Zajac, 2016; Percy, 2019), petrophysical (Marion, 2019), and organic petrography and geochemistry (Synnott et al., 2017; Aviles, 2021) studies completed on the Colorado Group strata within the study area. 5

Figure 1:3: Summary diagram illustrating allostratigraphic relationships within the Upper Cretaceous, lower Colorado Group in central to northern Alberta (from Tyagi et al., 2007). . 7

Figure 2:1: West-east cross section along 49°, 45' North latitude illustrating the evolution of the western Canada foreland thrust and fold belt from Early Jurassic to Paleocene. Modified from Price (1994). 12

Figure 2:2: Schematic illustration of foreland basin development. Modified from Allen and Allen (2005). 15

Figure 2:3: Schematic diagrams illustrating principle loads in (A) peripheral and (B) retroarc foreland basin systems. Both basins experience topographic and sediment/basin fill loading. Peripheral foreland basins may also experience subduction loading from a vertical shear force (V) and bending moment (M) acting on the end of the subducting slab. Retroarc foreland basins may incur additional subsidence from dynamic slab loading. (Modified from DeCelles and Giles, 1996). 16

Figure 2:4: Illustration demonstrating elastic and viscoelastic response to loading on the lithosphere. Under elastic lithosphere conditions, the plate has instantaneous flex during loading and the wavelength of flexure is controlled by its flexural rigidity. A viscoelastic lithosphere initially behaves elastically, but the basin continues to relax and flex under a constant load, with no variance over time. (Jordan, 1995 after Beaumont, 1981 and Quinlan and Beaumont, 1984). 17

Figure 2:5: Illustration demonstrating the effect of stress on the base of the lithosphere from a subducting slab producing a negative mass anomaly in the mantle (Modified from Burgess and Moresi, 1999). 18

Figure 2:6: Schematic summarizing the subsidence history of the Western Canada Sedimentary Basin. Arrows show direction of craton (dark grey) movement. Hatched = accretionary wedge; Stippled = sediment infill. Modified from Peper (1993). 20

Figure 2:7: Schematic of retroarc foreland basin depozones. Abbreviations and Symbols: one-arm arrows indicate thrust direction; sedimentary basin (stippled); basement rock (diagonal lines); D (duplex); TF (thrust front); TZ (frontal triangle zone). Modified from DeCelles and Giles (1996). 22

Figure 2:8: Relative sea level history curves (A) and paleogeographic setting during the Greenhorn cycle (B). A) Relative sea level fluctuations from the Lower Albian to Upper Santonian (Kauffman and Caldwell, 1993). Black arrows indicate sea level rise (transgression), and grey arrows reflect a relative fall in sea-level (regression). The short-term sea level curve by Haq (2014) broadly mirrors the long-term sea level fluctuations observed and the occurrence of major transgression cycles labeled in the adjacent column. B) Illustration of the paleogeographic setting during the late Cenomanian to early Turonian when the Boreal and Tethyan seas had joined (Blakey, 2014). The WIS circulation was counter-clockwise during this time, with warm, normal salinity marine water from the proto-Gulf of Mexico migrating northward along the eastern margin and cool Polar water flowing adjacent to the fold and thrust belt (Arthur and Sageman, 2004; Kauffman and Caldwell, 1993). 26

Figure 2:9: Summary chart listing formations and their relationship to the allostratigraphic framework incorporated in this study. *U/Pb dates from Tyagi (2009). **U/Pb dates from Barker et al. (2011). 28

Figure 2:10: Correlation of lithostratigraphy and allostratigraphy with foraminiferal zones established for the Upper Colorado group. Bentonite stratigraphy is based on this study and Tyagi (2009). Image is modified from Caldwell et al. (1978), Tyagi (2009), and Tyagi et al. (2007). 29

Figure 2:11: Allostratigraphic nomenclature summary chart. Refer to text for detailed description of surfaces. The U-Pb date for the “Green” bentonite is from Tyagi (2009). The Bighorn River and X bentonite U-Pb dates are from Barker et al. (2011). 39

Figure 2:12: Schematic demonstrating stratigraphic relationships between the Dunvegan alloformation and surrounding formations. Modified from Plint (2000). 41

Figure 3:1: Nomenclature proposed by Lazar et al. (2015) to classify fine-grained sedimentary rocks. A) Terms to describe lamina attributes: continuity, shape, and geometry. B) Ternary diagram showing division of composition percentages and associated nomenclature. (Diagrams modified from Lazar et al. (2015)). 53

Figure 3:2: Elements of a shallow marine depositional system. A) Waves passing into shallow water and within wave base change to an elliptical orbit, causing oscillatory water movement just above the seabed. Shoreward, the waves become asymmetric and are shorter in wavelength (red arrow length) and faster flowing (red arrow thickness), compared to a longer duration and weaker velocity seaward movement of water (see inset). Stronger landward velocities (thicker red arrow in image A and inset) produce landward bed-load transport characterized by landward-directed cross-bedding and ripple lamination, as well as textural sorting of clastic material on the beach and shoreface that was too heavy for the lower-velocity seaward current (Clifton, 2006). Modified from Plint (2010). B) Profile of a shallow marine shelf. Modified from Clifton (2006). 55

Figure 3:3: Geostrophic flow develops when offshore moving bottom currents are redirected near parallel to shore by Coriolis force, resulting in sediment transport along the shelf. Modified from Plint (2010). 58

Figure 3:4: Sediment transport by hypopycnal and hyperpycnal plumes. Lower density (fresh) water floats on top of saline water, producing a buoyant hypopycnal plume. A hyperpycnal plume is a turbidity current that occurs at a river mouth when the density of the river water is greater than the density of seawater because of the suspended load it carries (Mulder and Syvitski, 1995). Hyperpycnal flows transport sediment along the sea floor through slope driven turbulence or wave and current aided gravity flows. White dashed arrow

reflects sediment resuspension by storms. Image modified from Bhattacharya and MacEachern (2009) and Schieber (2016). 61

Figure 3:5: Schematic of a conceptual proximal to distal mudstone depositional system. This illustration reflects the processes acting on sediment transport in the Western Interior Seaway. The numbers indicate siliciclastic mudstones (1), calcareous mudstones (2), and pelagic limestones (3), with low, good, and low preservation potential for marine organic matter, respectively. Modified from Hart (2016). 64

Figure 3:6: Illustration summarizing the proposed depositional model for the current study. Sedimentation occurred on a very low gradient, shallow marine ramp. Cartoon adapted from Varban and Plint (2008), Plint et al. (2012), Plint (2014), Hart (2016), Mohebati (2016), and Marion (2019). 66

Figure 3:7: Core example of lithofacies 1. A) and B) are sharp-based, fine-grained sandstones with hummocky cross stratification (yellow bar) and combined-flow ripples interspersed with silty planar, parallel to very slightly nonparallel and discontinuous, wavy, nonparallel mudstone laminae (blue bar). Image A shows millimetre- to centimetre-thick bone beds rich in phosphatic bioclastic debris (red bar). 70

Figure 3:8: Examples of lithofacies 2 as observed in cores from 103/06-04-017-13W4, 101/06-11-014-26W3 and 111/03-22-055-25W3. The images demonstrate a range of bioturbation intensity and sedimentary structures present in lithofacies 2. A) Continuous, planar, parallel to nonparallel and continuous, wavy, nonparallel silty mudstone and very fine-grained sandstone lamination with a BI of 0 to 1. An isolated hummocky cross stratified bed at the 32- to 28-centimetre mark on the yellow measuring tape represents the amalgamation and winnowing of thinner storm-deposited beds that resulted from sediment reworking during a large storm event (Varban and Plint, 2008b). Images B) and C) show increased bioturbation concentrations with BI levels between 3 and 4 that are predominately Planolites (P) and Chondrites (Ch), with fewer Skolithos (S), and a transition into continuous, wavy parallel to nonparallel bedding. D) Core photo shows the erosive contacts between massive mudstone and hummocky cross stratified to cross-bedded sandstone beds (white dashed line). Yellow dashed line marks contact between a mudstone bed and overlying

erosional sandstone. Thin black lines highlight internal stratification within the sandstone deposits. 74

Figure: 3:9 Two examples of lithofacies 2 sedimentary structures observed in cores 121/06-35-013-13W3 and 101/06-11-014-26W3. A) A dewatering structure (blue arrow) illustrates where fluid escaped upward from a fine-grained silt bed, into an overlying graded sandstone bed. The top of the feature is eroded, with subsequent deposition of a thin mudstone bed. The convoluted bed (yellow arrow) shows an overturned, slightly graded sandstone bed. Both features indicate a relatively unstable sediment column with high-water content that became disturbed during a high-energy event with strong currents. B) A fine-grained sandstone bed with climbing (white arrows), oscillatory-dominant storm flow structures. 76

Figure 3:11: Lithofacies 3 as seen in core from wells 131/11-09-017-23W2, 141/07-34-035-01W2 and 101/06-11-014-26W3. A) In this image, lithofacies 3 exhibits millimetre-scale, planar-parallel bedding with an interval of disturbed bedding signifying a shift to discontinuous, wavy, nonparallel bedding and an increase in biogenic debris (yellow bar). B) This interval reflects an increase in calcareous biogenic sediment content, with shell-rich beds (light grey). C) Graded coccolith-rich beds (light grey colour) interbedded with coccolith-poor beds (medium grey colour). The beds are predominately planar-parallel, with some occurrences of low angle cross bedding. Larger pieces (a few millimetres in length) of prismatic inoceramid shells lie parallel to bedding (black arrow). D) Core photograph of interbedded lithofacies 3 (blue bar) and Lithofacies 4 (red bar). Lithofacies 4 has a sharp lower contact and a gradual upper contact with Lithofacies 3. Bioturbation index in lithofacies 3 is within BI 1 and 2, with occurrences of *Planolites* (P) and *Thalassinoides* (Th). E) Example of a strongly bioturbated Lithofacies 3. Trace fossils identified include: *Planolites* (P), *Phycosiphon* (Ph), *Palaeophycus* (Pa), and *Teichichnus* (T)..... 79

Figure 3:12: Lithofacies 3 photomicrograph collage from cores 141/07-34-035-01W2 (A through D) and 111/03-22-055-25W3 (E through I). Red boxes in images A and E refer to sample location for the associated thin-sections. Images C, D, and F through I are photomicrographs taken in plane-polarized light. A) Core photograph of Lithofacies 3 from 141/07-34-035-01W2, 205.7 m to 205.59 m. B) A back-lit thin section scan, cross sectional view, showing millimetre-scale coarsening upward successions and intervals with increased

coccolith content (grading from dark grey to light grey). C) Bedding-parallel thin section of the same sample used in image (B) showing foraminiferal tests (Ft), faecal pellets (FP), organo-minerallic aggregates (Om), and pyrite (Py). D) Zoomed-in photomicrograph of image (B) thin section showing foraminiferal tests (Ft), faecal pellets (FP), phosphatic debris (Phs), and inoceramid prisms (In.P). F) Horizontally cut sample from 111/03-22-055-25W3 displaying a bedding-parallel view of Lithofacies 3. The matrix comprises speckled pyrite (Py), foraminiferal tests (Ft), faecal pellets (FP, blue dashed line) and organo-minerallic aggregates (Om, yellow dashed line) mixed with clay and silt. G and H) Cross sectional views of the sample from 111/03-22-055-25W3. The yellow box in G highlights a lamina that is mixed with inoceramid shell debris, organic matter, phosphatic material, and pyrite that likely reflects a storm event. In image H), two silt lamina are observed (yellow dashed lines) comprising silt grains, organic matter, and pyrite. I). Sediment surrounding an inoceramid prism that has undergone differential compaction. 81

Figure 3:13: Examples of Lithofacies 4 (red boxes) as observed in cores 101/06-11-014-26W3, 101/16-23-023-28W2 and 131/11-09-017-23W2. A) Three occurrences of Lithofacies 4 in the 101/06-11-014-26W3 core are bound between Lithofacies 3 deposits and mark a sharp transition from the thinly bedded calcareous mudstone into the mud-poor, biotic-rich sediment. B) The upper Lithofacies 4 deposit located at approximately 518.76 m is a massive, foraminiferal-rich packstone sharply overlying the ‘green bentonite’ mapped surface at the top of Allomember XI (white arrow). At approximately 519.39 m in image B, the Lithofacies 4 deposit contains glauconite grains and shell debris. The yellow arrow points to the mapped K1 surface at the top of Allomember V. C) represents an unconformable deposit of Lithofacies 4, sharply overlying Lithofacies 5 and underlying Lithofacies 2. D) A thin section photomicrograph from 101/16-23-023-28W2 at 518.76 m (just above the top of the ‘green bentonite’ surface in Image B)) showing biogenic grain-supported matrix with foraminiferal tests (Ft) and phosphatic bone fragment (Phs). E) A close-up photograph of the Lithofacies 4 example at approximately 519.40 m in Image B (red box). The red bar in Image E corresponds to the bed outlined in Image B. The surface separating Lithofacies 4 from the underlying dark coloured and chemically and mechanically altered bed is the mapped K1 surface, representing the top of Allomember V. 84

Figure 3:14: Collage of lithofacies 5 examples from 103/06-04-017-13W4 (A), 100/07-19-045-06W5 (B), 101/16-23-023-28W2 (C), and 142/05-08-018-28W3. Yellow arrows in image B show scoured bases of silt beds. White arrow in image (C) points to a prismatic inoceramid shell fragment situated parallel to the bedding plane..... 86

Figure 3:15: Core and photomicrograph images of Lithofacies 5 in east-central Saskatchewan from well 141/07-34-035-01W2. Image A) and B) illustrate Lithofacies 5 in core. C) (215.5 mKB) and D) (232 mKB) are photomicrographs from a core analysis report (TerraTek, 2008). The yellow dotted outline in images C and D marks a thin silt bed oriented parallel to the bedding plane. OM = organic matter; Phs = Phosphatic bone debris (yellow dotted line in image D)..... 87

Figure 3:16: Schematic diagram illustrating lithofacies successions observed within the study area (Image A). Image B is a shallow marine ramp cartoon (modified from Hart (2016) showing possible depositional positions of FS-1, FS-2, and FS-3. The proximal position includes coarsening-upward successions (Lithofacies 5 – Lithofacies 2 – Lithofacies 1, respectively), and the maximum flooding surface lies within the classic mudstone (Lithofacies 5 - F5) deposited above Lithofacies 1 (F1). In the proximal offshore, clastic supply is limited and productivity increases. At this location during transgression, the maximum flooding corresponds to a calcareous mudstone succession (Lithofacies 3 - F3). As regression begins, clastic supply is renewed and F5 is deposited. Maximum transgression at the distal end of the shelf records deposition of pelagic organisms, such as coccoliths and foraminifera, and no clastic mud supply (F4). The schematic for the distal offshore succession illustrates a gradual upward transition from Lithofacies 3 to 4, but it is noted that a sharp flooding surface could occur beneath the carbonate deposit. Clastic supply is reintroduced as regression continues across the basin and F3 is deposited. It is noted that this succession does not consider lithofacies juxtapositions resulting from unconformities, and that the successions presented here may not include lithofacies that were omitted, due to erosion or non-deposition, in the rock record. 91

Figure 4:1: The lithostratigraphic nomenclature (after Bloch et al., 1993 and Bloch et al., 1999) and Blackstone Alloformation classification scheme applied in this study (from Tyagi et al., 2007 and Tyagi, 2009). Allomember names are in Roman numerals, I to XI. Previously

named allomember bounding surfaces are listed on the left in the “Allostratigraphic Framework” column. The surfaces bounding the tops of allomembers VII, IX, and X are titled VII, IX and X, respectively. Refer to Chapter 2 for a description on the nature of the allomember surfaces. 93

Figure 4:2: A) Schematic diagram showing relationships between relative sea level, water depth, eustasy, and datum reference points. Modified from Posamentier et al. (1988) and SEPM (2021). B) Illustration demonstrating the relationship between relative sea level rise or fall and changes in tectonic activity and/or eustasy. Modified from Catuneanu (2002) and Hooper (2019). 95

Figure 4:3: Illustration demonstrating the relationship between accommodation (A) and sediment supply (S). Modified from Possametier and Allen (1999). 97

Figure 4:4: A) Wheel diagram showing the progression of a system tract sequence, which begins at the sequence boundary. B) Illustration demonstrating the relationship between sea level change and system tract development. A change in relative sea level is indicated by a gradual change in colour from light to dark blue. Green text reflects sea level fall and blue coloured text signifies a rise in sea level. Red text defines the bounding surface type separating the system tracts. Modified from Nichols (2009) and Plint and Nummedal (2000). 98

Figure 4:5: Map showing working and summary cross-section lines. Summary cross-sections are presented at the end of the thesis. Cores assessed in the study are marked with a red star. Tyagi (2009) study area, from which the allostratigraphic framework of this study was based, is shown with a black dashed outline. 100

Figure 4:6: Comprehensive diagram highlighting geophysical well log responses to changes in lithology. The stratigraphic log describes core from well location 103/06-04-017-13W4, between 624 and 703 mKB. Bentonite beds, marked with red x's, produce a clear response on the log curves where the gamma ray curve sharply increases, accompanied with low spikes in both resistivity and P_e . Flooding surfaces identified in core correspond to a rise in gamma ray API values and decrease in resistivity. It is acknowledged that additional bounding discontinuities occur between the labeled allomembers (i.e. flooding surfaces),

however, this project only maps regionally extensive surfaces established in the original allostratigraphic study of Tyagi (2009). Correlating bounding discontinuities found within the allomembers to make conclusions about the internal stratigraphy of each unit would require a larger project scope. Intervals that have a higher amount of carbonate correspond to an increase in measured P_e values to about 3.5 or greater. 104

Figure 4:7: Diagram illustrating the different depths of investigation for laterolog and induction tools. The ‘distance’ represents distance from the wellbore. Modified from Glover (2000). 115

Figure 4:8: Photograph of core interval 624.0 mKB to 638.53 mKB at 103/06-04-017-13W4 (lower image) at 103/06-04-017-13W4 (A) with the corresponding stratigraphic log and litho code (upper image) illustrating the correlation between the core and the calculated lithologies. The core photo represents the stratigraphic column outline in the red box and shows what the calculated lithologies look like. Heterolithic sediment of lithofacies 2 at the base of the red box outline correlates to the left side of the core photo, within Allomember VI. Moving up section, the lithology transitions into a sandstone-rich rock, which registers in the calculated lithology column. The bentonite and overlying mudstones are recorded in the litho-code column (shown in brown) and is overlain by calcareous-rich mudstones (shown in light and dark blue). The dark blue colour in the litho-code column indicates photoelectric values greater than 4. ‘Green’ = Green bentonite at the top of allomember XI. ‘X’ is the top of allomember X. ‘Blue’ = blue bentonite at the top of allomember VIII. ‘Red’ = Bighorn River Bentonite at the top of allomember VI. ‘K1’ = the K1 disconformity at the top of allomember V. The top of allomember IV is the “X” transgressive surface. 120

Figure 5:1: Allostratigraphic and lithostratigraphic chart for the study interval. TS = transgressive surface. 124

Figure 5:2: FSU bioclastic lag (yellow arrow) and underlying bentonite (light-coloured interval with base depth of 8069.6 mKB) as observed in core 100/02-34-025-15W4. Base of the core is at the bottom left corner of image and the top of the core is upper right corner of image. 128

Figure 5:3: Core photograph showing the surfaces at the top of allomember III in cores 142/05-08-018-28W3 (A), 101/06-11-014-26W3 (B), and 111/03-22-055-25W3 (C). (A): Two calcareous lags (red bar and blue bar noting a recumbent folded lag) with abundant phosphatic fish debris. Yellow box is location of magnified core image from the recumbent folded lag. Yellow dotted circle shows intraclast at top of cross-bedded lag bed. (B): Fine-grained sandstone transgressive lag with fish debris (black bar). (C): Lag containing phosphatic fish debris, fine-grained sandstone and glauconitic sandstone grains, and rare millimetre-sized, rounded fine-grained glauconitic sandstone rip up clasts (orange bar). ... 132

Figure 5:4: Photo collage showing the K1 surface in core. The coloured stars correspond to the core locations on the inset map: Red star = 142/05-08-018-28W3; blue star = 101/06-11-014-26W3; yellow star = 111/03-22-055-23W3; green star = 101/16-23-023-28W2; and orange star = 141/07-34-035-01W2. K1 in southwestern Saskatchewan (101/06-11-014-26W3) is at the base of a condensed section (blue bar). The condensed section is overlain by a calcareous argillaceous mudstone bioturbated with *Planolites* (P) and *Thalassinoides* (Th). At 101/16-23-023-28W2 (green star), beneath the K1 surface is bioturbated carbonate mud with *Palaeophycus* (Pa), and *Teichichnus* (T), indicating a shifting substrate condition and an abrupt change from the depositional conditions of the underlying pelagic, calcareous mudstone. The trace fossils are proximal expressions of the Cruziana ichnofacies and include the lower energy environments within the offshore to very distal fringes of the lower shoreface. 135

Figure 5:5: Cross section 1-1' 141

Figure 5:6: Cross section 2-2' 142

Figure 5:7: Cross section 3-3' 143

Figure 5:8: Cross section 4-4' 144

Figure 5:9: Cross section 5-5' 145

Figure 5:10: Cross section A-A'' 149

Figure 5:11: Cross section B-B'' 150

Figure 5:12: Cross section C-C'	151
Figure 5:13: Cross section D-D'	152
Figure 5:14: Cross section E-E'	153
Figure 5:15: Cross section F-F'	154
Figure 5:16: Cross section G-G'	155
Figure 5:17: Cross section H-H'	156
Figure 5:18: Cross section I – I'	157
Figure 5:19: Cross section J-J'	158
Figure 5:20: Structural element map for the WCSB. Elements outlined in red reflect positive structural relief elements. Black lines and dashed lines outline tectonic domains underlying the WCSB. Modified from Wright et al. (1994) and Ross et al. (1994).	164
Figure 5:21: Processed magnetic map (Map 25) developed from potential-field geophysical data (Map modified from Lyatski et al. (2005)).	166
Figure 5:22: (A) Isopach map of allomember I. (B) Isopach map with structural features overlay. Lineaments mapped from Lyatski et al. (2005) = solid orange lines. Basement domains (black dashed lines) are from Ross et al. (1994). Lochend hinge zone = red dashed line. Mapped faults from Shank (2012) = blue lines. Eastend-Maple Creek lineament = purple dashed line. Base of Fish Scales to Viking Formation thickness = green lines; contours interval is 20 metres. Locations of the Punnichy Arch and Tabbenor lineament belt are from Christopher et al. (2006).	167
Figure 5:23: (A) Isopach map of allomember II. (B) Isopach map with structural features overlay. Lineaments (Lyatski et al. 2005) = solid orange lines. Basement domains (Ross et al., 1994) = black and blue dashed lines. Kevin Sunburst Dome and Bow Island Arch from Wright et al. (1994). Coburg Syncline from Frank (2006). Punnichy Arch and Tabbenor lineament belt are from Christopher et al. (2006).	169

Figure 5:24: (A) Isopach map of allomember III. (B) Isopach map with structural features overlay. Basement domains (Ross et al., 1994) = black dashed lines.	171
Figure 5:25: (A) Isopach map of allomember IV. (B) Isopach map with structural features overlay. Lineaments (Lyatski et al. 2005) = solid orange lines.	172
Figure 5:26: (A) Isopach map of allomember V. (B) Isopach map with structural features overlay. Basement domains (Ross et al., 1994) = black dashed lines. Lineaments (Lyatski et al. 2005) = solid orange lines.	173
Figure 5:27: (A) Isopach map of allomember VI. (B) Isopach map with structural features overlay. Lineaments (Lyatski et al. 2005) = solid orange lines.	175
Figure 5:28: Isopach map of allomember VII.	176
5:29: Isopach map of allomember VIII.	177
Figure 5:30: (A) Isopach map of allomember IX. (B) Isopach map with structural features overlay. Basement domains (Ross et al., 1994) = black dashed lines.	179
5:31: (A) Isopach map of allomember X. (B) Isopach map with structural features overlay. Lochend hinge zone = blue dashed line. Axis of subtle thickness high = orange dashed line.	180
5:32: (A) Isopach map of allomember XI. (B) Isopach map with structural features overlay. Basement domains (Ross et al., 1994) = solid black lines. Interpreted backbulge region = green dashed line.	181
Figure 6:1: Allomember I percent lithology maps.	184
Figure 6:2: Allomember I percent lithology summary map.	185
Figure 6:3: Allomember II percent lithology maps.	187
Figure 6:4: Allomember II percent lithology summary map.	188
Figure 6:5: Allomember III percent lithology map.	190

Figure 6:6: Allomember III percent lithology summary map. Red arrow = refer to text.	191
Figure 6:7: Allomember IV percent lithology maps.....	193
Figure 6:8: Allomember IV percent lithology summary map.	194
Figure 6:9: Allomember V percent lithology maps.	196
Figure 6:10: Allomember V percent lithology summary map.....	197
Figure 6:11: Allomember VI percent lithology maps.....	199
Figure 6:12: Percent lithology summary map.....	200
Figure 6:13: Lithofacies relationship between calcareous and non-calcareous Greenhorn Formation and Belle Fourche Formation, respectively. Sections were correlated using bentonite (X, G, T) and calcarenite (a, b, c) event marker beds. In a percentage lithofacies map, as used in this study, the lithofacies distribution would show non-calcareous mudstone at the Torgerson Draw, Model T, and Thompson Creek locations and calcareous for the Stoneville Flats and Bull Creek. Because the location on the lithofacies percentage map only shows what the predominant lithofacies is for that location, this can create areally separated patches in plan view on a map, compared to a laterally continuous, linear deposit. Illustration modified from Fisher et al. (1994).....	201
Figure 6:14: Illustration showing three hypothetical types of water mass boundaries occurring between Arctic (northern) and proto-Gulf of Mexico (southern) seaways, and the associated microfauna and microflora. Figure modified from Fisher et al. (1994).	203
Figure 6:15: Allomember VII percent lithology maps.	204
Figure 6:16: Allomember VII percent lithology summary map.....	205
Figure 6:17: Illustration of the Kaskapau Formation mud-dominated ramp sequence (Figure modified and text summarized from Varban and Plint, 2008a). Shoreface and coastal plain deposits in image A undergo aggradation during rapid sea-level rise, limiting basinward transport of mud. During lower rate of relative sea-level rise (image B), combined flows carry muddy heterolithic deposits seaward and form a broad sub-aqueous platform. In the	

Kaskapau Formation, the upper surface of the platform defines the accommodation envelope and the top of each allomember mapped by Varban and Plint (2008b). The authors inferred that sediment accumulated up to the accommodation envelope, which is equivalent to the top of each of their allomembers, and excess sediment beyond that upper boundary was reworked further offshore and along-shelf. During modest relative sea-level fall (image C), a sharp-based shoreface progrades across the shallow, near-horizontal surface of the inner ramp. . 207

Figure 6:18: Allomember VIII percent lithology maps. 208

Figure 6:19: Allomember VIII percent lithology summary map. 209

Figure 6:20: Allomember IX percent lithology maps. 211

Figure 6:21: Allomember IX percent lithology summary map. 212

Figure 6:22: Allomember X percent lithology maps. 213

Figure 6:23: Allomember X percent lithology summary map. 214

Figure 6:24: Allomember XI percent lithology maps. 216

Figure 6:25: Allomember XI percent lithology summary map. 217

Figure 7:1: Schematic of the factors that influence production of organic carbon in marine sediments. Modified from Suter (2006). 222

Figure 7:2: Illustration depicting the production of marine snow. Modified from Alldredge and Silver (1988). 223

Figure 7:3: Diagram of organic matter analyzed, and the associated variables produced during Rock-Eval 6 pyrolysis. OM = organic matter. HCs = hydrocarbons. (Modified from Lafargue *et al.*, 1998). 230

Figure 7:4: Graphic of pyrolysis and oxidation processes, illustrating the measurement and calculation of TOC and mineral carbon using a Rock-Eval 6 apparatus. Modified from Behar *et al.*, 2001. 231

Figure 7:5: HI₀ distribution of calcareous mudstone (A), silty argillaceous mudstone (B), and heterolithic sandstone lithofacies(C) classified, thermally immature samples. Exceedance probabilities (P10, P50, and P90) denoted with a red line..... 240

Figure 7:6: S2 vs. TOC diagram showing estimated HI₀ when data is segregated by formation (A) and lithofacies classification (B). 241

Figure 8:1: Pseudo-Van Krevelan (A) and HI vs. Tmax (B) diagrams for samples collected from the Fish Scales Formation. A) Diagram shows that the majority of data fall into Type II to Type III kerogen types and TOC (bubble size) decreases as thermal maturity increases (maturity increases as data approaches point of origin). B) Samples from W1, W2 and W3 are identified as immature, Meridian 4 data points are mainly immature with a few mature, and all samples from W5 and W6 wells plot within the mature hydrocarbon window. Similar to diagram A), the samples plot along the Type II-III classification. 246

Figure 8:2: Pseudo-Van Krevelan (A) and HI vs. Tmax (B) diagrams for samples collected from the Belle Fourche Formation. A) Diagram shows that TOC (bubble size) decreases as thermal maturity increases (maturity increases as data approaches point of origin). The samples lie within the Type II, III, and IV classification, but majority of the data is Type II. B) Immature samples are from wells located in W1, W2, W3 and W4 and mature data is largely from wells in W5 and W6. Much of the data is Type II-III to Type III kerogen. 247

Figure 8:3: Pseudo-Van Krevelan (A) and HI vs. Tmax (B) diagrams for samples collected from the Second White Specks Formation. Similar to the Fish Scales and Belle Fourche formations, the pseudo-Van Krevelan diagram (A) shows that TOC (bubble size) decreases as thermal maturity increases (maturity increases as data approaches point of origin). The samples are predominantly Type II, with some scatter in the Types III and IV domain. In diagram B), the immature samples have higher TOC and are from wells located in W2, W3 and W4. Samples from Meridian 5 are mostly mature with some immature data points, with all W6 data points plotting as mature. 249

Figure 8:4: Pseudo-Van Krevelan (A) and HI vs. Tmax (B) diagrams showing data segregated by lithofacies classification. Core samples from calcareous mudstone and silty argillaceous mudstone lithofacies are Type II to Type II-III kerogen and samples in both

plots are dominantly immature with some scatter of data suggesting increased thermal maturity. Samples with a heterolithic sandstone and mudstone classification are Type II to Type III, with higher occurrences of Type III and IV than of Type II. 250

Figure 8:5: Mean thermal maturity map for the Fish Scales, Belle Fourche, and Second White Specks formations of the Upper Cretaceous Colorado Group. Modified from Flynn and Cheadle (2013). 251

Figure 8:6: S2 vs TOC diagrams for the Second White Specks (A), Belle Fourche (B), and Fish Scales (C) formations. The diagrams show that source rock quality in the formations ranges between poor and excellent generation potential and fair to excellent organic matter richness. 254

Figure 8:7: S2 vs TOC diagram showing source rock generation potential and organic matter richness for data with corresponding lithofacies classification data. The trends show that the best source rock generation potential (S2) and organic matter richness (TOC) occurs in calcareous mudstones and silty argillaceous mudstones. No samples from sandstone (Lithofacies 1) or foraminifera- and coccolith-rich packstone-grainstone (Lithofacies 4) intervals in the cores had accompanying TOC data. 256

Figure 8:8: Core photo of 103/06-04-017-13W4 showing sandstone, calcareous mudstone and heterolithic sandstone and mudstone in allomembers VI, VIII and XI and TOC values obtained from samples. The TOC is lowest in heterolithic sandstone and mudstone and highest in calcareous mudstone. The increase in TOC that occurs in samples within allomember X compared to the samples in allomember VI may be associated with a relative decrease in quartz content, demonstrating a link between TOC preservation and changes in mineral content. 259

Figure 8:9: Core photo of 111/03-2-055-25W3 showing TOC results for samples collected from heterolithic sandstone and mudstone, silty argillaceous mudstone, and calcareous mudstone in allomember II. The highest TOC values are from silty argillaceous mudstone and calcareous mudstone samples. 260

Figure 8:10: Core photo of TOC results from samples collected from silty argillaceous mudstone and calcareous mudstone in well 141/07-34-035-01W2 and TOC results. The TOC varies between 4.10 and 11.08 wt.%. 261

Figure 8:11: North-south summary cross section showing total organic content and corresponding lithofacies classification. Thermally mature samples greater than the 1.5 wt.% cutoff criteria were restored to original total organic content. An estimated HI_0 of 800 was used for some samples in 100/07-22-040-04W where the TOC_{pd} remained higher than the estimated TOC_0 when using estimated HI_0 values 600, 450, 335 and 182. Data from all wells except for 100/07-19-045-06W5, where the core was logged and sampled in this study, were correlated to the adjacent well to designate a lithofacies classification. The red line at 2 wt.% indicates the total organic content cutoff for very good generation potential. The lithofacies classification in 100/07-19-045-01W6 is interpreted from core logged by K. Greff (date unknown) and Marion (2019). It is possible that the interpreted lithofacies that came from those descriptions did not match entirely and the material contained more sandstone than described. This could explain the distinct shift to lower TOC values within the middle to upper strata of allomember VI. 262

Figure 8:12: West to east summary cross section showing total organic content data with corresponding lithofacies classification. Data from 102/11-06-029-20W4 and 100/14-34-029-15W4 were correlated to 100/06-03-030-20W4 and 100/08-36-030-16W4, respectively, to assign lithofacies classifications to the samples. Well 141/07-34-035-01W2 was logged and sampled for this study. The red line at 2 wt.% indicates the total organic content cutoff for very good generation potential. 263

Figure 8:13: Stratigraphic log and lithofacies classification alongside geophysical well log and TOC data. Note that within the argillaceous mudstone intervals, TOC increases with decreasing quartz content. Also, within calcareous mudstone, TOC increases with decreasing calcite content. 267

Chapter 1

1 Introduction

The purpose of this thesis is to evaluate whether the controls on preservation and stratigraphic distribution of organic matter are unique to foreland basin depozones within the Western Canada Foreland Basin (WCFB). This is accomplished by integrating organic geochemical data obtained from programmed pyrolysis (Rock-Eval II and Rock-Eval 6) and direct combustion (LECO SC-444) into a basinwide allostratigraphic framework. The framework was created using high-resolution allostratigraphic correlations that link the established work by Tyagi (2009) and Tyagi et al. (2007) in the foredeep to the forebulge and backbulge regions of the basin. Results from this work will aid the current understanding of basin controls influencing organic matter distribution within an epicontinental basin.

1.1 Problem

Initial success with horizontal drilling and hydraulic fracturing in hydrocarbon-rich “shale” reservoirs, herein referred to as source-rock reservoirs, began in the Barnett Shale in 2000 (Kuuskraa et al., 2013). This paved the way for exploitation of other major shale basins in the United States, such as the Bakken, Fayetteville, Haynesville, Woodford and Marcellus (Figure 1.1). In Canada, shale basins under development include, but are not limited to, the WCFB in Alberta and Saskatchewan, Willison Basin in southern Saskatchewan, and the Horn River Basin in north-western British Columbia.

Although drilling practices have improved hydrocarbon extraction from unconventional reservoirs, production performance (i.e.: initial rate, decline rate, estimated ultimate recovery) remains largely inconsistent (Baihy et al., 2010). Recent studies suggest this is related to the extremely heterogeneous nature and complex internal fabric of the rock (i.e., Marion, 2019). The inability to characterize heterogeneity within mudstone petroleum systems introduces uncertainty into characterization models, resulting in



Figure 1:1: Regional map showing shale gas plays within North America. (United States Information and Administration, 2011).

inaccurate predictions of recoverable reserves and decline behaviour of the reservoir. Petroleum system characterization must explicitly address process dynamics leading to mudstone heterogeneity in order to predict hydrocarbon flow behaviour in these complex reservoirs (Aplin and MacQuaker, 2011; Cheadle, 2011). Relating depositional processes that encourage organic matter preservation to stratal packaging in a basin evolution context affords better prediction of stratigraphic and geographic limits of discrete carbonaceous mudstone petroleum systems.

Historically, it was believed that organic-rich mudstones were deposited under low-energy and anoxic to dysoxic conditions, where productivity was high and sediment accumulation rates were low (e.g., Didyk et al., 1978; Katz, 2005; Tyson, 2000). Recent studies have found evidence that organic matter can be preserved in relatively high energy, shallow water depositional environments through the formation of intraclastic and organo-mineralic aggregates (e.g., Ghadeer and Macquaker, 2012; Plint, 2014; Percy, 2019), and under conditions of fluctuating bottom water oxygenation (e.g., Wright and Friedrichs, 2006, Schieber et al., 2007; Macquaker et al., 2010b; Aplin and Macquaker, 2011). Recent studies on the Colorado Group in the foredeep region of the WCFB recognize heterogeneity at multiple scales and its influence on organic matter and reservoir quality in self-sourcing carbonaceous mudstones (Zajac, 2016; Synnott et al., 2017; Marion, 2019; Percy, 2019; Aviles, 2021) (Figure 1.2). Although long-distance advective transport and preservation of organic-rich mud floccule aggregates through storm-induced currents and wave-enhanced sediment gravity flows has been documented in the WCFB foredeep (e.g., Plint et al., 2012; Plint, 2014; Zajac, 2016; Percy, 2019), it is currently unknown if these controls contribute to organic matter distribution and preservation in forebulge or backbulge segments of the basin.

Hart (2016) proposed a conceptual lithofacies model for marine mudstone source rocks that used lithology, sedimentology, and bulk-geochemical data to assess the link between sedimentary processes and the preservation potential of marine organic matter. Using data from the Western Interior Seaway, Hart (2016) demonstrated that the model appropriately predicted lithology and marine organic matter distribution trends from proximal to distal settings (depositional dip orientation). Can organic matter distribution

be reliably predicted for the Blackstone Alloformation by upscaling lithofacies to basin scale?

Temporal and spatial controls on organic matter preservation in organic-rich mudstones can be revealed by mapping coeval stratal packages. Allostratigraphy divides units based on regionally mappable bounding discontinuities, such as marine flooding surfaces or bentonites (NACSN, 2005). This approach separates rock packages into genetic units that are considered to approximate chronostratigraphic units (Plint et al., 2009). High-frequency allostratigraphic correlations highlight lateral changes in the rock on a regional scale and provide a practical method for identifying temporal relationships within a chronostratigraphic framework (i.e. Bhattacharya and Walker, 1991). Recent studies have developed a chronostratigraphic context that exposes spatial and temporal relationships between tectonic loading, forebulge response and resulting stratal packaging in Western Canada foredeep to forebulge deposits (ie. Tyagi et al., 2007; Varban and Plint, 2008b; Tyagi, 2009). To date, lithostratigraphic (i.e.: Bloch et al., 1993, Bloch et al., 1999, Tu et al., 2007) and biostratigraphic (i.e. Schroder-Adams et al., 1996) frameworks have been developed for the distal forebulge and backbulge segments of the WCFB. Although these studies have provided valuable information regarding depositional history of the lower Colorado Group, the method is ineffective when evaluating time-related sedimentation and basin history. The relationship between foredeep and backbulge strata packages, and the conditions in which they were deposited remains poorly understood.

This varied record, along with abundant public domain data available from oil and gas exploration in Alberta and Saskatchewan, provides an exceptional opportunity to investigate the allogenic controls on carbonaceous mudstone reservoir development. Furthermore, extensive drilling in the WCFB has produced a valuable collection of well log and core data that allows correlation of key surfaces with confidence.

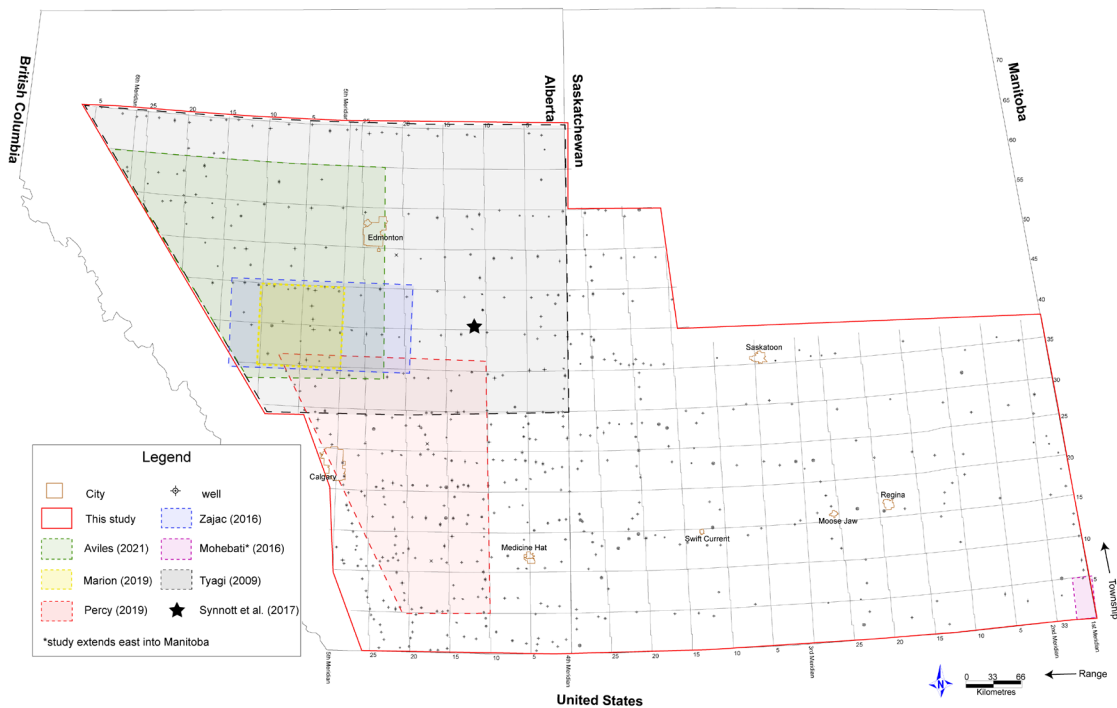


Figure 1:2: Location of recent sedimentological (Tyagi, 2009; Mohebati, 2016; Zajac, 2016; Percy, 2019), petrophysical (Marion, 2019), and organic petrography and geochemistry (Synnott et al., 2017; Aviles, 2021) studies completed on the Colorado Group strata within the study area.

1.2 Aim and Objectives

The goal of this work is to assess sediment distribution and organic geochemical properties of the Blackstone Alloformation strata within a basinwide allostratigraphic framework, using core, geophysical logs, and programmed pyrolysis data. **It is hypothesized that the depositional conditions required for the accumulation of organic matter across the Western Canada Foreland Basin during deposition of the Upper Cretaceous Colorado Group are inherently linked to basin-scale allogenic processes.**

This study has the following objectives:

- Create a basinwide allostratigraphic framework for the Blackstone Alloformation to reveal 3-Dimensional stratal architecture within the allomembers.
- Determine temporal and spatial evolution of subsidence during deposition of the study interval.
- Map lithofacies distribution across the basin within the allostratigraphic framework to reveal sedimentation patterns that occurred in response to tectonic and eustatic controls on sediment deposition and determine if the patterns are linked to specific depozones in the Western Canada Foreland Basin.
- Link programmed pyrolysis data to basinwide lithology distribution to investigate how allogenic drivers influence organic matter distribution, spatially and stratigraphically, across the Western Canada Foreland Basin.

1.3 Database

To address project objectives, a basinwide allostratigraphic framework was developed for the study interval, reconciling the established network by Tyagi (2009) in the foredeep with the lithostratigraphic-based framework (i.e. Bloch et al., 1993) in the backbulge segment of the WCFB (Figure 1.3). Previously published major marine flooding surfaces, unconformities, and regionally extensive bentonites identified in central to northern Alberta (Tyagi, 2009) were extended into southern Alberta (from Township 30 to Township 1) and eastward through Saskatchewan (extending from Township 1 to 65) to

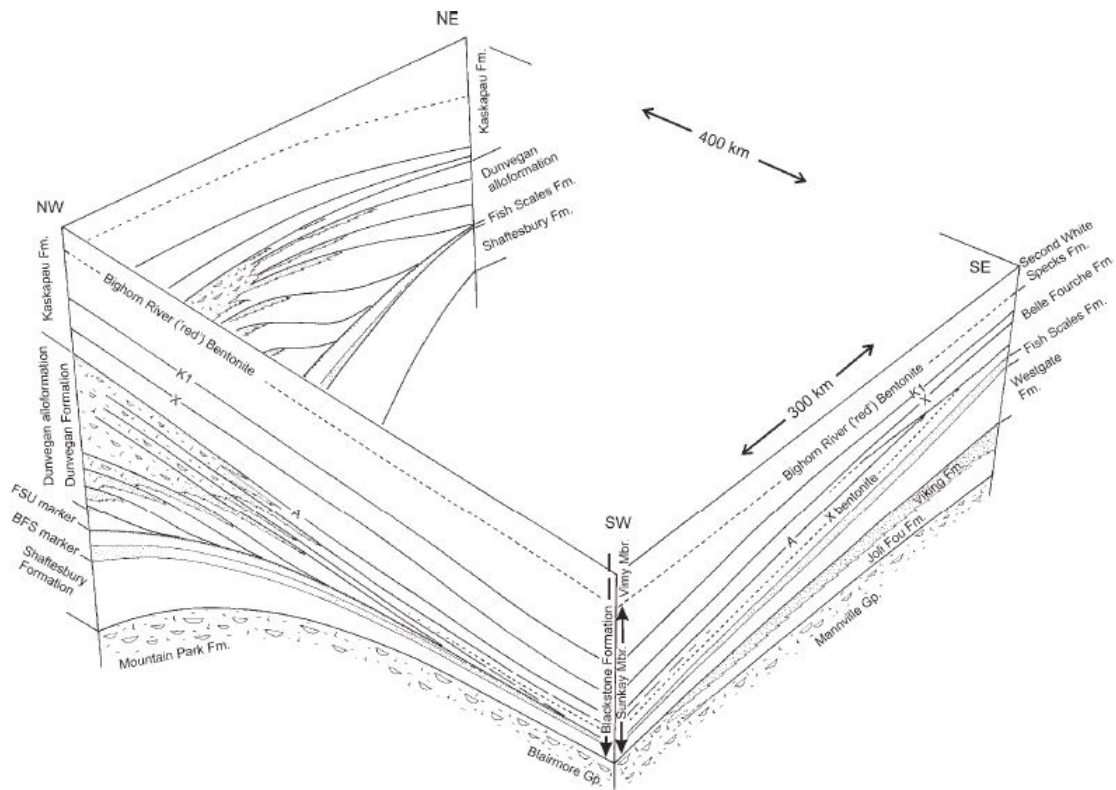


Figure 1:3: Summary diagram illustrating allostratigraphic relationships within the Upper Cretaceous, lower Colorado Group in central to northern Alberta (from Tyagi et al., 2007).

the Manitoba border (Figure 1.3). Twelve regional bounding surfaces were mapped in 574 wells using geophysical well logs and 18 cores located in Alberta and Saskatchewan. Surfaces observed in core were used to ground-truth geophysical log signatures, and then mapped through a grid of cross sections that span the study area. Well control is greatest in regions of high hydrocarbon production, typically in Alberta and southern Saskatchewan where correlation lines cross into the Williston Basin area. Where possible, cross sections in this study incorporate wells used in previously published studies for the lower Colorado Group (e.g. Bloch et al., 1993; Bloch et al., 1999; Christopher and Yurkowski, 2005; Schroder-Adams et al. 1996; Varban and Plint, 2005) to avoid re-examining wells that have already undergone geophysical sampling and to integrate legacy data into this new framework.

A database of over 2000 legacy and 482 newly-collected organic geochemical and thermal maturity data was compiled to assess organic matter preservation and distribution across the study area. Legacy data were collected from Bulletin and Open File reports published by the Geological Survey of Canada (Bloch and Leckie, 1993; Bloch et al., 1999; Fowler and Snowdon, 1998a; Fowler and Snowdon, 1998b; Snowdon, 1994a; Snowdon, 1994b; Snowdon, 1995; Snowdon and Riediger, 1995a; Snowdon and Riediger, 1995b; Snowdon, 1996; Snowdon, 1997). The Natural Resources Canada website provides access to the GEOSCAN database for searching and downloading Open File reports and associated raw data. Legacy data was filtered based on stratigraphic coverage within the Colorado Group interval and parameter cut-offs applied in the geochemical data report by Obermajer et al (2007). Data with less than or equal to 0.5% TOC and OI values greater than 150 mg/g TOC were filtered from the database.

New organic geochemical data was obtained from samples collected from cores located within the foredeep, forebulge, and backbulge segments of the basin. Samples were analyzed using Rock-Eval 6 and LECO CS-244. Core sample locations were chosen based on the amount of core recovery, presence of an organic-rich interval (indicated by a high Gamma-Ray log response ($> \sim 100$ API)), and well location within the basin.

Samples were collected at 1-metre intervals when permitted, with sample frequency increasing across zones of interest.

1.4 Significance

In the United States, production of shale gas and tight oil is projected to increase to nearly 34 trillion cubic feet by 2050 (Aizarani, 2023). Oil and gas extraction from shale and tight reservoirs in Canada is expected to increase as traditional oil production declines (NRC, 2020). This work will help improve the current understanding of controls on organic matter distribution and provide a predictive framework to reduce uncertainty in characterization models for tight oil and gas resources and improve predictions for recoverable reserves.

Chapter 2

2 Geological setting, development of the Western Canada Foreland Basin, and evolution of the Upper Cretaceous Colorado Group

This study focuses on the mudstone-dominated Upper Cretaceous, Colorado Group of the Western Canada Foreland Basin (WCFB), specifically the Fish Scales, Belle Fourche, and Second White Specks formations. The Fish Scales through Second White Specks were deposited as a shallow-marine sequence in the Western Interior Seaway (WIS) from Early Cenomanian to Middle Turonian (Schroder-Adams et al., 1996). Since the interval spans the foredeep, forebulge, and backbulge segments of the WCFB, it provides a record of a basinwide response to time-variant and paleogeographically diverse tectonic, eustatic and climatic controls that influenced a broad spectrum of depositional and burial histories of carbonaceous mudstone strata (Schröder-Adams, et al., 2001; Tyagi et al., 2007; Varban and Plint, 2008; Hu and Plint, 2009). The geologic (spatial and temporal) context of the study interval establishes the relationship between basin evolution, sedimentary lithofacies and organic matter preservation.

This chapter begins by summarizing the tectonic evolution of the Western Canada Sedimentary Basin (WCSB), mechanisms controlling foreland basin development, and subsidence history. The remainder of the chapter comprises the paleogeographic setting and a detailed literature review of the lithostratigraphic and allostratigraphic frameworks established for the Colorado Group in Western Canada.

2.1 Geological history of the Western Canada Sedimentary Basin

The WCSB formed during two stages of tectonic evolution: the Late Proterozoic to Late Jurassic passive margin stage and the Late Jurassic to Early Eocene foreland basin stage (Price, 1994). The passive margin stage developed during a prolonged period of thermal relaxation and subsidence following rifting from of the Rodinia supercontinent in latest Proterozoic or earliest Cambrian (Bond and Kominz, 1984; Price, 1994; Miall, 2010).

This stage is marked by thick siliciclastic and carbonate successions (Porter et al., 1982; Price, 1994).

The WCFB is a northeasterly tapering, supracrustal wedge of sedimentary rock that spans between British Columbia and Manitoba, eventually onlapping the underlying Precambrian crystalline rocks of the North American craton (Price, 1994). The basin is more than 6000 kilometres long and up to 6 kilometres deep along its western margin (Leckie and Smith, 1992). The WCFB formed in response to plate tectonic events that took place during Middle Jurassic to early Tertiary (Leckie and Smith, 1992). Sea floor spreading occurring in the North Atlantic caused the North American plate to migrate northwestward, overriding the Farallon plate that was subducting below the western edge of North America (Kauffman and Caldwell, 1993). The collision caused the supracrustal wedge to detach from the basement and undergo tectonic thickening and thrusting (Fig. 2.1) (Kauffman and Caldwell, 1993; Price, 1994). The folding and increased sediment loading induced flexural subsidence of the foreland basin, causing uplift and subsequent erosion of the supracrustal wedge (Price, 1994). The cycle of thrusting and folding, uplift, and deposition of cannibalized sediment in the WCFB continued until Early to Middle Eocene (Price, 1994).

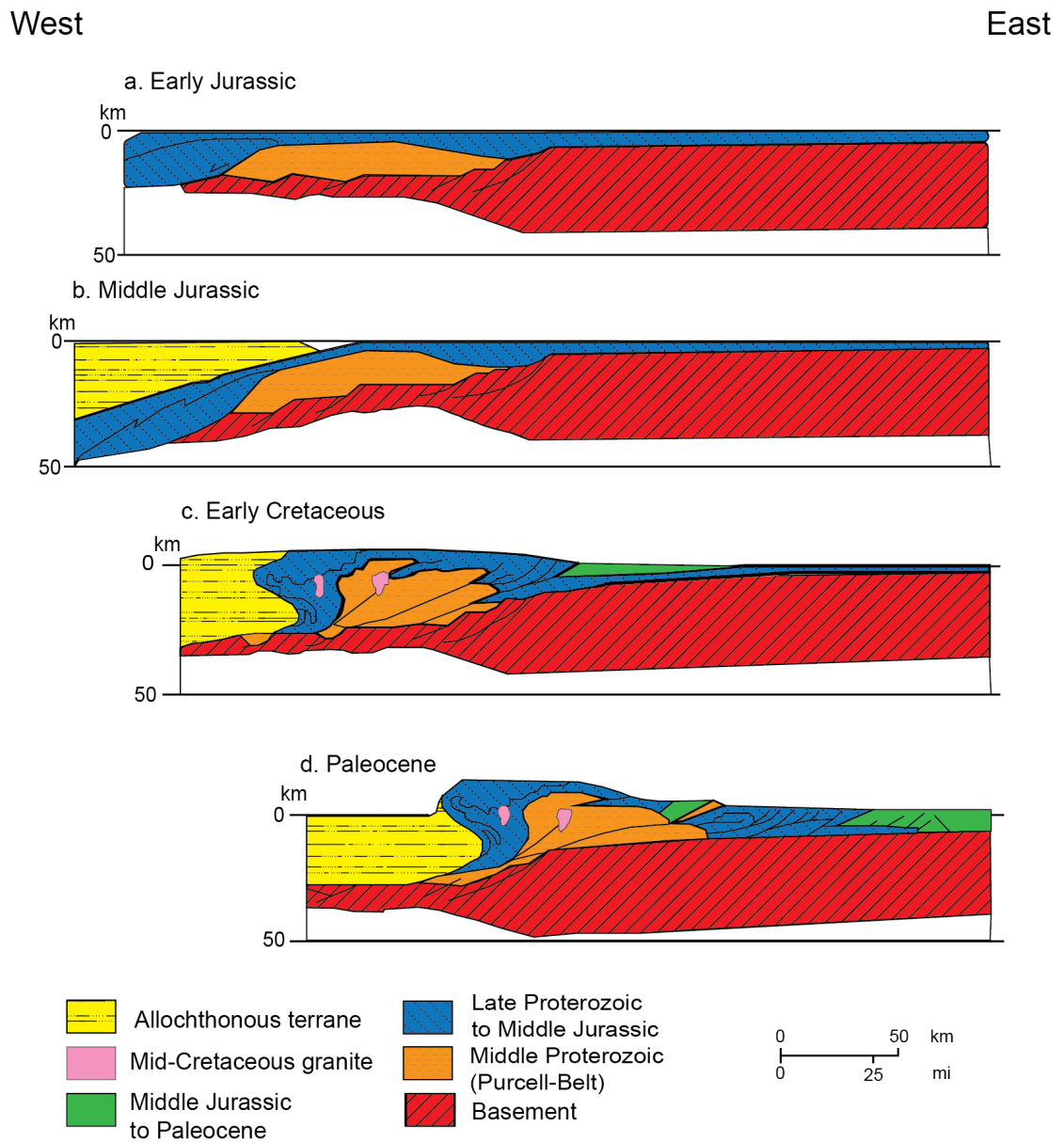


Figure 2:1: West-east cross section along 49°, 45' North latitude illustrating the evolution of the western Canada foreland thrust and fold belt from Early Jurassic to Paleocene. Modified from Price (1994).

2.2 Foreland basin development

Foreland basins are categorized into two types, peripheral and retroarc, and are set apart by the type of tectonic setting (Fig. 2.2) (Dickenson, 1974). Peripheral basins, such as the North Alpine Foreland Basin in Europe, form along the outer arc of a deformation front (on the subducting plate) during continent-continent collision (Dickenson, 1974). In an ocean-continent collision, when the rate of subduction is faster than the rate of convergence (subduction zone roll-back), a peripheral basin-trench forms in front of the subduction zone and a backarc extension on the continental plate (Royden, 1993).

Retroarc foreland basins, such as the Western Canada Foreland Basin where this study is located, form cratonward of an orogenic belt and are linked to the subduction of an oceanic plate beneath a continental plate (Dickenson, 1974; DeCelles and Giles, 1996). Both peripheral and retroarc basins form from isostatic flexure of the lithosphere and its response to increased loading (Fig. 2.3).

Total subsidence within a retroarc foreland basin is caused by attenuation of the crust through stretching or erosion, loading from eroded sediment or the uplifted thrust and fold belt, and the dynamic effects of asthenosphere flowing beneath the lithosphere (Jordan, 1995; DeCelles and Giles, 1996). Price (1973) proposed subsidence in a retroarc basin is due solely to supracrustal and laterally transferred loading taking place along a thrust belt. Two theories to further explain the retroarc foreland basin asymmetrical geometry and lithospheric response to loading include (Fig. 2.4): elastic response (Jordan, 1981; Flemings and Jordan, 1990) or viscoelastic response (Beaumont, 1981; Quinlan and Beaumont, 1984).

Elastic lithospheres undergo flexure when a load is applied, changing only when there is fluctuation with the added mass, or when the load is removed entirely (Jordan, 1995). The extent of lithospheric flexure under elastic conditions is a function of flexural rigidity (Jordan, 1995). Under viscoelastic conditions the lithosphere initially reacts elastically, but slowly relaxes and flexes over time while under continued loading. As relaxation-induced subsidence continues, the flexural rigidity is decreased until it progresses toward local isostatic equilibrium, resulting in a narrower basin with a deeper central depression (Quinlan and Beaumont, 1984). The initial flex of the lithosphere in response to loading

may cause primary subsidence in the basin, but subsequent subsidence events can be influenced by the age or density of the lithosphere. Old, stiff, or dense lithosphere is postulated to have less flexibility, resulting in shallow, broad basins, while younger, ductile lithosphere flexes along a shorter wavelength resulting in a deep, narrow basin (Beaumont *et al.*, 1993). The flexural rigidity of an elastic lithosphere model remains relatively constant over time.

In addition to crustal loading causing subsidence, a retroarc foreland basin can also be influenced by dynamic subsidence or dynamic topography (Fig. 2.5). Burgess and Moresi (1999) summarized dynamic topography as a time-varying vertical displacement of the Earth's surface in response to short-lived stresses applied to the base of the lithosphere. As the oceanic plate subducts beneath the continental plate, a drag force is produced by the viscous mantle interacting with the subducting plate (corner flow) (Catuneanu, 2004). The corner flow-driven subcrustal loading generates accommodation over a broad area, resulting in regional or long wavelength subsidence.

Dynamic subsidence is also influenced by the dip angle of the subducting plate. Mitrovica *et al.* (1989) used models to suggest that the wavelength of the lithosphere deflection increases as the angle of subducting plate is decreased, resulting in broad subsidence and sedimentation in the basin. A high dip angle of the subducting plate restricts subsidence to the near-trench region of the deformation zone (Beaumont *et al.*, 1993; Mitrovica *et al.*, 1989). Pang and Nummendal (1995) recognized spatial and temporal variations in the flexural subsidence of the Cretaceous Western Interior Basin, United States. Based on flexural backstripping analysis (estimation of basement depth in the absence of sediment and water loading), the authors recognized 'background' subsidence and suggested that dynamic topography provided the most plausible explanation, a point agreed on by Burgess and Moresi (1999).

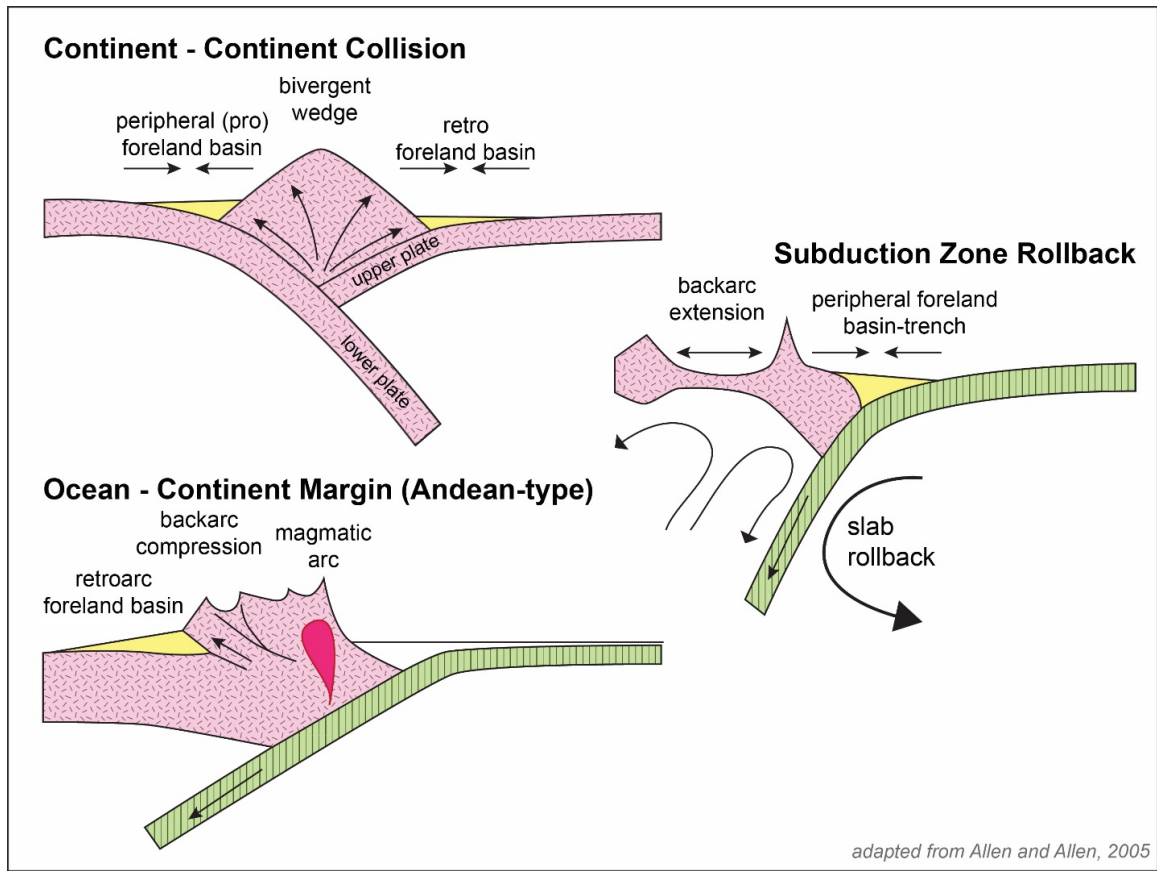
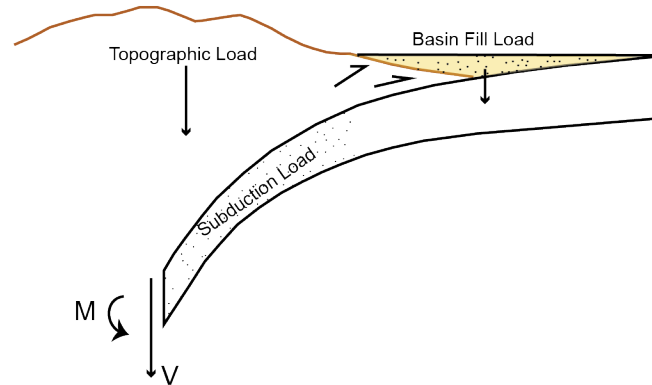


Figure 2:2: Schematic illustration of foreland basin development. Modified from Allen and Allen (2005).

A. Peripheral Foreland Basin System



B. Retroarc Foreland Basin System

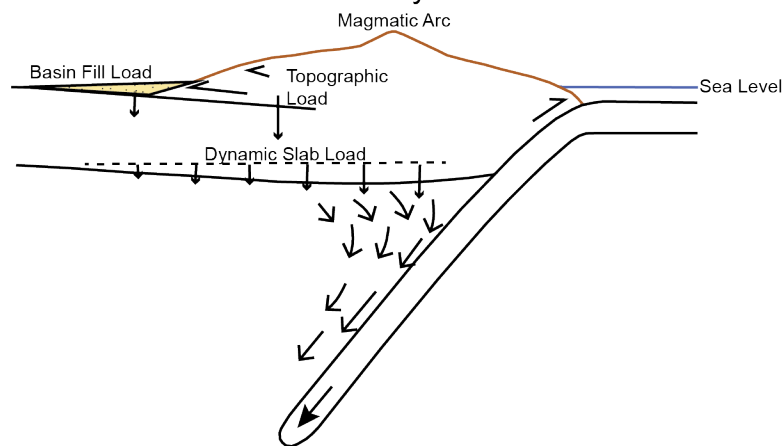
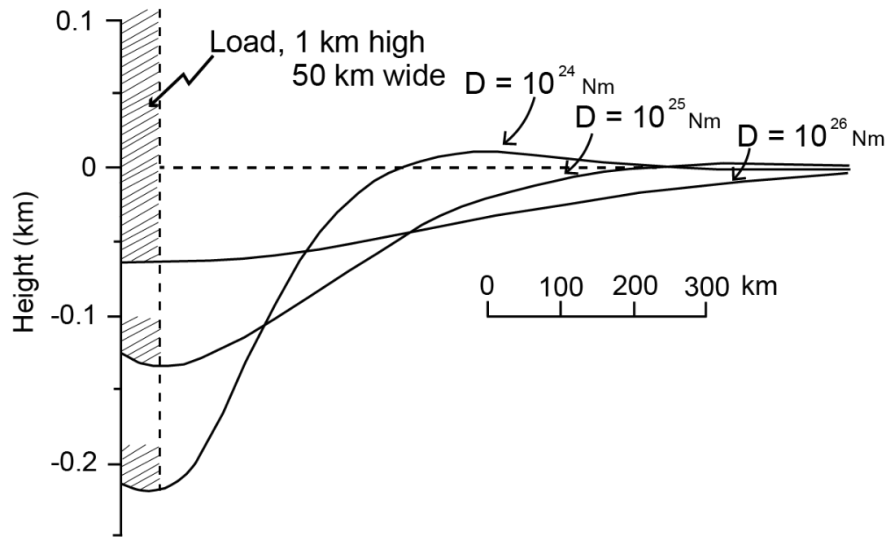


Figure 2:3: Schematic diagrams illustrating principle loads in (A) peripheral and (B) retroarc foreland basin systems. Both basins experience topographic and sediment/basin fill loading. Peripheral foreland basins may also experience subduction loading from a vertical shear force (V) and bending moment (M) acting on the end of the subducting slab. Retroarc foreland basins may incur additional subsidence from dynamic slab loading. (Modified from DeCelles and Giles, 1996).

Elastic lithosphere response



Viscoelastic lithosphere response

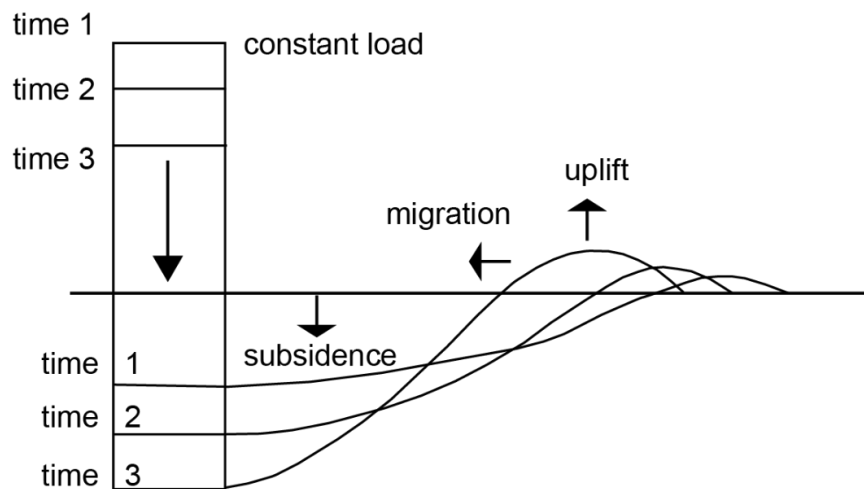


Figure 2:4: Illustration demonstrating elastic and viscoelastic response to loading on the lithosphere. Under elastic lithosphere conditions, the plate has instantaneous flex during loading and the wavelength of flexure is controlled by its flexural rigidity. A viscoelastic lithosphere initially behaves elastically, but the basin continues to relax and flex under a constant load, with no variance over time. (Jordan, 1995 after Beaumont, 1981 and Quinlan and Beaumont, 1984).

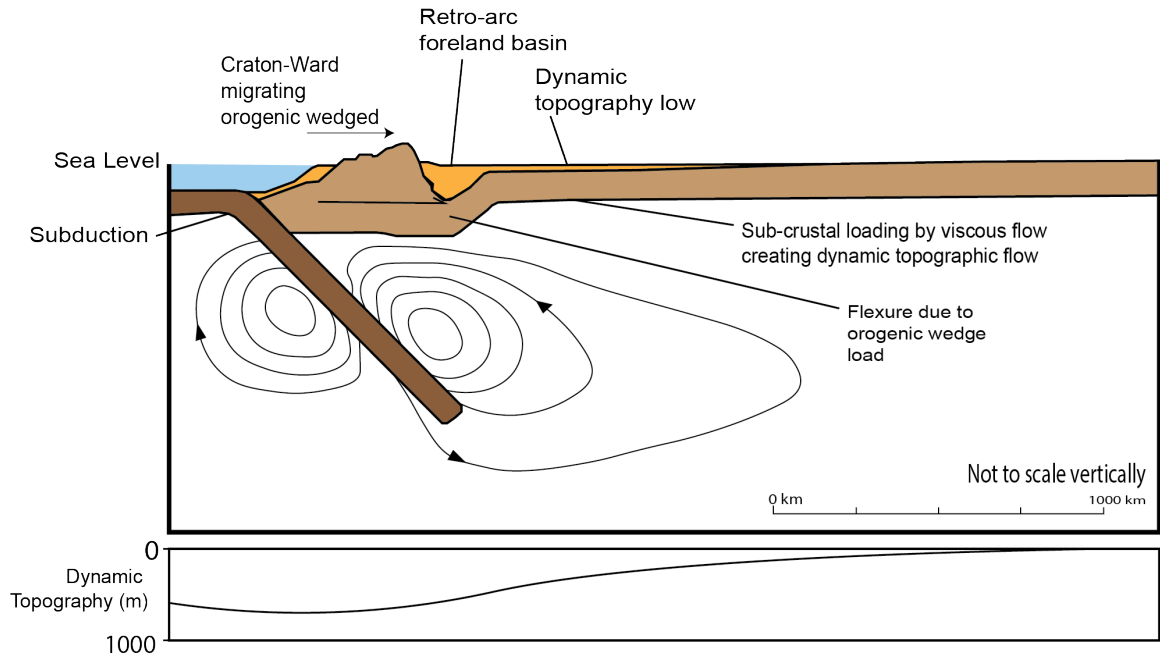


Figure 2:5: Illustration demonstrating the effect of stress on the base of the lithosphere from a subducting slab producing a negative mass anomaly in the mantle (Modified from Burgess and Moresi, 1999).

2.2.1 Subsidence history of the Western Canada Foreland Basin

The subsidence history of the WCFB was episodic and predominately related to tectonic activity and sediment loading (Caldwell, 1984; Stott, 1984; Chamberlain et al., 1989). Subsidence was greatest along the leading edge of the thrust sheets, producing westward-thickening, stacked wedges of coarse-grained, synorogenic, terrigenous clastic sediments deposited as coastal-plain to shallow-water marine lithofacies (Leckie and Smith, 1992; Kauffman and Caldwell, 1993). The eastern margin of the basin was relatively stable with conditions of episodic subsidence that led to deposition of thin, unconformity-bounded, fine-grained clastics and pelagic carbonate sediments on a broad, shallow-water marine shelf (Kauffman and Caldwell, 1993).

Peper (1993) subdivided the WCSB subsidence history into five stages based on variations in subsidence, uplift/erosion, and sediment accumulation (Fig. 2.6). Initial subsidence in the WCSB began with the collision between the Intermontane Superterrane and miogeocline in the Late Jurassic (Chamberlain et al., 1989; Peper, 1993; Price, 1994). Following a period of isostatic uplift, marked by the sub-Blairmore unconformity (Price, 1994), a second subsidence event from Aptian to Cenomanian (~124.5-104 Ma; Stage III from Peper, 1993) was initiated when the micro-continent, Cordillera, collided with the North American craton (Chamberlain et al., 1989). Subsidence rates increased from 0–20 m/Myr in the first event to upwards of 150 m/Myr during the second subsidence event and is represented in the stratigraphic record by the Blairmore, Fort St. John and lower Colorado groups (Chamberlain et al., 1989; Peper, 1993).

During a third subsidence event (Stage IV; Cenomanian to early Campanian (~104–77 Ma)) tectonic loading was renewed, causing downflexing of the lithosphere and increased accommodation space for deposition of the Alberta, Smoky, and upper Colorado Groups. Subsidence rates at this time ranged between 6 m/Myr in the north (~50° latitude) and up to 120 m/Myr in the south (~56° latitude), suggesting subsidence and sediment supply was constrained to the northern section of the basin (Chamberlain et al., 1989). Periods of active loading interspersed with tectonic quiescence continued into the Early Tertiary and is represented by a transition from marine shales to deposition of predominately sandy, shallow water sediments (Stage V) (Peper, 1993).

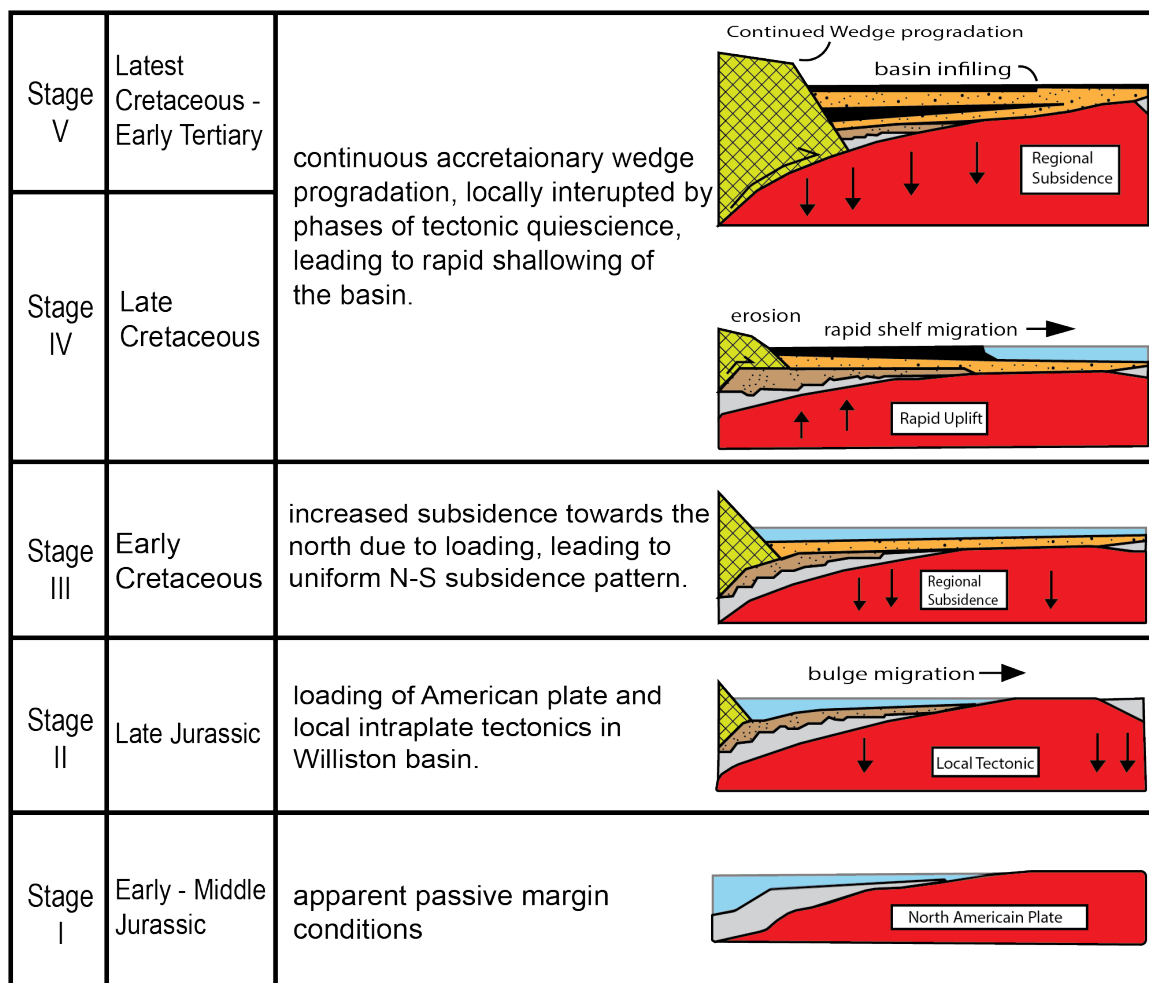


Figure 2:6: Schematic summarizing the subsidence history of the Western Canada Sedimentary Basin. Arrows show direction of craton (dark grey) movement. Hatched = accretionary wedge; Stippled = sediment infill. Modified from Peper (1993).

2.3 Foreland basin depozones

A retroarc foreland basin is subdivided into four depozones: wedge-top, foredeep, forebulge, and back-bulge (DeCelles and Giles (1996) (Fig. 2.7). A wedge-top depozone includes sediment that has accumulated proximal to the orogenic wedge and extends to the limit of deformation associated with that wedge. Wedge-top deposits typically consist of coarse alluvial and fluvial sediment deposited under a subaerial setting, or mass flows and fine-grained shelf sediments during subaqueous conditions. The boundary between wedge-top and the adjacent foredeep deposits may be difficult to distinguish due to shifting of the orogenic wedge. However, the presence of progressive deformation, local and regional unconformities, and thinning of sedimentary rock toward the orogenic wedge provide key distinguishing features for wedge-top depozone classification.

The foredeep depozone is cratonward of the wedge-top zone and incorporates sediment accumulated between the frontal tip of the orogenic wedge and forebulge. Geometry of the foredeep segment is typically a few hundred kilometres wide and up to eight kilometers thick (DeCelles and Giles, 1996). Sediment is predominately sourced from the orogenic belt, with sediment supply varying due to different carrying capacities between major and minor rivers (Jordan, 1995). Depositional environments in the foredeep include non-marine, fluvial, alluvial systems to marginal marine (e.g., deltaic/estuarine) environments, and shallow-marine with stratal packages composed of near shore sand, or shallow-marine muddy sequences (Jordan, 1995; DeCelles and Giles, 1996).

The forebulge depozone lies within the region of flexural uplift, where the lithosphere has flexed in response to subsidence in the orogenic front and foredeep depozone. Differential response to load-induced lithospheric flexure results in a dynamic forebulge position within the basin. Models by Waschbush and Royden (1992) suggest the heterogenous nature of the lithosphere may cause a forebulge to migrate in series of episodic movements instead of one fluid motion. Development of forebulges may be suppressed during periods of tectonic quiescence or dynamic topography driven subsidence (Jordan, 1995; Catuneanu, 2004). Uplift of the forebulge is recorded in the rock record by periods of non-deposition or erosion marked by unconformities (DeCelles and Giles, 1996). During submarine conditions with decreased clastic sediment supply,

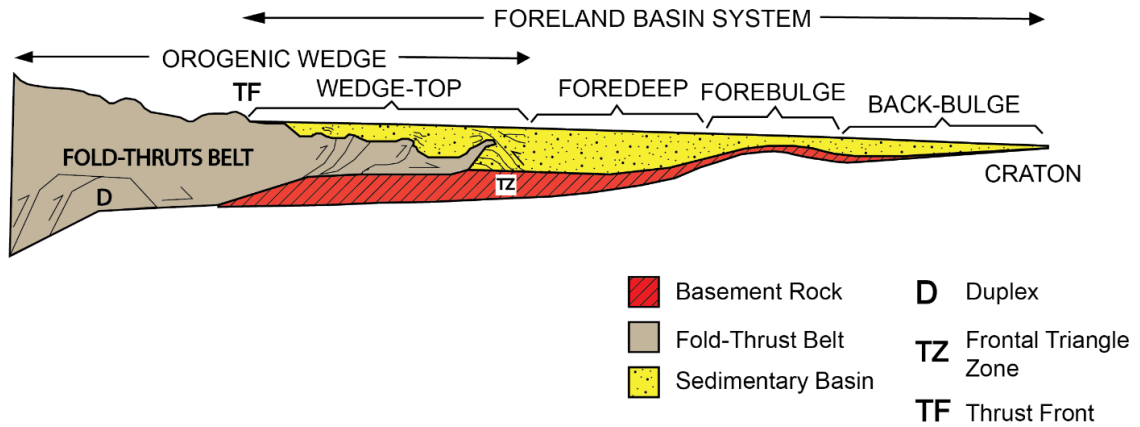


Figure 2:7: Schematic of retroarc foreland basin depozones. Abbreviations and Symbols: one-arm arrows indicate thrust direction; sedimentary basin (stippled); basement rock (diagonal lines); D (duplex); TF (thrust front); TZ (frontal triangle zone). Modified from DeCelles and Giles (1996).

the forebulge depozone can develop localized or extensive carbonate platforms, providing a stratal connection between the foredeep and back-bulge depozones (DeCelles and Giles, 1996).

The back-bulge section of the retroarc foreland basin represents the accommodation and accumulated sediment found between the forebulge and craton. Subsidence within the back-bulge is substantially less than the foredeep and is considered a result of dynamic topography induced subsidence or tectonically induced flexure. Slow and episodic subsidence results in deposition of thin, unconformity-bounded sequences of fine-grained terrigenous clastic and pelagic carbonate sediments, usually within shallow marine and nonmarine depositional settings (Kauffman and Caldwell, 1993; DeCelles and Giles, 1996).

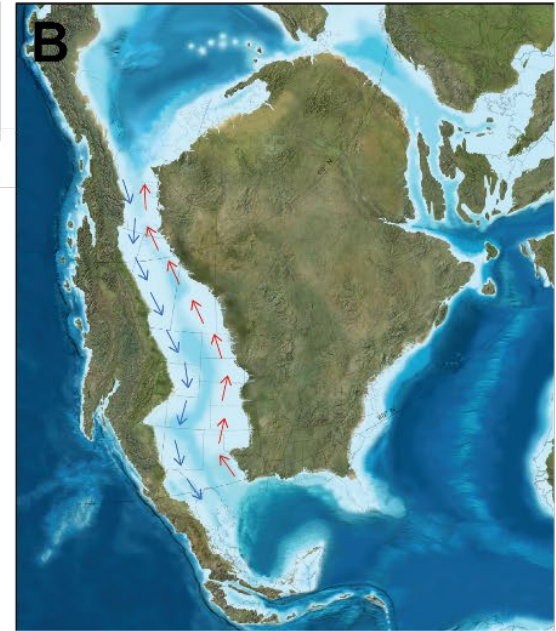
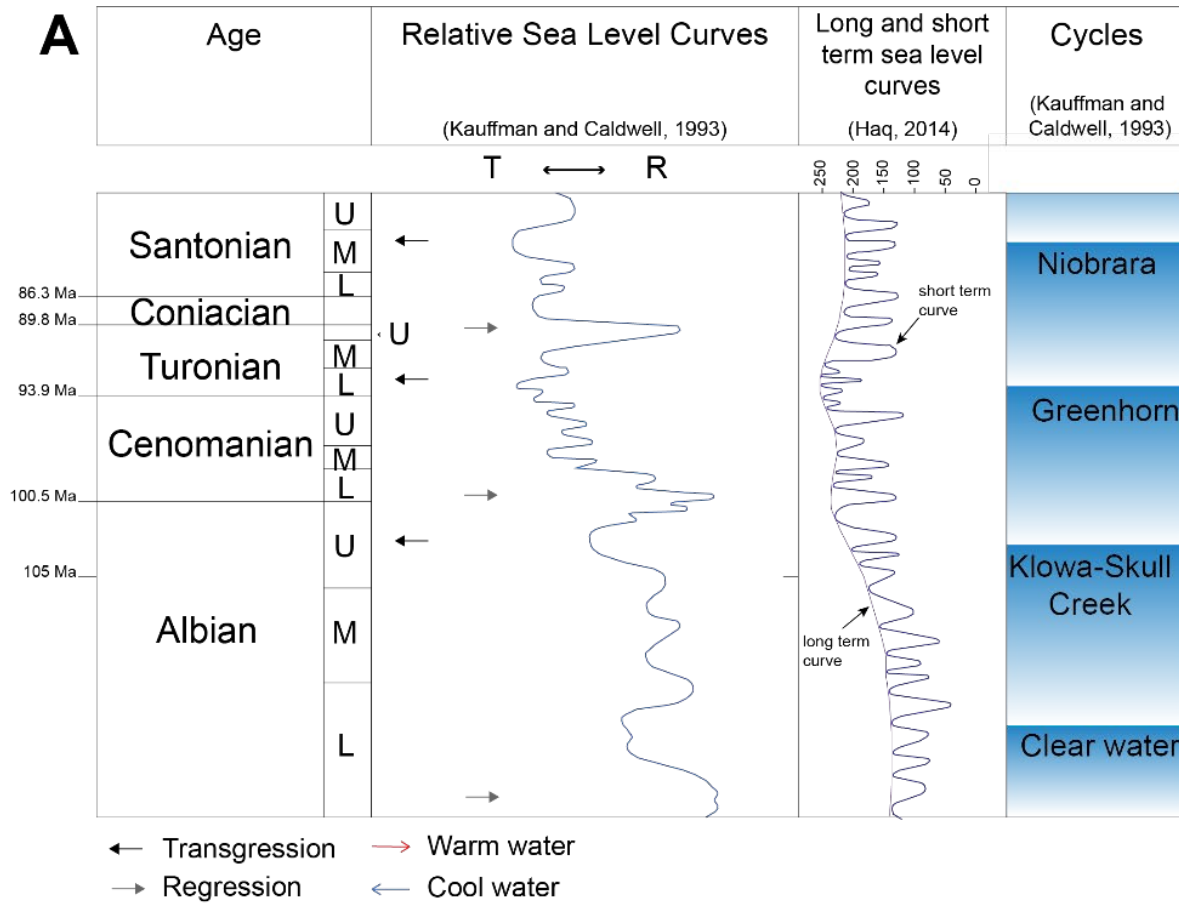
2.4 Paleogeography of the Western Interior Basin during the Upper Cretaceous

The Cretaceous paleoclimate was considerably warmer than present day, mimicking “greenhouse” conditions as global temperatures averaged between 21 and 24 degrees Celsius (Hay and Floegel, 2012). This period also marked a time of prolonged global sea level rise that reached a Mesozoic-Cenozoic peak in the early Turonian, during the Greenhorn cycle, and then declined throughout the remainder of the Cretaceous and the Cenozoic (Fig. 2.8) (Haq et al., 1987; Haq, 2014). In Late Albian time, cooler slightly brackish waters of the Boreal Sea began to blend with the warm, saline water from the Tethyan Sea (proto- Gulf of Mexico) (Caldwell et al., 1993). By the Middle to Late Cenomanian, the two water bodies joined to create a nearly 6000 km long epicontinental sea called the Western Interior Seaway (WIS) (Kaufman, 1977; Bloch et al., 1993; Caldwell et al., 1993; Kaufman and Caldwell, 1993; Leckie et al., 1994; Bloch et al., 1999; Schroder-Adams, 2014).

The Upper Cretaceous Colorado Group strata investigated in this study record a series of transgressive-regressive cycles (Fig. 2.8) (Haq et al., 1987; Kauffman and Caldwell, 1993;), starting with transgression in the WIS at the Albian-Cenomanian boundary. Connection between the proto-Gulf of Mexico (Fig. 2.8B) and Polar Ocean happened

gradually, over several short-term transgressive pulses (Caldwell et al., 1993). Intermittent mixing between the warmer, southern water and the denser, cooler mid-latitude water formed temperature and salinity gradients that generated bottom water anoxia and controlled migration of biota across the WIS (Caldwell et al., 1993; Schroder-Adams et al., 1996; Bloch et al., 1999; Schroder-Adams, 2014). This is most notably observed in the disappearance of benthic foraminiferal assemblages in the lower Cenomanian stratigraphic interval (Schroder-Adams et al., 1996; Bloch et al., 1999). Marine conditions improved slightly in the middle Cenomanian, with a limited number of benthic species and diversity being recorded (Kauffman, 1984; Schroder-Adams et al., 1996; Bloch et al., 1999).

At the time of the Greenhorn marine transgression in late Cenomanian-early Turonian, the WIS had a minimum width based on preserved strata of nearly 1600 kilometres and a maximum sea level of approximately 250 metres above present day mean sea level (Haq et al., 1987; Arthur and Sageman, 2004; Haq, 2014) (Fig. 2.8). Warm water with normal salinity levels from the Tethyan Sea had fully inundated the WIS, promoting northward migration of dinoflagellates, planktonic foraminifera and coccoliths (Caldwell, et al., 1993). Transgression and increasing fresh-water input to the WIS margins produced counter-clockwise circulation (Arthur and Sageman, 2004), and when combined with reduced sediment input, these events led to higher plankton concentrations along the eastern flanks of the seaway (Kauffman and Caldwell, 1993; Schroder-Adams, et al., 2001; Schroder-Adams, 2014). The Greenhorn cycle also coincided with the global ocean anoxic event OAE-II. During the OAE-II, enhanced circulation, decreased sedimentation, and primary productivity (upwelling) conditions combined with an oxygen-poor intermediate zone to increase organic matter preservation in the WIS (Eriksen and Slingerland, 1990; Arthur and Sageman, 1994; Arthur and Sageman, 2004; Schroder-Adams, 2014). Large ash-falls associated with intense volcanic activity during the Cretaceous also enhanced organic matter preservation by contributing to rapid burial of organic carbon and promoting anoxic conditions in the WIS (Arthur et al., 1985; Ohkouchi et al., 2015).



Global sea level rise during the Greenhorn transgression in late Cenomanian to early Turonian joined the proto-Gulf of Mexico Tethyan Sea with the Boreal sea. The warm and cool waters circulated in a counter-clockwise direction.

Figure 2:8: Relative sea level history curves (A) and paleogeographic setting during the Greenhorn cycle (B). A) Relative sea level fluctuations from the Lower Albian to Upper Santonian (Kauffman and Caldwell, 1993). Black arrows indicate sea level rise (transgression), and grey arrows reflect a relative fall in sea-level (regression). The short-term sea level curve by Haq (2014) broadly mirrors the long-term sea level fluctuations observed and the occurrence of major transgression cycles labeled in the adjacent column. B) Illustration of the paleogeographic setting during the late Cenomanian to early Turonian when the Boreal and Tethyan seas had joined (Blakey, 2014). The WIS circulation was counter-clockwise during this time, with warm, normal salinity marine water from the proto-Gulf of Mexico migrating northward along the eastern margin and cool Polar water flowing adjacent to the fold and thrust belt (Arthur and Sageman, 2004; Kauffman and Caldwell, 1993).

A basinwide bentonite ash bed mapped in this study, the Bighorn River Bentonite, or informally named “red” bentonite, represents the base of the Second White Specks Formation and lies just below the Cenomanian-Turonian boundary (Tyagi et al., 2007). Barker et al. (2011) dated the volcanic event that produced the “red” bentonite to 94.29 ± 0.13 Ma (U-Pb zircon), which is approximately coeval to the OAE-II $\delta^{13}\text{C}_{\text{org}}$ excursion provided by Prokoph et al., 2013. These dates precede the recognized age of the Cenomanian-Turonian boundary (93.9 Ma), suggesting the OAE-II and the volcanic eruption responsible for the “red” bentonite could have facilitated the shift in climate, biological activity, and ocean chemistry recorded in the WIS at the start the Turonian (e.g., Elderbak and Leckie, 2016).

2.5 Sedimentology and stratigraphy of the Colorado Group

The Colorado Group is a marine mudstone stratigraphic package that spans the WCFB. The succession of rock has been subdivided based on biostratigraphic, lithostratigraphic, and allostratigraphic principles. Biostratigraphy uses fossil assemblages to correlate and subdivide age-related packages. Lithostratigraphy subdivides rock into distinct packages based on changes in observable physical rock traits, such as chemical and mineralogical composition, colour, texture, and depositional structures. Allostratigraphy divides rock into discrete packages based on time-correlative, regionally mappable bounding surfaces (North American Commission on Stratigraphic Nomenclature, 2005). This study uses allostratigraphy to develop a basinwide stratigraphic framework because it provides a proxy time context in which to reconstruct the basin’s depositional history and paleogeography (Plint et al., 2009). This section summarizes the biostratigraphic, lithostratigraphic, and allostratigraphic frameworks previously constructed for the Upper Cretaceous Colorado Group study interval. Fig. 2.9 is a summary of the historic Colorado Group nomenclature and how it relates to the work presented herein.

2.5.1 Biostratigraphy of the Colorado Group

Mollusca and foraminifera invertebrate fossils are commonly found in the marine strata of the WIS. However, having a sensitivity to altering environmental conditions in the

Period	Epoch	Stage	Lithostratigraphic Framework		Allostratigraphic Framework	Basinwide Extension of Allostratigraphic Framework			
			Proximal Foredeep	Distal Foredeep		Proximal Foredeep	Distal Foredeep	Backbulge	
			Leckie et al., 1994	Bloch, et al. (1993, 1999) Schroder-Adams et al. (1996) Tu et al. (2007)	Tyagi (2009) Tyagi et al. (2007)	Varban & Plint (2005) Tyagi, et al. (2007) Roca et al. (2008)	This Study	This Study	
Cretaceous	Upper	Turonian	Cardium Fm	Carlile Fm	<i>E1</i>	Cardium Fm	Interval not studied	Interval not studied	
			Kaskapau Formation	Second White Specks Fm.	Green bentonite	(92.5 ± 0.13 Ma)*	Kaskapau Fm	Second White Specks Fm.	Second White Specks Fm.
		Blue Bentonite							
		Bighorn River (Red) Bentonite			(94.29 ± 0.13 Ma)**				
		Cenomanian	Dunvegan Formation	U. Colorado Grp.	Belle Fourche Fm.	Kl.		Dunvegan Alloformation	"forebulge unconformity"
	X								
	A					(95.87 ± 0.10 Ma)**			
	Shaftsby Fm.	U. Belle Fourche	Belle Fourche Fm.	II		FSU	FSU	FSU	
				X Bentonite					
	Lower	Albian	Fish Scales Fm.	L. Colorado Grp.	Barons Sst.	Fish Scales Fm.	I	Fish Scales Fm.	BFSM
BFSM									
		L. Shaftsby Fm.	L. Colorado Grp.	Westgate Fm.	Interval not studied				

U = Upper // // // // // inferred hiatus or erosional gap
L = Lower
Fm. = Formation

Figure 2:9: Summary chart listing formations and their relationship to the allostratigraphic framework incorporated in this study. *U/Pb dates from Tyagi (2009). **U/Pb dates from Barker et al. (2011).

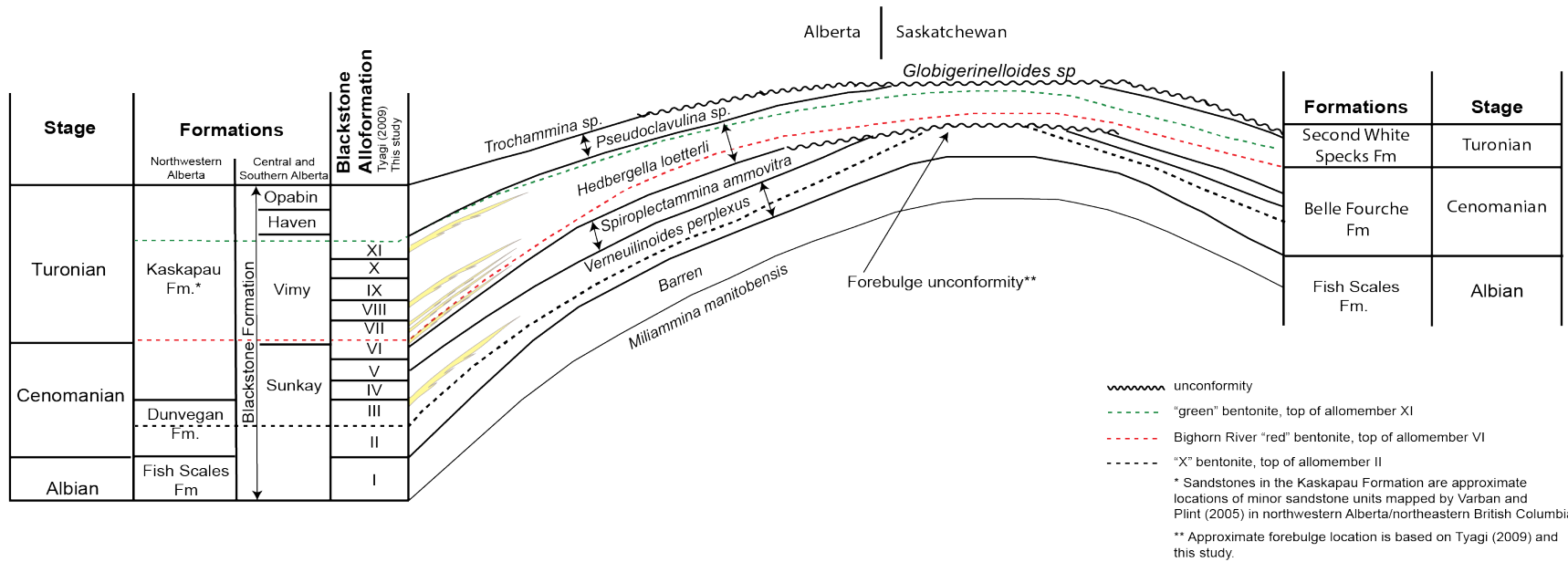


Figure 2:10: Correlation of lithostratigraphy and allostratigraphy with foraminiferal zones established for the Upper Colorado group. Bentonite stratigraphy is based on this study and Tyagi (2009). Image is modified from Caldwell et al. (1978), Tyagi (2009), and Tyagi et al. (2007).

water makes microfossils better indicators of marine environments and paleoecological change (Caldwell et al., 1993). Past studies have divided the Upper Colorado strata into three foraminiferal zones, in ascending order: upper Albian *Miliammina manitobensis*, middle to late Cenomanian *Verneuilinoides perplexus*, and latest Cenomanian to Turonian *Hedbergella loetterlei* (Bloch et al., 1993; Bloch et al., 1999; Caldwell et al., 1978; Schroder-Adams et al., 1996). Tyagi et al. (2007) proposed an additional late Cenomanian foraminiferal zone for the Upper Colorado strata based on agglutinated and planktonic biota observed in southern Alberta and southwestern Saskatchewan. The new biostratigraphic interval lies between the *Verneuilinoides perplexus* and *Hedbergella loetterlei* zones.

The four foraminiferal zones and their placement within the Blackstone allostratigraphic framework applied in this study is presented in Fig. 2.10. The Late Albian Fish Scales Formation is barren of foraminifera, and its assignment within the Cenomanian is based on dinoflagellate assemblage (Bloch et al., 1993; Schroder-Adams et al., 1996). The Middle Cenomanian *Verneuilinoides perplexus* zone is present within allomembers II through to the lower part of V (Tyagi, 2009). Allomember V is divided in age, where the lower section is assigned to the Middle Cenomanian based on foraminifera from the *Ammobaculites gravenori* Subzone and the upper section to the Late Cenomanian *Gaudryina irenensis* Subzone (Kreitner and Plint, 2006; Tyagi, 2009). Tyagi (2009) placed allomember VI within Late Cenomanian based on the presence of *Spiroplectammia ammovitrea* Zone in the Alberta plains region, which corresponded to the *Flabellammia gleddiei* Zone identified in the Peace River area of northwestern Alberta and northeastern British Columbia and the *Sciponoceras gracile* Zone of Kauffman et al. (1993) for the WIS.

Immediately overlying the Bighorn River “red” bentonite, the top of allomember VI, is the beginning of the *Hedbergella loetterlei* Zone. This Early Turonian zone marks the transition from agglutinated foraminifera to calcareous planktonic foraminifera in the WIS during the early Turonian global sea level rise (Caldwell et al., 1993; Schroder-Adams et al., 1996; Tyagi, 2009). Early Turonian age was also assigned to allomembers

VII through X as they contain molluscs from the *Watinoceras reesidei* Subzone and *Inoceramus labiatus* Zone (Tyagi, 2009). The “green” bentonite at the top of the study interval, the upper contact of allomember XI, was dated at 92.5 Ma, suggesting strata above this point are Middle Turonian in age (Tyagi, 2009).

2.5.2 Lithostratigraphy of the Colorado Group

The original stratigraphic nomenclature for the basinwide Colorado Group interval was based on lithostratigraphy and presented in Williams and Burke (1964) and Caldwell (1984), with revisions applied to the studies by Bloch et al. (1993), Bloch et al. (1999), Schroder-Adams et al. (1996), and Tu et al (2007). Bloch et al (1993) subdivided the upper Colorado Group in central-southern Alberta and Saskatchewan into three lithostratigraphic formations: Fish Scales, Belle Fourche, and Second White Specks (Fig. 2.9). This lithostratigraphic framework was adopted in several subsequent stratigraphic and paleoenvironmental studies of the Colorado Group (e.g., Bloch et al., 1999; Schroder-Adams et al., 1996; Schroder-Adams et al., 2001; Nielsen et al., 2003; Tu et al., 2007). In northwestern Alberta, the Dunvegan and Kaskapau formations of the Colorado Group are the proximal foredeep equivalents to the distal Belle Fourche and Second White Specks formations, respectively (Fig. 2.9) (Leckie et al., 1994).

2.5.2.1 Fish Scales Formation

The Fish Scales Formation is a finely-laminated, non-calcareous to calcareous mudstone interbedded with thinly-bedded, wave-rippled and non-bioturbated very fine sandstones and variable concentrations of phosphatic fish debris (Bloch et al., 1993; Schröder-Adams et al., 2001; Roca, 2007). It varies in thickness between ten and 20 metres (Bloch et al., 1999; Schroder-Adams et al, 1999). Bioturbation is rare to nonexistent in the strata and bentonites are common (Bloch et al., 1993). The Fish Scales Formation was deposited when the Boreal and Tethyan Seas started to join and form the WIS, developing a stratified water-column with widespread bottom-water anoxia for which evidence is provided by the absence of benthic foraminifera (Leckie et al., 1992; Bloch et al., 1993; Schröder-Adams et al., 1996; Schröder-Adams et al., 2001). Total organic content in the Fish Scales Formation from locations across the foreland basin ranges

between 1.8 to 8 wt% and hydrogen index values (refer to Chapter 7 for explanation) lie between 50 to 440 mg/HC/gOC (Bloch et al., 1993; Bloch et al., 1999).

Thin beds of phosphatic-rich fish debris within the Fish Scales Formation are interpreted as time-transgressive bone beds that are associated with winnowing of muds (Stelck et al., 1958) and produce a highly radioactive signature in geophysical well logs compared to the underlying Westgate Formation (Leckie et al., 1992). This specific curve character becomes less apparent towards eastern Alberta and into Saskatchewan, making it difficult to identify the Fish Scales Formation using gamma ray well logs. This shift in wireline log character may suggest the surface between the Fish Scales and Westgate formations represents a geochemical abnormality related to the beginning of anoxic conditions (Leckie et al., 1992; Roca et al., 2008).

The Fish Scales Formation sharply overlies the Albian Westgate Formation mudstones. A centimetre-scale, bioclastic conglomerate is observed at the base of the Fish Scales Formation and is largely composed of vertebrate and phosphatized bioclastic debris, with minor amounts of intraformational shale and siderite clasts (Schroder-Adams et al., 1996). The contact between the Fish Scales and overlying Belle Fourche Formations is conformable, with the reappearance of agglutinated foraminifers within Belle Fourche deposits indicating a transition into slightly improved environmental conditions for benthic organisms (Schroder-Adams et al., 1996; Bloch et al., 1999). The boundary between the Fish Scales and Belle Fourche Formations is also recognized from an apparent increase in thin bentonite deposits and the abrupt decrease in the abundance of phosphatic debris (Bloch et al., 1993; Bloch et al., 1999; Roca et al., 2008). In northwestern Alberta and northeastern British Columbia, the Fish Scales Formation is coeval with the Shaftsbury Formation and underlies the Dunvegan Formation.

The base of the Fish Scales Formation lies at the Albian–Cenomanian boundary (~100.5 Ma) (Warren and Stelck, 1969; Leckie et al., 1992). Ridgley et al. (2001) provide a $^{40}\text{Ar}/^{39}\text{Ar}$ age of 97.59 ± 0.40 Ma for a bentonite from the Fish Scales Formation in the Suffield area in southeastern Alberta. Given that U-Pb ages are systematically $\pm 0.65\%$ older than Ar-Ar ages (Kuiper et al., 2008), an equivalent U-Pb age for the Suffield Fish

Scales bentonite would be approximately 98.2 Ma, placing the sample just above the Albian-Cenomanian boundary.

2.5.2.2 Belle Fourche Formation

The Belle Fourche Formation is a fauna-impoverished, non-calcareous to slightly calcareous laminated mudstone and siltstone with occasional interbeds of very fine- to fine-grained sandstones (Bloch et al., 1993; Schroder-Adams et al., 1996; Bloch et al., 1999; Ridgley and Gilboy, 2001; Ridgley et al., 2001; Christopher et al., 2006; Tyagi et al., 2007). The sediments were deposited in a distal, shallow marine setting under dysoxic conditions (Schroder-Adams et al., 1996; Tyagi et al., 2007). In the eastern margin of the basin in Manitoba, the Belle Fourche Formation is equal to the Belle Fourche Member of the Ashville Formation (Schröder-Adams et al., 2001; Christopher et al., 2006; Dionne et al., 2016). In west-central Alberta, the Belle Fourche Formation is coeval with the Sunkay Member of the Blackstone Formation (Fig. 2.9). Mudstones of the Blackstone and Belle Fourche Formations found in central to eastern Alberta transition to sandier, delta-based proximal deposits of the Dunvegan Formation in northwest Alberta and northeastern British Columbia (Bhattacharya and Walker, 1991; Plint, 2000; Tyagi et al., 2007; Tyagi, 2009).

The Belle Fourche Formation is up to 150 metres thick in the Alberta foothills, thinning to approximately 20 metres at the distal margin of the basin in Saskatchewan (Bloch et al., 1993; Ridgely et al., 2001; Ridgely and Gilboy, 2001). In southwest Alberta, the strata include a nearly 10-metre-thick sandstone termed the Barons Sandstone that unconformably overlies Fish Scales Formation (Bloch et al., 1999; Tyagi et al., 2007; Roca et al., 2008). Organic content in the Belle Fourche Formation is a mixture of Type II and III and ranges between 0.4 to 2.7 1.7 wt% (Bloch et al., 1999; Schroder-Adams et al., 1996).

The Belle Fourche Formation was deposited during the middle to upper Cenomanian, between approximately 95.8 and 93.3 Ma (Schroder-Adams et al., 1996). The *Verneuilinoides perplexus* is a Middle Cenomanian foraminiferal zone that is regionally extensive in the lower Belle Fourche (2.11) (Caldwell et al., 1978; Caldwell et al., 1993;

Bloch et al., 1999; Schroder-Adams et al., 1996). Ridgley et al. (2001) subdivided the Belle Fourche Formation into informal upper and lower units based on foraminiferal and ammonite zones within the coeval Lincoln and Hartland members of the Greenhorn Formation in eastern Montana. A regionally extensive bentonite called the “X” bentonite within the lower Belle Fourche was dated at 95.87 ± 0.10 Ma (Barker et al., 2011) and provides a mappable, time-correlative surface to constrain the lower and upper Belle Fourche Formation. The “X” bentonite has been correlated across the WCSB (this study; Tyagi et al. 2007; Tyagi, 2009) and correlated with the A bentonite of Gilboy (1988) and the B bentonite in Ridgely et al. (2001). In the Belle Fourche Member of the Ashville Formation in the Manitoba Escarpment, McNeil and Caldwell (1974, 1981) linked the “X” bentonite with a mapped bentonite associated with the *Ostrea beloiti* Logan beds, which occur near the top of the *Verneulinoides perplexus* Zone.

Bloch et al. (1999) placed the boundary between the Belle Fourche and Second White Specks formations at a prominent erosion surface observed in core at well location 100/-6-34-030-08W4 in east-central Alberta. Allostratigraphic correlations by Tyagi et al. (2007) shifted the contact between the two formations to a bentonite bed higher up in the section that correlated to the Bighorn River “red” bentonite. The revised position for the Middle Cenomanian Belle Fourche Formation and Turonian Second White Specks boundary is also supported by the presence of *Spiroplectamina ammonitrea* Zone (Tyagi et al., 2007).

Ridgley et al. (2001) and Gilboy (1988) separated the Belle Fourche Formation into four units (A, B, C, D1, and D2) based on broad lithologic genetic characteristics. Mapping of these units demonstrated progressive loss of Upper Belle Fourche strata (unit D1), from south to north in southwestern Saskatchewan, below an observed unconformity at the contact to the overlying Second White Specks Formation. The mapped Upper Belle Fourche units thin across major northwest-southeast and minor northwest-southeast trending faults. Differential movement and rotation of fault-bounded basement blocks, as defined by the cross-cutting lineaments, appear to contribute to differential thickening and the creation of a regional erosional unconformity that has been mapped through eastern Alberta and western Saskatchewan (Bloch et al., 1993; Bloch et al., 1999;

Christopher et al., 2006; Schroder-Adams et al., 1996; Ridgley et al., 2001; Tyagi, 2009). Bloch et al. (1999) suggested this regional unconformity marked the base of the Second White Specks, however subsequent work by Tyagi et al. (2007) and Tyagi (2009) concluded that the surface was as a beveling unconformity controlled by forebulge uplift during loading events in the western margin of the basin. Ridgley et al. (2001) did not clearly define this surface, and cross-sections provided in their report place the equivalent unconformity within unit C.

2.5.2.3 Dunvegan Formation

The Dunvegan Formation is a sandy, clastic wedge present in northwestern Alberta and northeastern British Columbia, and consists of alluvial and shallow marine sandstones, siltstones and mudstones (Stott, 1982; Bhattacharya, 1993; Plint, 2000). It ranges from 90 to 270 metres thick and was dispersed in a series of prograding and aggrading delta complexes that extended more than 400 kilometres into the basin along a north-west to south-east trend (Bhattacharya and Walker, 1991; Plint, 2000; Plint et al.; 2009). The sandy delta plain sediments transition laterally into the distal marine shales of the Sunkay Member of the Blackstone Formation (Alberta Group) and the Belle Fourche Formation. The Dunvegan Formation has an interfingering and diachronous relationship with the bounding formations and, because of this, the contact between the units is placed at the first and last appearance of sandstones in a mudstone-dominant succession (Stott, 1982). In northwest Alberta, the Dunvegan Formation overlies the Shaftesbury Formation and underlies the Kaskapau Formation. Presence of benthic foraminifera and ammonites in the distal offshore facies coeval to the Dunvegan strata place the Formation at early to mid-Cenomanian in age (Plint, 2000).

2.5.2.4 Kaskapau Formation

The Kaskapau Formation comprises coastal plain, stacked shoreface and nearshore sandstones that transition seaward into offshore heterolithic mudstones, producing a stratigraphic wedge that thins seaward, with thickness decreasing from 700 metres to less than 50 metres over a 300-kilometre distance (Varban and Plint, 2005; Varban and Plint, 2008a). Sediment was deposited on a shallow water (less than a few tens of metres), very

low-gradient muddy ramp subject to storm reworking (Varban and Plint, 2005; Varban and Plint, 2008a). Mud and sand sediment were dispersed by combined and geostrophic flows, up to 100 kilometres from shore, with dispersed mud accumulating over 250 kilometres into the basin as a subaqueous ‘accommodation envelope’ (Varban and Plint, 2008a). Five nearshore sandstones lie at the proximal end of the basin within the Kaskapau Formation; in ascending order they are named the Dickebush, Trapper, Tuskoola, Wartenbe and Mount Robert (Varban and Plint, 2005).

In northwest Alberta, the Kaskapau is coeval with the Blackstone Formation of the Alberta Group and is subdivided into four members, in ascending order: Sunkay, Vimy, Haven and Opabin (Fig. 2.11) (Stott, 1963). Deposition of the Kaskapau Formation occurred during most of the Greenhorn transgressive-regressive cycle, encompassing the Cenomanian-Turonian stage boundary and the OAE-II (Stelck and Wall, 1954).

2.5.2.5 Second White Specks Formation

The Second White Specks Formation is dominated by fine-grained, calcareous sediments deposited at a time of global sea level rise during the later stage of the Greenhorn cycle (Cant and Stockmal, 1989; Leckie and Smith 1992). Proximal to the forebulge region, in central Alberta to western Saskatchewan, the formation consists predominately of very thinly bedded (pin-stripe appearance), non-bioturbated, calcareous mudstone that is rich in disseminated coccoliths (Bloch et al., 1993; Bloch et al., 1999; Ridgley et al., 2001; Schroder-Adams et al., 1996; Tu et al., 2007). Towards the eastern margin of the basin, close to the presumed backbulge region of the WCFB in eastern Saskatchewan and western Manitoba, the Second White Specks comprises bituminous bioclastic and calcarenitic limestone and marlstone, with interbeds of grey to black calcareous shale (Christopher et al., 2006). The Second White Specks Formation is a distal expression of the Vimy Member of the Blackstone Formation in Alberta. In Manitoba, the formation is coeval with the Favel Formation and is sub-divided into the limestone-dominant, coccolith-rich Keld and the inoceramid-dominated mudstone of the overlying Assiniboine members (Christopher et al., 2006). The presence of planktonic foraminifer from the *Whiteinella aprica* Subzone of the *Heterohelix loetterlei* Zone suggests the

Second White Specks Formation is Early to Middle Turonian in age (Bloch et al., 1999; Schroder-Adams et al., 2001; Schroder-Adams et al., 1996; Tu et al., 2007).

The formation is up to 90 metres thick in northwest Alberta and about 25 metres in Saskatchewan, forming a gradually eastward thinning, wedge-shape sediment package that extends out from the deformation front along the western margin of the WCSB (Bloch et al., 1993; Bloch et al., 1999). Christopher et al. (2006) noted Second White Specks strata thinning northward from the Williston Basin towards the Punnichy Arch, with thin bands of mapped units suggesting lineaments and an uplifted Punnichy Arch influenced pre-Morden erosion of the formation in central to eastern Saskatchewan.

In northwestern Alberta, the formation is bounded by the Sunkay Member of the Blackstone Formation and the Cardium Formation. Mudstones of the Niobrara Formation overlie the Second White Specks Formation at the distal end of the basin in eastern Saskatchewan. Several studies (Bloch et al., 1993; Bloch et al., 1999; Schroder-Adams et al., 1996; Tu et al., 2007) placed the boundary between the Second White Specks and Belle Fourche formations at a prominent lag bed that was mapped from western Alberta into eastern Saskatchewan. Christopher et al., (2006) placed the contact at a bentonite bed that was considered the “X” bentonite based solely on its position in the core. As discussed previously in Section 2.4.2.2, a revised boundary between the Second White Specks and Belle Fourche formations based on data from biostratigraphic, stratigraphic, and dating investigations places the contact at the regional Big Horn River “red” bentonite bed.

An unconformity surface that Ridgley et al. (2001) defines at the contact between D2 and the overlying Second White Specks is interpreted as the product of ravinement during marine transgression. This unconformity correlates with the mapped “red” bentonite of this study. Tyagi et al. (2007) and Tyagi (2009) placed the “red” bentonite just below the Cenomanian-Turonian boundary and the bentonite was interpreted to have been deposited during the Greenhorn cycle’s maximum sea level rise and OAE-II. No images or stratigraphic descriptions of cores that intersect this unconformity was provided in

Ridgley et al. (2001), making it difficult to determine if other evidence that provides support to their interpretation is present, such as sediment lags formed from winnowing.

2.5.3 Allostratigraphy of the Colorado Group

The Upper Cretaceous Colorado Group has been informally subdivided on allostratigraphic grounds into the lower and upper Colorado allogroups (Fig. 2.11) based on studies completed in northern Alberta and northeastern British Columbia (Bhattacharya, 1989; Bhattacharya and Walker, 1991; Plint, 1996; Plint, 2000; Kreitner, 2002; Varban, 2004; Varban and Plint, 2005; Hay, 2006; Kreitner and Plint, 2006; Roca, 2007; Roca et al., 2008; Varban and Plint, 2008a) and central Alberta to the Saskatchewan border (Tyagi, 2009). The following summarizes the allomembers and units found within the Lower and Upper Colorado allogroups. Although several studies conducted in northwestern Alberta and northeastern British Columbia are located outside of the author's study area, they are included in this review because they provide insight into the tectonic and eustatic history of the proximal end of the basin and how these processes have influenced coeval strata deposited or eroded at the eastern part of the basin. Sections 2.4.3.1 through 2.4.3.4 refer to the proximal foredeep and section 2.4.3.5 discusses allostratigraphy for the distal foredeep (Fig. 2.12).

2.5.3.1 Lower Colorado Allogroup

2.5.3.1.1 Fish Scales Alloformation – Allomembers FA and FB

Roca et al. (2008) established an allostratigraphic scheme for the Late Albian-Early Cenomanian Fish Scales Alloformation of the Lower Colorado Group that included two units: FA and FB (Fig. 2.11). The base of unit FA, and contact with the underlying Westgate Formation, is represented by the FE1 surface and the upper limit of FA is bound by the Base of Fish Scales marker (BFSM). The BFSM is the “fish-scale marker bed” and reflects a condensed section composed of silt, sand, and fish scales/bones in the Shaftesbury Formation in northwestern British Columbia (Tyagi, 2009). This bed is considered to represent the boundary between the Albian and Cenomanian and records a phase of bottom-water anoxia (Leckie et al., 1992; Bloch et al., 1993; Roca et al., 2008).

Period	Epoch	Stage	Allogroup	Proximal Foredeep		Distal Foredeep							
				Alloformation and Formation	Allomember nomenclature	Alloformation and Formation	Allomember nomenclature						
Cretaceous	Upper	Turonian	Upper Colorado	Cardium Allo. Fm	E1	Blackstone Alloformation	Carlile Fm.						
				Opabin M.	V		Vimy M.	Second White Specks Formation	XI	Green bentonite (equivalent to GS)	92.5 ± 0.13 Ma		
				Haven M.	IV				X	transgressive surfaces			
				Vimy M.	III				IX	Blue Bentonite			
					II				VIII	transgressive surface			
	Sunkay M.	I	VI	Bighorn River Bentonite	94.29 ± 0.13 Ma								
		A-X	V	K1 - regional disconformity									
	Lower	Albian	Cenomanian	Lower Colorado	Dunvegan Alloformation	A	Blackstone Alloformation	Sunkay M.	Belle Fourche Formation	IV	Top of Dunvegan alloformation	95.87 ± 0.10 Ma	
					Fish Scales Allo.Fm	FB				III	X Bentonite		
						FA				J			FishScales Upper
Westgate Alloformation					WC						I		Base of Fish Scales
					WB								
	WA												

Figure 2:11: Allostratigraphic nomenclature summary chart. Refer to text for detailed description of surfaces. The U-Pb date for the “Green” bentonite is from Tyagi (2009). The Bighorn River and X bentonite U-Pb dates are from Barker et al. (2011).

The FB unit is bound between the BFSM at the base and the “Fish Scales Upper” (FSU) surface at the top. The FSU horizon was first noted by Bhattacharya and Walker (1991) as a radioactive horizon that indicates a major condensed section linked to times of peak transgression. It has been used as a regional mappable geophysical log marker in Upper Cretaceous stratigraphic studies (ie. Plint, 2000; Roca et al., 2008; Tyagi, 2009; Angiel, 2013) and represents the base of the Dunvegan alloformation (Plint, 2000).

The FA unit is limited to a flexural depocenter in northwest Alberta and FB is regionally extensive with predominately sheet-like geometry, generally thinning towards the southern and eastern sections of the basin (Roca et al., 2008). The sheet-like appearance of allomember FB of the Fish Scales alloformation indicates lower subsidence rates over a greater area (Tyagi, 2009).

2.5.3.2 Upper Colorado Allogroup – Dunvegan Alloformation

The Dunvegan alloformation is composed of marine mudstones of the underlying upper Shaftsbury Formation and basinward Sunkay Member of the Blackstone Formation (south of the Athabasca River), and deltaic deposits of the Dunvegan Formation (Plint, 2000). Allostratigraphic subdivision of the Dunvegan Formation was first presented in Bhattacharya (1989), followed by Bhattacharya and Walker (1991), Plint (1996), Plint (2000), and Hay and Plint (2009). The Dunvegan alloformation framework for northwest Alberta and northeast British Columbia is represented by ten transgressive-regressive packages (A through J; Fig. 2.12) that responded to allogenic, tectonic controlled changes in relative sea level (Bhattacharya and Walker, 1991). The basal bounding surface is the Fish Scales Upper (FSU) marker bed recognized by Bhattacharya and Walker (1991) and the deltaic deposits of the Dunvegan alloformation down-lap onto the FSU marker surface (Plint, 2000).

The Middle Cenomanian “X” bentonite lies within the distal expression of the Dunvegan alloformation allomember C (Unit III of Tyagi et al., 2007 and Tyagi, 2009). However, the signal of the bentonite is lost in the shallow and reworked delta-front proximal deposits in northwest Alberta (Tyagi et al., 2007). It is estimated that the Dunvegan

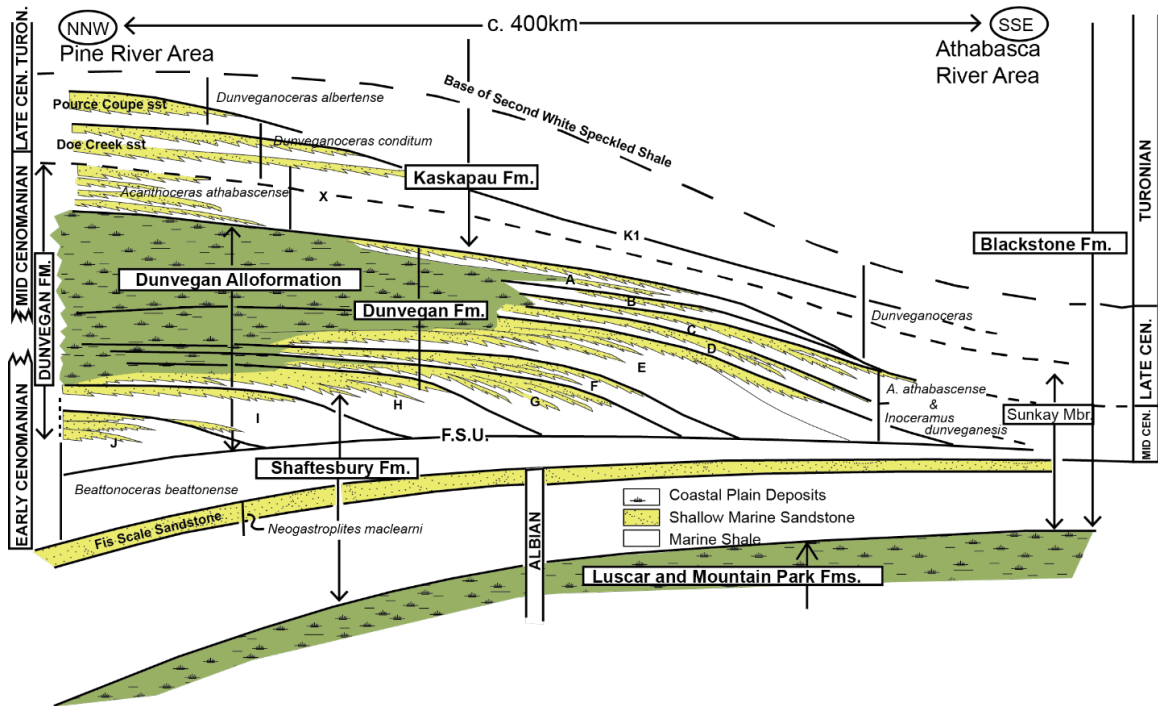


Figure 2:12: Schematic demonstrating stratigraphic relationships between the Dunvegan alloformation and surrounding formations. Modified from Plint (2000).

alloformation was deposited over a span of 2 Myr. during the Middle Cenomanian, with each of the allomembers representing up to 200,000 years (Plint, 2000).

2.5.3.2.1 Lower Kaskapau Formation: A-X unit and X-K1 unit (Doe Creek and Pouce Coupe sandstones)

A-X Unit

Plint (2000) divided the lower Kaskapau Formation, informally called the unit A-X, in west-central Alberta and northeastern British Columbia into four allomembers that separate the lower sandy deltaic deposits from the overlying offshore marine or lagoonal mudstone. Allostratigraphic surface A is the top of the Dunvegan alloformation and X is a regionally mappable transgressive surface that has been traced through Alberta and into Saskatchewan (Plint, 2000; Tyagi et al., 2007; Tyagi, 2009; Plint, 2019). Along the western margin of the basin, the X surface is observed as a disconformity where an oyster biostrome rests directly on a coal (Plint, 2000; Plint, 2019). The distal expression of the X transgressive surface separates near-shore sandy marine facies from overlying offshore mudstones, becoming a paraconformity surface closer to the eastern margin of the basin in Saskatchewan (Tyagi, 2009; Tyagi et al., 2007; Plint, 2019).

The A-X unit records the initial drowning of the Dunvegan delta and repeated transgressive-regressive cycles in response to high-frequency relative sea-level changes (Plint, 2019). Sediments were deposited in a broad, south-east opening embayment, with low-energy highstand deposits found adjacent to the fold and thrust belt, and clean, wave-reworked lowstand sandstone deposits deposited further into the basin (Plint, 2000). Plint (2019) extended the work of Plint (2000) with additional core and outcrop data and divided the A-X unit into five upward-shoaling allomembers (AX1 to AX5). Facies mapping identified three depositional environments in the A-X unit: river dominated deltas fringing an embayment that transitions to the southeast into mud-dominated heterolithic successions accumulated in a shallow, low-energy, brackish embayment with NE-SW trending, elongated and isolated strandplains or wave-dominated delta sandstone deposits (Plint, 2019).

The A-X unit is wedge-shaped and is thickest adjacent to the fold and thrust belt, thinning as it extends basinward, suggesting uniform subsidence with NW-SE trending tectonic load during its deposition (Plint, 2019). Isopach mapping of individual allomembers demonstrated that subsidence was more localized, with depocentres superseding each other and migrating along strike, and that deformation was spatially and temporarily discontinuous (Plint, 2019).

The A-X unit is wedge-shaped and is thickest adjacent to the fold and thrust belt, thinning as it extends basinward, suggesting uniform subsidence with NW-SE trending tectonic load during its deposition (Plint, 2019). Isopach mapping of individual allomembers demonstrated that subsidence was more localized, with depocentres superseding each other and migrating along strike, and that deformation was spatially and temporarily discontinuous (Plint, 2019).

X-K1: Doe Creek and Pouce Coupe Units

The Doe Creek and Pouce Coupe units lie between the X transgressive surface at the top of the A-X unit and the K1 surface, a beveling unconformity that truncates the top of the Pouce Coupe sandstones (Fig. 2.12; Plint et al. 1993; Plint, 2000). Kreitner (2002) divided the Doe Creek and Pouce Coupe into 16 allomembers, labelled 1-8 and 9-16, respectively. The Doe Creek allomembers comprise sandier-upward successions deposited on a southeast-dipping ramp within a broad, shallow water embayment (Plint and Kreitner, 2019). The Doe Creek deposits were controlled primarily by eustatic cycles that over-printed the long-term flexural subsidence (Plint and Kreitner, 2019).

Pouce Coupe shoreface sandstones are north-south, elongate, linear stacked deposits that are confined to a region west of 120°W, and truncated by the K1 unconformity east of this point (Plint and Kreitner, 2019). The uplift and non-deposition of Pouce Coupe sediment east of 120°W may have resulted from a north-south hinge zone that formed from plate flexure within the Kiskatinaw aeromagnetic domain (Plint and Kreitner, 2019). Facies distribution and stratal geometries of the sandstone packages suggest a reverse paleogeographic setting compared to the Doe Creek, with sandstones from the east grading westward into muddy, storm-influenced deposits (Plint and Kreitner, 2019).

2.5.3.3 Upper Kaskapau Alloformation – Units I-V

Varban and Plint (2005) presented an allostratigraphic framework for the upper Kaskapau Alloformation, in north-central Alberta and northeastern British Columbia, between Township 65 and the Peace River and Range 19W5 to the Rocky Mountain Foothills. The study interval comprises five allomembers composed of upward-shoaling successions defined by a marine flooding or ravinement surface, with five to seven shoaling-upwards sequences found within each unit. The strata span between 3 and 3.5 My between approximately 94.2 to 90.7 Ma (Varban and Plint, 2008a) and are bound between the lower K1 unconformity, which also defines the top of the Pouce Coupe sandstone, and a granular siderite erosional surface that lies just beneath the base of the Cardium Formation (Hart, 1990).

Prominent shoreface sandstone bodies in units I through V (Fig. 2.12), informally named Dickebush, Trapper, Tuskoola, Wartenbe, and Mount Robert, extend no more than 20 to 40 kilometers from their respective paleoshorelines and grade laterally into thinly bedded heterolithic sandstones and mudstones (Varban and Plint, 2005; Varban and Plint, 2008a). Three additional sandstone tongues were mapped within unit I (Erin Lodge, Howard Creek, and Josephine Creek, in ascending order) which pinch out to the east, south and west, suggesting each sandstone body was supplied from a low-relief peripheral forebulge located to the north and northeast (Varban and Plint, 2005). The lack of sandstones in units II and III in the east suggests that land uplifted near the peripheral forebulge region during this time was flooded by the Greenhorn transgression (Varban and Plint, 2005).

The Kaskapau Formation strata records a gradual decrease in subsidence rates, with allomembers transitioning from wedge-shaped, tapered packages to more sheet-like with slight tapering to the east (Varban and Plint, 2005). Shoreface sandstones were vertically stacked because of persistent back-tilting from tectonic and sediment loading, with nearly equal rates of sediment supply and accommodation limiting sandstone extents to approximately 20 to 40 kilometres into the basin (Varban and Plint, 2008a). Kaskapau allomember mapping indicated that tectonic loading occurred over a series of 0.5 to 0.7 Myr pulses, where forebulge offlap was coeval to transgressive back-step in the foredeep

and forebulge onlap corresponded to progradation of shoreface sandstones in the foredeep (Varban and Plint, 2008b). As loading persisted in the foredeep, sediments eroding from the western margin became trapped, which led to starvation of sediment in the distal region of the basin and the creation of a condensed section of Upper Colorado strata (Varban and Plint, 2005; Tu et al., 2007; Tyagi, 2009).

2.5.3.4 Blackstone Alloformation – Allomembers I to XI

The Blackstone Alloformation consists of 14 allomembers located between the Fish Scale Upper (FSU) surface and the base of the Cardium E2 allomember (Tyagi, 2009). The following descriptions of the Blackstone alloformations include only allomembers incorporated in this study from the established allostratigraphic framework of Tyagi (2009): I through XI (Fig. 2.11). The mapped allomembers are constrained between laterally traceable marine flooding surfaces, bentonites, hiatal surfaces, and unconformities. The Blackstone Alloformation spans from the late Albian ($\sim 97.59 \pm 0.40$ Ma, Ridgley et al., 2001) to Turonian ($\sim 92.5 \pm 0.1$ Ma, Tyagi, 2009).

2.5.3.4.1 Late Albian-Early Cenomanian - Allomember I

Allomember I

Allomember I is bound between two hiatal surfaces: at the base by the time-transgressive base of Fish Scales marker and at the top by the FSU surface (Tyagi, 2009), and is coeval to unit FB of Roca et al. (2008). Allostratigraphic mapping by Tyagi (2009) demonstrates that Unit I is equivalent to the Fish Scales Formation of Ridgley et al. (2001). Tyagi (2009) extended the BFSM and FSU surfaces of unit FB seaward from the western shoreline (Roca et al., 2008), demonstrating lateral continuity of the sequence and the influence of sedimentation over a forebulge as the unit thinned from 58 metres to approximately six metres near the Alberta-Saskatchewan border. The sheet-like, geometric shape of allomember I, the presence of paraconformities, and absence of foraminiferal biozones indicate the forebulge at this time was broad with relatively shallow water depths and underwent persistent sediment reworking along the sea floor (Tyagi, 2009).

2.5.3.4.2 Middle Cenomanian - Allomembers II through IV

Allomember II

Allomember II is a nearly 60-metre-thick unit that is bounded by the FSU surface and the “X” bentonite (Tyagi, 2009). The fine-grained sediments of this unit are the distal expression of the Dunvegan delta. When the “X” bentonite is traced towards northwestern Alberta, the surface lies within allomember C of Plint (2000). The gamma-ray signal for the “X” bentonite is lost in the proximal part of the basin in northwest Alberta, likely due to the reworking of sediments closer to the shoreface sandstones of the Dunvegan Formation (Tyagi et al., 2007). Isopach mapping by Tyagi (2009) shows allomember II has broad, sheet-like geometry in central and southern Alberta and transitions to wedge-shaped in northwest Alberta, representing a major depocenter that resulted from active flexural subsidence in the foredeep region (Bhattacharya and Walker, 1991; Plint, 1993; Plint, 2000). The basinward transition to sheet-like geometry, a northeast-southwest trending wide zone of flexure (Plint et al., 2009), and lack of erosion during deposition of allomember II suggest the presence of a broad forebulge during deposition (Tyagi, 2009).

Allomember III

Allomember III lies between the “X” bentonite and allomember A, the regional flooding surface at the top of the Dunvegan alloformation (Bhattacharya and Walker, 1991; Plint et al., 1993; Plint, 2000; Tyagi et al., 2007; Tyagi, 2009). It was deposited during the Middle Cenomanian, within the *Verneuilinoides perplexus* foraminiferal Zone, suggesting a time of relative sea level rise in the WIS (Cobban et al., 2006; Tyagi et al., 2007; Tyagi, 2009). Active subsidence in northwest Alberta resulted in an eastward-thinning wedge-shaped geometry, with unit thickness varying between 28 and 4 metres, that was progressively truncated by a post “X” bentonite forebulge uplift and erosion (Tyagi, 2009; Tyagi et al., 2007). The depocenter during allomember III time had begun to rotate parallel to the thrust belt (Tyagi, 2009). Based on high-frequency allostratigraphic mapping completed for the Colorado Group in western Canada, Plint et

al. (2012) suggested that depocenter positions had shifted laterally over 100 to 300 kilometres in under 1 Myr.

Allomember IV

Bounding surfaces for Allomember IV are the top of Dunvegan allomember A and the X transgressive surface of A-X in Plint (2000) and Plint (2019). Thickness of the strata ranged between 30 metres and 4 metres. Allomember IV contains foraminifera from the *Verneuilioides perplexus* Zone, and the *Inoceramus dunveganensis* and *Inoceramus rutherfordi* molluscan zones, assigning the unit to Middle Cenomanian age (Jeletzky, 1968; Caldwell et al., 1978; McNeil and Caldwell, 1981; Cobban et al., 2006; Tyagi et al., 2007). Hay and Plint (2020) concluded that the interval was probably Upper Cenomanian. The allomember IV depocenter was broad and extended across central and southern Alberta along the strike of the orogenic front (Tyagi, 2009). Isopach mapping by Tyagi (2009) showed tectonic loading along the entire length of the thrust belt resulted from terrane accretion events, producing a wide forebulge east of the fifth Meridian that uplifted and caused gradual thinning and eventual erosional truncation of allomember IV. This Middle Cenomanian forebulge unconformity is the same unconformity observed in Bloch et al. (1999) and Schroder-Adams et al. (1996) as discussed in section 2.4.2.2. Absence of the “X” bentonite east of the erosional boundary suggests uplift occurred post-deposition of the ash bed (Tyagi, 2009).

2.5.3.4.3 Late Cenomanian – Allomembers V and VI

Allomember V

Allomember V is a Late Cenomanian deposit that is up to 42 metres thick and extends between the X transgressive surface of allomember IV and the K1 disconformity, which correlates to the top of the X-K1 unit of Plint (2000), Kreitner and Plint (2006), and Plint (2019). In northwest Alberta, the K1 surface truncates up to 80 metres of strata within the lower Kaskapau from west to east (Plint, 2000). Mapping by Tyagi (2009) illustrated a low, tapering wedge that had two distinct depocenter regions, suggesting differential subsidence had occurred at that time. Towards the Alberta-Saskatchewan border, allomember V strata onlap onto the putative forebulge (Tyagi, 2009; Tyagi et al., 2007).

Allomember VI

The upper contact of allomember VI is the Bighorn River “red” bentonite and this surface marks both the top of the Sunkay Member of the Blackstone Formation and the approximate boundary between the Cenomanian and Turonian (Tyagi et al., 2007). Allomember VI was deposited in a distal shelf setting when the WIS was undergoing widespread marine flooding during the Greenhorn cycle. The pattern of subsidence created a wedge-shaped deposit similar to allomember V, where a higher tectonic subsidence rate in northwestern Alberta caused a forebulge uplift and erosion immediately to the east, and a second suppressed forebulge south of Township 45 resulted in allomember VI gradually onlapping onto the underlying non-erosional top of allomember V towards the east (Tyagi, 2009; Tyagi et al., 2007). Increased subsidence rates in the northwest trapped sediment along the deformation front (Varban, 2004) and the influx of warmer, normal marine water caused an increase in biotic productivity, resulting in deposition of calcareous, coccolith-rich mudstones typically observed in allomember VI (Schroder-Adams et al., 1996; Tyagi, 2009).

2.5.3.4.4 Early Turonian – Allomembers VII through XI

Allomember VII

Allomember VII lies between a regional flooding surface at the top and the Bighorn River “red” bentonite at the base. During the Early Turonian, major tectonic loading was limited to northwest Alberta and northeastern British Columbia and produced a nearly 150-metre-thick wedge of sediment that laps out east of the fourth Meridian (Tyagi, 2009). Allomember VII strata is composed of calcareous fine-grained sediment deposited during a time of peak transgression (Tyagi, 2009).

Allomember VIII

Allomember VIII is bound between a regionally traceable bentonite (informally termed the “blue” bentonite by Tyagi (2009)) and the marine transgression surface of allomember VII. Tyagi (2009) interpreted the “blue” bentonite as a distal expression of a chert and quartzite pebble ravinement surface mapped by Varban (2004). Allomember VIII is a wedge-shaped unit, up to 48 metres thick in the northwest, that progressively

laps out onto a non-erosional forebulge over 250 kilometers east of the deformation front (Tyagi (2009)).

Allomember IX

Bound between the underlying “blue” bentonite and a marine flooding surface, allomember IX is an Early Turonian fine-grained, wedge-shaped unit that was deposited at a time when tectonic loading was confined to northwest Alberta (Tyagi, 2009). Isopach mapping by Tyagi (2009) illustrated segmented thickness zones and suggested they could be related to flexural interaction of older and younger depocentres or variations in intraplate stresses.

Allomember X

Allomember X is bound between two subtle marine flooding surface and is composed of increased calcareous sediment seaward (Tyagi, 2009). In contrast to the underlying allomembers, allomember X has a linear depocenter parallel to the deformation front that thins towards the thrust belt and the forebulge, a trend that was not linked to basement tectonic domains (Tyagi, 2009).

Allomember XI

Allomember XI is a 36-metre-thick wedge-shaped unit that lies between the transgressive surface of allomember IX and a regional bentonite marker bed, informally called the ‘green’ bentonite by Tyagi (2009), which is coeval to the Gritty Siderite surface of Varban and Plint (2005). Tyagi (2009) recognized the “green” bentonite bed as a maximum flooding and a regional hiatal surface that, based on its proximity to the underlying *P. woollgari* Zone, provides a reliable marker to map the time equivalent strata of the Vimy Member (Blackstone Formation). Two major depocentres occur within allomember XI: one depocenter was confined to the northwest portion of the WCSB and developed an eastward tapering wedge that thins to about 12 metres from a 34-metre thickness, and the other formed a northeast-southwest trending depozone; neither depocenter could be related to reactivation of basement structures (Tyagi, 2009). The relatively continuous expression of allomember XI across northern and central Alberta

was thought to have been a result of progradation from increased sediment supply and a suppressed forebulge resulting from decreased tectonic loading in the Thrust Belt (Tyagi, 2009).

Chapter 3

3 Sedimentary lithofacies of the Upper Colorado Group

Mudstones (*sensu* Lazar, 2015) make up nearly 50 percent of all sedimentary rocks in the stratigraphic record, and in the present-day, fine-grained sediment accounts for more than 65% of the world's sediment supply (Potter et al., 1980; Aplin et al., 1999; Boggs, 2009). Mudstone composition is often highly variable and reflects the interrelated physical, chemical, and biological processes occurring during transport, deposition, and diagenesis (Lazar et al., 2015). Focused drilling activity in tight, self-sourcing mudstone reservoirs has heightened interest in understanding factors contributing to the transport and deposition of fine-grained sediments and, more importantly for hydrocarbon evaluation, how these mechanisms control organic matter preservation and distribution (e.g., Passey et al., 2010; Aplin et al., 2011; Slatt and O'Brian, 2011).

Historically, fine-grained rocks were commonly categorized as “shale” and thought to have formed through suspension settling in the water column and under calm conditions (Potter et al., 1980). The apparent homogeneity of fine-grained rocks during visual examination resulted in vague descriptions, often lumping meter-long sections of strata into one generic term that lacked any insight into the actual depositional processes. The evolution of research methods to study fine-grained sediments (e.g., Macquaker and Gawthorpe, 1993; Schieber et al., 2007; Macquaker et al., 2007; Plint, 2014) has demonstrated mud successions are typically lithologically heterogeneous (e.g., Macquaker and Gawthorpe, 1993; Schieber et al., 1998). The traditional mud accumulation model of suspension settling of individual fine-grain particles in quiet, relatively deep water (Potter et al., 1980) progressed into an understanding that, under certain conditions, composite particles of flocculated mud can be transported as migrating ripples under current velocities typically required to move sand (e.g., Macquaker and Bohacs, 2007; Schieber et al., 2007; Schieber and Southard, 2009; Macquaker et al., 2010). The evolved mudstone sedimentation concept led to a revised approach in classifying fine-grained rocks (Lazar et al., 2015) using a combination of compositional variation, texture, and fabric to yield a greater understanding of mudstone genetics and depositional history.

Lazar et al (2015) developed a scheme for evaluating, comparing and interpreting fine-grained sedimentary rocks. In this scheme, the name of a rock has three components: texture, bedding, and composition. The texture forms the root of the name and is based upon the percentage of sand, coarse mud, or fine mud found in the rock (see Fig. 1, Lazar et al., 2015). The bedding component considers laminae, laminasets, and beds. Lamina descriptions are based on their continuity, shape, and geometry (Figure 3.1A)). Laminae are millimetre-scale layers void of internal sedimentary structure and form over an “instant of geological time” (seconds to years) in response to small-scale fluctuations within a depositional event or single flow (Campbell, 1967). Laminasets comprise millimetre- to centimetre-thick, genetically associated laminae that are bounded by laminaset surfaces and can form over minutes to a year (Campbell, 1967). Beds are conformable successions of genetically related laminae or laminasets bounded by surfaces of erosion, nondeposition, or correlative conformity (Campbell, 1967). Rock composition is assigned using a ternary diagram (Figure 3.1B)) that separates composition components by their total percentage of quartz, carbonate (e.g., calcite, dolomite, etc.), and clay (e.g., illite, smectite, etc.) minerals, with the name reflecting which mineral component is greater than 50%, or two of the most common when none exceed 50%. The present study incorporates the mudstone classification scheme of Lazar et al. (2015) into core logging to: 1) better define mudstone sedimentology within the Upper Colorado Group and understand broad depositional conditions influencing fine-grained sedimentation across the WCFB, and 2) have a repeatable workflow that reduces uncertainty with subsequent interpretations presented in this thesis.

This chapter presents lithofacies descriptions and lithofacies relationships used to develop the compositional maps and depositional model for the Blackstone alloformation of the WCFB. The chapter begins with a literature review of shallow marine processes and mud transport concepts (Sections 3.1 to 3.4) and is followed by core facies descriptions and interpretations in Section 3.5 and 3.6, respectively.

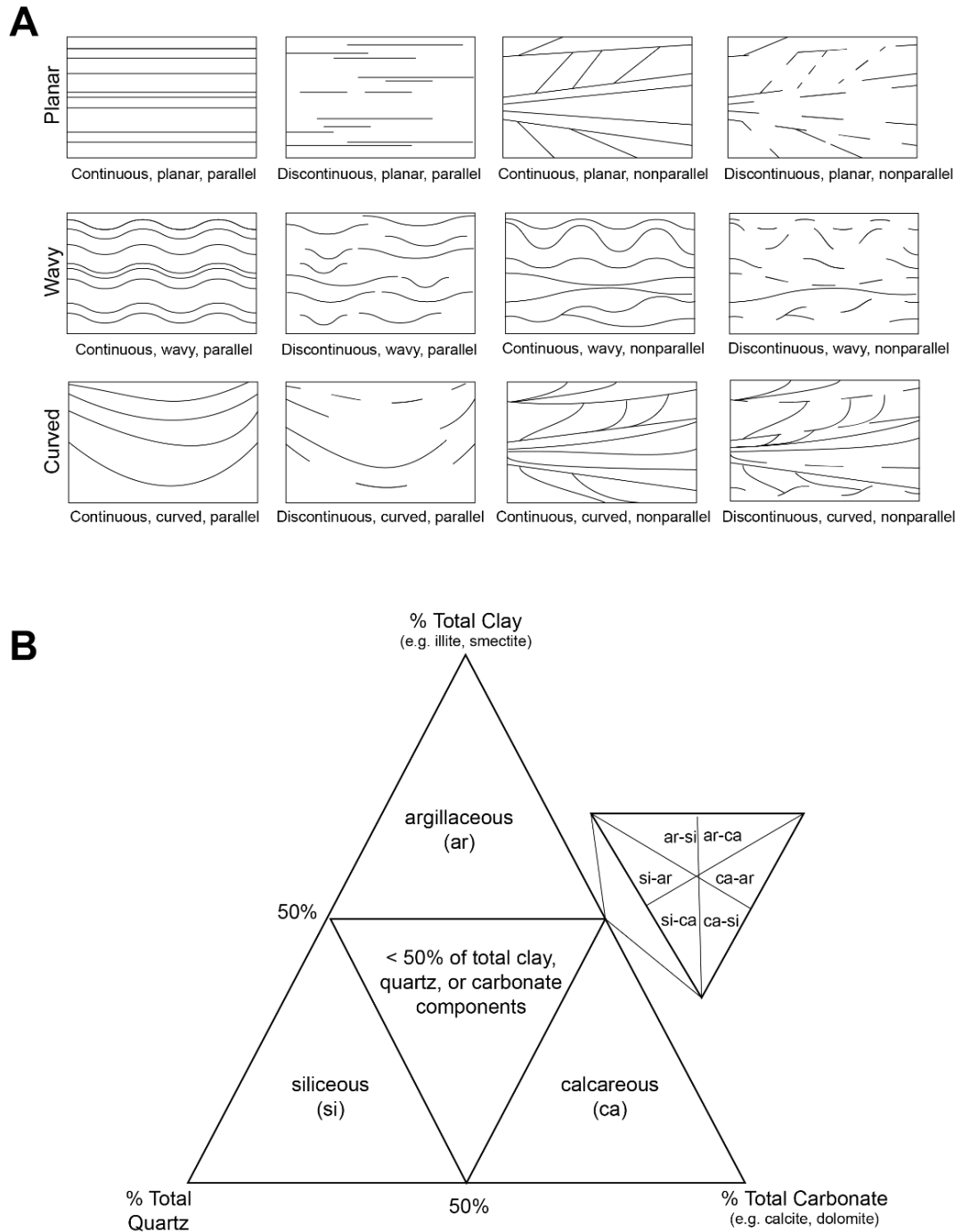


Figure 3:1: Nomenclature proposed by Lazar et al. (2015) to classify fine-grained sedimentary rocks. A) Terms to describe lamina attributes: continuity, shape, and geometry. B) Ternary diagram showing division of composition percentages and associated nomenclature. (Diagrams modified from Lazar et al. (2015)).

3.1 Shallow marine setting and processes

The Upper Colorado Group strata is a succession of fine-grained rocks deposited on a storm-dominated marine ramp within the Western Interior Seaway (WIS) (Plint et al., 2012). The WIS was a shallow (< 100 m deep) epicontinental sea with a gently dipping slope (between 0.005 to 0.001°) and a maximum width of ~1000 kilometres (Johnson and Baldwin, 1996; Suter, 2006; Plint 2010; Schieber, 2016). Although the WIS was technically a ramp (vs. a continental shelf), its marine environments can be compared to those observed in modern shelf-depositional systems.

A beach-to-offshore profile of a marine shelf-depositional system includes three main zones: termed foreshore, shoreface, and offshore (Figure 3.2) (Plint, 2010). The foreshore is located proximal to the shoreline and lies above the low-tide level. Sediment deposition in this zone is dominated by the back-and-forth swash and backwash of breaking waves, resulting in planar lamination (Clifton, 2006; Plint, 2010). Below the low tide line, sand is deposited within the shoreface/beach zone. Within this low-gradient (<0.3° slope) zone, sand is transported by shoaling waves, with the high-energy setting (dominated by swells) producing cross-bedding (upper shoreface), swaley cross-stratification (middle shoreface), and hummocky cross-stratification (lower shoreface/inner shelf transition zone) (Clifton, 2006; Plint, 2010). Below fair-weather wave base, the lower shoreface transitions into the offshore zone where the seabed gradient further decreases (~0.001 to 0.0005°) (Plint, 2010), bioturbation increases, and sediment type shifts from predominately sand to mud. This is reflected in the interstratification of storm-deposited wave rippled sand or silt beds and fairweather-deposited mud (Clifton, 2006),

Marine sediment is transported on the sea-bed by oscillatory motion induced by surface gravity waves, or through sustained bottom currents that are generated from shore-parallel, longshore currents and seaward-directed rip currents (Clifton, 2006). Waves are regular disturbances at the water surface created by the blowing of wind over the sea surface (surface waves) that causes water to move in an orbital motion. The size of the orbitals decreases in diameter until the water depth is greater than half the surface wavelength (effective wave base), rendering the movement inconsequential (Clifton,

Marine shelf depositional system

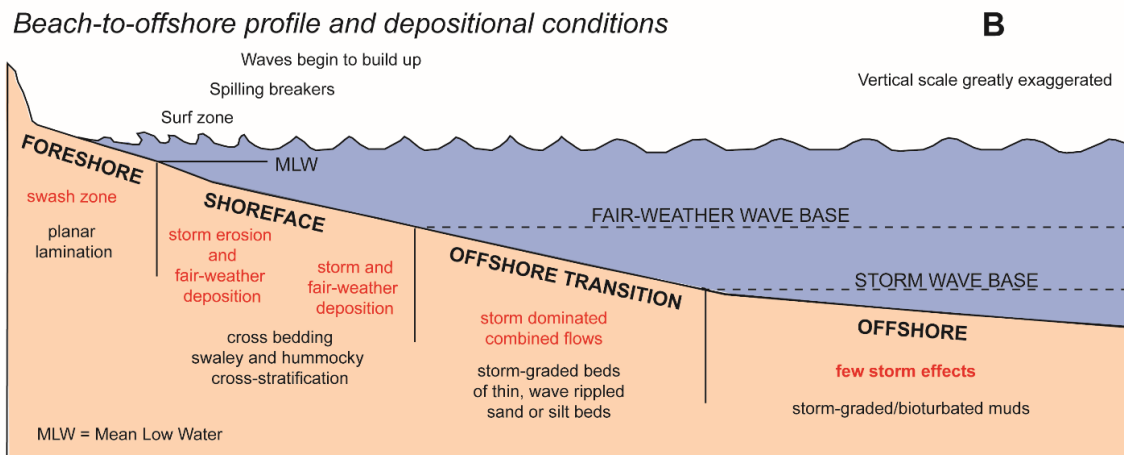
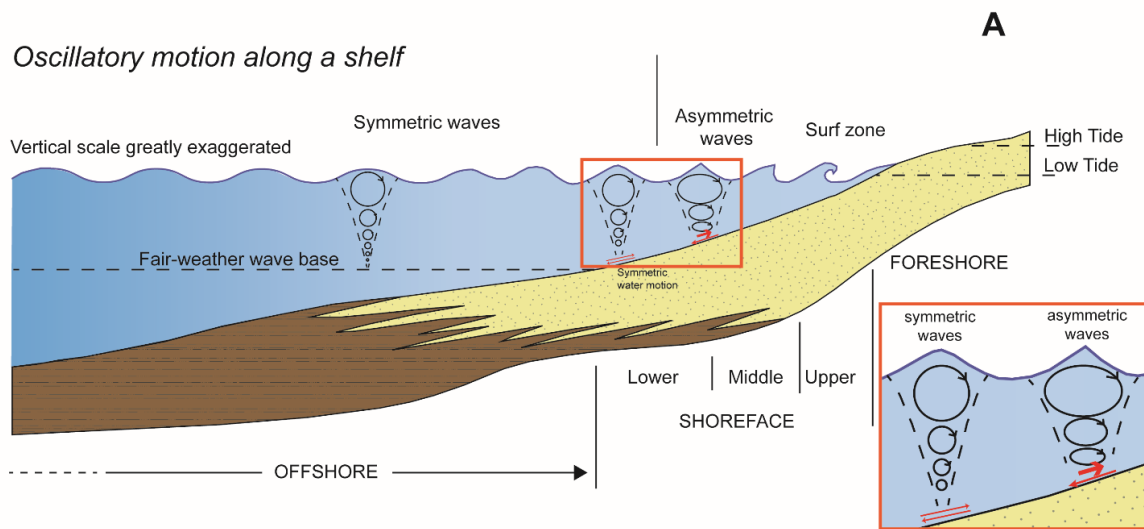


Figure 3:2: Elements of a shallow marine depositional system. A) Waves passing into shallow water and within wave base change to an elliptical orbit, causing oscillatory water movement just above the seabed. Shoreward, the waves become asymmetric and are shorter in wavelength (red arrow length) and faster flowing (red arrow thickness), compared to a longer duration and weaker velocity seaward movement of water (see inset). Stronger landward velocities (thicker red arrow in image A and inset) produce landward bed-load transport characterized by landward-directed cross-bedding and ripple lamination, as well as textural sorting of clastic material on the beach and shoreface that was too heavy for the lower-velocity seaward current (Clifton, 2006). Modified from Plint (2010). B) Profile of a shallow marine shelf. Modified from Clifton (2006).

2006; Plint, 2010). As the wave passes into shallow water and within wave base, frictional drag causes the circular orbital motion of water molecules to deform into an ellipsoidal orbit, causing nearly horizontal, oscillatory water movement just above the sea-bed (Clifton, 2006). Shoreward, the waves become sharp-crested and flow becomes asymmetric underneath, producing shorter, stronger landward movement and longer duration of weaker seaward flow (Clifton, 2006). The stronger landward flow promotes net transport of coarser-grained sediment toward the shoreline, effectively sorting material within the nearshore setting (Clifton, 2006). At a water depth of ~ 1.3 times the wave height, the wave crest topples forward and translates the wave energy landward, producing a swash on the beach/foreshore (Clifton, 2006; Plint, 2010).

Shore-parallel longshore currents and shore-normal rip currents are nearshore circulation cells driven by the difference in hydraulic head produced by the obliquely landward movement of swash onto the foreshore (Clifton, 2006; Suter, 2006). The unidirectional longshore currents transport and redistribute sediment along the coast (Komar, 1976). High-velocity rip currents are confined to narrow rip channels (20-40 metres wide) that are capable of transporting sand and gravel seaward, but their rapid deceleration as the current moves away from the swash zone means sediment remains within the foreshore setting (Plint, 2010). An exception to this is when wave energy is increased during a storm event and a storm surge is produced. The resulting larger waves prompt a greater degree of set up (sea rise from landward motion) and setdown (sea fall from seaward currents), effectively extending rip currents to the base of the shoreface (Clifton, 2006; Plint, 2010).

Offshore sediment transport is initiated when strong, storm-generated winds increase the pressure gradient between the set up and setdown in the nearshore zone. As the resulting bottom waters flow seaward, perpendicular to the shoreline, they become influenced by Coriolis force. The Coriolis force is a result of the Earth's rotation around its axis, whereby movement of any body moving towards or away from the poles (air mass or water in the ocean) is deflected — horizontally moving objects deflect to the right in the northern hemisphere and to the left in the southern hemisphere (Nichols, 2009; Suter, 2006). This force causes seaward bottom currents to deflect as much as 90° from the

wind direction, forming marine currents nearly parallel to the shoreline (geostrophic flow) (Figure 3.3) (Suter, 2006; Plint, 2010).

On a storm-dominated shelf, sediment is mainly transported by a combination of wave-induced oscillatory currents and geostrophic flows, specifically within the water column directly overlying the seabed (Duke, 1990; Nittrouer and Wright, 1994; Plint, 2010). Sediment within the boundary layer, approximately 10 centimetres above the seabed where fluid is slowed by viscous impedance, is kept in suspension, or resuspended, by strong, storm-driven oscillatory and combined flow currents that produce enough shear stress to erode and transport the material on the sea floor (Nittrouer and Wright, 1994; Plint, 2010). Once in suspension, the sediment particles are eventually combined with the unidirectional geostrophic flow component and transported along- and offshore (Plint, 2010). Net sediment transport in the net direction of the combined flow is influenced by the intensity and duration of the storm event, the volume of coastal set up, and shelf slope (Suter, 2006).

3.1.1 Sedimentological evidence of a storm-influenced system

Interpretations for shallow-marine storm- and wave-dominated settings are based on the assessment of sedimentary structures preserved in the rock record. Tempestite beds are storm-generated deposits typically represented by sandstone beds with an erosive base and by a general “fining-upward” in grain size. The erosive base commonly features sole marks, including tool and scour, and variably sized gutter casts (Myrow, 1992a, Myrow, 1992b; Myrow and Southard, 1996; Suter, 2006). These structures form from wave action, downwelling storm currents, or another type of combined flow system cutting into underlying sediment (Suter, 2006). Typically overlying the erosion surface is hummocky to swaley cross-stratified sand deposited under oscillatory-dominant or combined flow conditions (Arnott and Southard, 1990; Duke et al., 1991). As the storm event dissipates, opportunistic suspension-feeding fauna of *Skolithos* and proximal *Cruziana* ichnofacies begin to colonize the storm-deposited sand (Suter, 2006). The top of a tempestite bed is commonly pervasively bioturbated due to the post-storm establishment of deposit-feeding and grazing benthic organisms of the distal *Cruziana* and *Zoophycos* ichnofacies in fair weather-deposited mud (Suter, 2006).

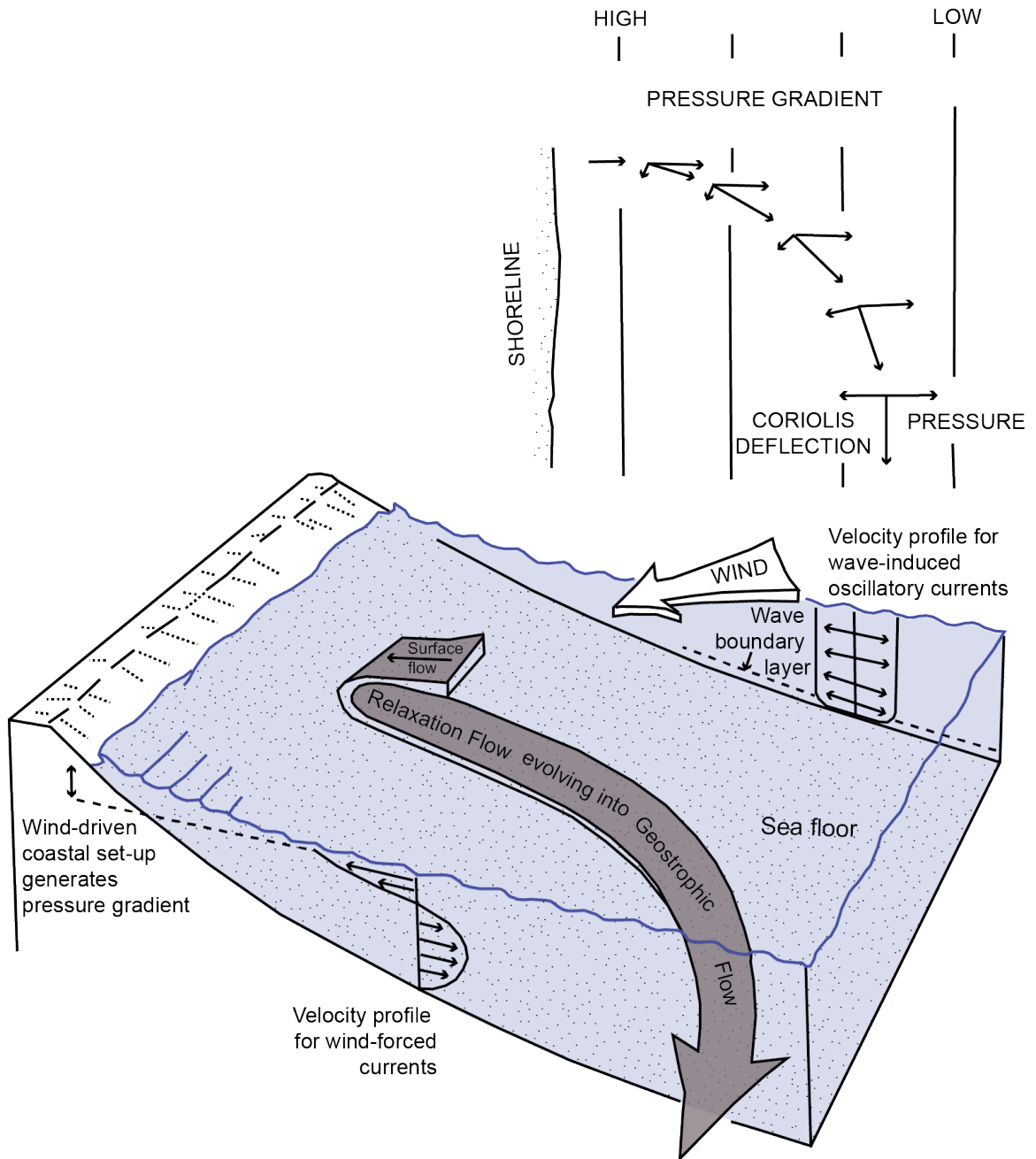


Figure 3:3: Geostrophic flow develops when offshore moving bottom currents are redirected near parallel to shore by Coriolis force, resulting in sediment transport along the shelf. Modified from Plint (2010).

3.2 Mud aggregate grains

Sediment delivered to the sea as suspended load via rivers either settles to the sea floor as bed load at the river mouth or remains in suspension (Syvitski, 2003; Plint, 2010). Fine-grained silt and clay particles that remain in suspension can be transported as individual flakes or as mud aggregates (Potter et al., 2005). Individual clay particles can be kept in suspension by weak currents and may be transported long distances, while larger aggregates of flocculated clay particles settle more rapidly (Potter et al., 2005).

Settling velocities of grains is a function of Stokes' Law, where particles remain in suspension if the upward forces of turbulence in the fluid equal or exceed the fall velocity. A clay particle will stay in suspension longer, and with greater ease, than silt- or sand-sized sediment, resulting in long transit times and lateral transport of fines in a basin (Potter et al., 2005). However, mud aggregates have grain sizes ranging from a few microns (silt-sized) to over 700 microns (coarse sand) (Potter et al., 1980), which results in higher settling velocities (Syvitski et al., 1985). The formation of mud aggregates is categorized into four major physical and biological processes: electrochemical coagulation, particle collisions, biogenic pelletization, and biophysical particle attachment (Pryor, 1975; Bennett et al. 1991; Syvitski, 1991).

The change in salinity between a freshwater river and a saltwater sea promotes the development of aggregates through chemical (coagulation) and physical (flocculation) processes. During electrochemical coagulation, small, platy particles in suspension are brought together by van der Waals attraction forces and the ions present in seawater counteract the electrostatic repulsion of clays, allowing them to aggregate together (Bennett et al., 1991; Grabowski et al., 2011; Potter et al., 2005). Aggregates also form through the physical collision of clay particles during suspension, allowing them to overpower the natural electrostatic repulsion of the particle surface. This type of flocculation is likely to occur at the river mouth where high sediment concentration forces particles to collide with each other, or wherever an increase in flow turbulence re-suspends sediment, causing inter-particle collisions (e.g., McAnally and Mehta, 2001). The gathering of biological matter into mud aggregates is an example of an *autochthonous* component of mudstones, which is related to productivity and includes

biogenic material such as shell debris, organo-minerallic aggregates (e.g., Macquaker et al., 2010; refer to Chapter 7 for details on the formation of organo-minerallic aggregates) and mineral-bearing faecal pellets excreted from grazing zooplankton (Hill et al., 2007; Syvitski, 1991). Pryor (1975) observed biogenic pelletization sedimentation when crustaceans feeding on suspended argillaceous particles deposited layers of fecal mud. Mucus secreted by bacteria and algae can cause the clay particles to flocculate, possibly combining the clay with silt and biological debris (Potter et al., 2005).

3.3 Mud transport and sedimentation

Fine-grained sediment delivered to the sea by rivers is distributed by one of two ways: as hypopycnal or hyperpycnal plumes (Figure 3.4). A hypopycnal river plume is formed when lower-density fresh water floats on top of higher density sea water (Nittrouer et al., 2007). These buoyant plumes produce surface nepheloid layers (turbid water) that spread seaward to the inner or middle shelf region (10 to 20 kilometres from shore) before they are redirected parallel to the coast by Coriolis force (Nittrouer et al., 2007; Nittrouer and Wright, 1994; Plint, 2010). If sediment concentration in river discharge is elevated to 35 – 45 kg/m³, as found in river floods with high turbidity, the density of the plume can exceed that of seawater and sink to the seafloor (hyperpycnal flow), forming a nepheloid layer at the seabed (Mulder and Syvitski, 1995; Nittrouer et al., 2007; Bhattacharya and MacEachern, 2009). Clay aggregate grains form within hours or days of a river flood event and can transform a hypopycnal river plume with low sediment concentration into a hyperpycnal flow (Bhattacharya and MacEachern, 2009).

Mud is transported offshore when storm waves or tidal currents produce enough shear stress at the seafloor to erode and resuspend sediment, permitting continued seaward migration driven by surface waves, long-term coastal currents, tides, geostrophic flows, and gravity-driven flows (Nittrouer and Wright, 1994; Traykovski et al., 2000; Wright et al., 2001; Hill et al., 2007). Fine-grained sediment within the bottom nepheloid layer migrates downslope when there is enough sediment in suspension to produce a pressure gradient along a shelf slope ($>0.7^\circ$ for fine-grained sand; >0.03 for mud), ensuring the turbidity threshold for sediment transport is maintained through auto-suspension (i.e., a river-fed hyperpycnal plume) (Traykovski et al., 2000; Bhattacharya and

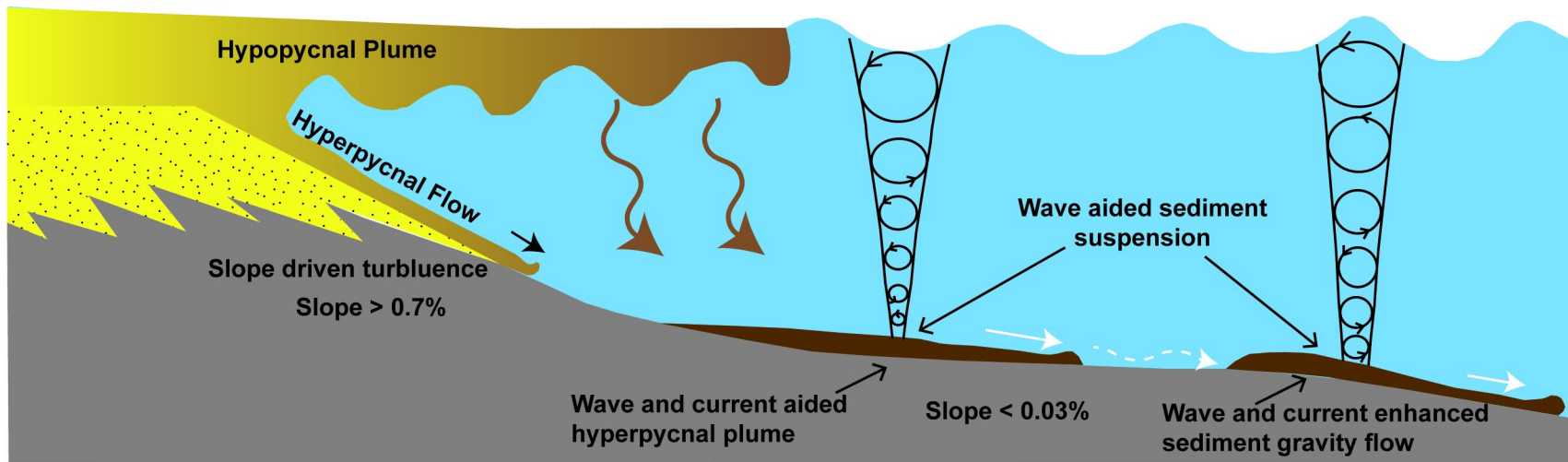


Figure 3:4: Sediment transport by hypopycnal and hyperpycnal plumes. Lower density (fresh) water floats on top of saline water, producing a buoyant hypopycnal plume. A hyperpycnal plume is a turbidity current that occurs at a river mouth when the density of the river water is greater than the density of seawater because of the suspended load it carries (Mulder and Syvitski, 1995). Hyperpycnal flows transport sediment along the sea floor through slope driven turbulence or wave and current aided gravity flows. White dashed arrow reflects sediment resuspension by storms. Image modified from Bhattacharya and MacEachern (2009) and Schieber (2016).

MacEachern, 2009). When the gradient of the continental slope is <0.03 , sediment transport requires higher energy marine conditions (such as storm-induced waves or tidal currents) to resuspend sediment at the seabed, encouraging transport along the shelf as fluid mud (Traykovski et al., 2000; Bhattacharya and MacEachern, 2009). Fluid muds with sediment concentrations greater than 10 g/L are categorized as fully turbid. The density of fluid mud is maintained by wave-generated turbulence, and the downslope migration of fluid mud is driven by gravity and the difference in density between the fluid mud and the clear water (Traykovski et al., 2000; Wright and Friedrichs, 2006; Hill et al. 2007). Wave-enhanced sediment gravity flows (WESGFs) are wave-induced turbulent flows characterized by a normally graded, “triplet” sedimentation pattern comprising an initial layer of largely homogenous silt, an intercalated silt and clay middle laminae set, followed by a homogenous clay-rich drape (Macquaker et al., 2010a). WESGFs can develop on shelves with slopes as low as 0.5 m/km and will cease to suspend mud when the waves are no longer in contact with the seabed, resulting in sediment settling out and producing a normally graded bed (Scully, 2006; Macquaker et al., 2010a; Plint, 2010). Continual mud transport to the offshore produces prismatic, shore-parallel subaqueous deltas (or mud wedges) characterized by seaward-dipping clinofolds that downlap onto a sediment-starved shelf (Cattaneo et al., 2007; Plint, 2010).

3.3.1 Mud transport on an ancient storm-dominated shelf

The Upper Colorado Group mudstones were transported and deposited within the storm-dominated, relatively shallow (<100 m water depth) WIS. Recent studies completed on Colorado Group mudstones suggest mud transport in the foredeep and distal regions of the WCFB was complex, and that sedimentation on the relatively flat seabed was strongly influenced by storm-induced bottom currents (Schieber et al., 2007). Storm-wave base for epicontinental basins is generally shallower than other marine shelf-like settings due to their low gradient slopes, with modern analogues for epicontinental seas suggesting effective water depths between 30 and 50 metres (Aigner and Reineck, 1982). Considering this, seaward sediment transport mechanisms, such as distal hyperpycnites and storm-induced sediment gravity flows, would likely only extend 100 km from the

shoreline by the time the 50-metre storm-wave base and minimal slope criteria (0.03°) were met (Schieber, 2016). Evidence from ancient shallow-marine deposits suggests storm-wave base for sand and silt between 40 and 70 metres water depth, and 70 to 100 metres for mud (Plint, 2014), enabling mud transport to the distal offshore. In the distal prodelta of the Dunvegan Formation, evidence suggests advective transport of mud aggregate grains up to 120 km offshore was aided by resuspension of sediment through storm-generated waves and transported off-shore by geostrophic flows (Plint et al., 2009; Plint, 2014). Varban and Plint (2008b) concluded offshore advective transport (greater than 300 km) of Kaskapau Formation mudstones on the low-gradient WIS resulted from storm-driven geostrophic flows, carrying fine grained silts and muds parallel to the shoreline. The continual wave reworking and transport of sediment limited the development of seaward-dipping clinothems. Mud aggregates observed in the Belle Fourche and Second White Specks formations in the foredeep indicated that mud was transported as bedload through wind-induced bottom current processes (Zajac, 2016; Percy, 2019). The resuspension of intraclastic aggregates in mudstones observed in Colorado Group mudrocks points to erosional reworking of partially consolidated mud on the seabed by storm waves (Jiang, 2013; Plint, 2014).

3.4 Facies model to link proximal shoreface to the distal offshore

The classic shoreface models (Figures 3.2, 3.3, and 3.4) are used to summarize siliciclastic depositional environments in a proximal setting. Facies observed in the distal end of the basin, beyond 120 km offshore (i.e. Plint et al. 2009, Plint, 2014) in the WIS require a model that links the nearshore with the offshore siliciclastic mudstones and pelagic carbonate facies. Hart (2016) proposed a conceptual facies model (Figure 3.5) that represents a mudstone depositional system in an epicontinental seaway. Shoreline sandstones comprise proximal deposits and are dominated by coarse-grained siliciclastics, which transition to siliciclastic mudstones and calcareous mudstones further offshore. Pelagic limestone is deposited in the centre of the basin where clastic sediment

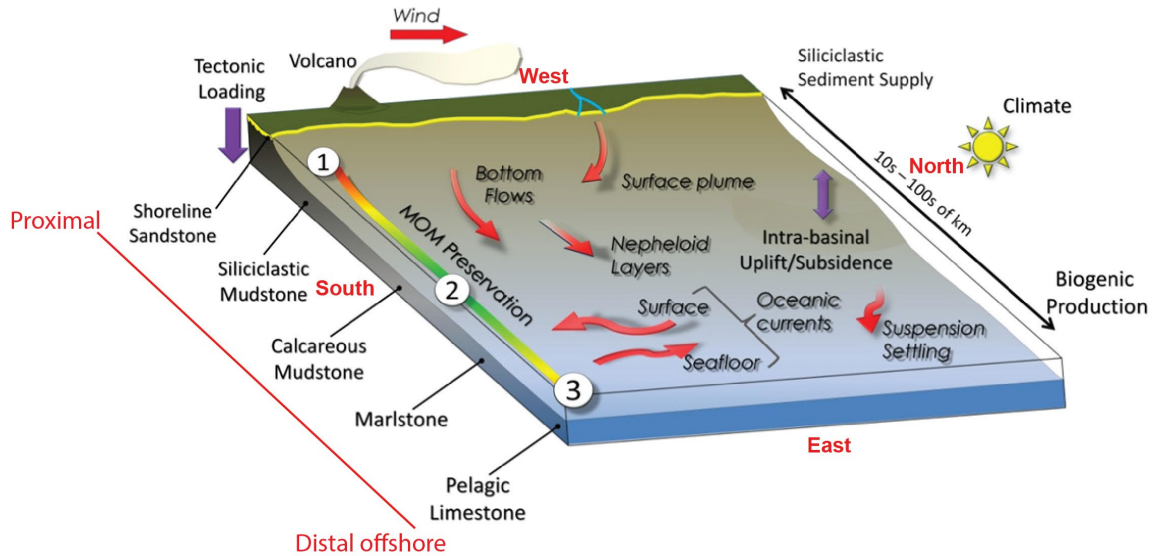


Figure 3:5: Schematic of a conceptual proximal to distal mudstone depositional system. This illustration reflects the processes acting on sediment transport in the Western Interior Seaway. The numbers indicate siliciclastic mudstones (1), calcareous mudstones (2), and pelagic limestones (3), with low, good, and low preservation potential for marine organic matter, respectively. Modified from Hart (2016).

supply is at its lowest and biogenic input is highest. At the eastern extent of the WIS in Manitoba, sedimentation is characterized by carbonates and fine-grained terrigenous clastics in a low-energy, photic marine ramp environment (Mohebati, 2016). The lithofacies observed in this study extend from a proximal offshore transition zone to distal offshore setting (Figure 3.6).

3.5 Sedimentary lithofacies of the Upper Colorado Group

Lithofacies are bodies of rock defined by a combination of composition, texture, fossils, and sedimentary structures that have genetic significance, differentiating from rock bodies found above, below, and adjacent to them (Dalrymple, 2010). Their distinctive characteristics correspond to conditions at the time of deposition, and the association of the lithofacies to neighbouring lithofacies aids in the interpretation of the depositional environment (Reading and Levell, 1996). A group of lithofacies that are genetically and environmentally related is termed a *lithofacies association*, whereas a *lithofacies succession* is a vertical succession of lithofacies based on a distinctive arrangement of multiple lithofacies (Dalrymple, 2010).

The fit-for-purpose lithofacies classification applied in this study separates the lithofacies of the Colorado Group into five recurring categories and are based on observations made from 18 cored wells (Table 3.1). The lithofacies are designated Lithofacies 1 through 5 and represent changes in composition, grain size, fossil and trace fossil content, and sedimentary structures observed within a distal shoreface to offshore shallow marine environment (Table 3.2). It is recognized that the lithofacies could be further subdivided into subtypes based on the wide range of lamina characteristics observed, however, it was decided that the classification used here is appropriate for basinwide-scale mapping because it still permits the separation of distinctive bodies of rock that formed under specific conditions of sedimentation, reflecting particular processes or depositional environments (Reading, 2001).

The logged cores were tied to corresponding geophysical well logs to ground-truth the log data, providing more accurate log depths for the core and allowing the integration of visual core descriptions with petrophysical responses to confirm rock properties of facies.

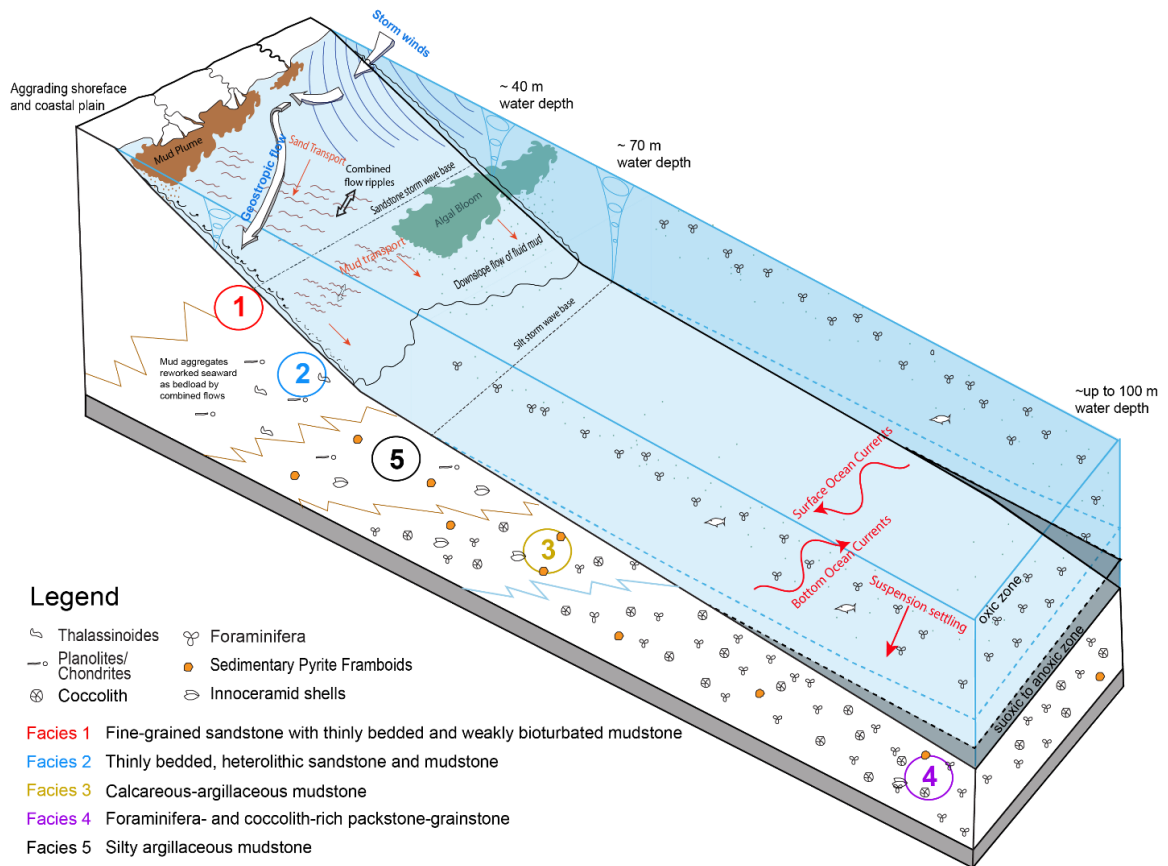


Figure 3:6: Illustration summarizing the proposed depositional model for the current study. Sedimentation occurred on a very low gradient, shallow marine ramp. Cartoon adapted from Varban and Plint (2008), Plint et al. (2012), Plint (2014), Hart (2016), Mohebaty (2016), and Marion (2019).

Table 3.1: List of cored wells logged for this study. Wells located in Alberta were logged and sampled at the Alberta Energy Regulator Core Research Centre in Calgary, Alberta. Saskatchewan-based wells were logged at the Saskatchewan Subsurface Geological Laboratory in Regina, Saskatchewan. *Data provided on the graphic log for 100/07-19-045-06W5 was collected by K. Greff in 2011 and shared with the author. This information was supplemented by lithofacies interpretations presented by Marion (2019).

Alberta	interval top (m)	interval base (m)	Core length (m)
100/14-07-036-05W5	2298.75	2306.25	7.5
100/07-19-045-06W5*	1793.75	1870.23	76.48
100/16-28-041-04W5	1823.25	1828.39	5.14
100/11-12-006-16W4	601.67	628.5	26.82
102/07-04-028-18W4	986	1024.5	38.5
103/06-04-017-13W4	624	703	79
100/02-34-024-15W4	798	831	33
102/16-18-023-03W4	654	680.5	26.5
100/06-23-043-11W4	542.5	560	17.5
Saskatchewan			
141/07-34-035-01W2	199.85	238.2	38.35
111/03-22-055-25W3	309.75	328	18.25
142/05-08-028-28W3	662.5	691	28.5
101/16-23-023-28W2	517	535.88	18.88
101/06-11-014-26W3	650	665.55	15.55
121/06-35-013-13W3	866	883	17
101/06-15-015-13W2	607.75	625	17.25
131/11-09-017-23W2	669	697	28
101/06-28-029-24W2	431.2	446	14.8

Table 3.2: Summary of lithofacies recorded in this study.

Lithofacies	Description
Lithofacies 1	Fine-grained sandstone with thinly bedded and weakly bioturbated mudstone
Lithofacies 2	Thinly bedded, heterolithic sandstone and mudstone
Lithofacies 3	Very thinly bedded, carbonaceous, calcareous-argillaceous mudstone
Lithofacies 4	Foraminifera- and coccolith-rich packstone-grainstone
Lithofacies 5	Thinly bedded silty argillaceous mudstone

The calibrated log data was used to map regional compositional changes within the Blackstone allostratigraphic framework (Chapter 6).

3.5.1 Bentonite

Bentonite beds are observed throughout the stratigraphic interval and across the study area. Bentonites are soft, diagenetically altered, volcanic ash deposits that accumulate in the sea after a volcanic eruption. Ash is distributed by high altitude winds (10-15 km), and preservation is enhanced in low-energy, distal marine settings where reworking from high-energy waves or clastic dilution is minimal. Ancient volcanic ash beds are useful in chronostratigraphic investigations because they are:

- Contemporaneous deposits that produce distinct geophysical well log readings (due to elevated radioactive clay content compared to the adjacent rock), resulting in time-equivalent markers that are regionally extensive,
- Found parallel to marine flooding surfaces, providing reliable proxy-time-lines for regional mapping, and
- Relatively easy to correlate in the subsurface (e.g. Tyagi et al., 2007; Tyagi, 2009).

Bentonites that contain zircon can be extracted and used for radiometric dating, revealing the timing of volcanic events, or to determine volcanic source areas and wind patterns (Elder, 1988).

3.5.2 Lithofacies 1 – Fine-grained sandstone with thinly bedded and weakly bioturbated mudstone

Lithofacies 1 is a light to medium grey, moderately- to well-sorted, fine- to medium-grained sandstone interlaminated with dark, organic-rich mudstone (Figure 3.7). The centimetre- to decimetre-scale sandstone beds are continuous to discontinuous, wavy-parallel, wavy-nonparallel to continuous, and planar-nonparallel to planar-parallel. Medium mudstone laminae are millimeter-scale and present as continuous planar non-parallel laminae or discontinuous, wavy non-parallel laminae draped over wave ripples. Mudstone comprises up to five percent of the facies. Contacts between the sandstone and mudstone laminae are sharp.

Sedimentary structures observed in Lithofacies 1 include combined-flow ripples, low-angle cross beds, and hummocky cross-stratified oscillatory-flow-generated bedforms. Gutter casts (a few millimetres wide and deep) are observed but not common. Abundant phosphatic fish debris is observed in some instances within millimeter- to centimeter-scale laminae/beds and mixed with medium to coarse siliceous sand. The bonebeds have sharp contacts with bounding sediment. Lithofacies 1 has a low bioturbation index (BI) of 0 to 2. The bioturbation index quantifies bioturbation using seven grades from BI 0 indicating unburrowed rock to BI 6 representing complete (100%) bioturbation (Taylor and Goldring, 1993; MacEachern et al., 2010). Bioturbation is localized within the thin mudstone beds. Trace fossils include common *Planolites*, rare *Chondrites* and *Rhizocorallium*, and cryptic, unidentifiable traces.

Lithofacies 1 is commonly bound between units of Lithofacies 2, except in cored well 121/06-35-013-13W3 where Lithofacies 1 is sharply overlain by Lithofacies 5. Units of Lithofacies 1 is between 0.3 and just over 1-metre-thick and is observed in units I, III, and VI. The phosphatic bioclastic sediment is commonly observed in the Fish Scales Formation, which lies within Unit I of this study.

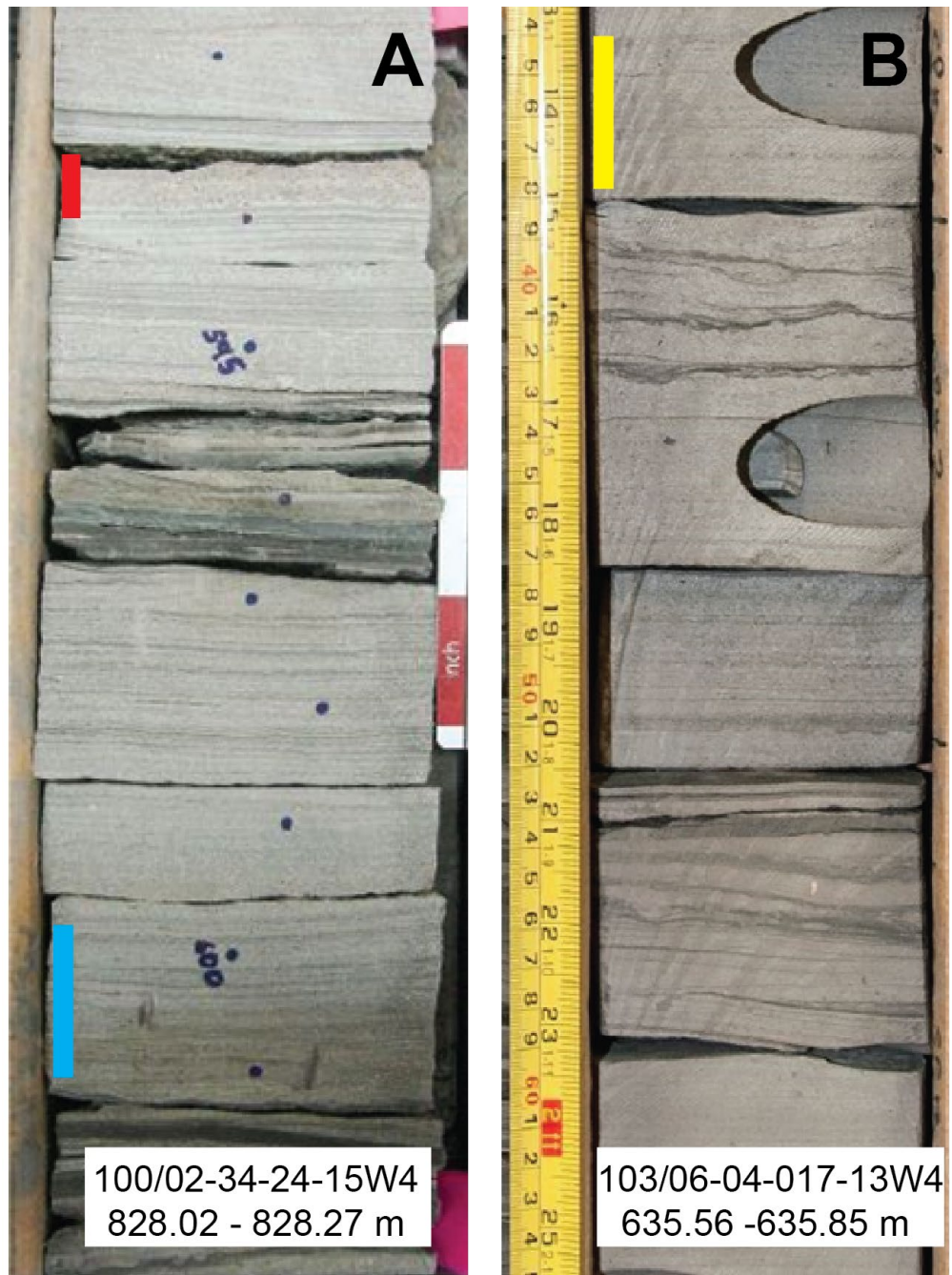


Figure 3:7: Core example of lithofacies 1. A) and B) are sharp-based, fine-grained sandstones with hummocky cross stratification (yellow bar) and combined-flow ripples interspersed with silty planar, parallel to very slightly nonparallel and discontinuous, wavy, nonparallel mudstone laminae (blue bar). Image A shows millimetre- to centimetre-thick bone beds rich in phosphatic bioclastic debris (red bar).

Interpretation

The coarse silt to fine- to medium-grained sandstone with draping mudstone interlamination and erosive-based sedimentary structures indicate Lithofacies 1 was deposited in an offshore setting, between fair-weather and storm wave base where erosional, storm-generated waves reworked the seafloor. Sand was transported from the shoreface environment to the offshore by oscillatory waves and unidirectional geostrophic currents, under conditions strong enough to transport decimetre thick deposits of Lithofacies 1 (Duke, 1990; Duke et al., 1991; Snedden and Nummedal, 1991). The presence of hummocky cross stratification overlain by combined-flow ripples indicates deposition occurred after fine-grained sediment was eroded at the early stage of the storm and during subsequent oscillatory-dominant flow as the storm event was waning (Arnott and Southard, 1990; Plint, 2010). As storms transitioned into fair-weather conditions, mud was deposited as discontinuous to continuous wavy to parallel laminae or draped over wave ripples. Evidence of bottom-water conditions is supported by a lack of bioturbation in the lithofacies– the inhospitable, high-energy environment undergoing rapid sedimentation discouraged sediment reworking by organisms.

3.5.3 Lithofacies 2 - Thinly bedded, heterolithic sandstone and mudstone

Lithofacies 2 consists of interbedded millimetre- to centimeter-scale, thinly bedded light to medium grey, very fine-grained, moderate to poorly sorted sandstone and dark to medium grey silty mudstone. Laminae in the sandstone interbeds are characterized as discontinuous to continuous planar-parallel to planar-nonparallel and discontinuous to continuous wavy-parallel to wavy-nonparallel. The mudstone interbeds are commonly continuous planar-parallel to discontinuous planar-nonparallel and discontinuous wavy-nonparallel laminated. Mudstone beds account for nearly 50 percent of the sediment volume within the lithofacies. Contacts between the sandstone and mudstone beds are sharp, with some instances of mudstone appearing to drape over the sandstone beds. Observed sedimentary structures in Lithofacies 2 include wave ripples and low-angle cross stratification, rare instances of combined flow structures, sandstone rip-up clasts imbedded within the mudstone, and soft- sediment deformation in the form of contorted

beds and dewatering structures (Figures 3.8 and 3.9). Gutter casts in sandstone are noted but are not common within the facies. Phosphatic, bone-rich sandstone beds are rare. The lithofacies can be interspersed with bentonite beds ranging between centimetres and a decimeter or more in thickness.

Bioturbation in Lithofacies 2 ranges from BI 0 to 5 but is typically BI 3 with localized BI 0 and 5. Trace fossils are sporadically distributed and where the traces can be identified, they include *Planolites*, *Skolithos*, and *Chondrites*.

Lithofacies 2 is predominately observed between Lithofacies 5 deposits. The lower contact is gradual as sediment coarsens upward from Lithofacies 5 into Lithofacies 2 and the upper contact is sharp, signaling a flooding surface. Deposits of Lithofacies 2 are commonly 1-4 metres thick but can reach up to 20 metres thick. Lithofacies 2 is noted in Units I through III, VI-VIII, and XI, with the thickest interval of Lithofacies 2 occurring in Unit I.

Interpretation

Like Lithofacies 1, Lithofacies 2 was deposited in a proximal offshore (inner shelf/offshore transition zone) setting during intermittent storm events. Scoured and sharp-based sandstone beds in Lithofacies 2 suggest erosion from high-energy wave action and sediment deposition within storm wave base. Sand beds that gradually fine upwards into mudstone indicate sedimentation during flow deceleration and a transition into fair-weather conditions (Figure 3.8 A) (de Raaf, et al, 1977). Soft-sediment deformation structures (Figure 3.8A) indicate rapid deposition of fine-grained sand and silt onto an unconsolidated mud bed on the seafloor, and the overturned stratification resulted from shear-induced drag by continued flow occurring above (Middleton, 2003). Increasing mudstone content and intensified bioturbation signifies a longer hiatus between storm events. The presence of opportunistic suspension feeders (as indicated by

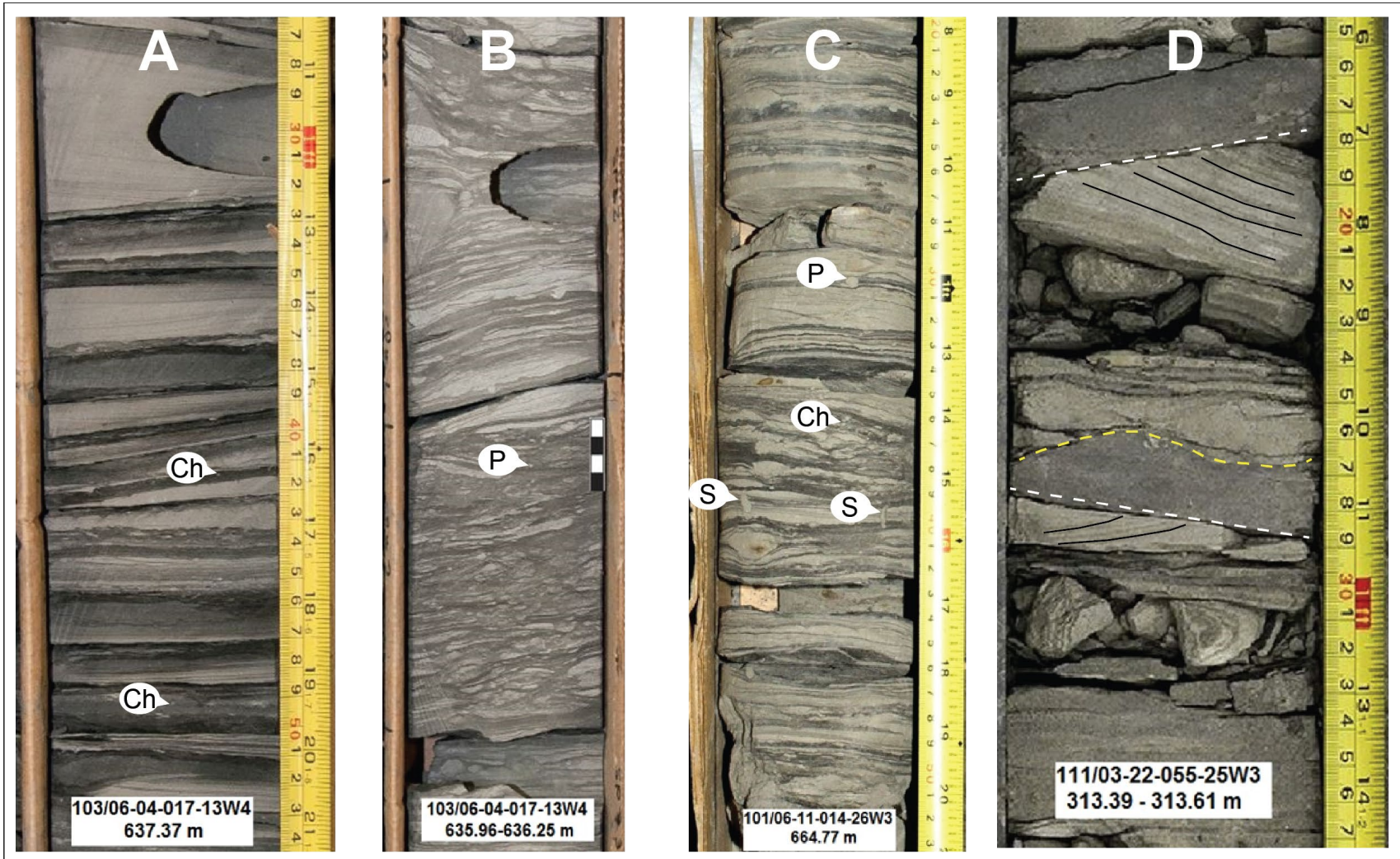


Figure 3:8: Examples of lithofacies 2 as observed in cores from 103/06-04-017-13W4, 101/06-11-014-26W3 and 111/03-22-055-25W3. The images demonstrate a range of bioturbation intensity and sedimentary structures present in lithofacies 2. A) Continuous, planar, parallel to nonparallel and continuous, wavy, nonparallel silty mudstone and very fine-grained sandstone lamination with a BI of 0 to 1. An isolated hummocky cross stratified bed at the 32- to 28-centimetre mark on the yellow measuring tape represents the amalgamation and winnowing of thinner storm-deposited beds that resulted from sediment reworking during a large storm event (Varban and Plint, 2008b). Images B) and C) show increased bioturbation concentrations with BI levels between 3 and 4 that are predominately Planolites (P) and Chondrites (Ch), with fewer Skolithos (S), and a transition into continuous, wavy parallel to nonparallel bedding. D) Core photo shows the erosive contacts between massive mudstone and hummocky cross stratified to cross-bedded sandstone beds (white dashed line). Yellow dashed line marks contact between a mudstone bed and overlying erosional sandstone. Thin black lines highlight internal stratification within the sandstone deposits.

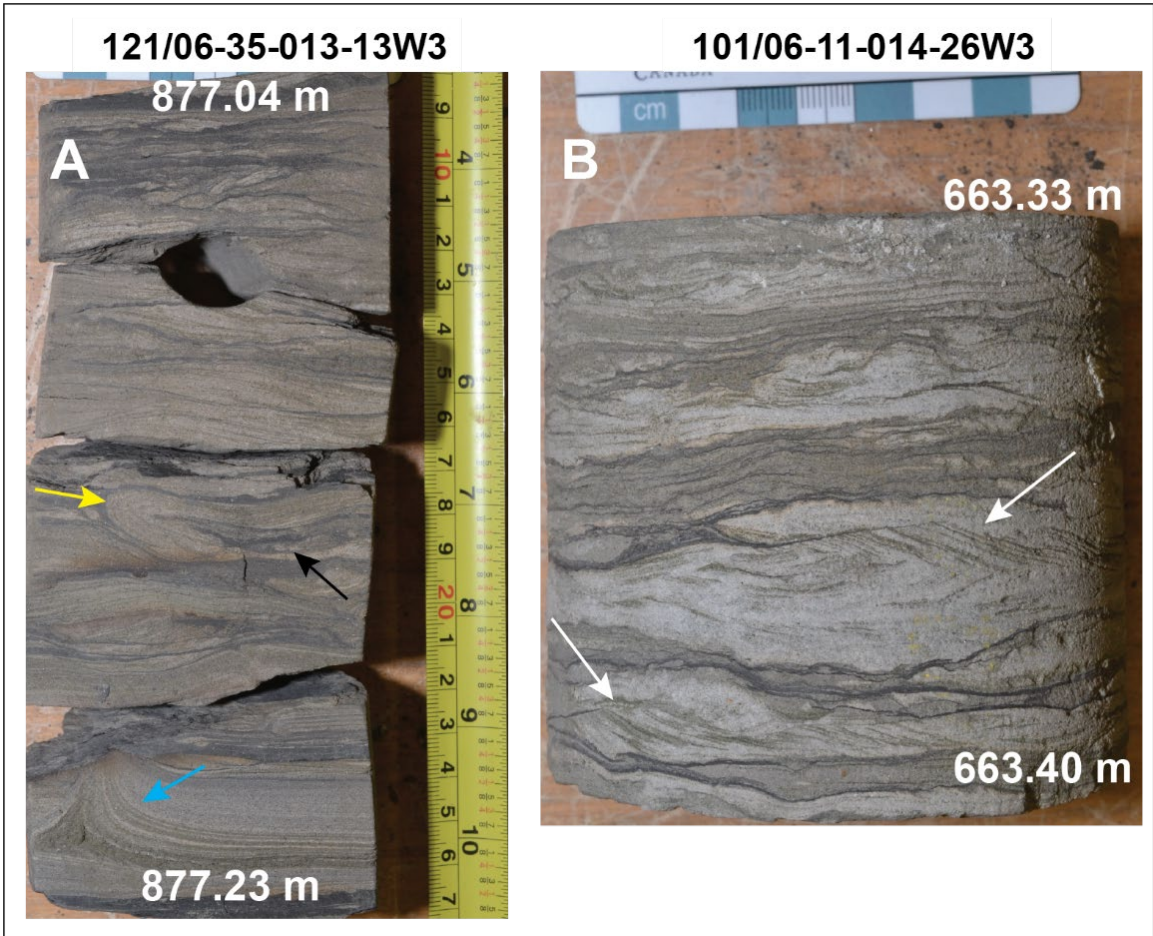


Figure: 3:9 Two examples of lithofacies 2 sedimentary structures observed in cores 121/06-35-013-13W3 and 101/06-11-014-26W3. A) A dewatering structure (blue arrow) illustrates where fluid escaped upward from a fine-grained silt bed, into an overlying graded sandstone bed. The top of the feature is eroded, with subsequent deposition of a thin mudstone bed. The convoluted bed (yellow arrow) shows an overturned, slightly graded sandstone bed. Both features indicate a relatively unstable sediment column with high-water content that became disturbed during a high-energy event with strong currents. B) A fine-grained sandstone bed with climbing (white arrows), oscillatory-dominant storm flow structures.

Skolithos) in the sandier beds indicate a well oxygenated environment within a high energy, shallow marine setting. However, the scarcity of Planolites and Chondrites suggests a shallow marine, distal expression of Skolithos and proximal Cruziana ichnofacies (lower shoreface) - both characteristic of an unconsolidated muddy substrate with varying salinity and low to moderate energy levels (MacEachern et al., 2007).

3.5.4 Lithofacies 3 – Very thinly bedded, carbonaceous, calcareous-argillaceous mudstone

Lithofacies 3 is a dark to medium grey, calcareous-argillaceous mudstone characterized by millimetre-scale, continuous to discontinuous planar-parallel and discontinuous, wavy non-parallel beds rich in biogenic grains of inoceramid shells, faecal pellets, and foraminifera. In hand-sample, Lithofacies 3 has very thin to faintly visible bedding (Figure 3.10A through C, and Figure 3.11A and E). Under the microscope the calcareous-argillaceous mudstone has millimetre-scale bedding with a graded appearance based on variation in coccolith concentration (Figure 3.11B) and discontinuous silt-lags (Figure 3.11H). Where bioturbation is abundant the bedding in Lithofacies 3 is completely disturbed (Figure 3.10, E). Within the matrix of Lithofacies 3 are organo-minerallic aggregates, fecal pellets, foraminiferal tests, prismatic inoceramid shells, phosphatic bone debris, and disseminated pyrite (Figure 3.11C through D, and F through I). The lithofacies is non-bioturbated to strongly bioturbated (BI 0 – 4) and trace fossils observed in core include *Palaeophycus*, *Planolites*, *Phycosiphon*, *Teichichnus*, and *Thalassinoides*.

It is common to observe Lithofacies 3 overlying Lithofacies 5 with a gradational contact. The transition from Lithofacies 3 to overlying lithofacies can be gradual or sharp and is typically overlain by either Lithofacies 4, with a subsequent interbedded succession of Lithofacies 3 and 4, or a bentonite deposit. In well 111/03-22-055-25W3, the uppermost occurrence of Lithofacies 3 coarsens upward and gradually transitions into Lithofacies 2. Lithofacies 3 is between 3 and 8 metres thick and is found within Units II through VI and XI.

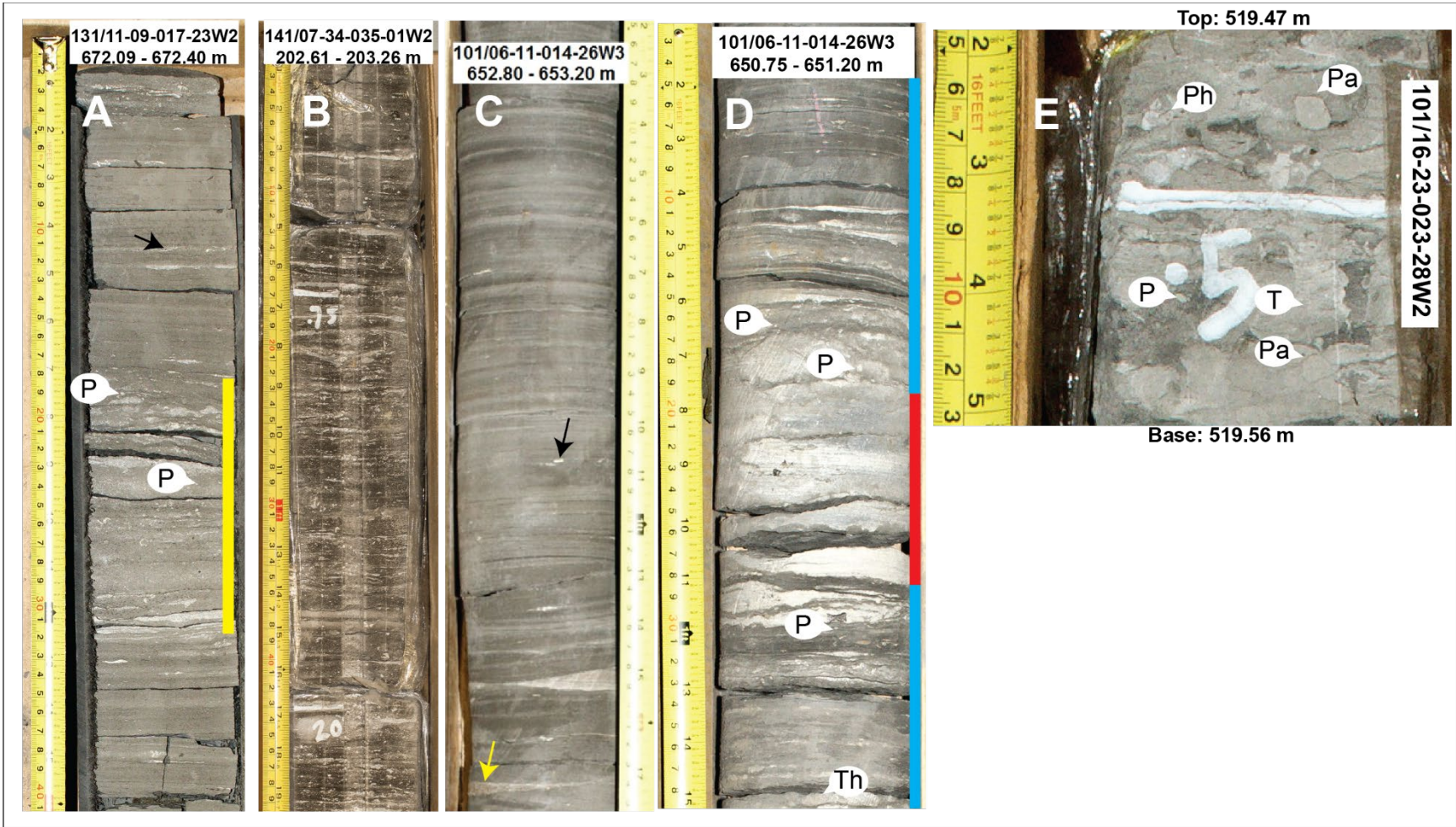


Figure 3:10: Lithofacies 3 as seen in core from wells 131/11-09-017-23W2, 141/07-34-035-01W2 and 101/06-11-014-26W3. A) In this image, lithofacies 3 exhibits millimetre-scale, planar-parallel bedding with an interval of disturbed bedding signifying a shift to discontinuous, wavy, nonparallel bedding and an increase in biogenic debris (yellow bar). B) This interval reflects an increase in calcareous biogenic sediment content, with shell-rich beds (light grey). C) Graded coccolith-rich beds (light grey colour) interbedded with coccolith-poor beds (medium grey colour). The beds are predominately planar-parallel, with some occurrences of low angle cross bedding. Larger pieces (a few millimetres in length) of prismatic inoceramid shells lie parallel to bedding (black arrow). D) Core photograph of interbedded lithofacies 3 (blue bar) and Lithofacies 4 (red bar). Lithofacies 4 has a sharp lower contact and a gradual upper contact with Lithofacies 3. Bioturbation index in lithofacies 3 is within BI 1 and 2, with occurrences of *Planolites* (P) and *Thalassinoides* (Th). E) Example of a strongly bioturbated Lithofacies 3. Trace fossils identified include: *Planolites* (P), *Phycosiphon* (Ph), *Palaeophycus* (Pa), and *Teichichnus* (T).

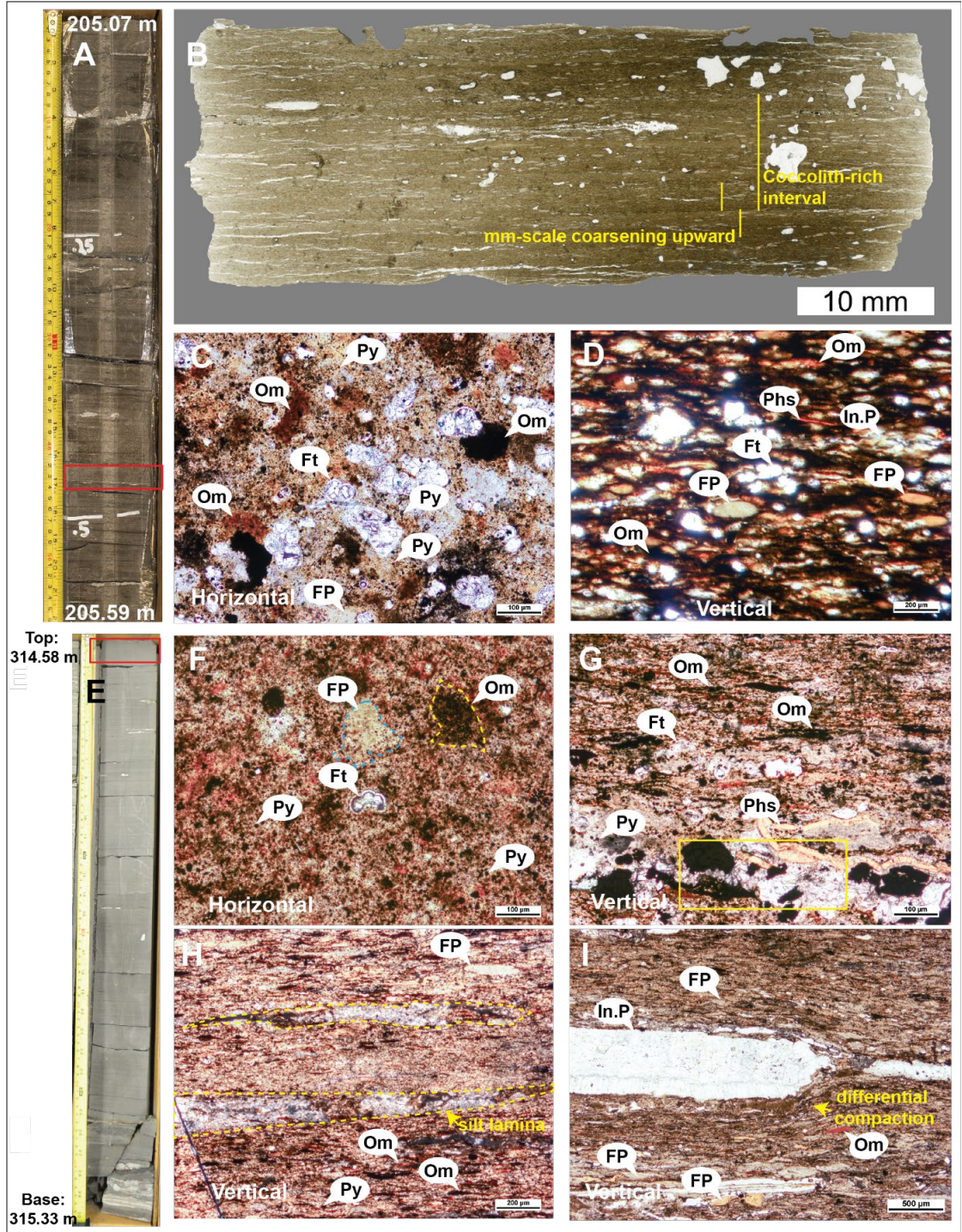


Figure 3:11: Lithofacies 3 photomicrograph collage from cores 141/07-34-035-01W2 (A through D) and 111/03-22-055-25W3 (E through I). Red boxes in images A and E refer to sample location for the associated thin-sections. Images C, D, and F through I are photomicrographs taken in plane-polarized light. A) Core photograph of Lithofacies 3 from 141/07-34-035-01W2, 205.7 m to 205.59 m. B) A back-lit thin section scan, cross sectional view, showing millimetre-scale coarsening upward successions and intervals with increased coccolith content (grading from dark grey to light grey). C) Bedding-parallel thin section of the same sample used in image (B) showing foraminiferal tests (Ft), faecal pellets (FP), organo-minerallic aggregates (Om), and pyrite (Py). D) Zoomed-in photomicrograph of image (B) thin section showing foraminiferal tests (Ft), faecal pellets (FP), phosphatic debris (Phs), and inoceramid prisms (In.P). F) Horizontally cut sample from 111/03-22-055-25W3 displaying a bedding-parallel view of Lithofacies 3. The matrix comprises speckled pyrite (Py), foraminiferal tests (Ft), faecal pellets (FP, blue dashed line) and organo-minerallic aggregates (Om, yellow dashed line) mixed with clay and silt. G and H) Cross sectional views of the sample from 111/03-22-055-25W3. The yellow box in G highlights a lamina that is mixed with inoceramid shell debris, organic matter, phosphatic material, and pyrite that likely reflects a storm event. In image H), two silt lamina are observed (yellow dashed lines) comprising silt grains, organic matter, and pyrite. I). Sediment surrounding an inoceramid prism that has undergone differential compaction.

Interpretation:

Abundant coccoliths indicates Lithofacies 3 is pelagic carbonate deposited in a distal shelf setting with low sedimentation rates, marking a transition from siliciclastic mudstones to calcareous, planktonic-rich mudstones. Coccolithophorids are unicellular, primary producers that live in the photic zone of open bodies of water (Huneke and Henrich, 2011). Coccoliths in the rock record are concentrated in fecal pellets excreted from planktonic foraminifers that fed on the coccolithophorids (Huneke and Henrich, 2011). Preservation of this material is promoted in dysoxic to anoxic benthic environments where benthic scavengers and deposit feeders are excluded (Hart, 2016). The continuous to discontinuous planar-parallel and discontinuous, wavy non-parallel beds of silty and organic detritus as well as inoceramid shell fragments indicates the influence of traction processes and intermittent storm waves on the deposition of this material (Percy, 2019).

The *Cruziana* trace fossil assemblage places Lithofacies 3 within a distal lower shoreface environment that was dominated by deposit-feeding structures. The low degree of bioturbation typically observed in Lithofacies 3 likely reflects a stressed environment. However, the notable increase in bioturbation in Lithofacies 3 (Figure 3.10E) represents a more proximal expression of the *Cruziana* ichnofacies that records a transition from mainly suspension settling to shifting substrate conditions under higher energy (MacEachern et al., 2007).

3.5.5 Lithofacies 4 – Foraminifera- and coccolith-rich packstone-grainstone

Lithofacies 4 is a light grey, foraminifera- and coccolith-rich packstone-grainstone with discontinuous, wavy-nonparallel carbonaceous mudstone laminae (Figure 3.12). The name describing Lithofacies 4 incorporates the terminology outlined by Dunham (1962) because the lithofacies is primarily composed of biogenic carbonate sediment. Contacts with underlying and overlying lithofacies are sharp. Lithofacies 4 is commonly massive, with rare millimetre-scale planar to wavy, organic-rich mudstone lamina and stylolites

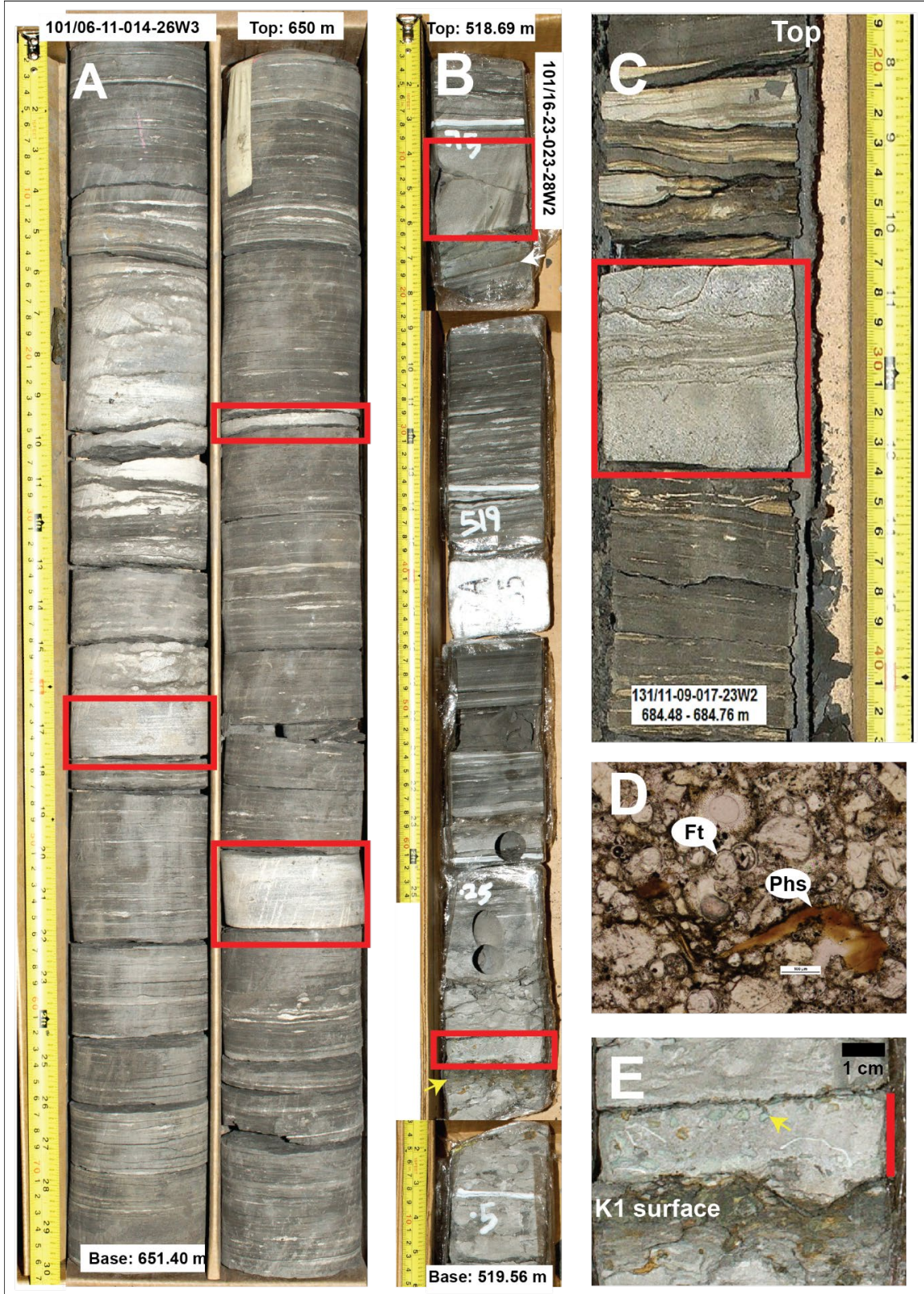


Figure 3:12: Examples of Lithofacies 4 (red boxes) as observed in cores 101/06-11-014-26W3, 101/16-23-023-28W2 and 131/11-09-017-23W2. A) Three occurrences of Lithofacies 4 in the 101/06-11-014-26W3 core are bound between Lithofacies 3 deposits and mark a sharp transition from the thinly bedded calcareous mudstone into the mud-poor, biotic-rich sediment. B) The upper Lithofacies 4 deposit located at approximately 518.76 m is a massive, foraminiferal-rich packstone sharply overlying the ‘green bentonite’ mapped surface at the top of Allomember XI (white arrow). At approximately 519.39 m in image B, the Lithofacies 4 deposit contains glauconite grains and shell debris. The yellow arrow points to the mapped K1 surface at the top of Allomember V. C) represents an unconformable deposit of Lithofacies 4, sharply overlying Lithofacies 5 and underlying Lithofacies 2. D) A thin section photomicrograph from 101/16-23-023-28W2 at 518.76 m (just above the top of the ‘green bentonite’ surface in Image B)) showing biogenic grain-supported matrix with foraminiferal tests (Ft) and phosphatic bone fragment (Phs). E) A close-up photograph of the Lithofacies 4 example at approximately 519.40 m in Image B (red box). The red bar in Image E corresponds to the bed outlined in Image B. The surface separating Lithofacies 4 from the underlying dark coloured and chemically and mechanically altered bed is the mapped K1 surface, representing the top of Allomember V.

(Figure 3.12C). Rare examples contain glauconite grains and mollusc and phosphatic debris (Figure 3.12E). Bioturbation is weak to non-existent (BI 0 - 1).

Lithofacies 4 is localized to central to southern Saskatchewan and observed in allomembers II, VI, and XI. It comprises thin beds, typically less than 10 centimetres in thickness, that are sharply bounded by Lithofacies 3 (Figure 3.12A) and Lithofacies 2 (Figure 3.12C). At 101/16-23-023-28W2 (Figure 3.12B and E), the basal contact is an erosion surface marked by the allostratigraphic surface K1.

Interpretation

Lithofacies 4 is of pelagic origin, with little to no input of terrigenous material, suggesting deposition occurred under anoxic conditions and during a time of low sedimentation. The abundance of biogenic carbonate sediment suggests that food supply, water temperature, and salinity conditions at the time of deposition were favourable for continued, high productivity in the surface waters. In Figure 3.12E, Lithofacies 4 includes relatively intact oyster shells, phosphatic material (yellow arrow in Image E, Figure 3.12), and green, sub-rounded glauconite intraclasts. The intact shells imply deposition in a low-energy environment with minimal sediment transport and reworking.

In Figure 3.12E, Lithofacies 4 is a hemipelagic, hardground deposit (where the sediments are biogenic but also include increased amounts of terrigenous content) overlying a clastic firmground deposit (Kennedy and Garrison, 1975). The K1 regional unconformity surface (observed as a major lowstand beveling unconformity in the proximal end of the basin in northeast British Columbia and northwest Alberta – see Chapter 2) separates the underlying dark-coloured, chemically and physically altered clastic deposit from the overlying Lithofacies 4. This surface represents a major hiatus and its importance to the depositional history within the Blackstone allostratigraphic framework will be discussed further in Chapter 5.

3.5.6 Lithofacies 5 – Thinly bedded silty argillaceous mudstone

Lithofacies 5 is a non-calcareous, dark grey, silty argillaceous mudstone with millimetre-scale continuous to discontinuous planar-parallel silt beds (Figure 3.13A through D;

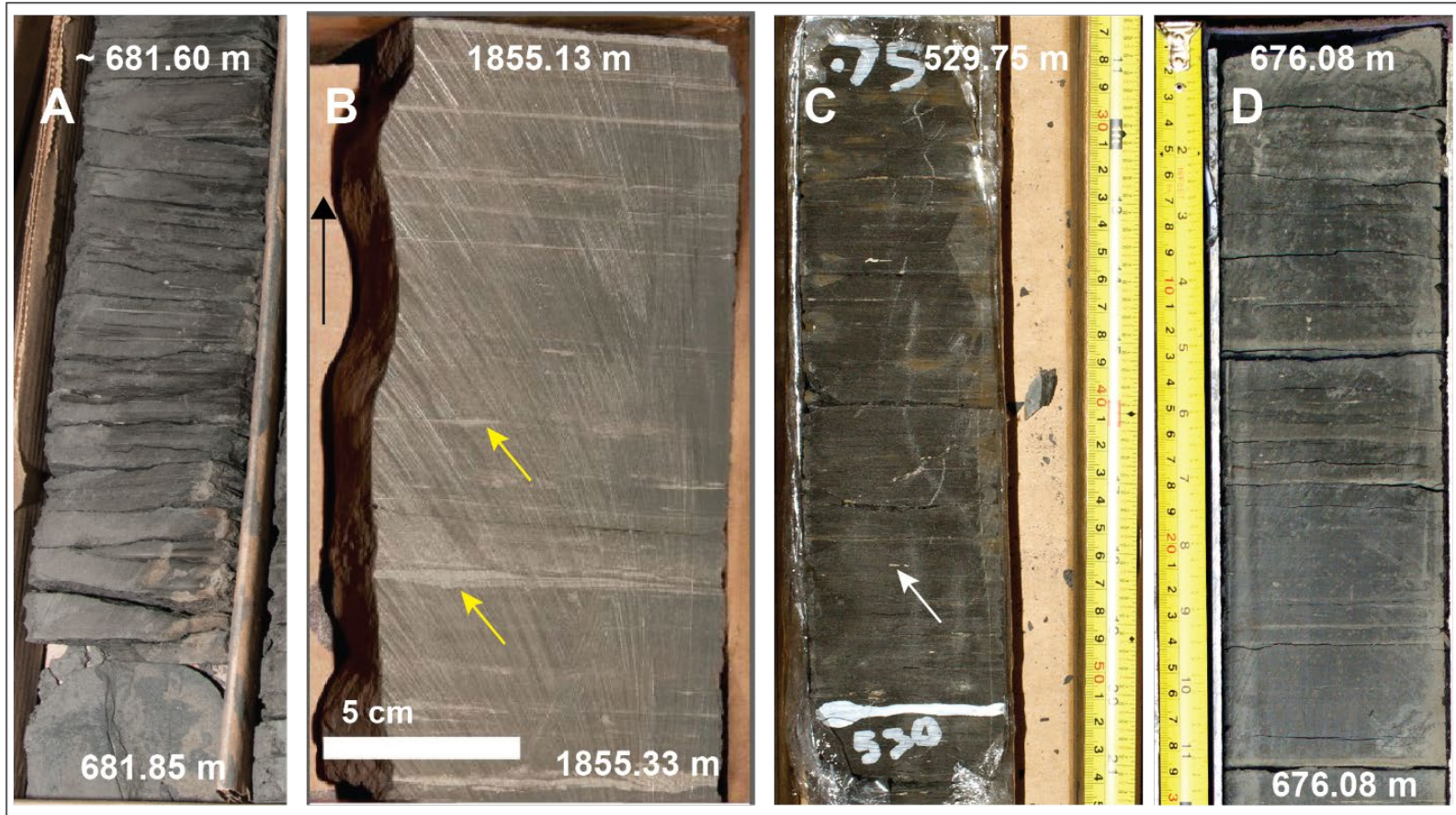


Figure 3:13: Collage of lithofacies 5 examples from 103/06-04-017-13W4 (A), 100/07-19-045-06W5 (B), 101/16-23-023-28W2 (C), and 142/05-08-018-28W3. Yellow arrows in image B show scoured bases of silt beds. White arrow in image (C) points to a prismatic inoceramid shell fragment situated parallel to the bedding plane.

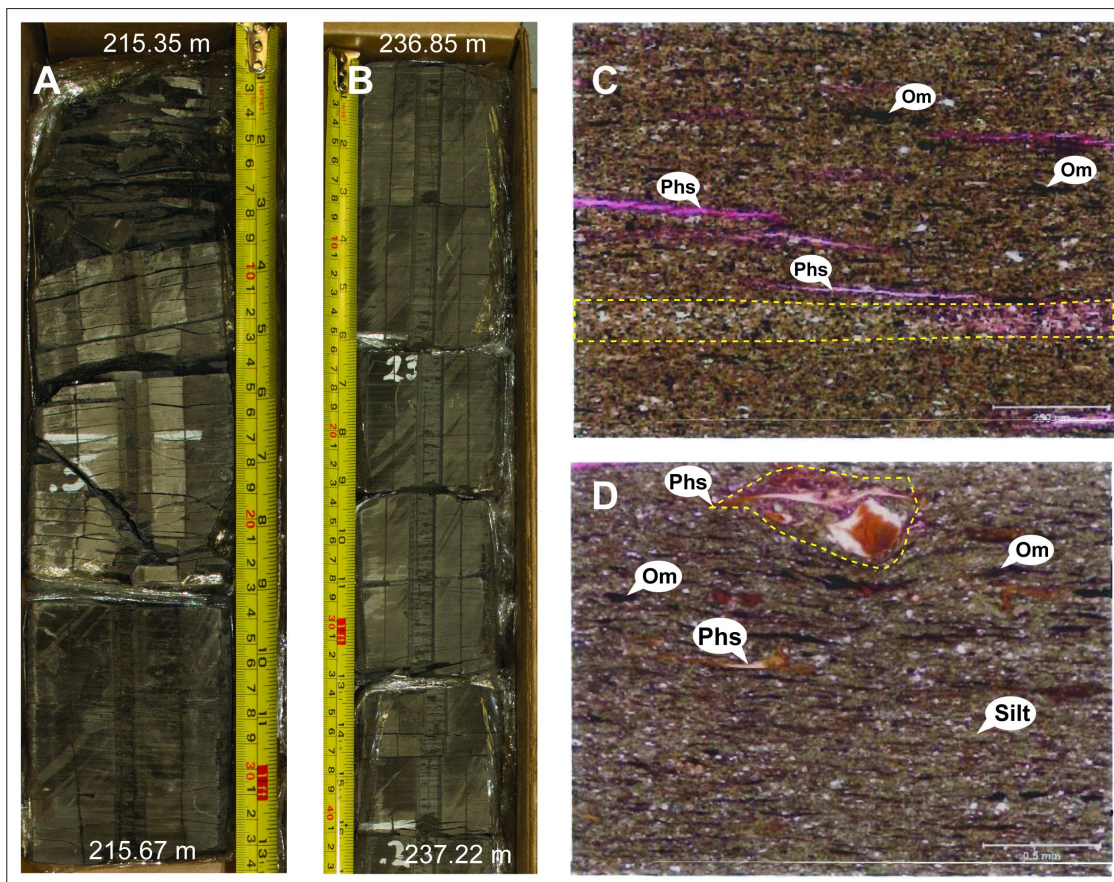


Figure 3:14: Core and photomicrograph images of Lithofacies 5 in east-central Saskatchewan from well 141/07-34-035-01W2. Image A) and B) illustrate Lithofacies 5 in core. C) (215.5 mKB) and D) (232 mKB) are photomicrographs from a core analysis report (TerraTek, 2008). The yellow dotted outline in images C and D marks a thin silt bed oriented parallel to the bedding plane. OM = organic matter; Phs = Phosphatic bone debris (yellow dotted line in image D).

Figure 3.14). Silt bed contacts are sharp-based with localized scouring (Figure 3.13B). There are a few occurrences of disseminated pyrite and rusty surface staining on the core. Inoceramid prisms are rare and disseminated phosphatic fish debris is poor to non-existent. Bioturbation is generally absent (BI 0), with isolated occurrences of BI 1 where *Planolites* trace fossils are present.

Lithofacies 5 is present in Units I through VIII with bed thicknesses ranging from 2 and 22 metres. Lithofacies 5 is observed either above a flooding surface, sharply overlying sandstones of Lithofacies 1, or gradually transitioning upward to the interbedded, heterolithic sandstone and mudstone of Lithofacies 2.

Interpretation

The presence of thin, planar-parallel silt beds and a lack of sandstone in Lithofacies 5 indicates sediment was deposited in a distal shallow ramp setting that was below wave base for sand and occasionally within storm wave base for silt and mud. During storm events, the silt and mud sediment was transported by longshore advection and bedload processes (Plint et al., 2012; Plint, 2014). The low to absent bioturbation suggests a dysoxic to anoxic marine environment, which is supported by the presence of authigenic pyrite. Pyrite is an early diagenetic mineral that is typically produced and preserved in anoxic marine settings. The formation of pyrite depends on the amount of decaying organic matter, dissolved sulfate in the pore water, and reactive iron minerals (Bernier, 1984). Anoxia forms beneath an oxygenated water column, a few millimetres below the sediment/water interface, when aerobic organisms metabolize organic rich sediment (Bernier, 1970; Taylor and Macquaker, 2011). If iron is present in the anoxic sediment, it is reduced, and iron sulfide is produced. Further burial and persistent reducing conditions will promote formation of pyrite (Bernier, 1970).

3.6 Lithofacies successions

Lithofacies successions record changes in depositional environments, helping to establish a paleogeographic history within a chronostratigraphic framework. The Upper Colorado Group strata in this study are composed of gradational, transgressive-regressive successions deposited on a shallow marine ramp. The successions have been subdivided

based on their location in relation to the orogenic front: proximal (FS-1), proximal offshore (FS-2), and distal offshore (FS-3) (Figure 3.15). The proximal position is closest to the shoreline (within the foredeep) and the distal is considered representative of the backbulge segment of the WCFB, located furthest from the orogenic front.

Proximal and distal lithofacies successions in this study are mainly differentiated by the carbonate content in the mudstones. In FS-1, the coarsening-upward succession begins with a siliciclastic mudstone (Lithofacies 5) base that grades upward into mildly to strongly bioturbated, heterogenic sandstone, siltstone, and mudstone (Lithofacies 2). The succession is capped by poorly- to non-bioturbated, wave rippled to hummocky cross-stratified sandstone (Lithofacies 1). A sharp contact representing a flooding surface separates Lithofacies 1 from the overlying Lithofacies 5. The base of FS-2 (Lithofacies 5) is the distal expression of the proximal, coarsening upward succession of FS-1 (Lithofacies 2). Calcareous mudstones (Lithofacies 3) are deposited after transgression instead of clastic mudstone in FS-2 because clastic supply is lower at the position in the basin and marine conditions are favorable for increased productivity. In FS-3, siliciclastic mudstones (Lithofacies 5) underlying calcareous mudstone (Lithofacies 3) represent decreasing accommodation and progradation of the shoreline. As accommodation increases, conditions favorable for marine biological activity returns and calcareous mudstones transition into pelagic carbonate deposits.

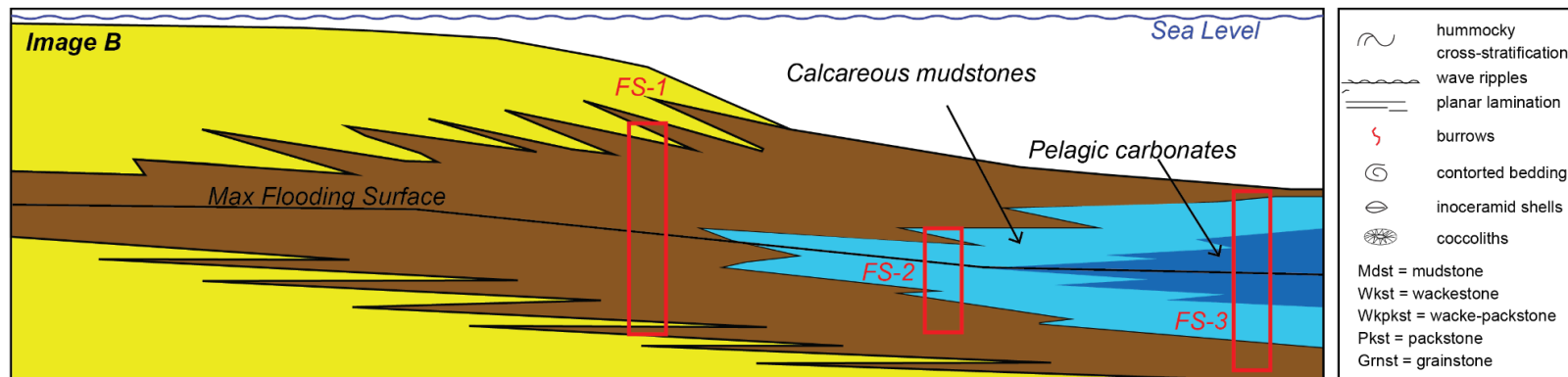
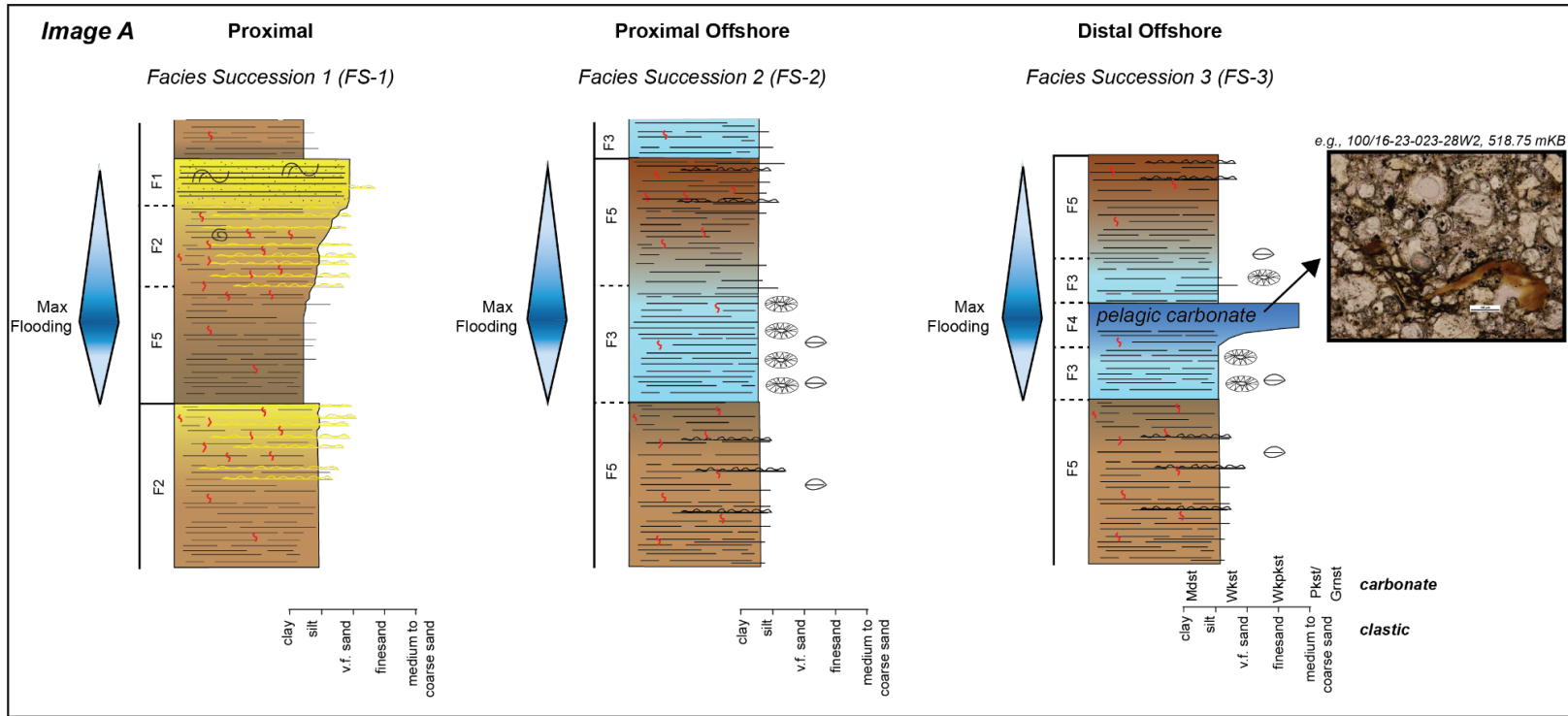


Figure 3:15: Schematic diagram illustrating lithofacies successions observed within the study area (Image A). Image B is a shallow marine ramp cartoon (modified from Hart (2016) showing possible depositional positions of FS-1, FS-2, and FS-3. The proximal position includes coarsening-upward successions (Lithofacies 5 – Lithofacies 2 – Lithofacies 1, respectively), and the maximum flooding surface lies within the classic mudstone (Lithofacies 5 - F5) deposited above Lithofacies 1 (F1). In the proximal offshore, clastic supply is limited and productivity increases. At this location during transgression, the maximum flooding corresponds to a calcareous mudstone succession (Lithofacies 3 - F3). As regression begins, clastic supply is renewed and F5 is deposited. Maximum transgression at the distal end of the shelf records deposition of pelagic organisms, such as coccoliths and foraminifera, and no clastic mud supply (F4). The schematic for the distal offshore succession illustrates a gradual upward transition from Lithofacies 3 to 4, but it is noted that a sharp flooding surface could occur beneath the carbonate deposit. Clastic supply is reintroduced as regression continues across the basin and F3 is deposited. It is noted that this succession does not consider lithofacies juxtapositions resulting from unconformities, and that the successions presented here may not include lithofacies that were omitted, due to erosion or non-deposition, in the rock record.

Chapter 4

4 Sequence stratigraphy and mapping methods

Stratigraphic analysis involves the subdivision of rock successions for the purpose of interpreting the geological history of a particular region. The vertical and spatial arrangement of sedimentary strata can be considered in terms of lithological characteristics (lithostratigraphy), fossil content (biostratigraphy) or genetic, time-correlative relationships (sequence stratigraphy and allostratigraphy). The current study uses allostratigraphy to develop a chronostratigraphic framework into which lithofacies and total organic content data from core analysis are integrated. This chapter describes the methods used in the evaluation of the allostratigraphy and sedimentology of the Upper Colorado Group that encompasses the lithostratigraphic Fish Scales, Belle Fourche, and Second White Specks formations (Fig. 4.1).

4.1 Sequence stratigraphy

Sequence stratigraphy predicts temporal and spatial stratigraphic relationships of sedimentary packages based on the analysis of cyclical fluctuations in sea level and their influence on sediment supply and the accommodation space available for that sediment to accumulate (Posamentier et al., 1988; Posamentier and Allen, 1999). The original model for sequence stratigraphy, referred to as the “EXXON model” (Vail et al., 1977), subdivided depositional sequences into systems tracts based on internal stratal stacking patterns, with their position within the sequence commonly associated with a specific segment of the eustatic sea level curve (Posamentier et al., 1988; Posamentier and Vail, 1988; Catuneanu, 2002). Internally, the sequences are composed of parasequences (or parasequence sets when stacked), which are a relatively conformable, genetically related succession of beds or bedsets that are bounded by marine flooding surfaces or their correlative surfaces (Van Wagoner et al., 1988).

The eustatic-based model of Vail et al. (1977) was subsequently expanded to include non-eustatic controls on relative sea level change such as tectonic movements (Posamentier et al., 1988). Relative sea level is the position of the sea surface with

Period	Epoch	Stage	<i>Lithostratigraphic Framework</i>		<i>Allostratigraphic Framework</i>			
Cretaceous	Upper	Turonian	Second White Specks Fm.		Green bentonite			
						TS XI		
					TS X			
			Second White Specks Fm.		Blue Bentonite	IX		
					TS VIII			
			Second White Specks Fm.		Bighorn River (Red) Bentonite	VII		
					K1	TS VI		
	Upper	Cenomanian	U. Colorado Grp.	U. Belle Fourche	Belle Fourche Fm.	x	TS V	
						A	TS IV	
			L. Belle Fourche	Belle Fourche Fm.	X Bentonite	TS III		
								II
			Fish Scales Fm.		FSU			
								I
			Fish Scales Fm.		BFSM			
Lower	Albian	L. Colorado Grp.			<i>U = Upper</i> <i>L = Lower</i> <i>Fm. = Formation</i>			

Figure 4:1: The lithostratigraphic nomenclature (after Bloch et al., 1993 and Bloch et al., 1999) and Blackstone Alloformation classification scheme applied in this study (from Tyagi et al., 2007 and Tyagi, 2009). Allomember names are in Roman numerals, I to XI. Previously named allomember bounding surfaces are listed on the left in the “Allostratigraphic Framework” column. The surfaces bounding the tops of allomembers VII, IX, and X are titled VII, IX and X, respectively. Refer to Chapter 2 for a description on the nature of the allomember surfaces.

respect to a datum at or near the sea floor that can vary with local influences of subsidence or uplift (Fig. 4.2A) (Posamentier et al., 1988). Relative sea level rise or fall can occur from tectonic (subsidence) or eustatic (sea level rise) fluctuations, or through a combination of both, resulting in the creation or removal of accommodation (Fig. 4.2B). The term “accommodation” refers to the space available for sediment to accumulate below base level and is controlled by changes in eustatic sea level and tectonic uplift and/or subsidence of the sea floor (Posamentier et al., 1988; Catuneanu, 2002).

4.1.1 Eustasy

Eustasy, or global sea level, refers to the position of the sea surface with reference to a fixed datum and is independent of local factors (Posamentier et al., 1988). Eustatic processes are episodic and operate at different frequencies (Vail et al., 1977; Miall, 2010). The longest (first order) cycles operate on a 400 to 500 Myr periodicity and are related to global supercontinent cycles. Second order cycles operating on 10 to 100 Myr frequencies are linked to volume changes in mid-oceanic spreading centres and the warping of lithospheric plates. Third order cycles of 10,000 yr to 10 Myr frequency reflect basement movement induced by regional plate kinematics. Fourth order frequencies are global cycles produced by orbital forcing, termed Milankovitch cyclicity, and occur at 10,000 yr to 2 Myr periodicity. Of note, of the ‘cycles’ described above, only those resulting from orbital changes (fourth order – Milankovitch cycles) are truly cyclical.

Milankovitch cycles are linked to changes in the shape of Earth’s orbit around the sun (eccentricity), its tilt (obliquity), and the precession (wobble) of the axis (Plint et al., 1992). Fluctuations in these parameters produce cyclical variations that influence global climate, most notably the global volume of continental ice sheets (glacioeustasy). Glacioeustasy appears to have had a significant influence on climate during the Upper Cretaceous (Gale et al., 2002) and has been recognized as a possible mechanism for high frequency eustatic variation and cyclical sedimentation recorded in the Western Interior Seaway (WIS) during the Cenomanian and Turonian (Plint, 1991; Sageman et al., 1997; Sageman et al., 1998; Prokoph et al., 2001; Varban and Plint, 2008a).

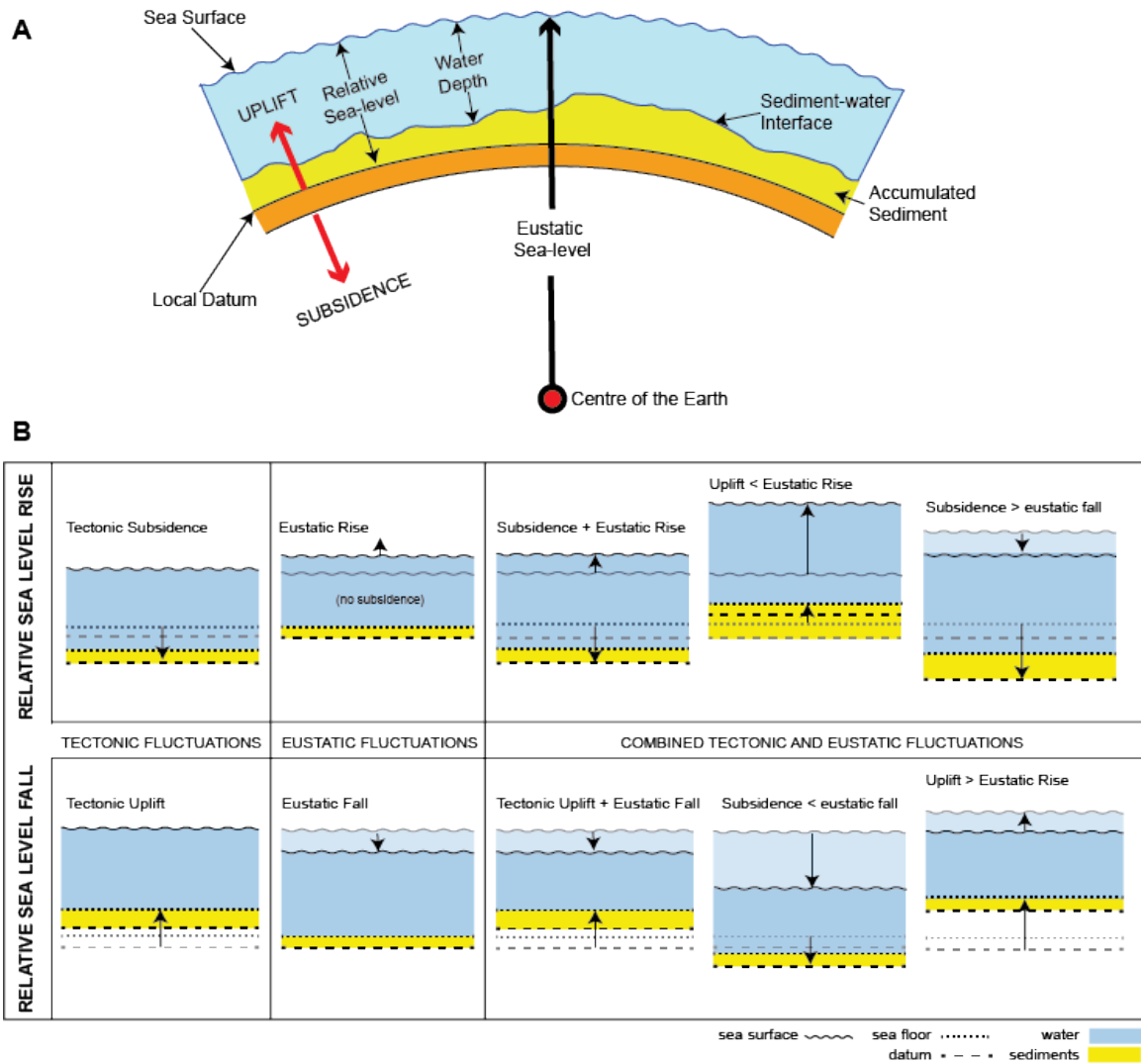


Figure 4:2: A) Schematic diagram showing relationships between relative sea level, water depth, eustasy, and datum reference points. Modified from Posamentier et al. (1988) and SEPM (2021). B) Illustration demonstrating the relationship between relative sea level rise or fall and changes in tectonic activity and/or eustasy. Modified from Catuneanu (2002) and Hooper (2019).

4.1.2 Systems tracts

Systems tracts are controlled by the relationship between the rate of accommodation change (A) and the rate of sediment supply (S) (Fig. 4.3). When accommodation is created faster than sediment is supplied ($A > S$), transgression occurs, and the shoreline begins to migrate landward. This could be associated with tectonic subsidence, eustatic sea-level rise, or a combination of both (Fig. 4.2B). When accommodation and sediment supply are in equilibrium ($A = S$), sedimentary deposits build up (i.e., “aggrade”). When sediment supply is greater than the rate of accommodation ($A < S$), sediment begins to fill the basin and causes the shoreline to prograde basinward.

The four stage systems tracts sequence stratigraphic model (Fig. 4.4A) consists of a lowstand systems tract (LST), transgressive systems tract (TST), highstand systems tract (HST) (Posamentier and Vail, 1988) and a falling stage systems tract (FSST) (Plint and Nummedal, 2000). The depositional sequence begins at the top of the LST when relative sea level has reached its lowest point and the rate of sediment supplied to the basin is greater than the rate of accommodation ($S > A$) (Fig. 4.4B). During this stage, sediment deposition shifts from progradational (seaward) to retrogradational (landward) as sea level rise begins to outpace sediment supply (Miall, 2010). Transition into the TST occurs as the rate of accommodation is greater than sediment supply ($A > S$). Nearshore, the TST is characterized by a widespread transgressive ravinement surface that develops during retrogradation of the shoreline (Posamentier and Vail, 1988). Offshore, rapid transgression during the TST limits sediment supply, leading to low sedimentation rates. This, in turn, produces a condensed section comprising concentrated biogenic debris (e.g., fish skeletal fragments and/or shells), concentrated radioactive clays, or pelagic limestone deposits (Miall, 2010). When the shoreline reaches its maximum landward position, a maximum flooding surface is produced in the condensed section, separating TST deposits from the overlying HST, and comprising concentrations of biogenic material, authigenic minerals, or a bored firmground (Loutit et al., 1988).

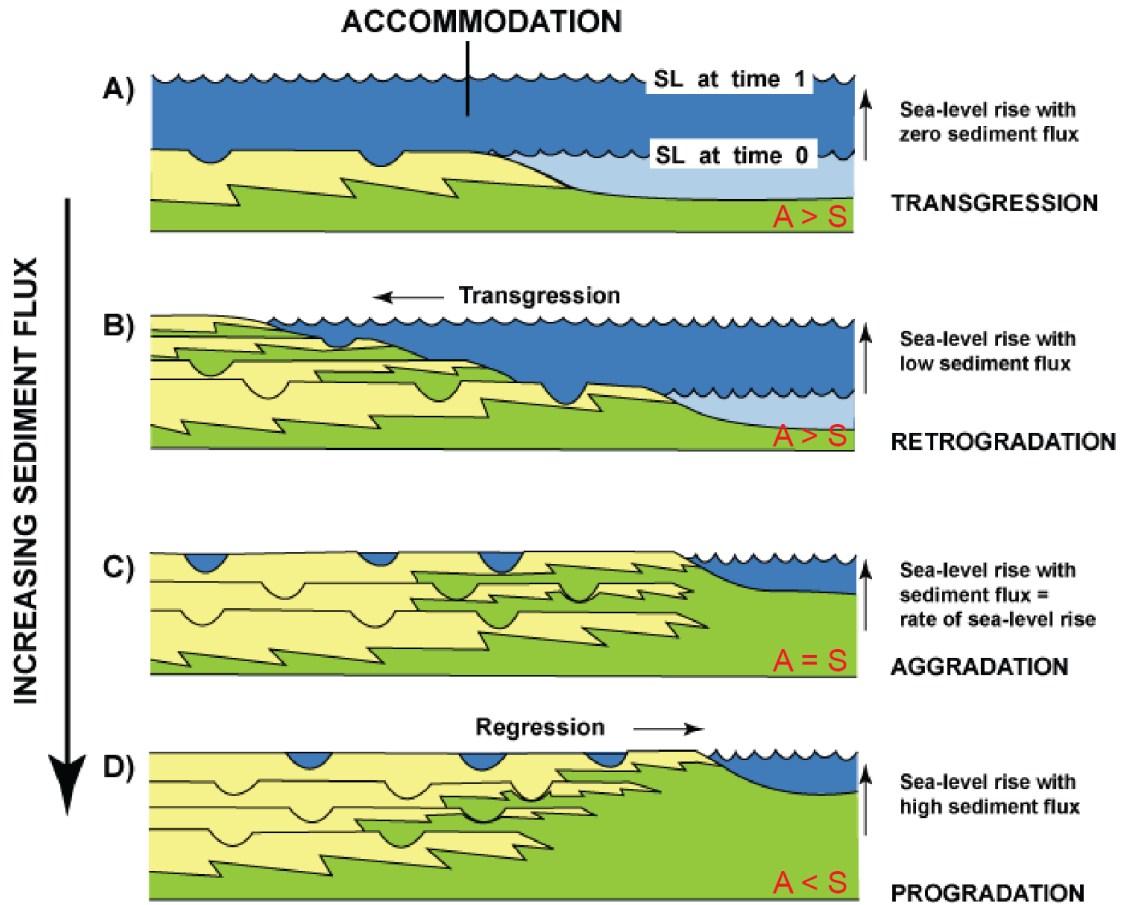


Figure 4:3: Illustration demonstrating the relationship between accommodation (A) and sediment supply (S). Modified from Possameter and Allen (1999).

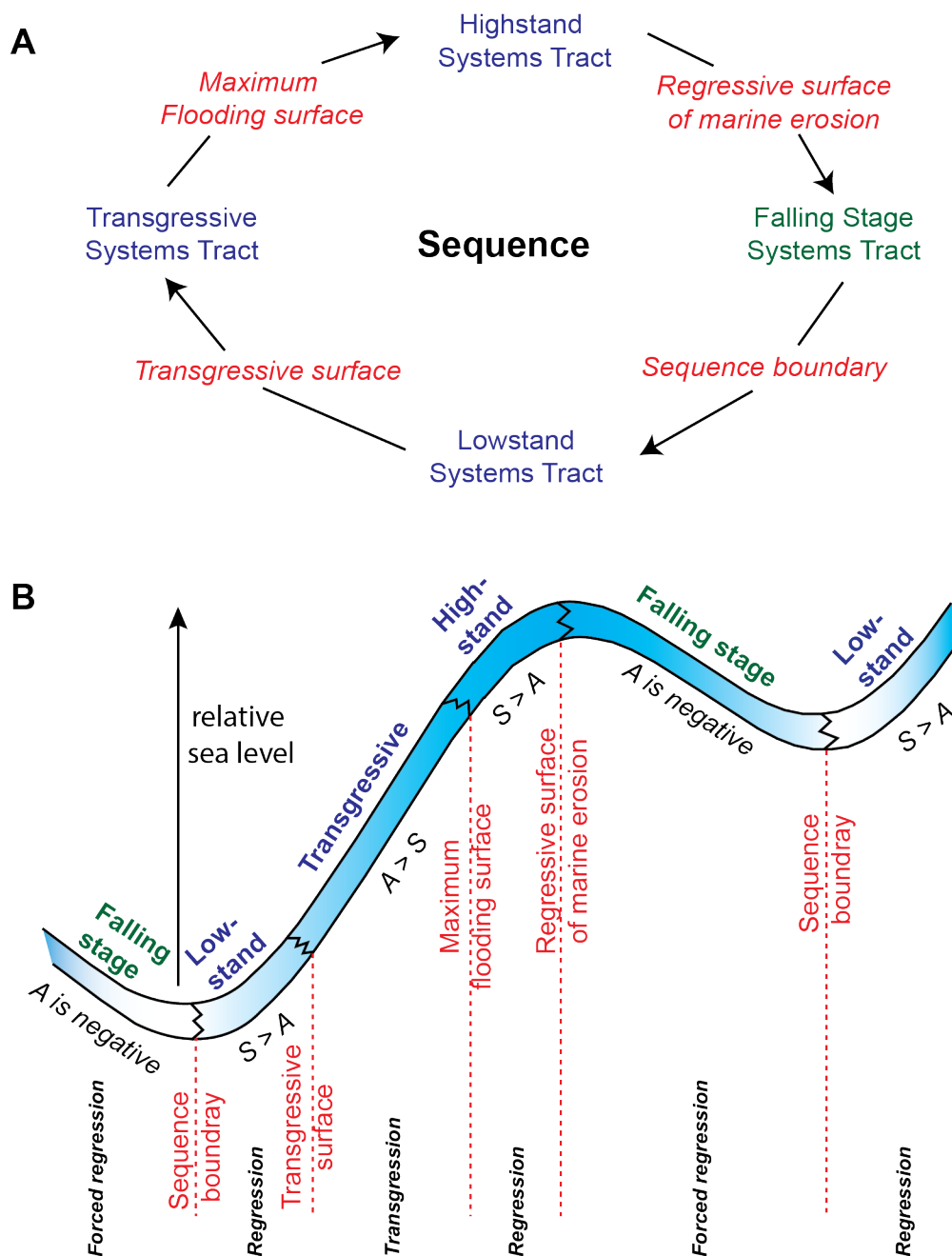


Figure 4:4: A) Wheel diagram showing the progression of a system tract sequence, which begins at the sequence boundary. B) Illustration demonstrating the relationship between sea level change and system tract development. A change in relative sea level is indicated by a gradual change in colour from light to dark blue. Green text reflects sea level fall and blue coloured text signifies a rise in sea level. Red text defines the bounding surface type separating the system tracts. Modified from Nichols (2009) and Plint and Nummedal (2000).

During the HST, the rate of sea level rise slows, and sediment supply becomes greater than accommodation ($A < S$), causing the shoreline to undergo normal regression. As sea level begins to fall, the system transitions into the FSST and the shoreface progrades seaward under forced regression (Plint, 1991). During the FSST, both the coastal plain and continental shelf undergo erosion that creates a subaerial unconformity and a wave-induced regressive surface of marine erosion that is marked with intraclasts and gutter clasts, respectively (Miall, 2010; Plint and Nummedal, 2000). The subaerial unconformity, or correlative conformity in the offshore, produced at the lowest point of sea level fall, is defined by a sequence boundary that marks the end of the FSST and the systems tract sequence. The next systems tracts sequence begins as sea level rises and the LST develop, with progradation continuing until $A = S$.

4.2 Allostratigraphic cross-sections

The allostratigraphic framework developed for the current study is based on geophysical well log data from 574 wells. The logs were used to construct 27 regional and loop-tie working cross-section lines that extend the allostratigraphic framework of Tyagi (2009) to span the breadth of the southern and eastern region of the WCFB. The working cross-sections include 15 north-south cross-section lines approximating depositional strike and 12 west-east cross-section lines approximating depositional dip, were directly linked into cross-section lines used in Tyagi (2009) and Tyagi et al. (2007). A map of the working correlation grid with an overlay of 15 summary cross-section lines included in this thesis is shown in Fig. 4.5. The summary cross-sections include 10 W-E trending (B through K) and 5 N-S trending (1 to 3, 5 to 6) lines.

The cross-section grid was constructed to optimize well and core control across the study area. Every effort was made to select wells for the cross-sections that had at least gamma ray and resistivity curves. Additional curves compiled in the database include photoelectric, and density and neutron porosity (if/when available). Raster-based well logs were digitized to fill in data gaps and improve well spacing in the grid. Digital well

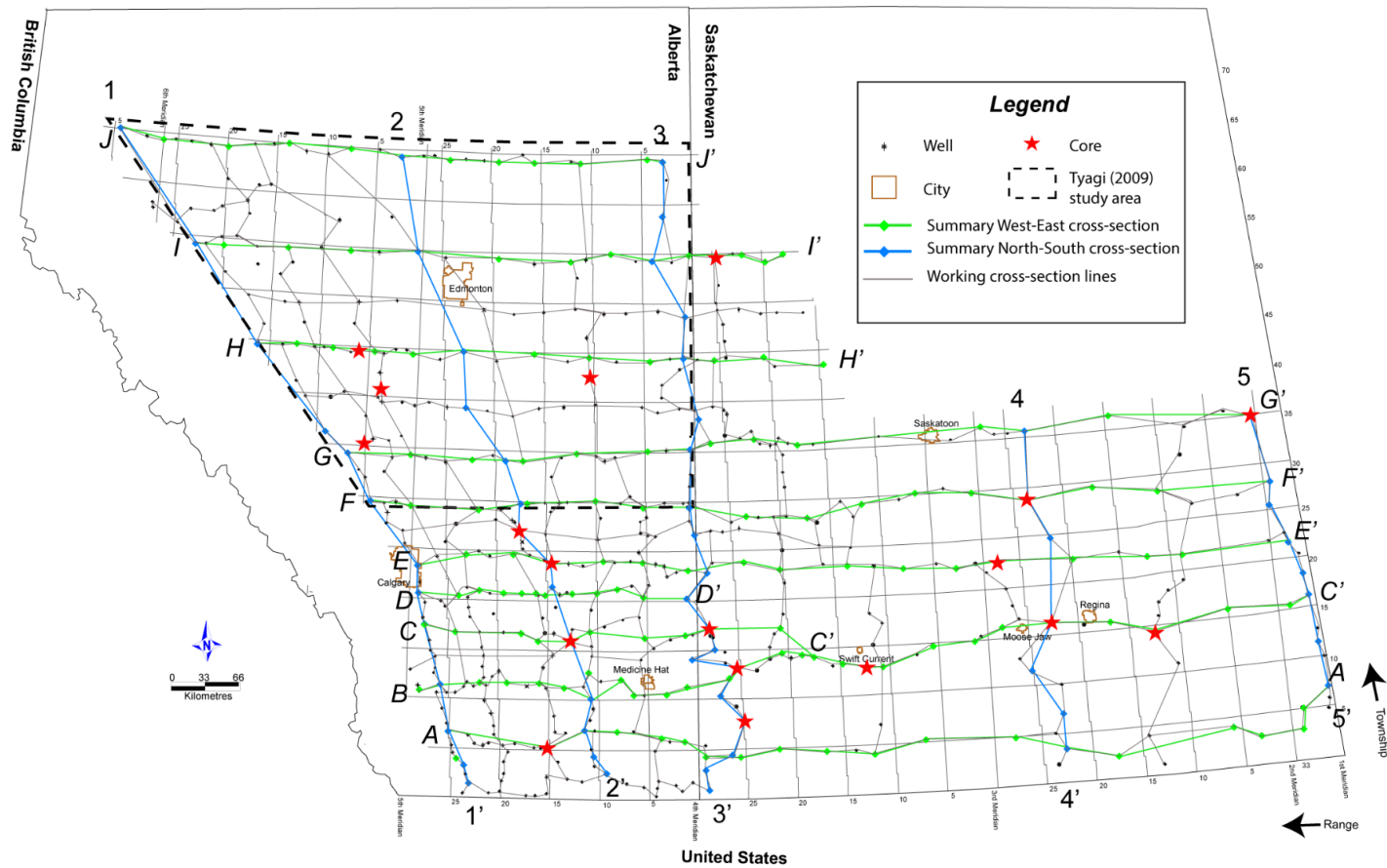


Figure 4:5: Map showing working and summary cross-section lines. Summary cross-sections are presented at the end of the thesis. Cores assessed in the study are marked with a red star. Tyagi (2009) study area, from which the allostratigraphic framework of this study was based, is shown with a black dashed outline.

log data was obtained from EnerGISite of Divestco Inc. and imported into IHS Petra™, a geological mapping and data management software system by IHS Markit. Cross-sections were constructed using the map module in Petra, in which interpreted tops were automatically updated in Petra's well data manager and accessed for contour mapping. Core from 18 wells, nine wells from Alberta and nine from Saskatchewan, were logged with the objective of ground-truthing the wireline logs to core and improving correlation control across the basin (Table 4.1). Core was considered suitable if it intersected the study interval, was continuous, and had corresponding well logs to assist with depth shifting.

A typical wireline log expression of a flooding surface is a sudden increase in the gamma ray reading, accompanied by a simultaneous decrease in the resistivity, indicating an increase in clay content in the rock (other factors controlling log readings are discussed in section 4.4) (Fig. 4.6). However, this log characteristic is also typical for other deposits rich in clay, such as carbonaceous mudstone and bentonite beds. To manage this uncertainty, geophysical well log data was used together with core to integrate the lithofacies context into well log signatures and determine whether a given surface was indeed a discontinuity.

The Upper Colorado Group strata investigated in this study include rocks rich in calcareous bioclastic remains, including calcareous shells of planktonic foraminifera and remains of larger benthic invertebrates, that are interbedded with non-calcareous siliciclastic sediments. Incorporating the photoelectric curve into the geological interpretation aided in the differentiation of clastic and carbonate-rich deposits found within mapped allomembers across the basin.

Table 4.1: List of wells and the core intervals used in this study. An ‘X’ indicates the allomember was observed in core at that well location. Grey shaded boxes indicate missing core interval. Yellow shaded boxes indicate the allomember was not preserved (i.e., lapped out) at that well location.

				Allomembers										
Alberta	interval top (m)	interval base (m)	Core length (m)	I	II	III	IV	V	VI	VII	VIII	IX	X	XI
100/07-19-045-06W5	1793.8	1870.2	76.5			X	X	X	X	X	X			
100/14-07-036-05W5	2298.8	2306.3	7.5						X	X				
100/16-28-041-04W5	1823.3	1828.4	5.14						X	X	X			
102/07-04-028-18W4	986	1024.5	38.5	X	X	X	X	X						
100/11-12-006-16W4	601.7	628.5	26.8	X	X									
100/02-34-024-15W4	798	831	33	X	X	X								
103/06-04-017-13W4	624	703	79	X	X	X	X	X	X	X	X		X	XI
100/06-23-043-11W4	542.5	560	17.5						X	X	X			X
102/16-18-023-03W4	654	680.5	26.5	X	X									
Saskatchewan	interval top (m)	interval base (m)	Core length (m)	I	II	III	IV	V	VI	VII	VIII	IX	X	XI
142/05-08-028-28W3	662.5	691	28.5	X	X	X	X	X	X					
101/06-11-014-26W3	650	665.6	15.6			X	X	X	X					
111/03-22-055-25W3	309.8	328	18.3		X	X		X	X					X
121/06-35-013-13W3	866	883	17		X	X	X							X
101/16-23-023-28W2	517	535.9	18.9		X	X	X	X						X
101/06-28-029-24W2	431.2	446	14.8		X	X	X	X	X					X
131/11-09-017-23W2	669	697	28		X	X	X	X	X					X
101/06-15-015-13W2	607.8	625	17.3						X					X
141/07-34-035-01W2	199.9	238.2	38.4	X	X	X	X	X	X					X

UWI: 103/06-04-017-13W4

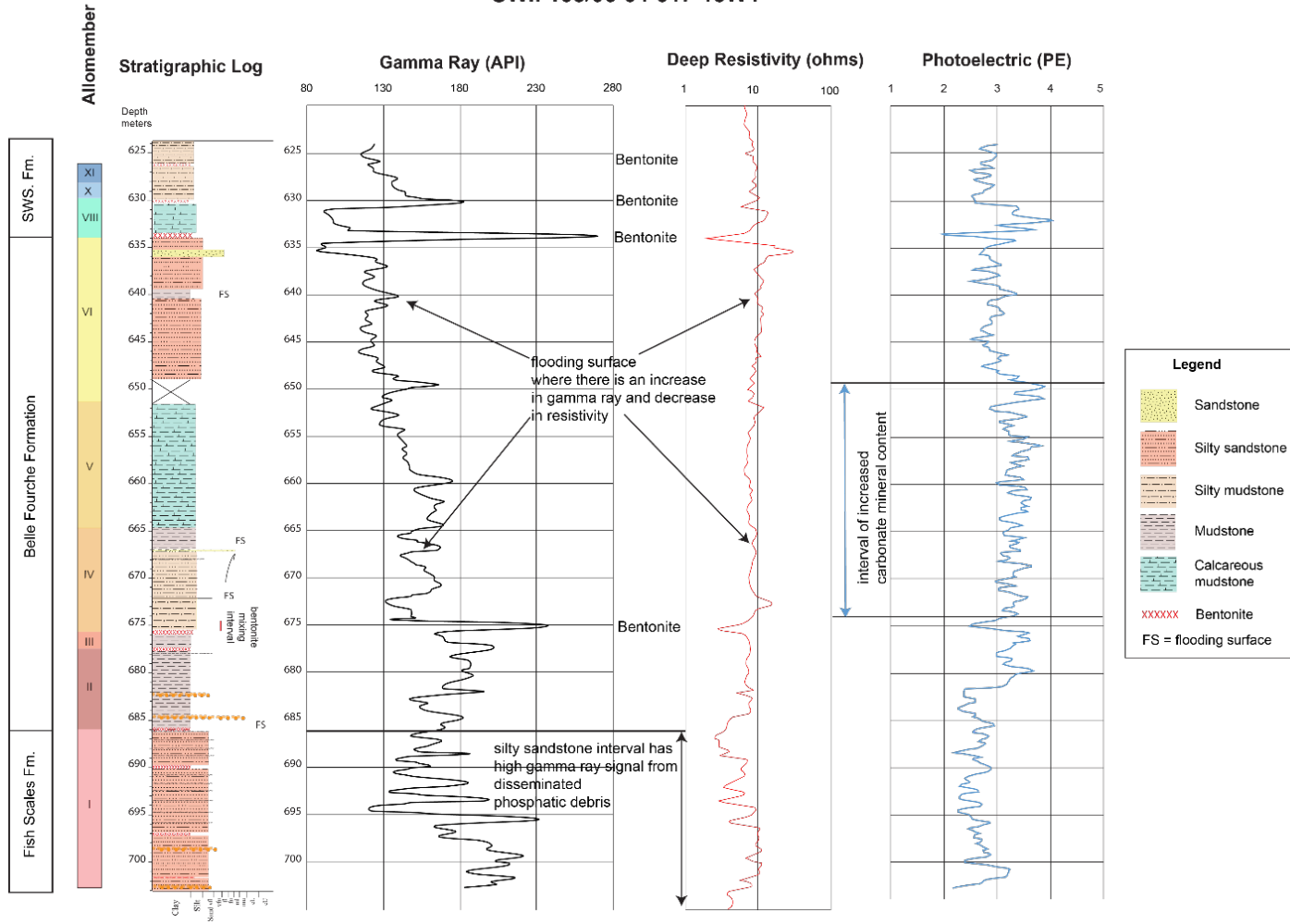


Figure 4:6: Comprehensive diagram highlighting geophysical well log responses to changes in lithology. The stratigraphic log describes core from well location 103/06-04-017-13W4, between 624 and 703 mKB. Bentonite beds, marked with red x's, produce a clear response on the log curves where the gamma ray curve sharply increases, accompanied with low spikes in both resistivity and P_e . Flooding surfaces identified in core correspond to a rise in gamma ray API values and decrease in resistivity. It is acknowledged that additional bounding discontinuities occur between the labeled allomembers (i.e. flooding surfaces), however, this project only maps regionally extensive surfaces established in the original allostratigraphic study of Tyagi (2009). Correlating bounding discontinuities found within the allomembers to make conclusions about the internal stratigraphy of each unit would require a larger project scope. Intervals that have a higher amount of carbonate correspond to an increase in measured P_e values to about 3.5 or greater.

4.3 Geophysical well log database

Geophysical well logs provide an excellent alternative for assessing rock properties when core and outcrop data are limited. Logging tools measure a set of indirect physical properties that can be modeled to estimate mineralogy, porosity, and fluid properties. At a predetermined depth interval, each tool records a signal that is developed from the mineralogy and pore network of the adjacent rock body, fluid type, and borehole conditions. This study uses gamma ray, resistivity, and photoelectric curve (Pe) data to identify lithological changes associated with correlatable bounding discontinuities and to map these surfaces in well locations across the basin. Density and neutron porosity logs provided supplementary data during the early stages of well log correlation and lithology assessment. The following section reviews the physics of the measurements, applications, and limitations to using well logs when investigating rock properties.

4.3.1 Gamma Ray

Gamma ray (GR) logs, measured in American Petroleum Institute (API) units, are commonly used to identify changes in lithology in a borehole, specifically variations in clay content, by measuring the naturally occurring gamma radiation emitted from sedimentary rock. The gamma ray logging tool consists of a detector comprising a sodium iodide scintillation crystal and a counting device, called a photomultiplier, that converts the measured electrons into an electric signal. When energetic electrons become absorbed and trapped into the scintillation crystal lattice, they emit a light that is detected by the photomultiplier and converted to an electrical pulse (Ellis and Singer, 2008). The resulting pulse height is related to the total energy collected in the crystal by the initial electrons (Ellis and Singer, 2008).

The measured radioactivity originates from the decay of three isotopes: potassium (^{40}K), uranium (^{238}U), and thorium (^{232}Th). Potassium is the largest source of radioactivity in sedimentary rocks and is largely related to the abundance of clay minerals found in the bedrock (Ellis and Singer, 2008). Potassium-rich shales, glauconitic sands, and arkoses produce high, or “hot”, API readings, while clean sandstones and carbonates read low, or “cold”. Organic-rich shales that typically produce high gamma ray values, otherwise

known as ‘hot shales’, can contain high concentrations of ^{238}U salts that precipitated through the reduction of organic matter in low-oxygen to intermittently anoxic marine environments (Aplin and Macquaker, 2011). Thorium is sourced from weathered igneous rocks, and in contrast to uranium, it is extremely insoluble and can adsorb onto clay platelets (e.g., kaolinite) rather than organic sedimentary components and be transported into the sedimentary basin (Gluyas and Swarbrick, 2004).

An abrupt change in API values provides a reliable, visual aid when initially reviewing data and attempting to identify surfaces where a predominant depositional or diagenetic change may have occurred. However, lithologic trends interpreted solely on gamma ray log signatures should be treated with caution. Gamma ray readings above 100 API typically indicate a clay-rich lithology, while values below 30 API reflect clean sandstones (with negligible clay content) or carbonate/evaporitic lithologies. Since low API readings can represent both carbonates and sandstones, it is necessary to incorporate other geophysical data to confirm mineralogy. The photoelectric log is the most reliable tool to distinguish between carbonate and sandstone rocks and will be discussed in the following section. Where sandstones or dolomites produce API values similar to that of a mudstone (e.g., the Fish Scales Formation in southern Alberta and western Saskatchewan; Fig. 4.3), a density-sonic cross-plot may be used to aid in distinguishing between them if core is unavailable (Krygowski, 2003).

4.3.1.1 Limitations

Limitations to gamma ray tools that result in erroneous curve data are related to environmental conditions that change gamma ray counts, specifically the depth of investigation and the borehole environment:

1. Count rates can decrease if the tool encounters a change in borehole size, the logging speed of the tool increases, or if the drilling mud composition includes barite. Boreholes can become enlarged when a hole collapses or a cave-in occurs, resulting in lowered count rates because the emitting gamma rays have farther to travel to the detector. If the logging tool speed increases, the tool has less time to measure the true gamma ray activity from the rock, resulting in a reduced measurement resolution.

2. Drilling mud with barite absorbs gamma radiation and causes a reduced count rate, whereas drilling mud with potassium chlorite can cause count rates to rise because the mud has become more radioactive.

4.3.2 Bulk-Density

The bulk density measurement (measured in g/cm^3 or kg/m^3) is based on the mineralogy, porosity, and fluid density in the rock. A bulk density tool is an induced radiation tool whereby high energy gamma rays are emitted from a radioactive source (usually caesium-137 or cobalt-60) and interact with the electrons of the elements in the adjacent formation (Glover, 2000). Two heavily shielded detectors, one short range and one long range, are placed 7 inches and 16 inches, respectively, from the source to count the number of returning gamma rays which are related to the formation electron density (Krygowski, 2003). The returning gamma rays undergo Compton scattering by interacting with the electrons in the atoms within the formation, resulting in a reduction of the gamma ray energy and scattering of gamma rays in all directions (Glover, 2000). Compton scattering is when a “gamma ray collides with an electron, transferring part of its energy to the electron, while itself being scattered at a reduced energy” (Schlumberger, 2022). The amount of returning gamma rays in the higher energy range (influenced by Compton scattering) is proportional to the electron density of the formation and is used to determine bulk density and porosity (Asquith and Krygowski, 2004). Low energy range gamma ray interactions are governed by the photoelectric effect, which is used to determine formation lithology (Krygowski, 2003). Gamma rays undergoing greater attenuation in high bulk density formations due to high electron density produce a lower gamma ray count, while higher gamma ray counts are measured in formations with low bulk density from low electron density (Glover, 2000).

Density porosity (ϕ_D) is calculated simultaneously from bulk density (ρ_b) when the matrix density (ρ_{ma}) and pore filling fluid density (ρ_{fl}) are known and consistent in the formation (Asquith and Krygowski, 2004):

$$\rho_b = (1 - \phi_D) \times \rho_{ma} + \phi \times \rho_{fl}$$

Matrix density values depend on the encountered lithology and its dominant rock forming mineral. Matrix density values for sandstones and limestones is 2.65 g/cm^3 and 2.71 g/cm^3 , respectively. The fluid density component is either 1.0 g/cm^3 for fresh water or 1.1 g/cm^3 for salt water; however, as the bulk density tool measures the invaded zone, fluid density for mud filtrate is likely most relevant in the calculation (Glover, 2000).

4.3.2.1 Limitations

Limitations associated with bulk density tool measurements are related to a limited depth of investigation, borehole environment, composition of drilling fluids, presence of hydrocarbons, and reliance on consistent parameters for proper calculation of density porosity (Glover, 2000; Krygowski, 2003):

- 1) The bulk density tool has a shallow depth of investigation that only measures the invaded zone (the first 10 to 13 centimetres from the borehole wall) and can be easily influenced by local factors. For example, mud filtrate that has invaded the formation during drilling can influence porosity calculations if an incorrect fluid density value was used.
- 2) The tool operates with an eccentricing arm that pushes the device against the wall of the borehole to ensure it remains in contact with the formation as it measures. If the hole size is increased, from hole collapse or cave-ins, the bulk density readings will decrease relative to the true bulk density since the tool is no longer in contact with the adjacent rock, and the measurements will be of the mud cake and drilling fluid in the hole;
- 3) Similar to the GR logging tool, gamma ray radiation is absorbed when barite is added to drilling mud, lowering the gamma ray count and increasing bulk density readings for the formation.
- 4) Light hydrocarbons present in the formation pore space increases the calculated density porosity to levels higher than the actual porosity.
- 5) Calculation of density porosity from bulk density may be erroneous if the matrix or fluid densities have been incorrectly calibrated. For example, sandstones with variable amounts of biotite can increase bulk density, resulting in an error up to 10%, or formations with anhydrite present will have a negative density porosity

since the assumed density is less than the actual formation density (Glover, 2000; Krygowski, 2003).

4.3.3 Photoelectric Effect (PEF)

The photoelectric effect (P_e , barns/electron) is measured simultaneously with bulk density (litho-density) by detectors that count high energy gamma ray returns from the formation. Gamma rays begin with an initial energy that is subsequently lost through pair production (gamma rays with energy >3 MeV) or undergoes Compton scattering (gamma ray energy of 0.5 to 3 MeV) until the energy is low enough to be absorbed by photo-electric absorption (<0.5 MeV gamma ray energy) (Glover, 2000). The probability of photoelectric absorption is proportional to the gamma ray energy and the atomic number of the scattering material (Ellis and Singer, 2008). When a low energy photon interacts with material of sufficiently high atomic number, the photon is absorbed, and its energy is transferred to a bound electron within the material (Ellis and Singer, 2008).

The photoelectric adsorption factor measured by the tool is sensitive to the average atomic number and insensitive to changes in porosity and fluid saturation of the rock, allowing a direct measure of lithology to be taken (Ellis and Singer, 2008). The higher the P_e recorded, the higher the mean atomic number of the formation, and vice versa (Glover, 2000). Table 4.2 lists mineral matrices and their associated P_e . Isolated peaks in the P_e curve may suggest local deposits of heavy minerals, such as iron, and a generally high value may reflect the presence of igneous or metamorphic rocks (Glover, 2000). Coal beds may appear as thin bands of low P_e .

4.3.3.1 Limitations

Since the photoelectric effect is measured on the same tool as bulk density, its source and detectors are pressed against the borehole wall and encounters the same problems with when the borehole environment is altered/enlarged. Although P_e is not influenced by porosity or fluid in the formation, it is affected by barite. The addition of barite to drilling mud would overwhelm log responses from the formation with its large P_e value, and therefore, it is common practice not to use P_e logs in boreholes drilled with this additive. Anhydrite and limestone cannot be distinguished solely in the P_e log; however, the low

porosity and a bulk density above 2.9 g/cm³ of anhydrite will be observed on an accompanying neutron log (Glover, 2000).

Table 4.2: Photoelectric effect measured values for different matrix materials. (From Ellis and Singer, 2008).

Matrix Material	Photoelectric Effect Value
Quartz	1.8
Calcite	5.1
Dolomite	3.1
Halite	4.7
Coal	0.2
Average shale	3.4
“Dirty” sandstone	2.7
“Clean” sandstone	1.7

4.3.4 Neutron Porosity

A neutron log can be used to indirectly calculate porosity. The tool measures hydrogen atoms in a formation by emitting high energy neutrons (fast neutrons) into the rock from a radioactive source, composed of a mixture of americium and beryllium, and counting the returned low energy neutrons or gamma rays at two detectors (Asquith and Krygowski, 2004; Glover, 2000). Three tool types exist that measure the different energies: gamma ray-neutron tools (detect both gamma rays and thermal neutrons), sidewall tools (detect epithermal neutrons), and compensated tools (detect thermal neutrons). When the fast neutrons scatter and collide with the nuclei of atoms in the rock, the neutrons are slowed to epithermal and thermal energies. When collisions decrease because the rate of movement between nuclei is slower and the neutron is eventually

absorbed by the formation nuclei, a gamma ray is emitted (Asquith and Krygowski, 2004). Scattering reactions are most efficient with hydrogen atoms because the hydrogen atom is nearly equal in mass to the neutron, meaning the incurred energy loss is dominated by the rock's hydrogen concentration (Asquith and Krygowski, 2004; Glover, 2000).

The count rate measured by the logging tool is inversely proportional to the amount of hydrogen in the rock (hydrogen index) (Krygowski, 2003). Neutrons are slowed down and quickly absorbed over short distances in formations with an abundance of hydrogen atoms, giving low count rates for high porosity rocks. In formations with a small amount of hydrogen atoms, the slowed neutrons absorb slowly and travel further into the formation before being absorbed, producing higher count rates for low porosity rocks (Glover, 2000). Lithologies with clay matrices rich in hydroxyl, water or hydrocarbon filled pores, or those that contain bitumen or kerogen will generate low neutron count rates, and high-count rates are detected from clay free, low porosity rocks (Ellis and Singer, 2008). Other elements that may contribute to the measurement include chlorine in the formation water, mud filtrates, and some evaporite formations (Glover, 2000).

4.3.4.1 Limitations

Porosity readings from a neutron log can be influenced by borehole diameter and rock formation properties, both of which can affect the detected hydrogen index.

- 1) A larger borehole diameter increases the amount of hydrogen in the space between the tool and the borehole wall, making the tool less sensitive to hydrogen changes in the rock (Ellis and Singer, 2007). This is corrected using known tool characteristics and hole diameter changes from a caliper log.
- 2) The presence of gas leads to underestimations in porosity because it has a lower hydrocarbon index related to its low density (Glover, 2000).
- 3) Low porosity shales with a significant amount of bound water molecules increases the hydrogen index of the rock (Asquith and Krygowski, 2004).
- 4) Gamma ray-neutron (GRN) and compensated tools are influenced by chloride-rich muds. The GRN tool requires correction for the drilling mud, mud cake, and mud

filtrate, but the compensated tool uses two detectors that compensate for the chloride-rich drilling mud.

4.3.5 Resistivity/Conductivity

Modern electrical logs are used to determine fluid type (i.e., hydrocarbon and water bearing zones within a reservoir), lithology, shale porosity, and compaction. The tool produces medium frequency alternating currents that are emitted to energize multiple transmitter coils and induce eddy currents in the adjacent rock. Receiver coils measure the response from the formation, which is proportional to its conductivity (inverse to resistivity). The ability of a formation to transmit a current is a function of water in the pores because the rock's matrix and hydrocarbons are nonconductive (or highly resistive) (Asquith and Krygowski, 2004). Producing a current and measuring the response can be done via two methods: laterologs (resistivity) and induction logs (conductivity). Only the logs applied in this study are discussed. The reader is referred to Glover (2000) for more information on the laterolog and induction tools not included in this section.

Laterologs (laterolog and dual laterolog) are electrode-based tools that measure formation resistivity (Ωm) in boreholes drilled with high salinity muds (Asquith and Krygowski, 2004). The current is emitted from a surveying electrode and sent into the formation by focusing electrodes (guard electrodes) that are placed above and below the surveying electrode position on the tool (Asquith and Krygowski, 2004). The position of the guard electrodes prevents the surveying current from flowing up the borehole. The difference between laterologs and dual laterologs is the latter is a combination of earlier versions of the laterolog and can conduct deep and shallow penetration evaluations of 1.5 to 2.1 metres and 0.6 to 0.9 metres, respectively (Glover, 2000). The depth of investigation is controlled by the extent to which the surveying current is focused; deep-reading laterologs are strongly focused compared to shallow-reading. The current and voltage in the tool are varied during the measurement to keep consistent power and achieve improved sensitivity (0.2 to 20,000 Ωm). The dual laterolog uses the deep (LLd), shallow (LLs), and very shallow (MSFL; microspherically focused resistivity) readings to correct for invasion effects and calculate the formation's true resistivity in real time (Asquith and Krygowski, 2004; Krygowski, 2003). Formation measurements using a spherically

focused log (SFL) focuses only on the invaded zone of the borehole. The microlaterolog (MLL) is a micro-scale version of the laterolog tool to measure within the invaded zone.

Induction tools (induction log or dual-induction log) measure conductivity (mmho/m) in boreholes with very resistive, low-conductivity drilling fluids (oil-based muds or gas) but is most effective when used with fresh water-based muds (Krygowski, 2003). The induction tool has several transmitting coils that emit a high-frequency alternating current (20 kHz) of constant amplitude and give rise to an alternating electromagnetic field that induces secondary, ground-loop currents in the formation. These currents flow perpendicular to the axis of the logging tool, in turn creating their own electromagnetic fields that induce signals in the receiver coils of the tool (Glover, 2000). Responses from individual coils in the receiver are combined to minimize effects from the borehole, invaded zone, and neighboring rocks (Asquith and Krygowski, 2004). The dual induction-laterolog has a deep-reading induction device that aims to measure true resistivity (ILd), a medium device for resistivity of the invaded zone (ILm), and a shallow reading range (LspLs). This tool is useful in boreholes with deeply invaded mud filtrate; however, to obtain an accurate true resistivity the data is corrected using a combination of the three curves.

Deciding which tool is appropriate to use, laterolog or induction, depends on the depth of investigation required for that particular purpose (Fig. 4.6). Bed resolution in stratigraphic investigations would be best achieved with a tool that has small electrode spacing (e.g., very shallow, microspherically focused resistivity). Medium penetration log data are best for thin formations and deep for studies that require true formation data from the uninvaded zone, such as water or hydrocarbon saturation calculations or stratigraphic correlation of formations between wells (Glover, 2000).

Resistivity is not a reliable indicator of lithology on its own since the measurement is based on porosity, pore geometry, resistivity of the formation water, and the water, oil, and gas saturations – traits that are not necessarily linked to a one specific rock type. The logs can discriminate between lithologies of different types because the tool is sensitive to textures; however, definitive identification would require review of data from other

lithology-specific log suites. Shales can have lower resistivity values due to bound water in clays that undergo surface conduction (Glover, 2000). By comparing very shallow, shallow (medium), and deep curves on a log, the following interpretations could be considered from their response (Glover, 2000):

- a) The formation is an impermeable shale when three curves all have low resistivity and overlie each other;
- b) If the curves have a higher resistivity compare to surrounding shales, but still overlie each other, the formation is an impermeable sandstone or limestone;
- c) If the shallow reading is low resistivity while the deep and medium curves have slightly higher resistivity and overlap each other, the formation is permeable and only contains formation water.
- d) A permeable and hydrocarbon-rich interval is interpreted when the shallow curve has low resistivity, the medium curve reads higher, and the deep curve is high enough that a separation occurs between it and the medium response.

4.3.5.1 Limitations

Limitations and effects on measurements when using laterolog and induction logs include the following:

- 1) The dual-induction ILd curve may provide inaccurate resistivity readings for thin, resistive zones, requiring the combined use of the dual induction curve and a tornado chart (a sensitivity analysis tool) (Asquith and Krygowski, 2004).
- 2) Drilling with fresh water strongly affects the laterolog tool, and it is common practice to avoid.
- 3) The laterolog tool cannot be used in air-filled boreholes or with oil-based muds because water-based drilling mud enables constant contact to the formation, a requirement for sending and receiving currents during the measurement process.
- 4) Bed thickness can influence readings when beds are less than two and a half metres (or eight feet) thick or when adjacent beds have significant resistivity contrasts.
- 5) Standard induction measurements may be suspect when formation resistivity is greater than 100 ohm metres (Ωm)

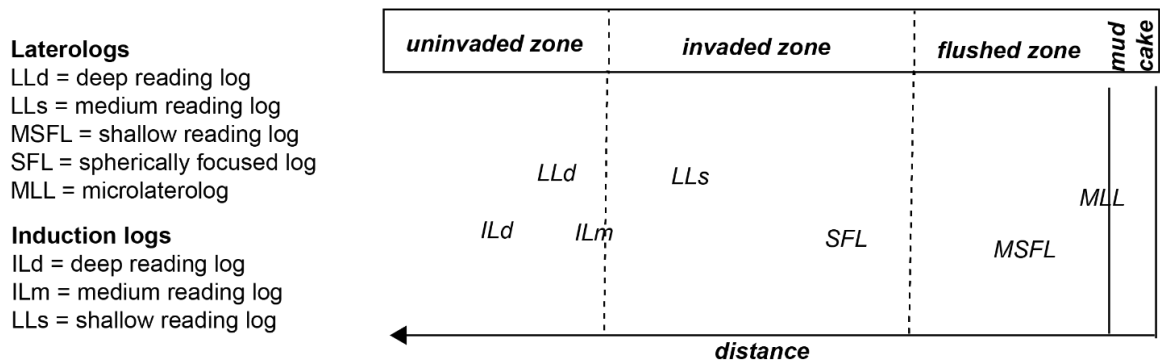


Figure 4:7: Diagram illustrating the different depths of investigation for laterolog and induction tools. The ‘distance’ represents distance from the wellbore. Modified from Glover (2000).

4.4 Isopach and lithology mapping

A series of isopach and percent of lithology maps created in this study were generated using IHS Petra's contour mapping program. This study used the kriging option in IHS Petra's mapping program to create an interpolation grid from the distributed thickness and lithology percentage values. This method is appropriate for creating contour maps with data that is spatially correlated with respect to distance and azimuth.

Kriging is an advanced geostatistical procedure that estimates the value of a variable over a spatial area using randomly distributed measured points (Chiles and Delfiner, 2012). The prediction at the unknown point is a linear combination of the closest neighbours, and data points in closer proximity are weighted higher to best estimate the values at unknown locations. The unknown value ($Z_{(s_0)}$) is calculated using the measured value at the i th location ($Z(S_i)$), the unknown weight for the measured value (w_i) at the i th location, and the number of measured values (N):

$$Z_{(s_0)} = \sum_{i=1}^N w_i Z(S_i)$$

The weights for the known data points (w_i) are calculated using a variogram that measures dissimilarity between data points and formalizes the method to assign weights to the known data points (Webster and Oliver, 2007). The difference between two variables at sample locations separated by distance is measured and plotted in a variance versus distance plot, where N_h is the count of pairs of points separated by a grouped distance (the lag distance) (Webster and Oliver, 2007). A model is then used to fit the variogram and estimate the weights for the kriging algorithm to use.

It is recognized that in parts of the study area where there is less well control, the mapping program could produce contours not geologically reasonable. To manage this limitation, contour maps were manually edited to improve interpretations and data credibility.

4.4.1 Isopach mapping

Isopach maps depict spatial variations of thickness of a stratigraphic unit. The resulting geometry provides insight into the tectonic and eustatic processes that influenced sedimentation patterns observed from unit to unit. A series of isopach maps (presented in Chapter 5) was created for this study to illustrate the basinward geometry of allomember units within the Blackstone alloformation (Fig. 4.1), linking the geometric interpretations of Tyagi (2009) to the distal forebulge and backbulge regions of the WCFB.

Allomember unit thicknesses were calculated in IHS Petra's map manager using interpreted tops for each well in the database. The thickness data, and corresponding well location coordinates, were mapped using the software's contour mapping program. It is noted that allomember thickness measurements used to create the contour maps do not account for compaction.

4.4.2 Lithology mapping

Developing lithology maps for strata confined within an allostratigraphic framework illustrates the lateral compositional variability of each interval, reflecting depositional conditions that influenced sedimentation across the basin at that time. This study used four lithological categories based on lithofacies observed in Chapter 3 for the lithology maps (Table 4.3). Each map (shown in Chapter 6) comprises percentages of mudstone, heterolithic sandstone and mudstone (herein termed "heterolithic"), sandstone, and carbonate rich lithologies that were calculated using cut-off criteria from GR and PE log data. Cut-off criteria were selected for each allomember by comparing well log responses of lithofacies identified in core (Fig. 4.8). Assigning allomember-specific cut-offs for the lithology categories was done to normalize the data ranges, reducing the influence of anomalies, and more accurately representing the interval. Table 4.4 presents the cut-off criteria used to create the lithology maps for allomembers I through XI of the Blackstone Alloformation.

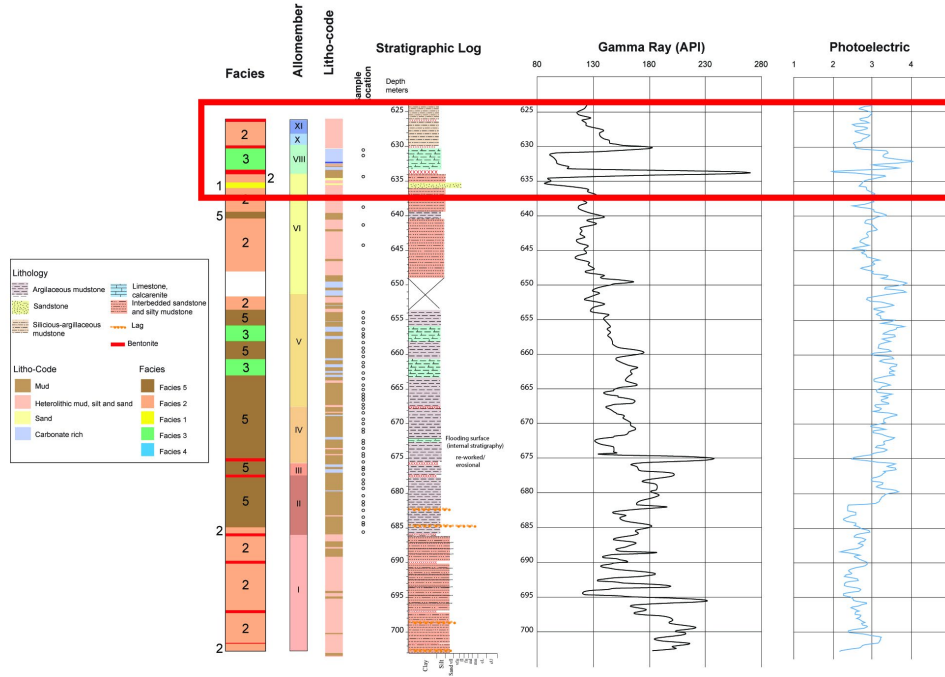
Table 4.3: Summary of lithofacies equivalent for the lithology maps shown in this study. Lithofacies descriptions are found in Chapter 3.

Lithology Map	Lithofacies
Mudstone	Lithofacies5
Heterolithic (sandstone and mudstone)	Lithofacies2
Sandstone	Lithofacies1
Carbonate-rich/Calcareous mudstone	Lithofacies3 and 4

Well locations in the geophysical log database with gamma ray and photoelectric curve data were exported into Microsoft Excel, along with accompanying allomember tops from the map manager in IHS Petra. After each allomember was filtered into its own worksheet, two columns were added: one to calculate the thickness between depth interval measurements and the other to assign a value to a cell that represented either sandstone, mudstone, heterolithic, or carbonate rich lithologies. Percentages were calculated by dividing the thickness of each lithology by the total thickness of the allomember interval a given well location. Lithologies were identified by applying a formula in Excel, whereby the program read a series of statements in sequential order to decide whether the data in question is either true or false based on a set of criteria. For example, using the cut off values in Table 4.4 for core within allomember XI, the Excel formula would read:

$$= IF(AND(F2 < 3.1, AND(E2 < 160, E > 90)), "HeteroSandSiltMud", IF(AND(E2 < 90, F2 < 3.1), "Sand", IF(AND(E2 > 90, F2 > 3.5), "CalcareousMud", "Mud")))$$

UWI: 103/06-04-017-13W4



TOP
624 mKB

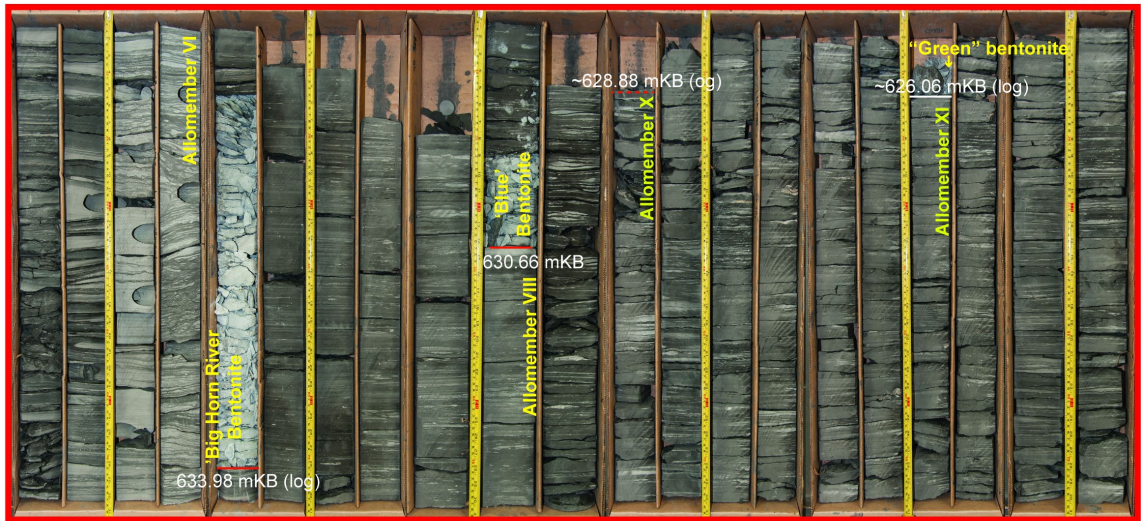


Figure 4:8: Photograph of core interval 624.0 mKB to 638.53 mKB at 103/06-04-017-13W4 (lower image) at 103/06-04-017-13W4 (A) with the corresponding stratigraphic log and litho code (upper image) illustrating the correlation between the core and the calculated lithologies. The core photo represents the stratigraphic column outline in the red box and shows what the calculated lithologies look like. Heterolithic sediment of lithofacies 2 at the base of the red box outline correlates to the left side of the core photo, within Allomember VI. Moving up section, the lithology transitions into a sandstone-rich rock, which registers in the calculated lithology column. The bentonite and overlying mudstones are recorded in the litho-code column (shown in brown) and is overlain by calcareous-rich mudstones (shown in light and dark blue). The dark blue colour in the litho-code column indicates photoelectric values greater than 4. ‘Green’ = Green bentonite at the top of allomember XI. ‘X’ is the top of allomember X. ‘Blue’ = blue bentonite at the top of allomember VIII. ‘Red’ = Bighorn River Bentonite at the top of allomember VI. ‘K1’ = the K1 disconformity at the top of allomember V. The top of allomember IV is the “X” transgressive surface.

Table 4.4: Geophysical log data cut-off criteria used to classify mudstone, heterolithic, sandstone, and carbonate rich lithofacies in the lithology distribution maps. GR = Gamma ray. PE = photoelectric.

<i>Allomember</i>	Lithologies							
	<i>Mudstone</i>		<i>Heterolithic</i>		<i>Sandstone</i>		<i>Carbonate rich</i>	
	GR	PE	GR	PE	GR	PE	GR	PE
I	default	default	>210, <300 <200, >90	<2.8 >2.5, <3.2	<100	<2.8	>90	>3.2
II	*	*	>147, <157 <150, >122 <145, >110	>2.5, <2.83 >2.6, <2.8 >2.2, <2.8	<105	<2.8	>81	>3.2
III	*	*	<160, >90	<3.1	<100	<2.8	>90	>3.2
IV	*	*	<160, >90	<3.1	<100	<2.8	>90	>3.2
V	*	*	<160, >90	<3.1	<90	<2.8	>90	>3.2
VI	*	*	<160, >90	<3.1	<90	<2.8	>90	>3.2
VII	*	*	<160, >90	<3.1	<100	<2.8	>90	>3.2
VIII	*	*	<160, >90	<3.1	<100	<2.8	>90	>3.2
IX	*	*	<160, >90	<3.1	<100	<2.8	>90	>3.2
X	*	*	<160, >90	<3.1	<100	<2.8	>90	>3.2
XI	*	*	<160, >90	<3.1	<100	<2.8	>90	>3.2

The statements are continually read until one is found true, at which point a cell is given the assigned value named in the formula. Based on this methodology, the formula was first required to check the criteria for heterolithic units, followed by criteria for sandstone, and carbonate-rich lithologies. The formula would assign mudstone lithology if none of the statements were true. Results were checked against wells with core and cut-off criteria were adjusted until appropriately calibrated to the rock.

To best match observations in core, the heterolithic lithology maps for allomembers I and II required multiple cut-off combinations for GR and P_e curve values. The same cut-off criterion was applied to allomembers III through XI. For sandstone and carbonate-rich lithologies, the GR and PE data cut-off ranges were relatively consistent between the allomembers. A P_e criterion closer to 3 in the sandstone category reflects higher clay content in the matrix and supports the interpretation of deposition in an offshore setting, between fair-weather and storm wave base (Chapter 3).

The carbonate-rich lithology category comprises lithofacies 3 and 4, corresponding to rock intervals containing abundant calcareous skeletal remains. The P_e cut-off criteria of greater than 3.5 for the carbonate-rich lithology was consistent for each allomember. The GR cut-off of greater than 81, which is higher than readings for a clean carbonate deposit, likely reflects the mudstone content of lithofacies 3. Lithofacies 4, which is a mud-deficient packstone-grainstone deposit, is higher than what would be registered for a clean, carbonate rock because the thickest lithofacies 4 deposit is under 10 centimetres thick, the signal would be muted and mostly reflect muddier strata bounding it.

Chapter 5

5 Allostratigraphy and stratigraphic geometries of the Blackstone Alloformation

An allostratigraphic framework permits the comparison of time-correlative units within the Colorado Group across the foredeep, forebulge and backbulge sections of the WCFB. The allostratigraphic scheme presented in this chapter extends the framework of Tyagi (2009) to the southern and eastern limits of the WCFB to better understand subsidence history in the distal portions of the basin. Thickness changes illustrated in isopach maps provide a snapshot in time of a basin whose geometry of which was constantly evolving in response to a complex flexural history (Waschbusch and Royden, 1992). This chapter summarizes the bounding discontinuities observed in core and mapped within the Blackstone alloformation, followed by a review of the allostratigraphic cross sections (approximately dip-oriented and strike-oriented). The chapter finishes with isopach mapping results and the influence of tectonism on deep-seated Precambrian structures.

5.1 Bounding discontinuities of the Blackstone Alloformation

The allostratigraphic naming scheme used by Tyagi (2009) subdivided the Fish Scales Formation of the Lower Colorado Group and the Belle Fourche and Second White Specks formations of the Upper Colorado Group (Blackstone Formation equivalent) into 14 allomembers (Figure 5.1; Section 2.4.3.5). The allomembers are informally named with a roman numeral sequence, I (oldest) through XIV (youngest). The current study, which only extends the framework for allomembers I through XI, uses the same naming organization to maintain nomenclature continuity and prevent confusion when comparing time-correlative units across the basin. Except for allomember I (a time-transgressive lithological boundary), the surfaces of the Blackstone alloformations II through XI are marked by either regional marine flooding surfaces or bentonites. The following section describes the allomember bounding discontinuities observed in cores (Table 5.1). Surfaces marking the tops of allomembers IX and X were not captured in cores viewed for this study and will not be discussed.

Period	Epoch	Stage	<i>Lithostratigraphic Framework</i>	<i>Allostratigraphic Framework</i>
Cretaceous	Upper	Turonian	Second White Specks Fm.	Green bentonite
				TS XI
	Cenomanian	U. Colorado Grp.	U. Belle Fourche	TS X
				Blue Bentonite
Lower	Albian	L. Colorado Grp.	L. Belle Fourche	IX
				TS VIII
				Bighorn River (Red) Bentonite
				VII
				K1
				TS VI
				x
				TS V
				A
				TS IV
				X Bentonite
				TS III
				II
				FSU
			Fish Scales Fm.	I
				BFSM
			<i>U = Upper</i> <i>L = Lower</i> <i>Fm. = Formation</i>	

Figure 5:1: Allostratigraphic and lithostratigraphic chart for the study interval. TS = transgressive surface.

(next page)

Table 5.1: List of surfaces observed in cores. B = Bentonite. FS = Flooding surface. DF = Discrete flooding. CS = Condensed section. L = Lag. DL = Discrete lag. GF = Gradual flooding. LP = Geophysical log pick. *Not sampled. **Rubbled core.

Allomember/Surface	100/14-07-036-05W5	100/07-19-045-06W5	100/16-28-041-04W5	100/11-12-006-16W4	102/07-04-028-18W4	103/06-04-017-13W4	100/02-34-024-15W4	102/16-18-023-03W4	100/06-23-043-11W4	142/05-018-028W3	101/06-11-014-26W3	111/03-22-055-25W3	121/06-35-013-13W3	101/16-23-023-28W2	101/06-28-029-24W2	131/11-09-017-23W2*	141/07-34-035-01W2
XI/Green bentonite						B**								B			B
X						**											
IX																	
VIII/Blue bentonite						B			DL								
VII		FS	FS						DF								
VI/Big Horn River (“Red”) bentonite	B	FS	B			B			B			B					B
V/K1		FS								CS	CS	L		CS	LP	**	DF
IV/”X transgressive”		FS				FS				FS	FS			FS	FS	**	FS
III/Dunvegan “A”					DL	FS				FS	FS		**		**	**	B
II/X bentonite				B	L	B	B**			B	B	B**		B	B	B**	B
I/FSU				L	L	L	L	L		L							B

no core interval
 lapped out
 missing core interval
 erosional
 truncated

5.1.1 Allomember I (Fish Scales Alloformation) – BFSM and FSU surfaces

5.1.1.1 Base of Fish Scales Marker (BFSM)

The BFSM is observed in core 100/11-12-006-16W4 as a nearly one-centimetre-thick lag of reworked bioclastic debris sharply overlying a thinly laminated mudstone. Deposits of abundant fish debris in lags can result from periods of very low rates of siliciclastic sedimentation during rapid transgression or from storm reworking of fish debris (Schroder-Adams et al., 2001; Macquaker et al., 1996).

5.1.1.2 FSU

The Fish Scales Upper (FSU) surface is a condensed interval of organic-rich rock that defines the top of allomember I. The surface is recognized on gamma ray geophysical logs as a sharp spike that is readily observed in wells in Alberta and into western Saskatchewan. Except for one core in eastern Saskatchewan (141/07-34-035-01W2), the surface correlates to a bioclastic lag of fish debris (Figures 5.2) that denotes the top of the radioactive sediment package of allomember I. The bentonite deposit directly beneath the bioclastic lag in Figure 5.3 correlates to a bentonite in the 6-34-30-08W4 well of Tyagi et al. (2007). In core 141/07-34-035-01W2, the FSU surface correlates to a reworked bentonitic interval. It is interpreted that the reworked bentonite is a distal expression of the lag observed in core in the western part of the study area.

5.1.2 Allomember II – X Bentonite

The “X bentonite” represents a regional volcanic ash deposit that defines the top of allomember II and lies within the distal expression of the Dunvegan Formation wedge (the “X Bentonite” was not recognized in the northwest portion of the original Blackstone alloformation framework by Tyagi (2009)). The “X Bentonite” was observed in 11 cores logged for this study and comprises light gray to light blueish gray, highly radioactive clay. The bed ranges in thickness from 15 centimetres to 75 centimetres. The lower contact is typically sharp, and there is a varying degree of mixing with overlying

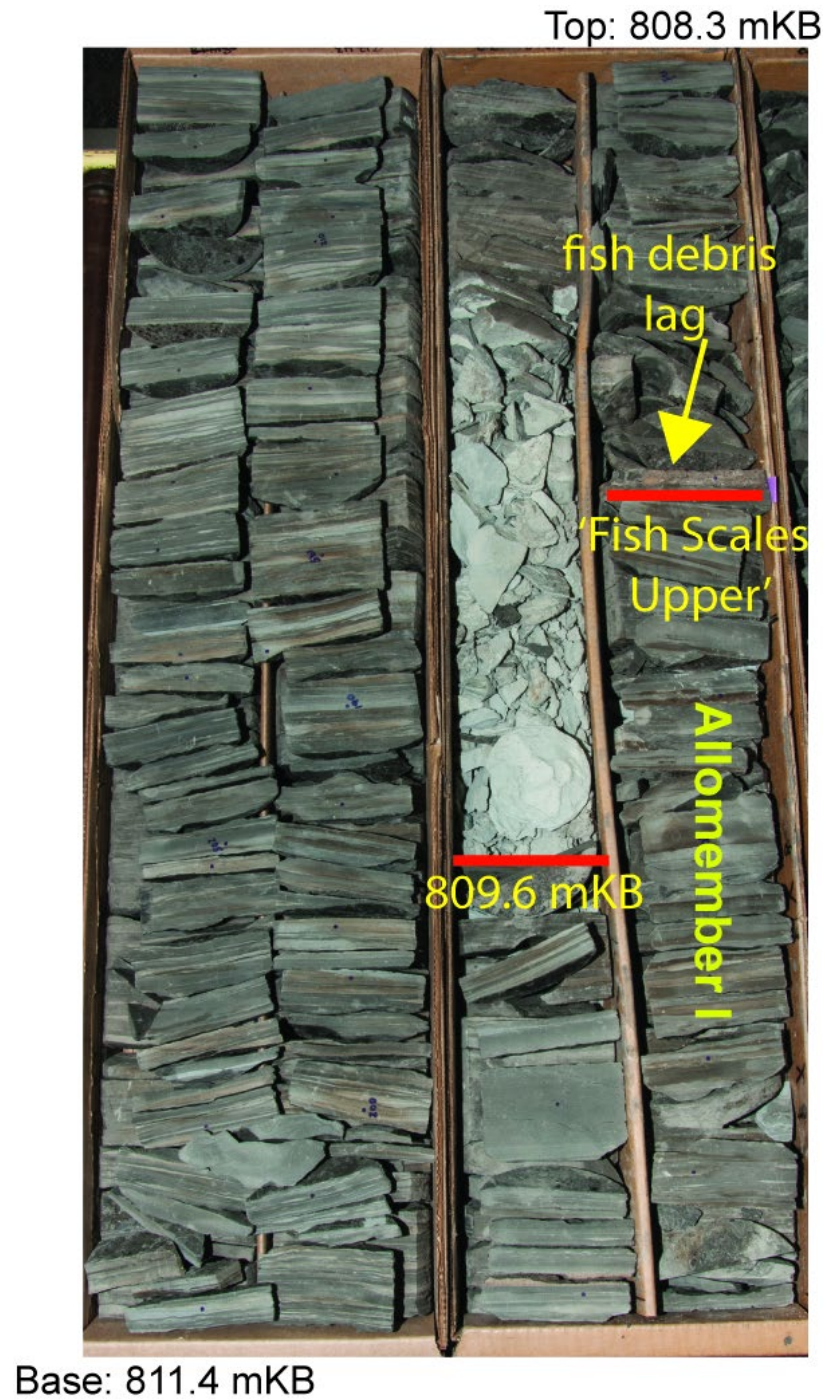


Figure 5:2: FSU bioclastic lag (yellow arrow) and underlying bentonite (light-coloured interval with base depth of 8069.6 mKB) as observed in core 100/02-34-025-15W4. Base of the core is at the bottom left corner of image and the top of the core is upper right corner of image.

sediment at the upper contact. The homogeneity of the bentonite suggests that the volcanic ash was deposited under low energy conditions. The bentonite is not preserved at one location, well 102/07-04-028-18W4, where the top of allomember II is instead defined as an erosion surface where a less than one-centimetre-thick lag of fish and inoceramid debris is present.

5.1.3 Allomember III – “Dunvegan A” equivalent

The top of allomember III is a marine transgressive surface associated with the initial drowning of the Dunvegan Delta in northwestern Alberta and northeastern British Columbia (Plint, 2000). This discontinuity is observed in six cores as millimetre- to centimeter-thick lag beds (103/06-04-017-13W4; 102/07-04-028-18W4; 142/05-08-018-28W3; 101/06-11-014-26W3; and 111/03-22-055-25W3) and as a correlative conformity (141/07-34-035-01W2).

The presence of a coarse lag at the top of allomember III is evidence that transgressive marine reworking took place at that location. In south central Alberta at well 103/06-04-017-13W4, the top of allomember III is a flooding surface that separates a one-metre-thick heterolithic sandstone and mudstone (Lithofacies 2) from overlying silty mudstone (Lithofacies 5). At core 102/07-04-028-18W4, the top of allomember III corresponds to a thin, discrete lenticular lag of fine-grained sand and minor fish debris that lies between a calcareous mudstone on calcareous mudstone (Lithofacies 3) deposit. Allomember III at this location is very thin and is less than 15 centimetres from the lag bed denoting the top of the underlying allomember II, where the X bentonite has not been preserved. Tyagi et al. (2007) recognized a bevelling unconformity caused by forebulge uplift in the vicinity of well 102/07-04-028-18W4.

At well 142/05-08-018-28W3, east of the Alberta-Saskatchewan border, the Dunvegan “A” surface correlates to a five centimetre interval with two prominent lag beds deposited within a calcareous mudstone (Lithofacies 3) interval: 1) a one-centimetre-thick calcareous, recumbently folded, lag bed with abundant phosphatic fish debris (Fig. 5.3A, yellow box) and 2) a two-centimetre-thick calcareous lag with abundant phosphatic fish debris and low-angle cross-bedding (Fig. 5.3A, red bar). A thin, one-centimetre-thick

bentonite occurs 0.5 metres beneath the interval. The “A” surface at well 101/06-11-014-26W3 correlates to a three-centimetre-thick, fine-grained transgressive lag with fish debris (Fig. 5.3B) that lies between a unit of heterolithic sandstone and mudstone (Lithofacies 2) and an overlying deposit of silty mudstone (Lithofacies 3). A 15-centimetre-thick bentonite is located approximately 1.6 metres below the surface of allomember III at this location.

The top of allomember III in northwestern Saskatchewan at core 111/03-22-055-25W3 correlates to a two-centimetre-thick lag that denotes the K1 disconformity (Figure 5.3C). The lag comprises phosphatic fish debris, fine-grained sandstone and glauconitic sandstone grains, and rare millimetre-sized, rounded rip up clasts of glauconitic sandstone at the base. Allomembers IV and V are eroded at this location and the underlying allomember III is just over one-metre thick. A thin, one-centimetre-thick bentonite bed is preserved about 18 centimetres beneath the contact, which could be the bentonite underlying the “A” surface as noted in the cores from southwestern Saskatchewan and south-central Alberta. The bentonite at 111/03-22-055-25W3 is sharp-based but its upper contact grades into silty mudstone, suggesting that the ash bed underwent reworking.

At the distal end of the basin, in eastern Saskatchewan at well 141/07-34-035-01W2, the top of allomember III is expressed as a correlative conformity, whereby a time boundary with the overlying silty argillaceous mudstone deposits is not easily identified. The bentonite correlated at this location is interpreted as the bentonite observed just beneath the contact in cores previously discussed and is interpreted to mark the marine transgression event at the distal end of the basin.

5.1.4 Allomember IV – X transgressive surface

In this study, the marine transgression surface marking the top of allomember IV is recorded in core by lithofacies changes. The surface was observed in two cores from northwest and south-central Alberta (100/07-19-045-06W5 and 103/06-04-017-13W4), where the top of allomember IV is marked by the boundary between heterolithic sandstone and mudstone (Lithofacies 2) and an overlying unit of silty argillaceous

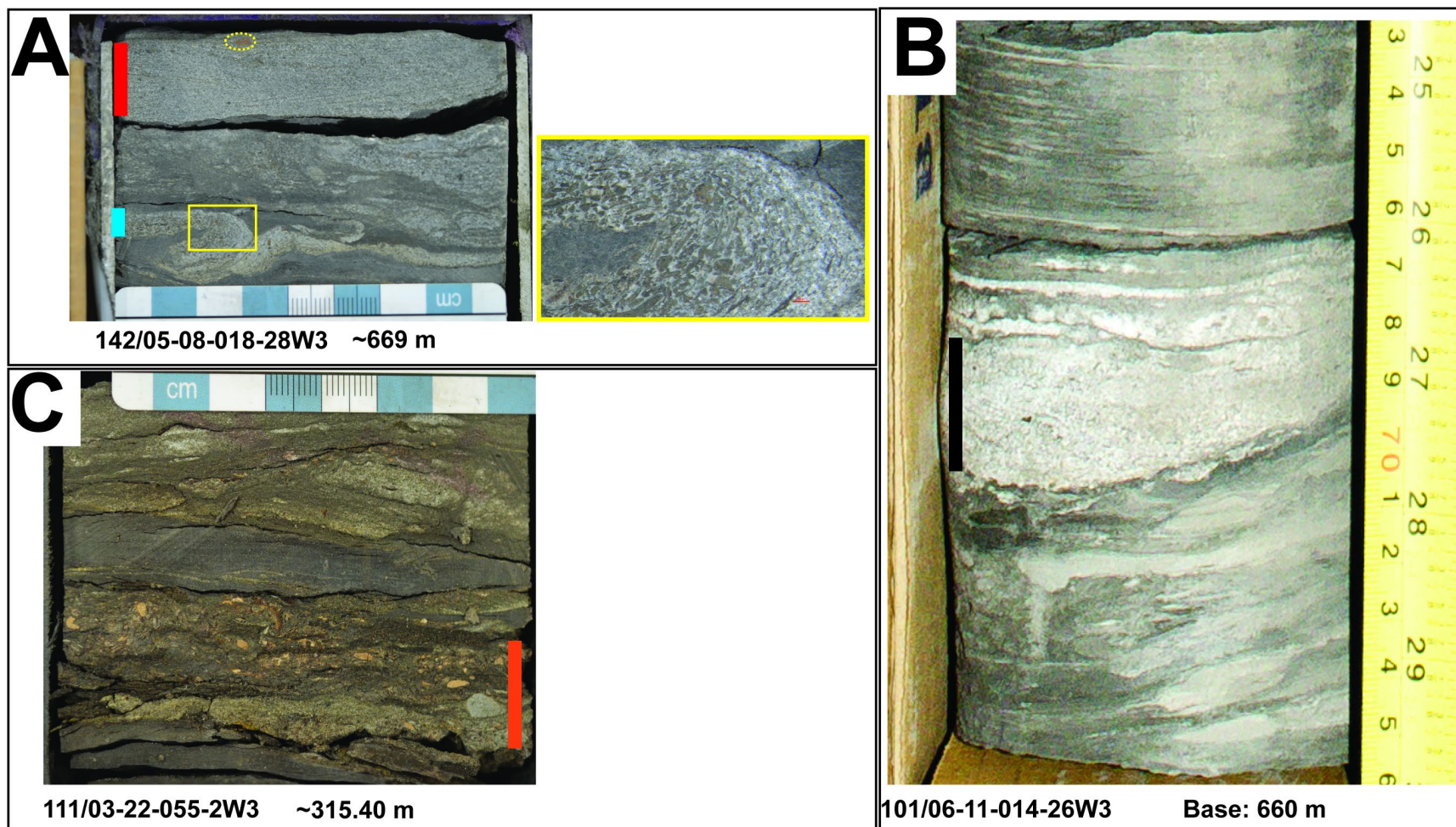


Figure 5:3: Core photograph showing the surfaces at the top of allomember III in cores 142/05-08-018-28W3 (A), 101/06-11-014-26W3 (B), and 111/03-22-055-25W3 (C). (A): Two calcareous lags (red bar and blue bar noting a recumbent folded lag) with abundant phosphatic fish debris. Yellow box is location of magnified core image from the recumbent folded lag. Yellow dotted circle shows intraclast at top of cross-bedded lag bed. (B): Fine-grained sandstone transgressive lag with fish debris (black bar). (C): Lag containing phosphatic fish debris, fine-grained sandstone and glauconitic sandstone grains, and rare millimetre-sized, rounded fine-grained glauconitic sandstone rip up clasts (orange bar).

mudstone (Lithofacies 5). In southeastern and south-central Saskatchewan, the X transgressive surface is inferred in cores from 142/05-08-018-28W3, 10/06-11-014-26W3, 101/06-28-029-24W2 and 101/16-23-023-28W2 by a cryptic transition separating an underlying silty argillaceous mudstone (Lithofacies 5) from overlying calcareous mudstone (Lithofacies 3).

The transition from silty mudstone to calcareous mudstone records transgression in a distal offshore setting in the basin (Figure 3.14), where clastic sediment supply was limited, and primary productivity was high or there was less dilution from siliciclastic components. Tyagi et al. (2007) traced the X transgressive surface to a flooding contact and a bentonite bed. Based on correlations, the bentonite bed, which is observed just beneath the flooding surface at the wells located in southeastern and south-central Saskatchewan, is contemporaneous with the flooding surface that is represented by the transition from silty mudstone (Lithofacies 5) into clastic-poor calcareous mudstones (Lithofacies 3). The bentonite bed was not observed in the southern Alberta foothills (Tyagi et al., 2007) or in the cores from central to southeastern Alberta, suggesting the persistence of higher energy depositional conditions that prevented its preservation.

5.1.5 Allomember V – K1 surface

The K1 surface was observed in seven cores and its sedimentological expression varies across the basin. In west-central Alberta (100/07-19-045-06W5) and east-central Saskatchewan (141/07-34-035-01W2), K1 is defined by a flooding surface that records a shift from proximal to distal marine lithologies. Elsewhere in Saskatchewan, K1 correlates to erosional surfaces (111/03-22-055-26W3 and 101/16-23-023-28W2) and condensed intervals (142/05-08-018-28W3 and 101/06-11-014-26W3).

At core 100/07-19-045-06W5, the flooding surface is represented by the transition from heterolithic sandstone and mudstone (Lithofacies 2) to overlying planar-laminated, silty mudstone (Lithofacies 5). In east-central Saskatchewan (141/07-34-035-01W2), the transgressive surface is indicated by a shift in the calcareous component of mudstone, from subequal proportions of clay to non-clay content to distribution to calcite accounting for over 85 wt% of the non-clay component (TerraTek, 2008).

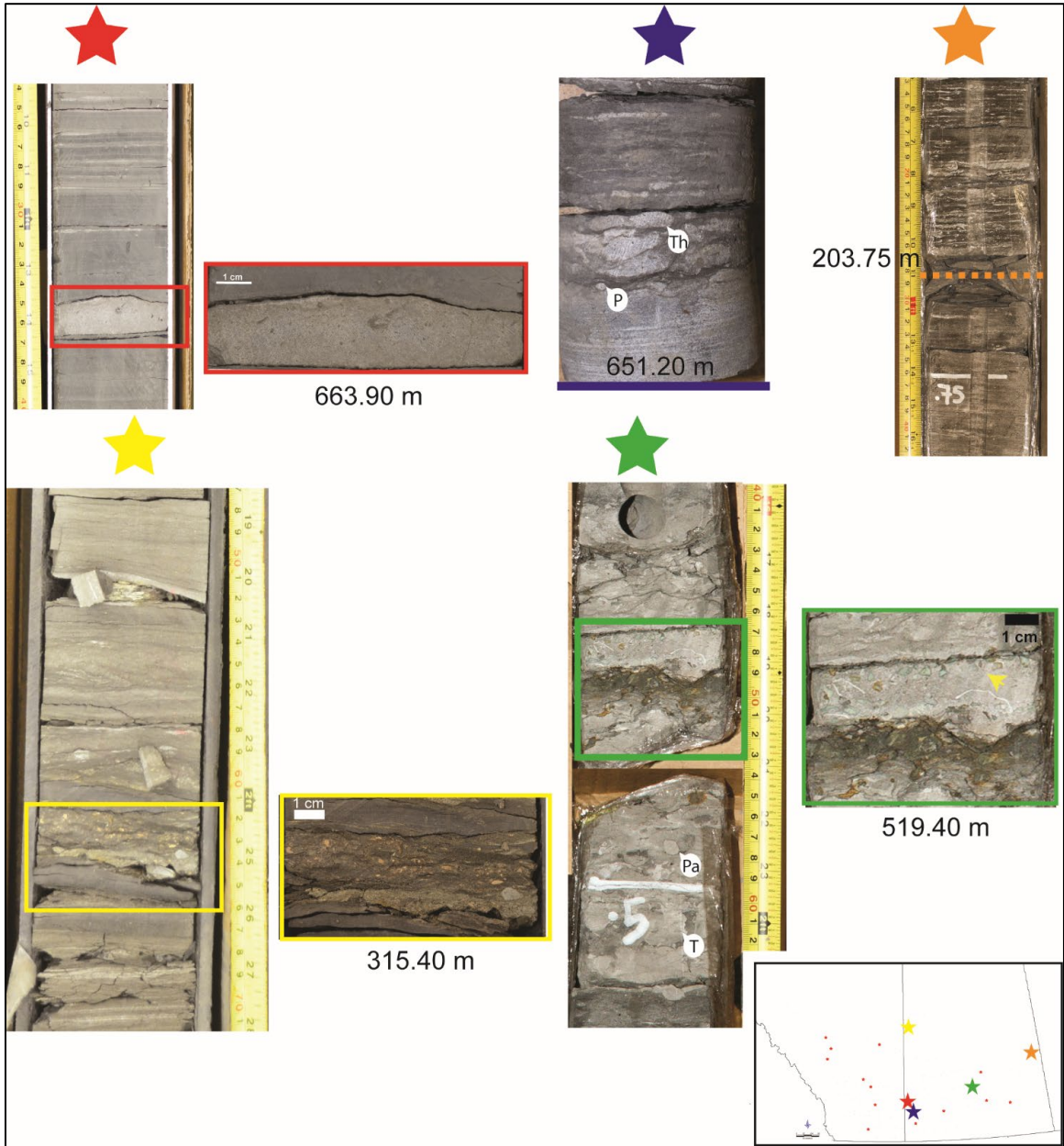


Figure 5:4: Photo collage showing the K1 surface in core. The coloured stars correspond to the core locations on the inset map: Red star = 142/05-08-018-28W3; blue star = 101/06-11-014-26W3; yellow star = 111/03-22-055-23W3; green star = 101/16-23-023-28W2; and orange star = 141/07-34-035-01W2. K1 in southwestern Saskatchewan (101/06-11-014-26W3) is at the base of a condensed section (blue bar). The condensed section is overlain by a calcareous argillaceous mudstone bioturbated with *Planolites* (P) and *Thalassinoides* (Th). At 101/16-23-023-28W2 (green star), beneath the K1 surface is bioturbated carbonate mud with *Palaeophycus* (Pa), and *Teichichnus* (T), indicating a shifting substrate condition and an abrupt change from the depositional conditions of the underlying pelagic, calcareous mudstone. The trace fossils are proximal expressions of the Cruziana ichnofacies and include the lower energy environments within the offshore to very distal fringes of the lower shoreface.

At 142/05-08-018-28W3 in southwestern Saskatchewan, K1 is marked by a two-centimetre-thick condensed, bioclastic bed (Lithofacies 4) containing abundant foraminiferal tests and phosphatic bone fragments. Southeast of this location at 101/06-11-014-26W3, K1 is correlated with a condensed bed of Lithofacies 4 sharply overlying calcareous argillaceous mudstone (Lithofacies 3). Overlying the condensed section is a moderately bioturbated (BI 3) section with *Planolites* and *Thalassinoides* of the *Cruziana* Ichnofacies (MacEachern et al., 2010). At core 101/16-23-023-28W2 (Figure 5.4, green star and box), the K1 surface separates the underlying dark-coloured, chemically and physically altered clastic deposit from the overlying Lithofacies 4. Post-K1, a sea level rise shut off clastic supply, allowing for the deposition of sediment with a higher proportion of pelagic carbonate. The condensed section was burrowed, lithified (during the time of hiatus), and then completely reworked into another carbonate bed comprising diagenetic sediment (green glauconite intraclasts) and intact biogenic material (oyster shells). Christopher and Yurkowski (2005) noted an unconformity in wells 131/01-24-020-33W1 and 101/15-36-002-03W2 at the top of their Keld A that correlates to the mapped K1 surface in the current study, which comprise a paleosol and a burrowed hardground, respectively.

Correlation of K1 into northwestern Saskatchewan (111/03-22-055-26W3) places the surface at a two-centimetre-thick lag, comprising phosphatic fish debris, glauconitic sand, and fine-grained sandstone intraclasts (Fig. 5.4; yellow star).

Variable expressions of the K1 surface across the study interval result from a complex tectonic and eustatic history. Northwest of the study area, the K1 disconformity correlates with a beveling unconformity that eroded the Doe Creek and Pouce Coupe Sandstones of the Kaskapau Formation in northeastern British Columbia in response to flexural uplift driven by tectonic loading to the west (Plint, 2000; Varban and Plint, 2005; Kreitner and Plint, 2006; Plint and Kreitner, 2019). Into northwestern Alberta, K1 is sharply overlain by an oolitic ironstone, and both the K1 surface and overlying oolitic ironstone deposit are penetrated by abundant *Thalassinoides* (Plint, 2000; Varban and Plint, 2005; Plint and Kreitner, 2019). Ooidal ironstones tend to be deposited in conjunction with sequence boundaries, flooding surfaces, or maximum flood surfaces (MacQuaker et al., 1996).

They form under very low sedimentation rates, high energy conditions, and when detrital ferric iron is available (MacQuaker et al., 1996). These circumstances can occur during periods of sediment by-pass with limited accommodation, or when sediment is trapped near its source (MacQuaker et al., 1996). Well-defined, *Thalassinoides* are common in firmground substrates, reflecting sea floor conditions that postdate deposition of the host material, and are commonly associated with stratigraphic discontinuities (MacEachern et al., 2010). Plint (2000) interpreted the ooidal ironstone unit mantling the K1 surface in northwestern Alberta as being a product of winnowing and clastic starvation over an intra-basinal swell. Penetration of *Thalassinoides* (*Glossifungites* Ichnofacies) into the basal surface of the ooidal ironstone unit and the K1 unconformity suggests these discontinuity surfaces formed in firm but unlithified substrates after regression and during initial transgression following the lowstand phase, when sedimentation had ceased and erosion dominated (Kreitner and Plint, 2006; MacEachern et al., 2010; Plint and Kreitner, 2019). Towards central Alberta, the surface becomes conformable and correlates to a regional transgression (Plint and Kreitner, 2005; Tyagi, 2009) represented in central Alberta by a flooding surface.

Basinward, time-equivalent condensed sections in central Saskatchewan also record the initial re-flooding of an uplifted, eroded area, when both accommodation and detrital sediment supply were limited (Plint et al., 1993; Plint and Kreitner, 2019). The flooding surface marking K1 in central Alberta and east-central Saskatchewan suggests that clastic sediment supply was not restricted everywhere in the basin during transgression, compared to the condensed sections observed in central Saskatchewan.

5.1.6 Allomember VI – Bighorn River bentonite

The Bighorn River bentonite denotes the top of allomember VI and approximately coincides with the Cenomanian-Turonian boundary (Tyagi et al., 2007). Based on lapout patterns observed in regional correlations, Tyagi (2009) considered the regional bentonites (X bentonite, Bighorn River, “blue”- top of allomember VIII, and “green” – top of allomember XI) as basinwide hiatal surfaces. The Bighorn River bentonite was observed in five cores: 100/14-07-036-05W5, 103/06-04-017-13W4, 100/06-23-043-11W4, 111/03-22-055-25W3, and 141/07-34-035-01W2. The bentonite is sharply bound

between overlying and underlying strata and thins from 50 cm in southern Alberta at 103/06-04-017-13W4 to 5 cm in northeastern Alberta at 111/03-22-055-25W3. At 100/07-19-045-06W5, the Bighorn River bentonite is not preserved in the study area and is interpreted to have been eroded in that area (Marion, 2018; Percy, 2019).

5.1.7 Allomember VII – Regional flooding surface

Allomember VII is bound at the base by the Bighorn River Bentonite and at the top by a regional flooding surface. Where the allomember has not lapped out, this transgressive surface is observed in three cores viewed for this study: 100/07-19-045-06W5, 100/16-18-041-04W5, and 100/06-23-043-11W4. It is defined as a flooding surface that separates underlying heterolithic sandstone and mudstone deposits (Lithofacies 2) of allomember VII from the overlying argillaceous mudstone deposits (Lithofacies 5) of allomember VIII. At 100/06-23-043-11W4, the flooding surface is marked by a subtle transition from silty argillaceous mudstone (Lithofacies 5; allomember VII) to calcareous mudstone (Lithofacies 3) of allomember VIII. The vertical shift from argillaceous mudstone to calcareous mudstone at the top of allomember VII is interpreted as basinward lithofacies change. A lateral change in lithofacies is denoted by the more offshore conditions at 100/06-23-043-11W4 compared to the other two wells (100/07-19-045-06W5 and 100/16-18-041-04W5) to the west. This lateral change suggests enhanced primary productivity in surface waters and increased subsidence in northwestern Alberta that restricted basinward transport of clastic material (Tyagi, 2009).

5.1.8 Allomember VIII- ‘Blue’ bentonite

The informally named “Blue” bentonite by Tyagi (2009) marks the top of allomember VIII and is preserved in a single core at 103/06-04-017-13W4 in southern Alberta. It is approximately 12 centimetres thick and has a sharp contact with the overlying argillaceous mudstone (Facies 5) and underlying calcareous mudstone (Facies 3) strata. In core 100/06-23-043-11W4 located in east-central Alberta, this surface is correlative with a discrete millimeter-scale, fine- to medium-grained lenticular sandstone bed at the top of an interval that has an upward progression of increasingly reworked sediment. The

ash bed was not preserved here, probably due to storm-related reworking events that redistributed the ash over the sea floor.

5.1.9 Allomember XI – “Green” bentonite

The “Green” bentonite defines the top of allomember XI and was observed in three cores: one in southern Alberta (103/06-04-017-13W4) and two in Saskatchewan (101/16-23-023-28W2 and 141/07-34-035-01W2). The bentonite lies within a rubbled/damaged section of core at well 103/06-04-017-13W4 and is 3 to 5 centimetres thick in wells 101/16-23-023-28W2 and 141/07-34-035-01W2, respectively. Its lower and upper bounding strata are sharp, with no evidence of sediment mixing and this bentonite represents the last maximum flooding event before regression began in the upper Turonian.

5.2 Allostratigraphic cross-sections and stratal geometries

Variability in allomember thickness and geometry records changes in accommodation and sediment supply at time of deposition. A westward-thickening wedge-shaped geometry reflects increased subsidence that resulted from active tectonism and loading within the orogenic belt, and a tabular, or sheet-like allomember indicates a time of decreased flexural subsidence (Varban and Plint, 2008a). The following allomember geometry descriptions expand on the existing stratal architecture determined from studies outside of the current work (see section 2.5.3).

5.2.1 Approximately strike-oriented correlation lines (North-South trending)

The north-south trending cross section lines (Lines 1 through 6) approximate the depositional strike direction of the Upper Cretaceous Colorado Group (Plint et al., 1993; Plint, 2000; Varban, 2004; Varban and Plint, 2005; Tyagi et al., 2007; Tyagi, 2009), with the northwest-southeast cross-section Line 1 trending nearly parallel to strike. Cross-section Lines 1, 2 and 3 tie into the correlation work of Tyagi et al (2007) and Tyagi (2009), with cross-section Line 1 also tying into work by Roca et al (2008) on the Lower Colorado Group. The correlation lines vary in length between 200 and 700 kilometres. The greatest change to stratal thickness occurs in Line 1, where the study interval is over

400 metres thick at the northwest limit (Township 65, Range 5W6) of the study area and thins to about 90 metres at Township 1. In eastern Saskatchewan, along Range 30W1, the stratal thickness change is substantially less, with a difference of less than 14 metres between the north and south limits of the study area.

5.2.1.1 Allomember I

Allomember I thins dramatically from north to south along Line 1 (Figure 5.5), displaying a wedge-like geometry. The geometry shifts in Lines 2 and 3 to a very subtle, wedge-shape that thins to the north (Fig. 5.6 and 5.7). In central to eastern Saskatchewan (Lines 4 and 5; Fig. 5.8 and 5.9, respectively), allomember I shows minimal change in thickness between the northern and southern limits of the cross-section lines (5 metres to 4 metres, respectively) thus defining a tabular shape.

5.2.1.2 Allomember II

When viewed along Line 1, allomember II is wedge-shaped, gradually thinning to the south. In central to eastern Alberta, the geometry of the north-south transects transition from a subtle wedge-shaped geometry in Line 2 (Fig. 5.6) to nearly tabular in Line 3 (Fig. 5.7), respectively. Along the Alberta-Saskatchewan border in Line 3, allomember II has a nearly consistent thickness of approximately 24 to 30 metres between north and south, respectively, with localized thinning to less than 15 metres within the area of Township 18, Range 28W3. Lines 4 and 5 (Fig. 5.8 and 5.9) demonstrate a slight wedge-shaped geometry as allomember II thickens to the south from approximately 14 metres to 30 metres.

5.2.1.3 Allomember III

Along the western edge of the study area, allomember III is thickest in the north along Township 65, Range 3W6 at 45 metres and thins to just a few metres in Township 2. In contrast to allomembers I and II, the wedge-shape of allomember III in Line 1 (Figure 5.5) is quite subtle and only changes from just under 14 metres thick in the north to approximately 5 metres in the south. Between the Alberta-Saskatchewan border and central Saskatchewan (Lines 3 and 4; Figures 5.7 and 5.8), allomember III generally thins northward, with localized thickening and thinning. In Line 3, the

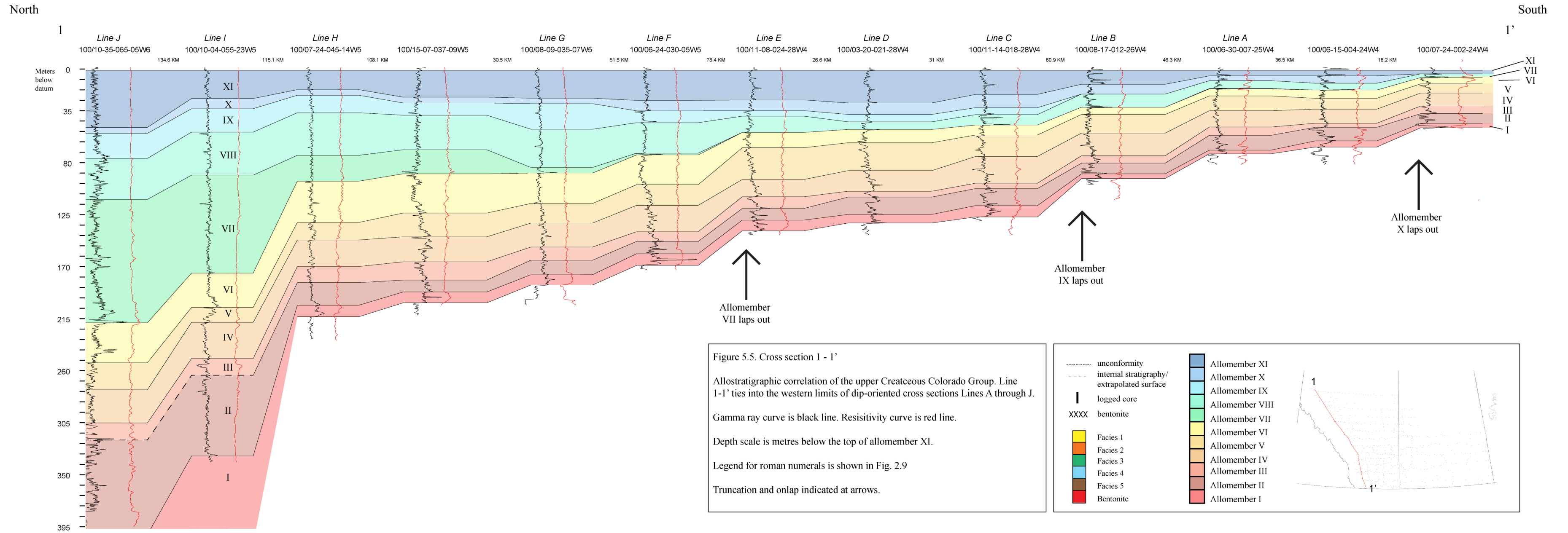


Figure 5.5: Cross section 1-1'

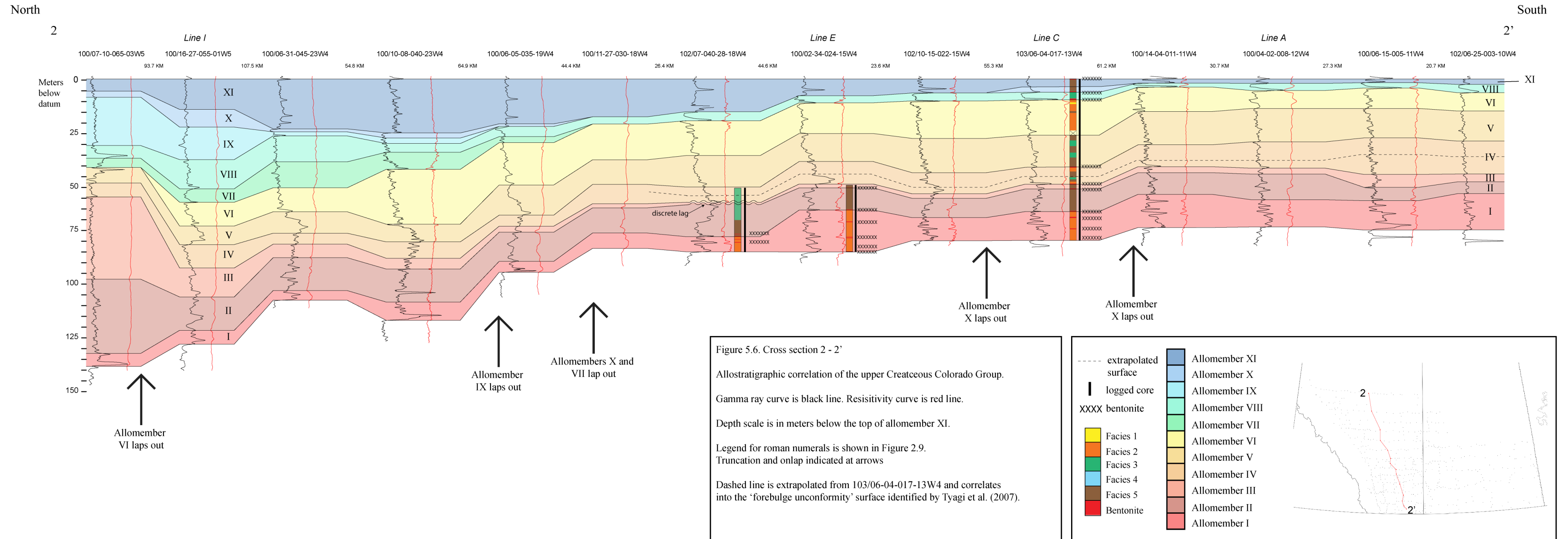


Figure 5:6: Cross section 2-2'.

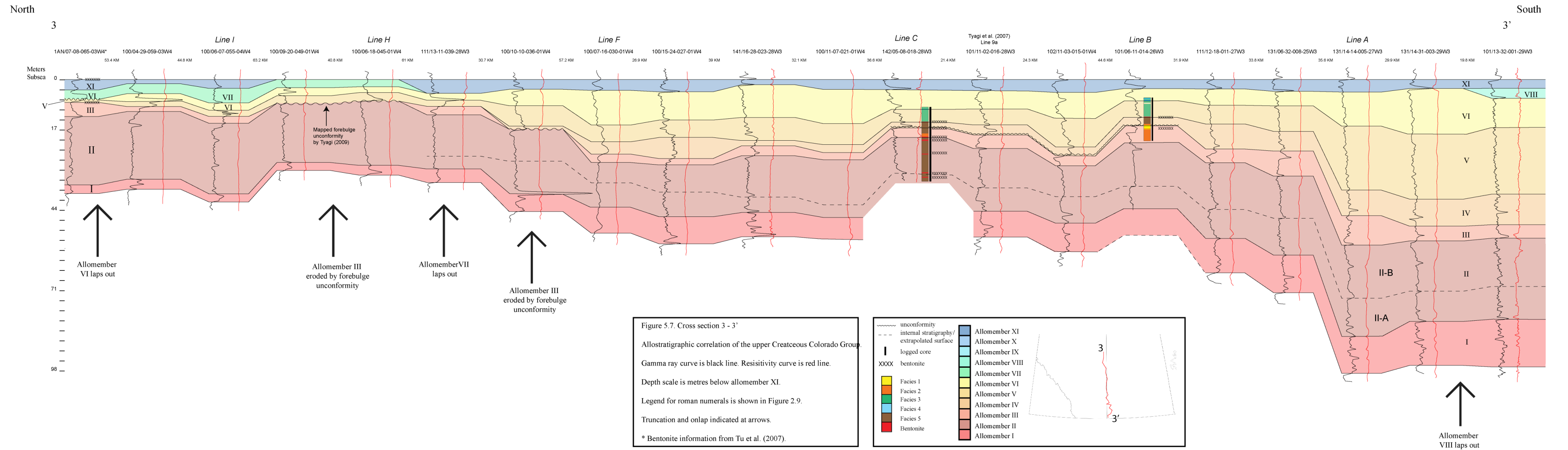


Figure 5.7: Cross section 3-3'.

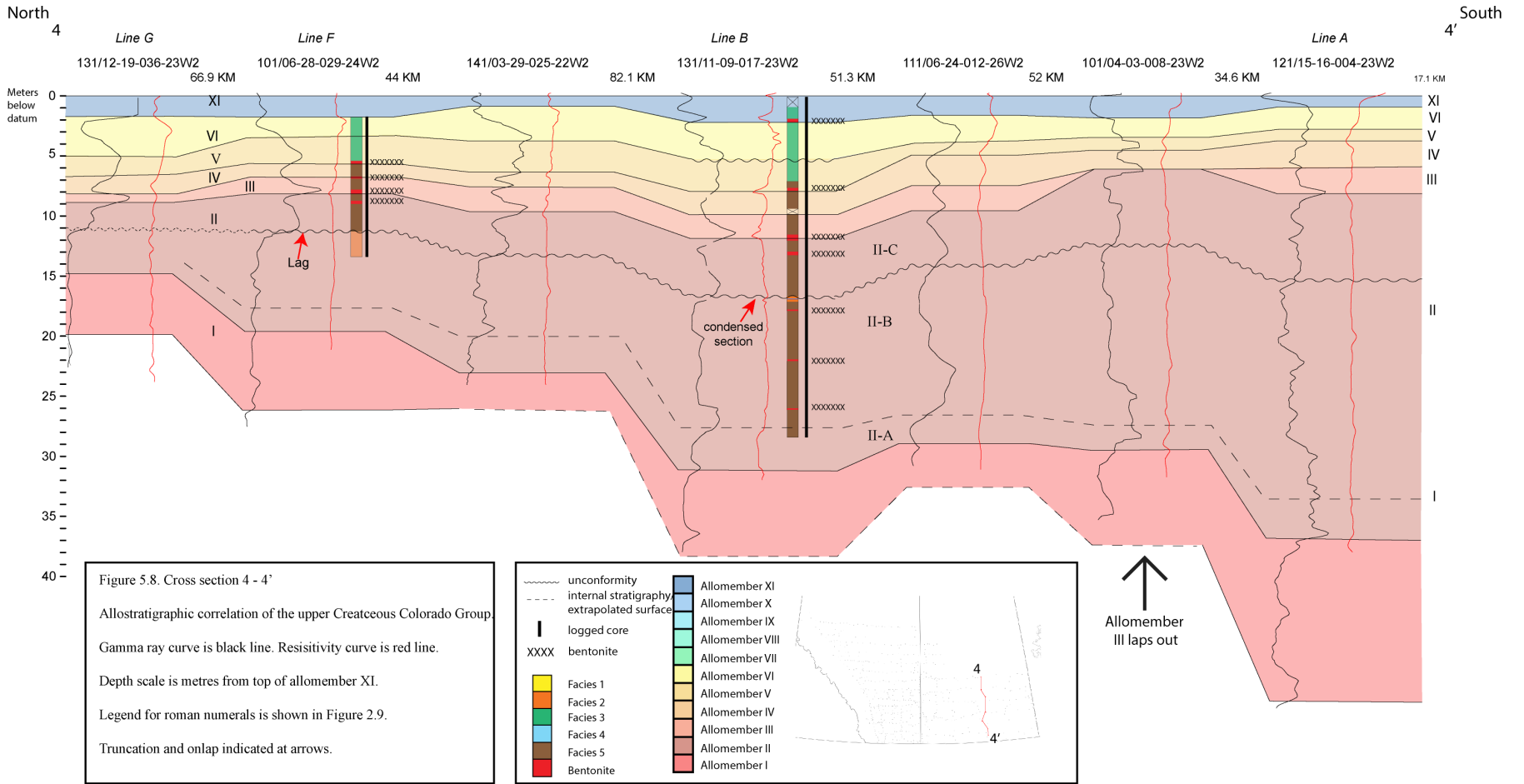


Figure 5:8: Cross section 4-4'.

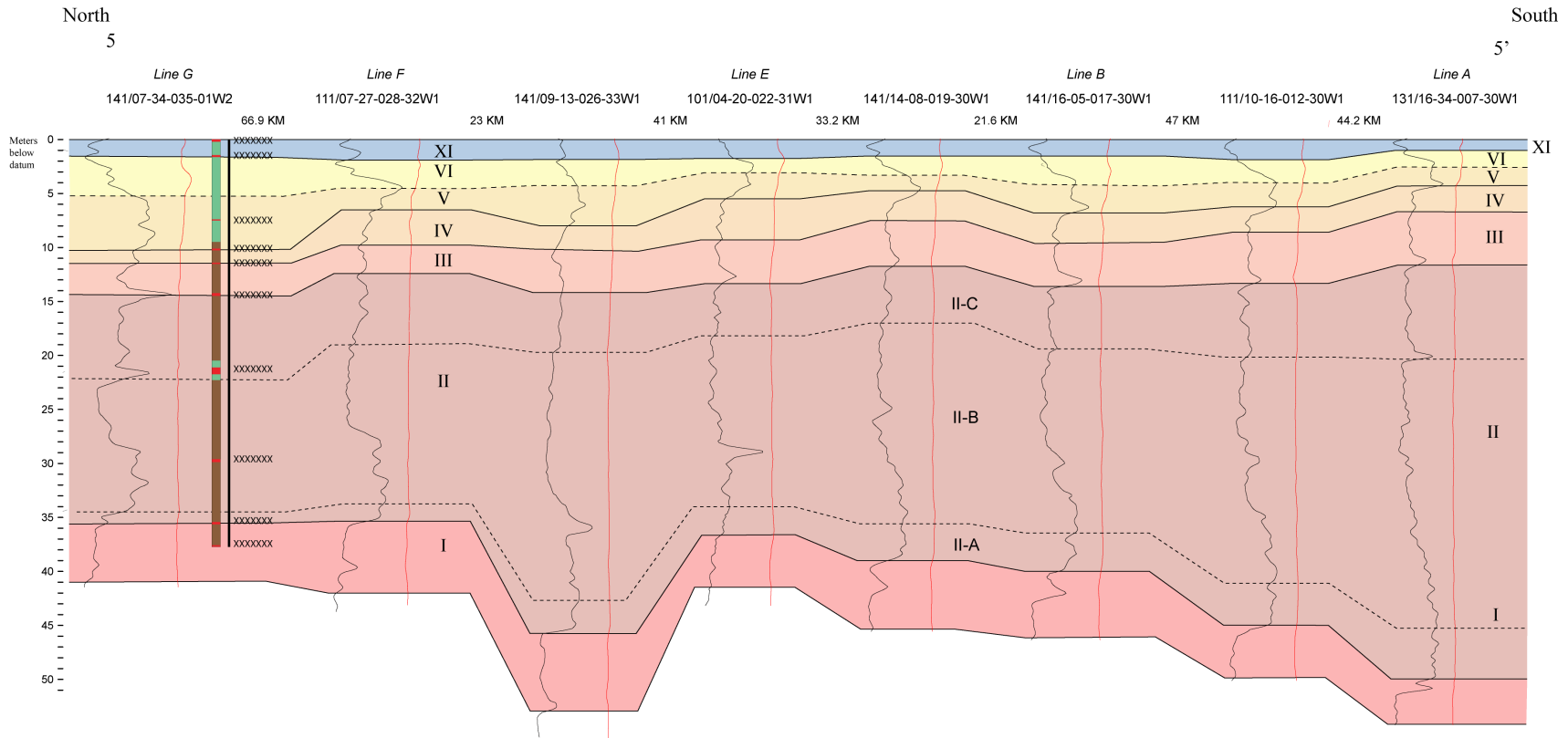


Figure 5.9. Cross section 5-5'
 Allostratigraphic correlation of the upper Cretaceous Colorado Group.
 Gamma ray curve is black line. Resistivity curve is red line.
 Depth scale is metres below allomember XI.
 Legend for roman numerals is shown in Figure 2.9.
 Truncation and onlap indicated at arrows.

<ul style="list-style-type: none"> ~~~~~ unconformity - - - - internal stratigraphy/ extrapolated surface I logged core XXXX bentonite 	<ul style="list-style-type: none"> Allomember XI Allomember X Allomember IX Allomember VIII Allomember VII Allomember VI Allomember V Allomember IV Allomember III Allomember II Allomember I 	<ul style="list-style-type: none"> Facies 1 Facies 2 Facies 3 Facies 4 Facies 5 Bentonite
--	--	---

Figure 5.9: Cross section 5-5'.

allomember is eroded at two locations (100/10-10-036-01W4 and 100/09-20-049-01W4) and then reappears north of township 49. Allomember III becomes tabular along eastern Saskatchewan (Line 5), with a relatively consistent thickness that becomes slightly thinner to the north.

5.2.1.4 Allomember IV

The overall geometric pattern for allomember IV varies across the study area, thinning and thickening on a local scale. When viewed along Line 2 (Figure 5.6), allomember IV transitions from a southward thinning wedge-shaped geometry in western Alberta, to a tabular geometry with consistent thickness. Along Line 3, the allomember transitions from a southward thickening wedge to a tabular geometry, then thickens again further southward. However, in central Saskatchewan (Line 4: Figure 5.8), allomember IV maintains a southward thickening trend.

5.2.1.5 Allomember V

The geometries of allomember V demonstrated across the basin show a general west-east transition from tabular- to wedge-shaped. Along Line 1 in western Alberta (Figure 5.5) the allomember maintains a thickness between 16 and 25 metres. Towards central and eastern Alberta, allomember V begins to thicken toward the south, then into central and eastern Saskatchewan, the thickness becomes more uniform again resulting a shift back to a sheet-like geometry.

5.2.1.6 Allomember VI

Allomember VI forms a subtle, wedge-shaped package that thins to the south in Line 1, along the western boundary of the study area. In Lines 2 and 3, in central Alberta and along the Alberta-Saskatchewan border, respectively, allomember VI onlaps allomember VI in the north and switches to a southward thickening wedge (Figures 5.6 and 5.7). Towards the eastern end of the basin in Saskatchewan (Lines 4 and 5), allomember VI has relatively consistent thickness and a predominantly sheet-like shape.

5.2.1.7 Allomember VII

Allomember VII is observed in Lines 1 through 4 (Figures 5.5 to 5.8). The wedge-shape of the allomember is thickest in the north in Line 1 (Figure 5.5), then thins to zero by approximately 500 kilometres to the south, marking the approximate halfway point of the transect. The change in thickness from north to south lessens substantially in Line 2 and the southward thinning trend is more gradual. The allomember then transitions to a tabular geometry at the Alberta-Saskatchewan border (Line 3: Figure 5.7) where the interval is locally preserved.

5.2.1.8 Allomember VIII

Allomember VIII is observed in Lines 1 and 2 (Figures 5.5 and 5.6). Line 1 gradually thins to the south, from about 35 metres to less than 5 metres thick. The geometry of allomember VIII in Line 2 is generally sheet-like, with a slight thickening between Townships 55 and 40. The allomember also shows isolated thinning around Township 11, with consistent thickness north and south of this point.

5.2.1.9 Allomember IX and X

Allomembers IX and X are observed in cross-section Lines 1 and 2 (Figures 5.5 and 5.6). Allomember IX presents a wedge-shaped geometry in both transects, with a subtle thinning to the south in Line 1 and a more abrupt thinning being observed in Line 2. The geometry of allomember X in Line 1 is generally tabular but shows slight thinning in the north and south, with a thickened section south of Township 30 to north of Township 7. Near Township 55, allomember X in Line 2 thickens to nearly 10 metres at well 100/16-27-055-01W5 and then to zero as it reaches Township 30.

5.2.1.10 Allomember XI

Viewed along strike in western and central Alberta (Lines 1 and 2; Figures 5.5 and 5.6), allomember XI exhibits an overall wedge-shaped geometry that gradually thins to the south with local zones of thinning or thickening. For example, in Line 1 allomember XI thins between Townships 55 and 37, increases in thickness, then thins south of Township 21. In Line 2, allomember XI thickens from five metres thick to over 25 metres between

Townships 45 and 40 before transitioning to a southward-thinning wedge. Aside from a zone of zero thickness between Townships 40 and 45 (Line 3; Figure 5.7) and at Township 36 (Line 4; Figure 5.8), allomember XI is predominantly tabular with a thickness ranging between three and four metres. In eastern Saskatchewan, the allomember is tabular in shape and reaches zero thickness by Township 8 (Line 5; Figure 5.9).

5.2.2 Approximately dip-oriented correlation lines (West-East trending)

The depositional dip of the Blackstone Alloformation conforms to the westward-thickening wedge-shape observed in the west-east cross-sections presented herein (Lines A through J; Figures 5.10 to 5.19). South of township 30 (Lines A through F; Figures 5.10 to 5.15), the study interval thins from between 75 to 175 metres in the west to between 30 to 55 metres in the east. The interval thickness between townships 65 and 30 (Lines G through J; Figures 5.16 to 5.19) in the west is approximately 185 to 485 metres in the west and thins to 25 – 45 metres in the east. The longest cross-section is over 880 kilometres (Line F) and the shortest is 264 kilometres (Line D).

5.2.2.1 Allomember I

Allomember I extends across the entire study interval and transitions from a slightly eastward thickening wedge-shaped geometry in the southern section of the study area to sheet-like north of Township 25 to Township 55. The allomember reverts to a wedge-shape north of Township 55 but thins eastward instead of thickening as is otherwise observed south of Township 25. South of Township 20 (Lines A, B, and C; Figures 5.10 to 5.12), allomember I thickens from approximately five metres in southwestern Alberta to nearly 20 metres to southeastern Alberta and southwestern Saskatchewan, and then thins east of 18W2. At Township 65 in Line J (Figure 5.19), allomember I is over 30 metres thick in the west and thins to less than five metres in the east.

5.2.2.2 Allomember II

In west to east Lines A through H (Figures 5.10 through 5.17), allomember II has an eastward-thickening, wedge-like geometry. The eastward thickening pattern is most

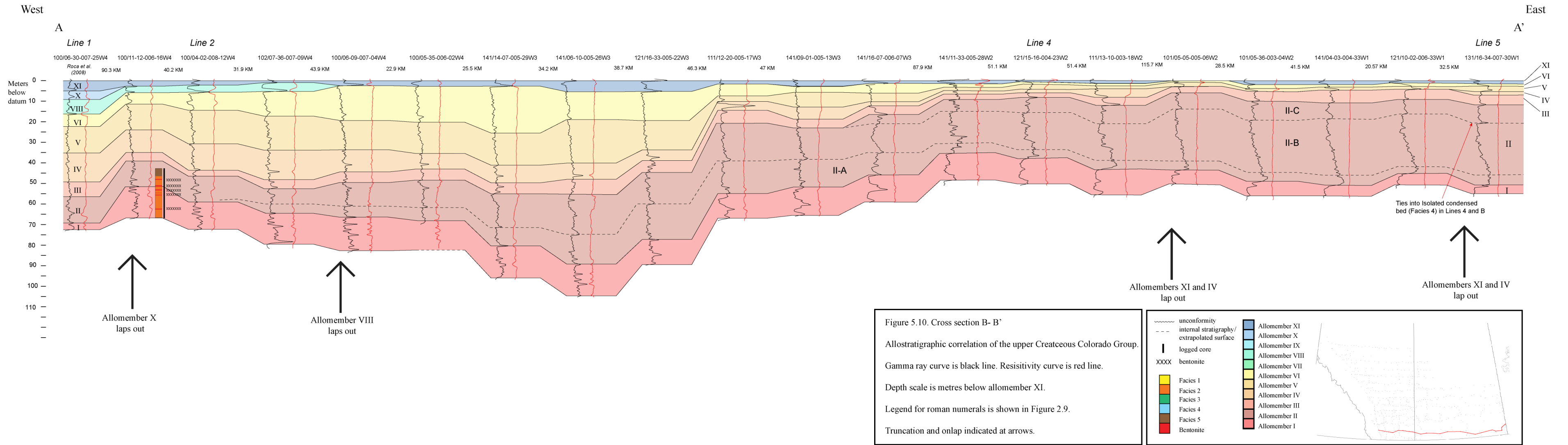


Figure 5.10: Cross section A-A''.

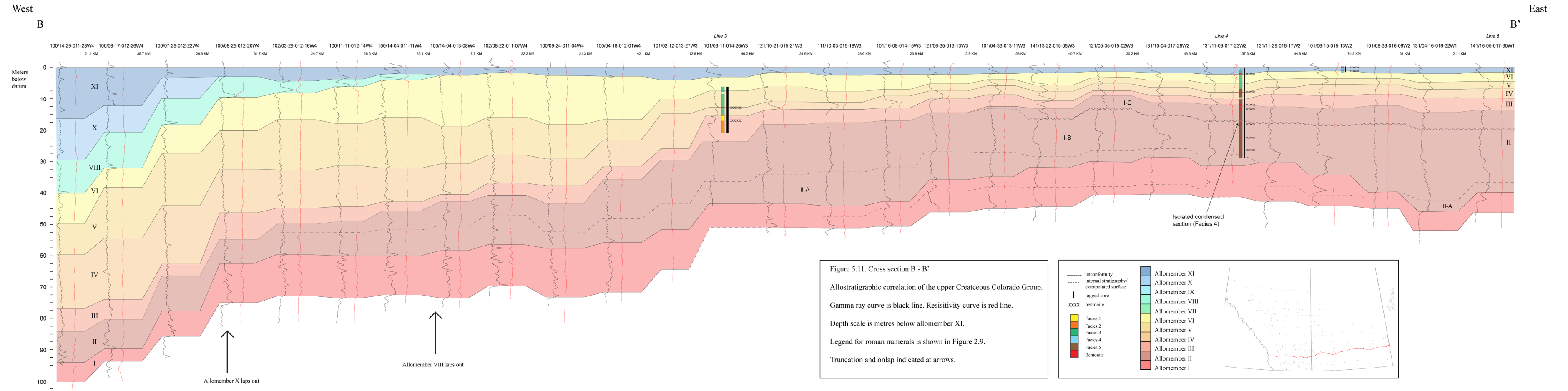


Figure 5.11: Cross section B-B''.

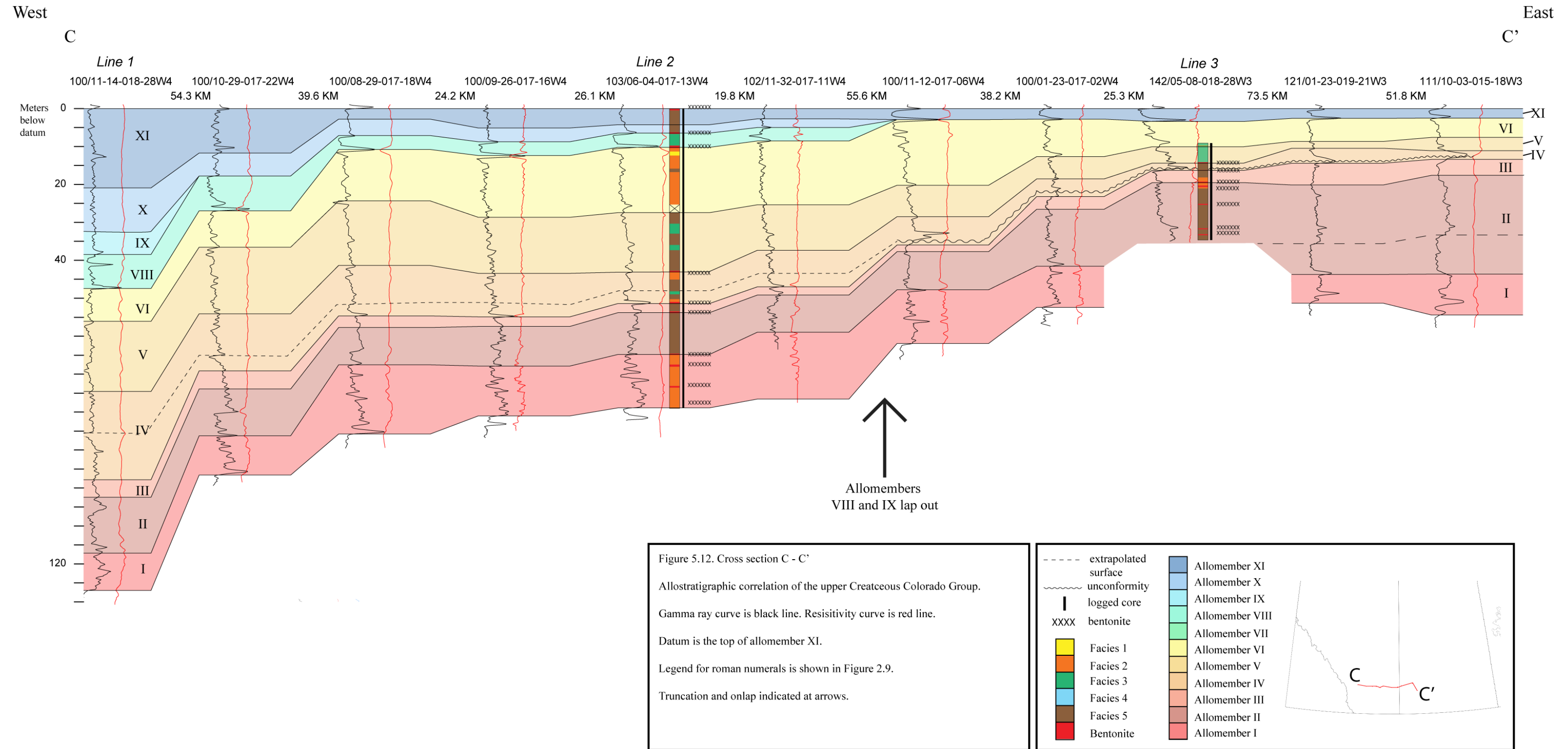


Figure 5.12: Cross section C-C'.

D
West

D'
East

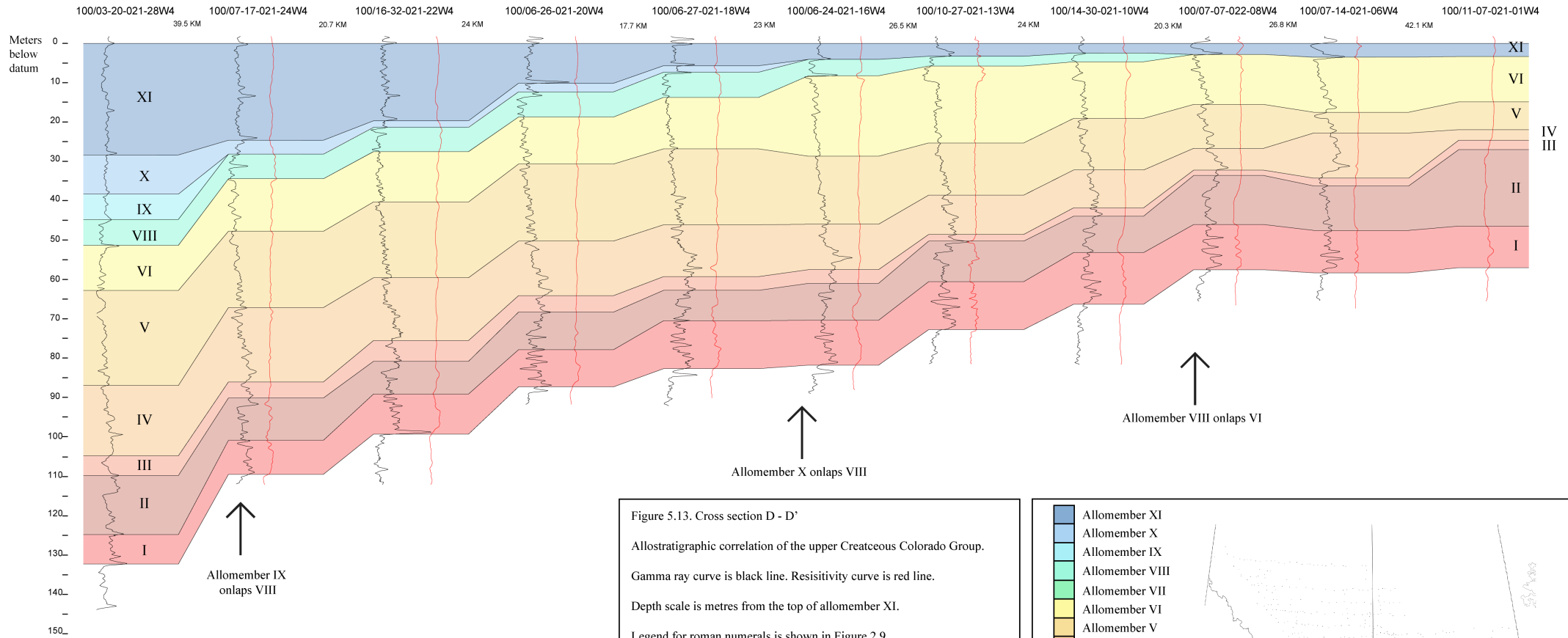


Figure 5.13. Cross section D - D'
 Allostratigraphic correlation of the upper Cretaceous Colorado Group.
 Gamma ray curve is black line. Resistivity curve is red line.
 Depth scale is metres from the top of allomember XI.
 Legend for roman numerals is shown in Figure 2.9.
 Truncation and onlap indicated at arrows.

	Allomember XI
	Allomember X
	Allomember IX
	Allomember VIII
	Allomember VII
	Allomember VI
	Allomember V
	Allomember IV
	Allomember III
	Allomember II
	Allomember I

Figure 5:13: Cross section D-D'.

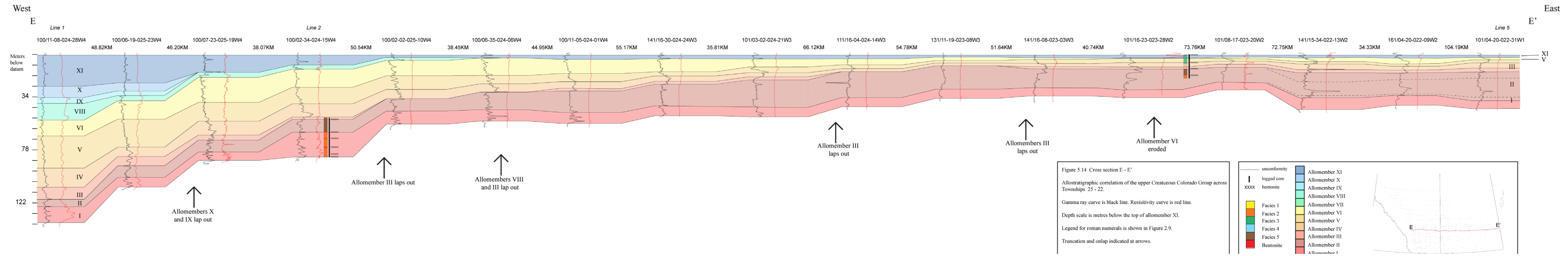


Figure 5:14: Cross section E-E'.

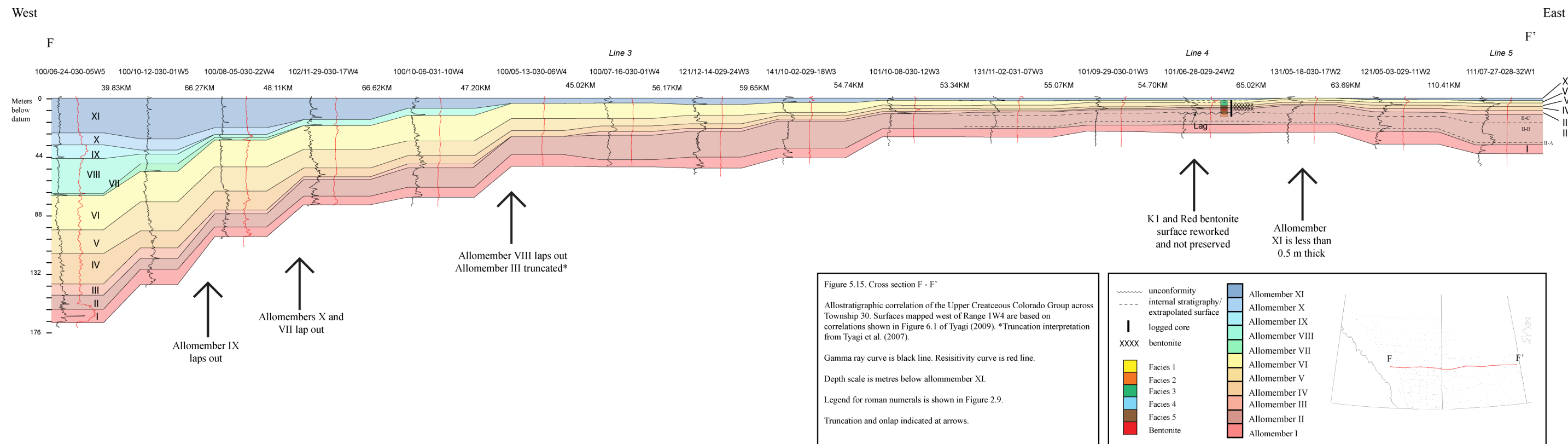


Figure 5:15: Cross section F-F'.

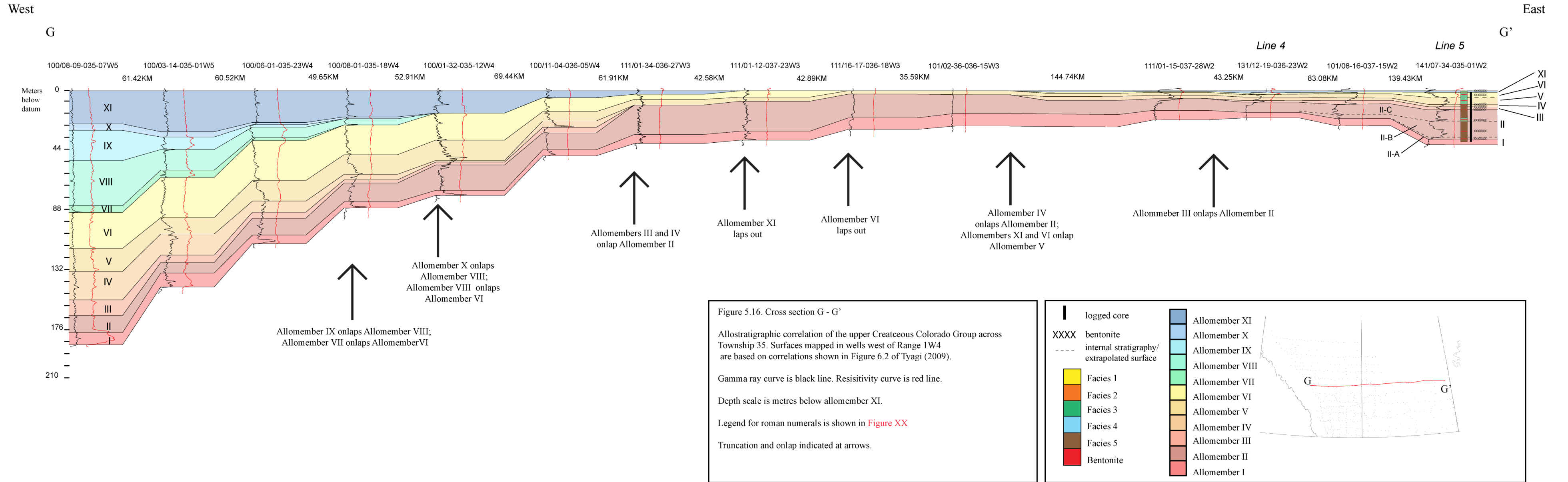


Figure 5:16: Cross section G-G'.

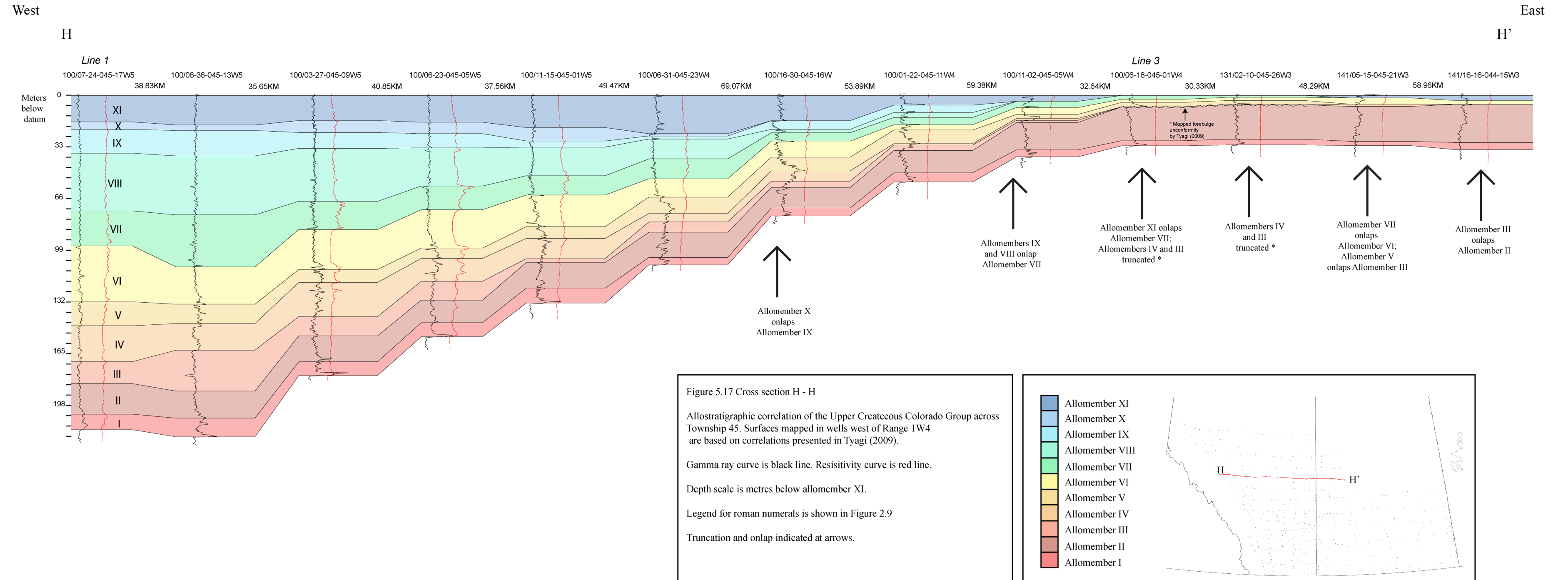


Figure 5:17: Cross section H-H'

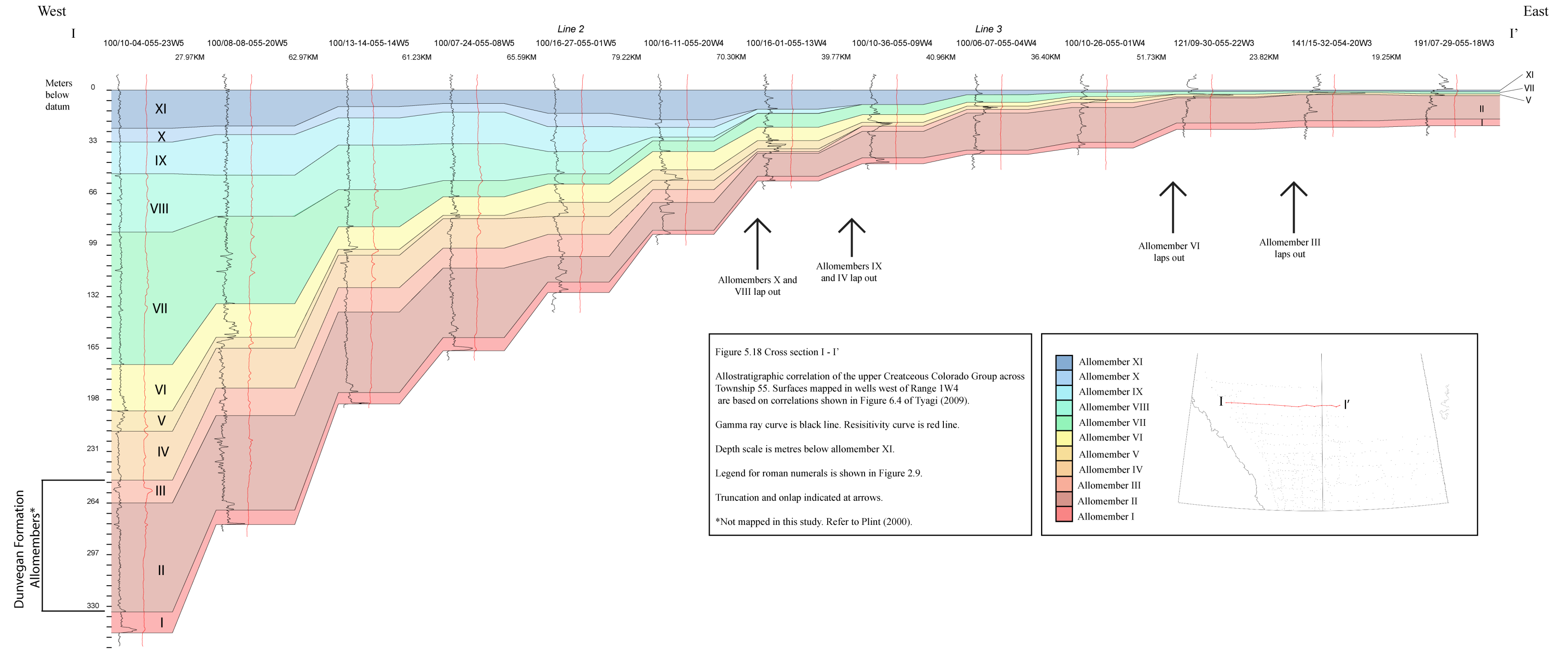


Figure 5:18: Cross section I – I'.

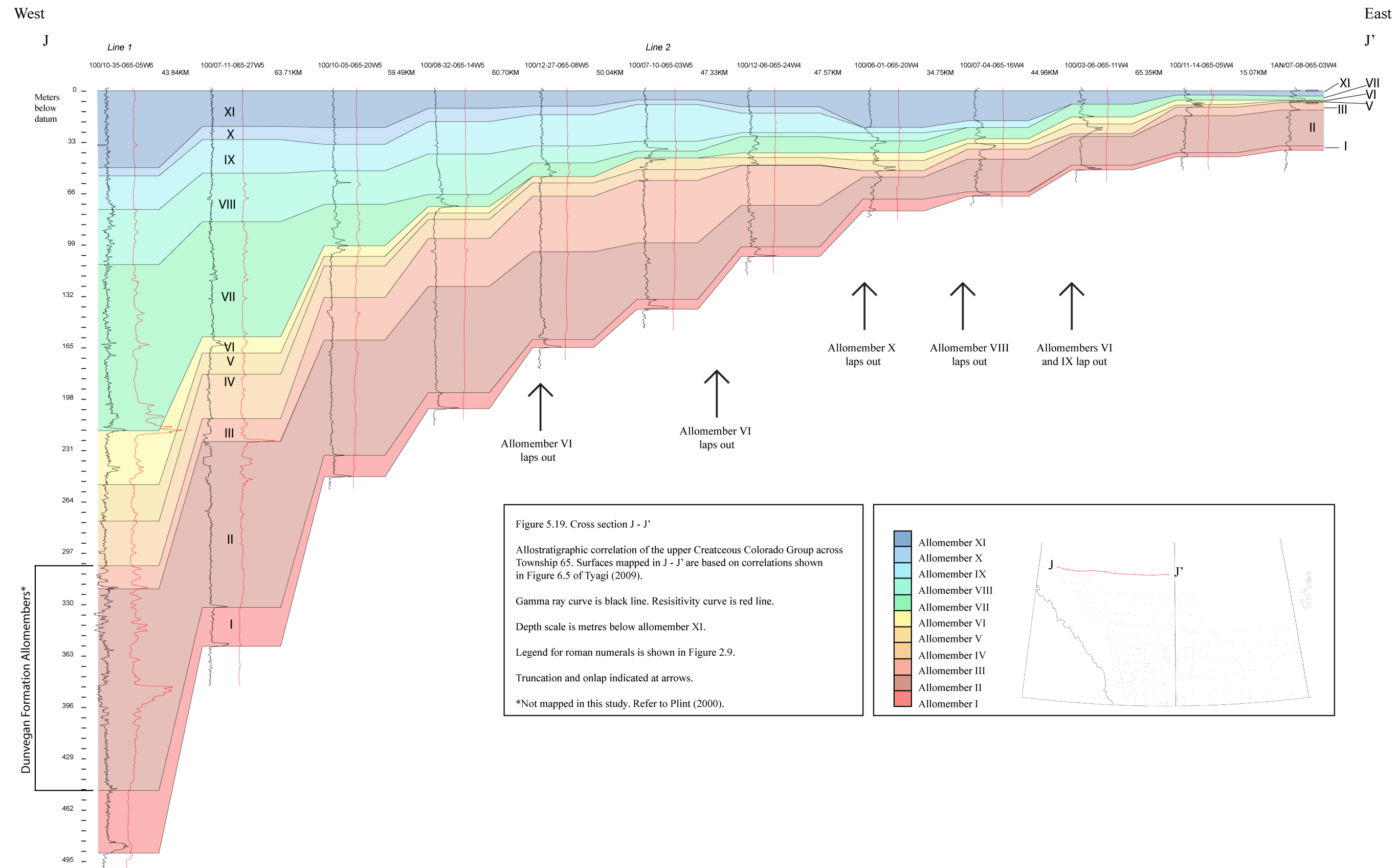


Figure 5:19: Cross section J-J'.

prominent south of Township 15, where the allomember thickens from 15 metres to over 40 metres. In Lines I and J (Figures 5.18 and 5.19), the wedge shape is thickest in the west (over 70 metres) and gradually thins towards the east. A slight thickening of allomember II occurs in Line J between ranges 09W4 and 01W4.

The informal internal stratigraphic packages (II-A, II-B, and II-C) correlated in Lines A and B (Figures 5.10 and 5.11) illustrate migrating depocentres within allomember II. Basal internal package II-A is bound by the underlying FSU and an overlying flooding surface. During the deposition of II-A, the basin deepened in southeastern Alberta and southeastern Saskatchewan. Internal package II-B was subsequently deposited when the locus of basin subsidence migrated to central and eastern Saskatchewan. The top of II-B is marked by a condensed interval (131/11-09-017-23W2) that correlates to a lag bed in core 101/06-28-029-24W2 (Lines 5 and F; Figures 5.9 and 5.15). Eastward thickening continued during deposition of the top internal package, II-C. Mapped internal stratigraphy for allomember II also demonstrates correct chronostratigraphic placement of the “hot” gamma-ray package above allomember I that emerges east of meridian W3 (Lines A, B, E, F, and G; Figures 5.10, 5.11, and 5.14 through 5.16). This interval was previously identified by Dionne et al. (2016) as marking the Fish Scales Formation, however the correlations presented in this study show it belongs with the overlying Belle Fourche Formation. Only one sample was collected by Dionne et al. (2016) at the base of their study interval and, based on the correlation completed in the current work, it is questionable whether samples below this point would also be barren of foraminifera.

5.2.2.3 Allomember III

Allomember III forms a sheet-like package south of Township 20 (Lines A through E; Figures 5.10 to 5.14), with localized thickening and thinning from west to east. In Line A, allomember III thickens from eight metres in southwestern Alberta to 10 metres in southwestern Saskatchewan and thins gradually to five metres in eastern Saskatchewan. North of Township 20 (Lines G through J; Figures 5.16 to 5.19), the allomember becomes wedge-shaped and thins to the east. Allomember III onlaps the underlying allomember II in Lines G to J, with zero thicknesses coinciding with the mapped

forebulge unconformity of Tyagi (2009). Line H gradually thins to the east until range 17W2, beyond which the allomember thickens to approximately 3 metres. Allomember II has zero thickness along lines E through I (Figures 5.14 to 5.18).

5.2.2.4 Allomember IV

In the southern portion of the study area, allomember IV is sheet-like, with isolated segments of thickening between ranges 29W3 and 22W3. North of township five, overall allomember geometry shifts to a wedge that thins to the east (Lines A through J; Figures 5.10 to 5.19). Line E thins to the east until range 20W2, then thickens towards the eastern limit of the study area. Line G (Figure 5.16) reaches zero thickness between ranges 27W3 and 15W3, and then reemerges and maintains a thickness of approximately 3 metres until the Manitoba boundary.

5.2.2.5 Allomember V

Like allomember IV, the geometry of the allomember V package is sheet-like in Line B, along the southern boundary of the study area, with a steady thickness of 15 to 20 metres until 22W3, then maintains a nearly 3 metre thickness to the east. Lines B through F, and Lines I and J, illustrate wedge-shaped geometry that gradually thins to the east. Allomember V becomes sheet-like east of 08W3, 12W3, and 23W3 in Lines E, F, and G (Figures 5.14 to 5.16), respectively. By township 45, the allomember is sheet-like from western Alberta to western Saskatchewan, then to the north the package transitions back to wedge-shaped (Lines I and J; Figures 5.18 and 5.19).

5.2.2.6 Allomember VI

Allomember VI forms a wedge-shaped package that thins to the east but shows localized thickening in some places. Lines A and B (Figures 5.10 and 5.11) show thickening between ranges 04W4 and 22W3, and 11W4 and 01W4, respectively. Allomember VI thickness thins to zero in Line E between ranges 03W3 and 27W2, where it is truncated by an uplifted underlying allomember V, and between 19W3 and 8W3 in Line G. In township 65 (Line J; Figure 5.19), the package thins to zero thickness between 13W5 and 26W4 (zero thickness boundary is based on the isopach map in Figure 5.27 because not all wells were included in the summary cross-section figure).

5.2.2.7 Allomember VII

Allomember VII is only present in cross-sections north of township 25. It is mainly wedge-shaped, thinning gradually to the east. In Line H, allomember VII onlaps onto the underlying VI by range 21W3. Allomember VII has a sheet-like geometry in Line F because it captures the eastward limit of the allomember.

5.2.2.8 Allomember VIII, IX, and X

The geometries exhibited by allomembers VIII, IX and X are wedge-shaped and thin progressively to the east to zero thickness. Allomember VIII is mapped in Lines A through J (Figure 5.10 to 5.19), with the greatest thickness of 35 metres occurring in the western limit of Line G. The wedge-shaped package of allomember IX occurs in Lines E through J and thins to the east from 20 metres to zero thickness. Allomember X abruptly thins to the east in Lines A, B, E, and F, and has sheet-like geometry with gradual thinning in Lines C, D, and G through J. Allomember thickness along township 45 (Line H) illustrates thinning and thickening to the east, until eventual onlap onto allomember IX.

5.2.2.9 Allomember XI

Allomember XI displays both wedge and sheet-like geometries along the depositional dip. Most cross-sections wedge shaped geometry in the west that gradually thin to the east and become sheet-like (Lines B through G, and H to I: Figures 5.11 to 5.16 and 5.17 to 5.18). Lines A, E, and J show local variations in thickness. An overall eastward thinning trend in Line J changes to an abrupt thickening between ranges 24W4 and 11W4, then thins towards western Alberta.

5.3 Precambrian basement structures in the Western Canada Sedimentary Basin

It is important to recognize Precambrian basement structures and associated lineaments when investigating regional stratigraphy because their presence can have a significant impact on sedimentation in the Western Canada Foreland Basin (e.g., Ridgley et al., 2001; Christopher et al., 2006; Plint and Wadsworth, 2006; Schultz et al., 2019). The

Precambrian basement underlying the WCSB is composed of accreted terranes with varying rheologies (Kreis et al., 2000, 2004; Catuneanu, 2004). Boundaries between these terranes, or basement domains, can produce preferential flexural hingelines between the foredeep, forebulge and backbulge components (Catuneanu, 2004). Strength variations in foreland basin lithosphere, whereby local weak zones in the foreland basin influence the position of a flexure forebulge when responding to bending, causes increased sensitivity to tectonic loading between the basement domains (Waschbusch and Royden, 1992). Basement block reactivation by foreland system tectonism and the resulting differential subsidence is used to explain paleogeographic trends and lithofacies thickness and distribution patterns that appeared to correspond to boundaries between basement terranes (i.e., Hart and Plint, 1993; Plint et al. 1993; Pang and Nummedal, 1995; Christopher et al., 2006).

The study area for this work extends across two sedimentary basins (the Alberta Basin and the Williston Basin), three positive relief structures (Bow Island Arch, Punnichy Arch, and Swift Current Platform), and 12 tectonic domains (Ksituan, Chinchaga, Vulcan Low, Medicine Hat Block, Eyehill high, Matzhiwin High, Trans-Hudson Orogen, Wabamun, Thorsby, Lacombe, Hearne, and Wollaston) that are potentially relevant to Upper Colorado Group sedimentation during the Late Cretaceous (Fig. 5.20). Although additional basement structures are present in the WCFB (i.e., Wright et al., 1994), this study focuses on features relevant to Late Cretaceous sedimentation.

The study area encompasses two sedimentary basins: the Western Canada Foreland Basin (WCFB; refer to Chapter 2) and the Williston Basin. The Williston Basin is an intracratonic basin that is centred in North Dakota, with the northern limit extending into southeastern Saskatchewan (Kent and Christopher, 1994). The two basins were intermittently separated by topographic highs resulting from the up and down movement of the Bow Island Arch and the Swift Current Platform, first in the late Paleozoic and again in the Mesozoic and Cenozoic (Podruski, 1988; Wright et al, 1994). The Swift Current Platform is an eastern extension of the Sweetgrass Arch structural complex of northwestern Montana, southeastern Alberta, and southwestern Saskatchewan (Kent and Christopher, 1994). The Punnichy Arch is an east-southeast trending monoclinial flexure

that trends south towards the Williston Basin and forms the northern solution limit of the Prairie Evaporite salt beds in eastern Saskatchewan (Kent and Christopher, 1994). In Early Cretaceous, the Punnichy Arch was uplifted in response to a downwarp of the Swift Current Platform, causing severe truncation of overlying Cretaceous-aged Mannville strata (Kent and Christopher, 1994). The domains illustrated in Fig. 5.20 are the locations of Precambrian crustal blocks that have been joined by suture zones (Ross et al., 1994). The domains are considered potential weak crustal zones where flexural stresses triggered from loading along the fold and thrust belt caused differential subsidence in the WCFB (e.g., Waschbusch and Royden, 1992; Zaitlin et al., 2002; Plint and Wadsworth, 2006).

Illustrated basement domains and lineaments sourced from previously interpreted filtered potential-field aeromagnetic and Bouguer gravity maps for Alberta and Saskatchewan (Ross et al., 1991; Ross et al., 1994; Kreis et al., 2004; Lyatsky et al., 2005) are used to evaluate the role played by Precambrian basement structures on subsidence and sedimentation patterns of the study interval. Aeromagnetic surveys measure changes in magnetic rock properties. This type of geophysical survey is useful for mapping regional basement domains in the Western Canada Sedimentary Basin because the overlying sedimentary rock volume is mainly non-magnetic and lacks significant density contrasts, implying observed anomalies reflect heterogeneities in the underlying crystalline basement (Lyatsky et al., 2005). Localized anomalies linked to sedimentary sources could be related to concentrated deposits of magnetic minerals or to circulating brines that caused secondary magnetization in sedimentary rocks (Lyatsky, et al., 2005). Bouguer gravity data measures changes in rock density and is considered to reasonably represent rock density variations in the crust and asthenosphere (Lyatsky et al., 2005). Rocks with high density provide high gravity values, and lower gravity data corresponds to rock that are less dense (USGS, 1997). Gravity data can be useful to identify high-angle faults through the juxtaposition of rock with different densities, however, subtle gravity signatures of basement faults can be obscured by high density sedimentary rocks immediately overlying the Precambrian (Lyatsky et al., 2005).

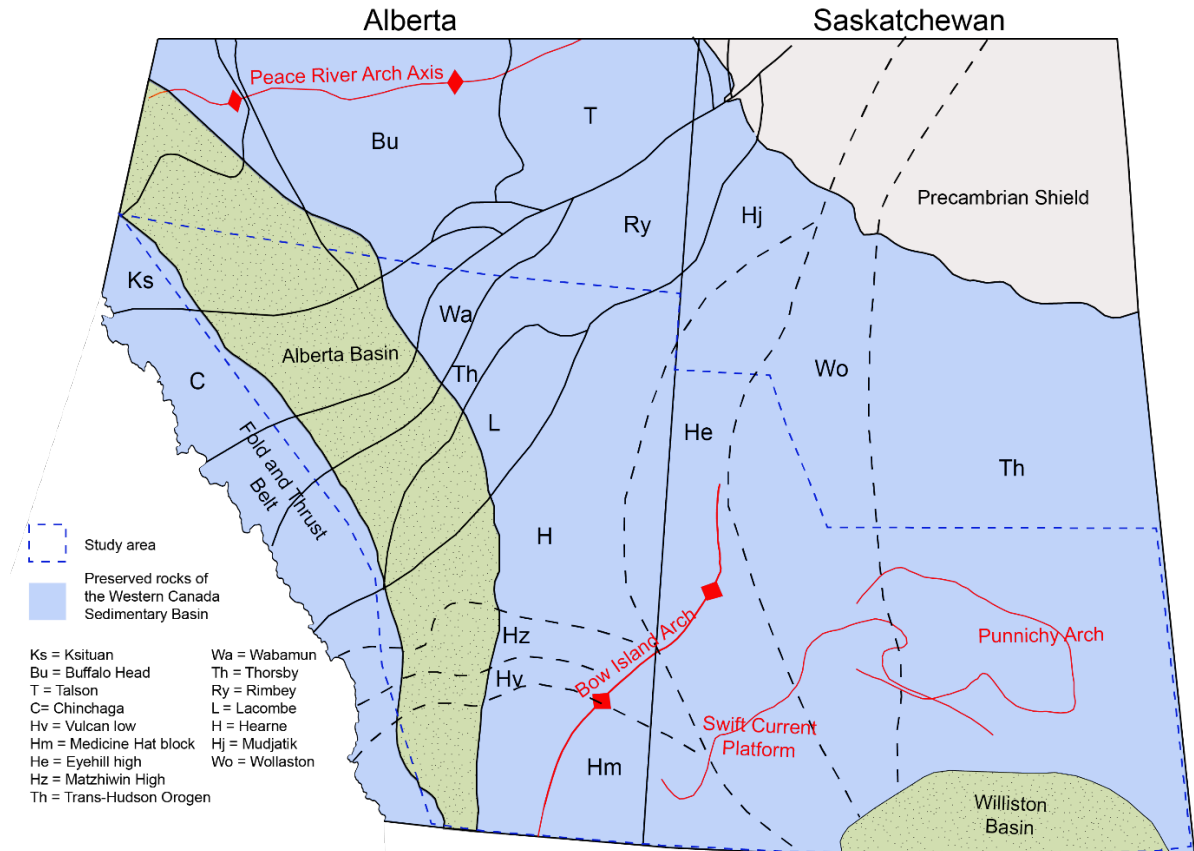


Figure 5:20: Structural element map for the WCSB. Elements outlined in red reflect positive structural relief elements. Black lines and dashed lines outline tectonic domains underlying the WCSB. Modified from Wright et al. (1994) and Ross et al. (1994).

Lyatski et al. (2005) published a series of gravity and magnetic maps that identify subtle gravity and magnetic lineaments in Alberta that could be related to brittle basement faults. Lineament picks from Lyatski et al. (2005) were interpreted from enhanced local, low-amplitude and short-wavelength anomalies. This study overlays the magnetic map with automatic amplitude gain (local AGC) Map 25 (Figure 5.21) of the published series by Lyatski et al. (2005) that provides a sharpened appearance for anomaly trends and subtle breaks used to identify the lineaments. Sheet 1 from Kreis et al. (2004) was used as an overlay to identify basement domains in Saskatchewan.

5.3.1 Subsidence patterns and Precambrian basement influence

5.3.1.1 Allomember I

The basin-wide isopach map created in this study for allomember I (Figure 5.22A) reveals a major depocentre in northwestern Alberta and northeastern British Columbia and localized depositional anomalies in southern Alberta and southern Saskatchewan. It is postulated here that the northwest-southeast trending depocentre in southern Alberta, and an adjacent thinning to the southwest (townships 1 to 5, range 20 to 24W4), resulted from preferential movement along basement structures. The thickening pattern in southern Alberta trends parallel to northwest-southeast lineaments identified in Lyatski et al. (2005) (Figure 5.22B). The limit of this depocentre appears to correlate with the boundary between the Vulcan low (Hy) and the Medicine Hat (Hm) blocks, indicating reduced subsidence northwest of these features. Shank (2012) noted that differential subsidence and thickening of allomembers within the Cardium Formation was influenced by the Vulcan low and a possible flexural hinge line termed the Lochend hinge zone (red dashed line, Figure 5.22B). The Allomember I thickening pattern runs nearly parallel to the hinge zone and thins east of the northwest-southeast trending lineament, suggesting that these features influenced subsidence and uplift in response to tectonic loading. This interpretation is supported further by the thinning of allomember I west of northwest-southeast trending faults mapped in Shank (2012) (blue lines, Figure 5.22B) and the thickening to the east between lineaments. Evidence for basement influence continues into southwestern Saskatchewan with eastward limit of the southern Alberta depocentre

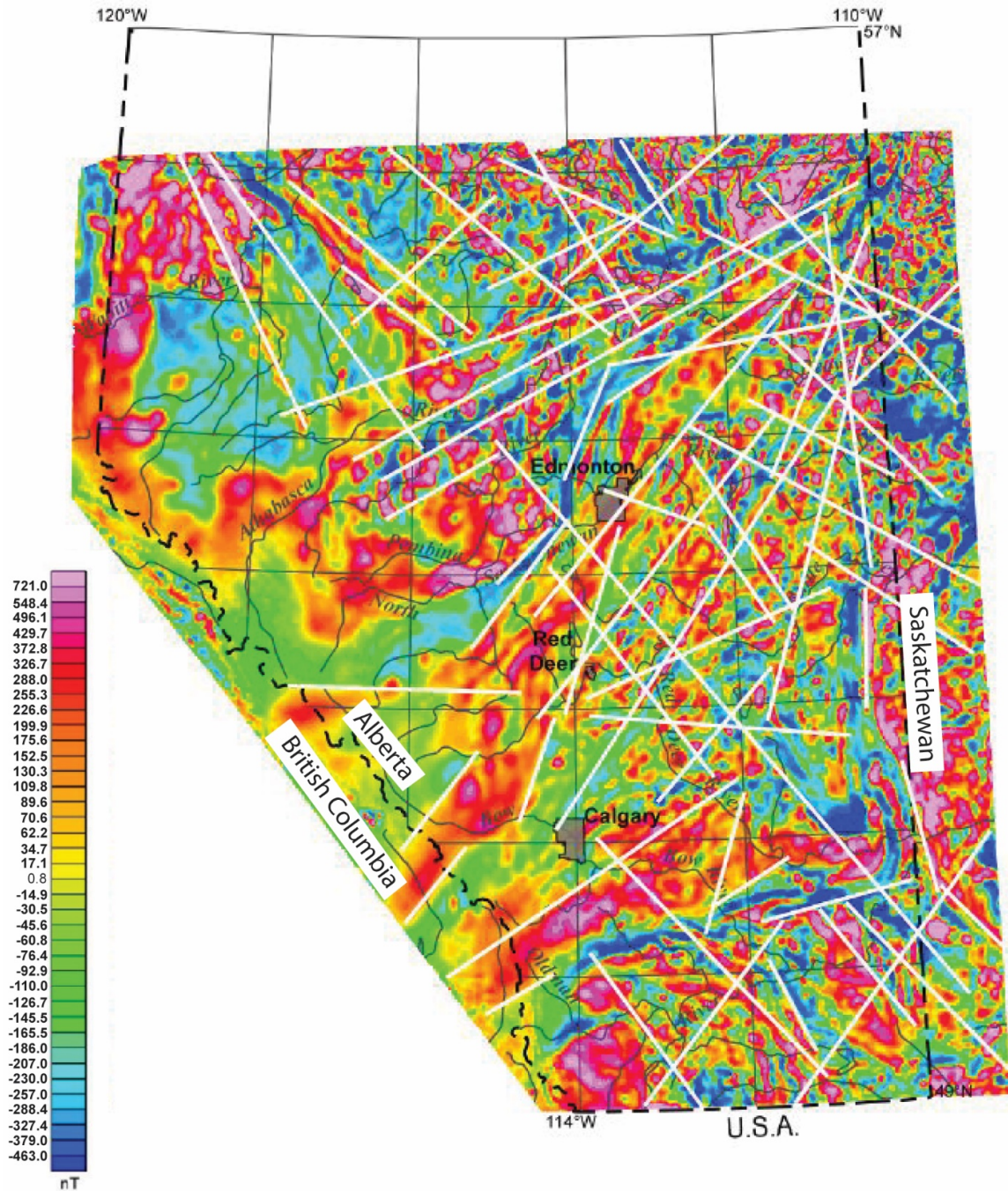


Figure 5:21: Processed magnetic map (Map 25) developed from potential-field geophysical data (Map modified from Lyatski et al. (2005)).

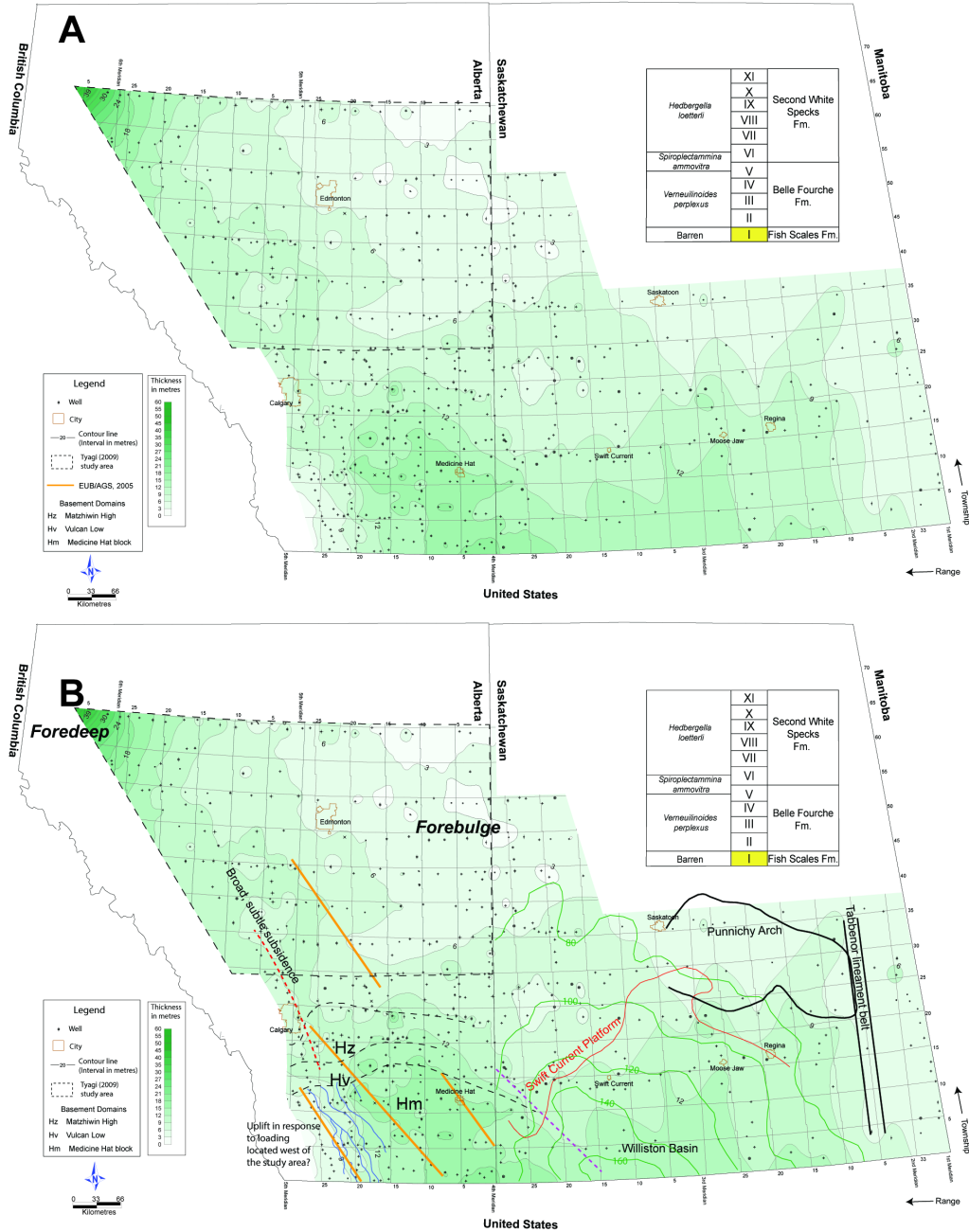


Figure 5:22: (A) Isopach map of allomember I. (B) Isopach map with structural features overlay. Lineaments mapped from Lyatski et al. (2005) = solid orange lines. Basement domains (black dashed lines) are from Ross et al. (1994). Lochend hinge zone = red dashed line. Mapped faults from Shank (2012) = blue lines. Eastend-Maple Creek lineament = purple dashed line. Base of Fish Scales to Viking Formation thickness = green lines; contours interval is 20 metres. Locations of the Punnichy Arch and Tabbenor lineament belt are from Christopher et al. (2006).

aligning with the Eastend-Maple Creek lineament (purple dashed line) (Christopher, 2003). The northwest-southeast trending lineaments and overall thickening of allomember I in this region could reflect flexural response to contemporaneous tectonic loading to the southwest of the study area as the Laramide orogen encroached onto the Sweetgrass Arch from the west (Kent and Christopher, 1994).

Increased allomember I thickness trends in southern Saskatchewan mirror the generalized thickness trends of the Base of Fish Scales to Viking Formation interval from Leckie et al. (1994) (solid green contours; Figure 5.22B). Kent and Christopher (1994) noted that during the Early Cretaceous, tectonic relaxation led to subsidence of the Swift Current and Central Montana Platforms and shifting of the Williston Basin depocentre to southwestern Saskatchewan and adjacent Montana. Thickness trends from allomember I and the mapped interval by Leckie et al. (1994) could be evidence of this past shift before the basin centre was restored to a position in western North Dakota during the Laramide orogeny (Kent and Christopher, 1994). In central Saskatchewan, allomember I thins over the Punnichy Arch which was up-lifted in response to downwarping of the Williston Basin (Christopher et al., 2006). North-south-aligned thinning of allomember I may be related to tectonic movements along the Precambrian Tabbenor lineament belt (Christopher et al., 2006).

5.3.1.2 Allomember II

The isopach map for allomember II shows prominent thickening in northwestern Alberta been favored by preferential movement along these features (Figure 5.23B). The general north-south thickening along the Alberta-Saskatchewan border overlies the Eyehill magnetic high domain. Uplift of the forebulge caused a downwarp to the east that produced a backbulge depozone preferentially oriented to basement with a wedge-shaped geometry that transitions to a broad sheet in central and southern Alberta (Figure 5.23A). Allomember thinning in Alberta aligns with the Wabamun tectonic domain and basement lineaments, suggesting the forebulge position may have lineaments and the Eyehill magnetic high basement domain. A thickening trend in southeastern Saskatchewan, towards the Williston Basin coincided with a reciprocal uplift of the Punnichy Arch in central Saskatchewan and thinning of allomember II (Christopher and Yurkowski, 2005);

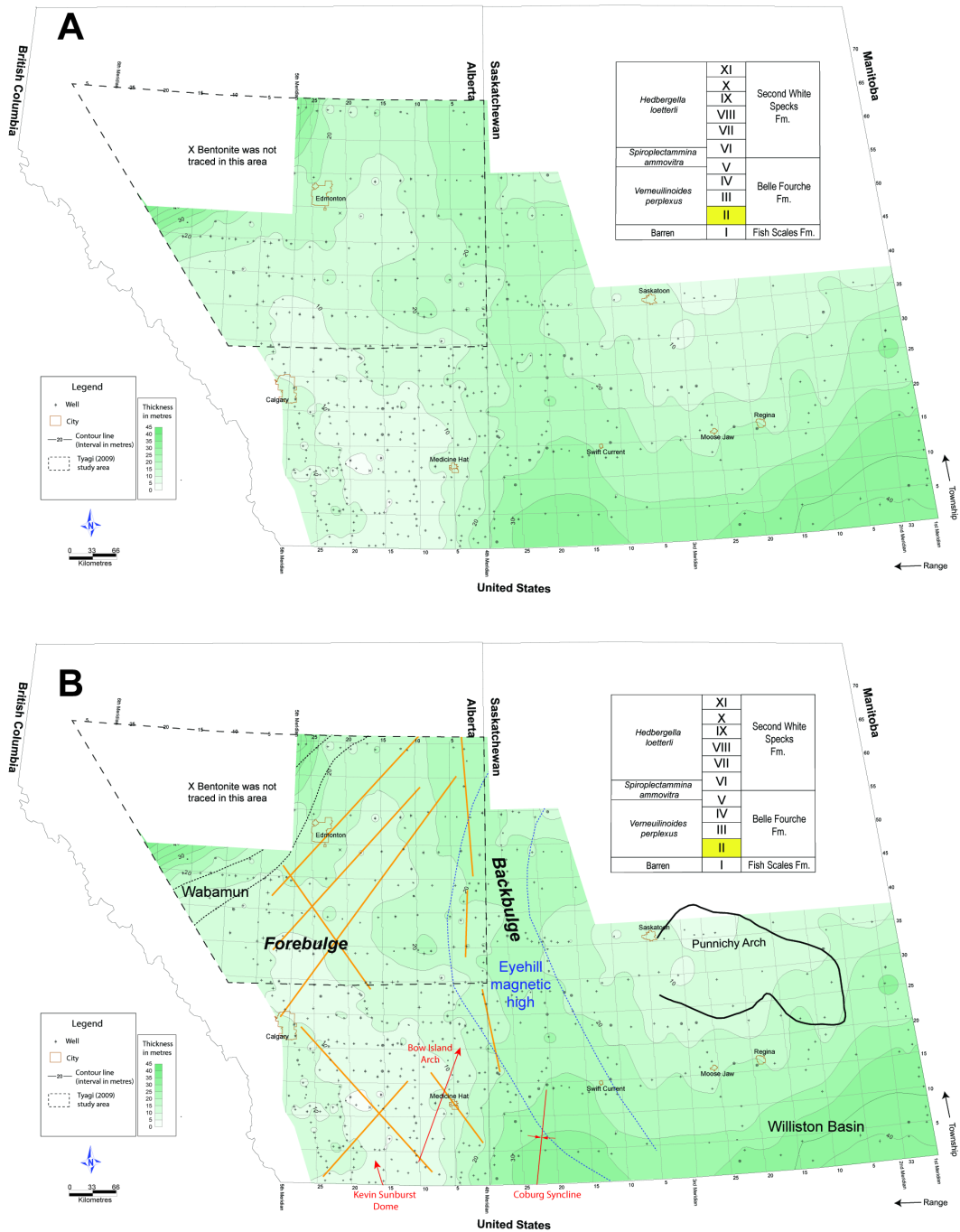


Figure 5:23: (A) Isopach map of allomember II. (B) Isopach map with structural features overlay. Lineaments (Lyatski et al. 2005) = solid orange lines. Basement domains (Ross et al., 1994) = black and blue dashed lines. Kevin Sunburst Dome and Bow Island Arch from Wright et al. (1994). Coburg Syncline from Frank (2006). Punnichy Arch and Tabbenor lineament belt are from Christopher et al. (2006).

Christopher et al., 2006). In southwestern Saskatchewan, allomember II thickens over the Coburg Syncline, a basement feature that underwent episodic subsidence during the Upper Cretaceous (McLean, 1971; Frank, 2006).

5.3.1.3 Allomember III

Deposition of the Dunvegan Formation (section 2.4.3.2) in response to loading in the west is supported in Figure 5.24A by the fact that the thickest deposit occurs in northwest Alberta (Figure 5.24A). The uplift inferred to have occurred in eastern Alberta and west-central Saskatchewan in response to the active loading occurring northwest of the study area marks the position of the forebulge during this time, during which the Belle Fourche Formation must have been eroded in the region. A backbulge is not obvious on the map but may be reflected in the slight thickening of allomember III in central Saskatchewan. The north-south thickening trend of allomember III in southwestern Saskatchewan suggests an actively subsiding Coburg Syncline, and vertical movement along the Tabbenor lineament belt could have caused the abrupt north-south trending thickness changes in eastern Saskatchewan (Figure 5.24B).

5.3.1.4 Allomember IV

By allomember IV time (late Cenomanian), the depocentre shifted dramatically to follow a northwest-southeast trend running parallel to basement lineaments (Figure 5.25). A slight thinning of the allomember is noted in the southwest corner of Alberta, which may be related to movement of an unspecified basement feature in response to loading in the west (as noted in allomember I). A prominent forebulge is observed where the strata have been eroded.

5.3.1.5 Allomember V

The broad, northwest-southeast subsidence pattern in western Alberta that runs parallel to the strike of the Thrust Belt and the mapped basement lineaments continued during allomember V time but shifted its trajectory more to the east in southern Alberta (5.26). The deepest part of the depocentre lies between townships 20 and 25, at the 5th meridian boundary. A region of thinning occurring between the Chinchaga (C), Ksituan (Ks), and

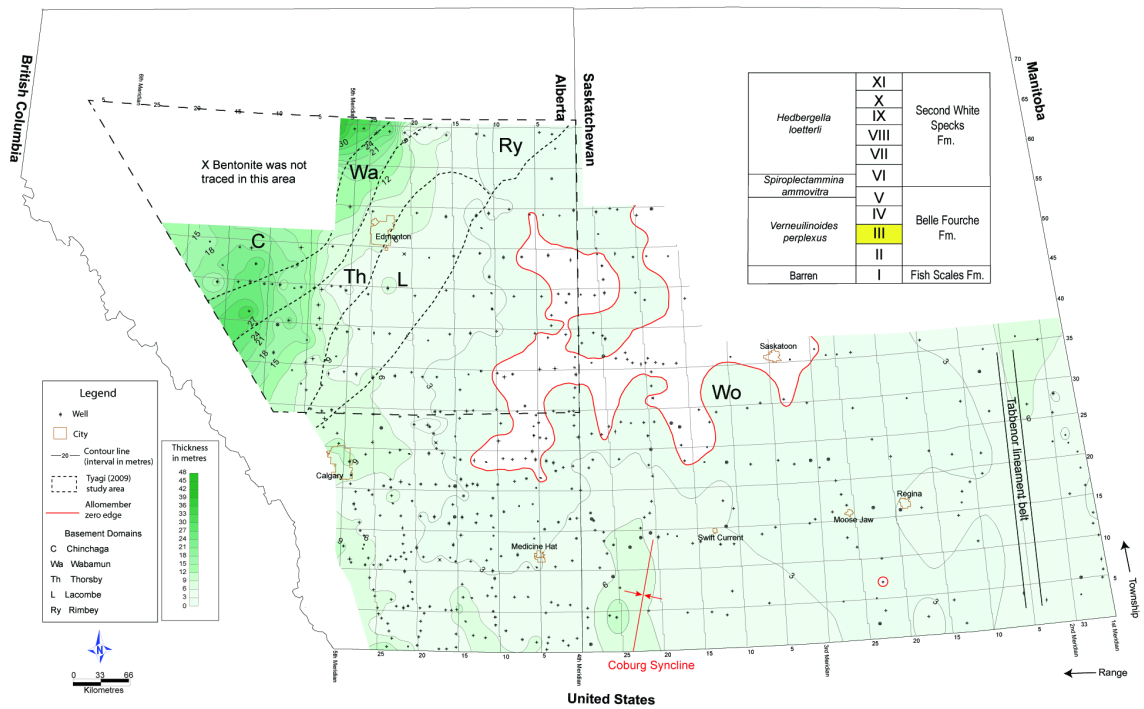
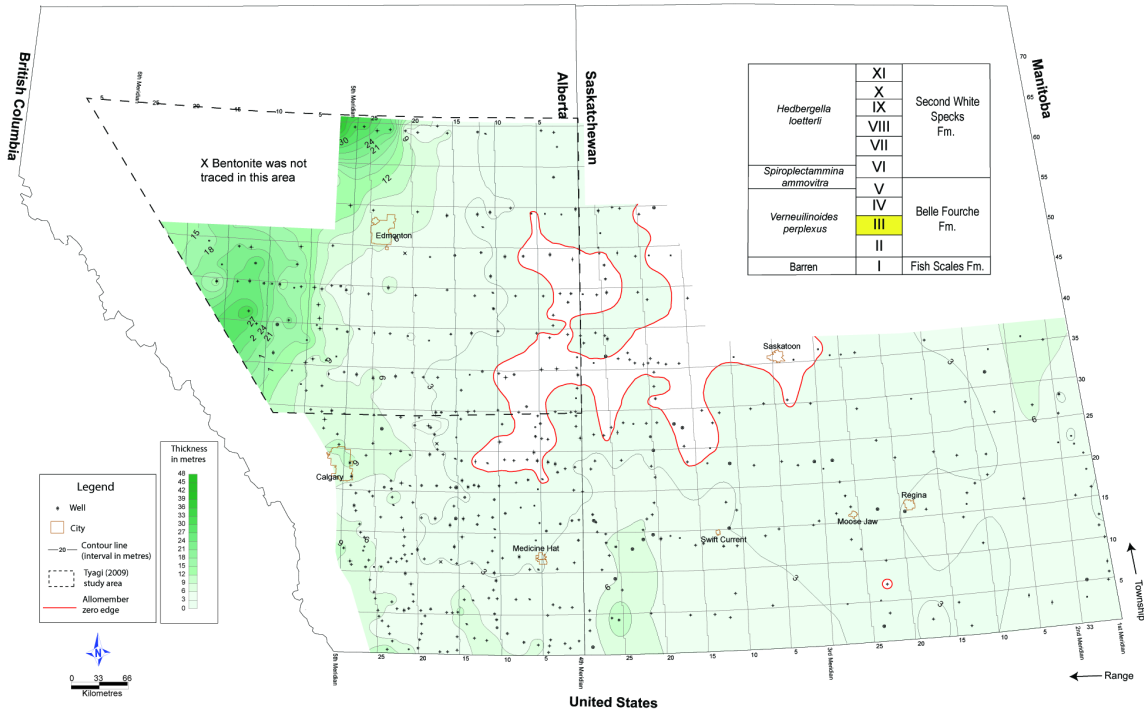


Figure 5:24: (A) Isopach map of allomember III. (B) Isopach map with structural features overlay. Basement domains (Ross et al., 1994) = black dashed lines.

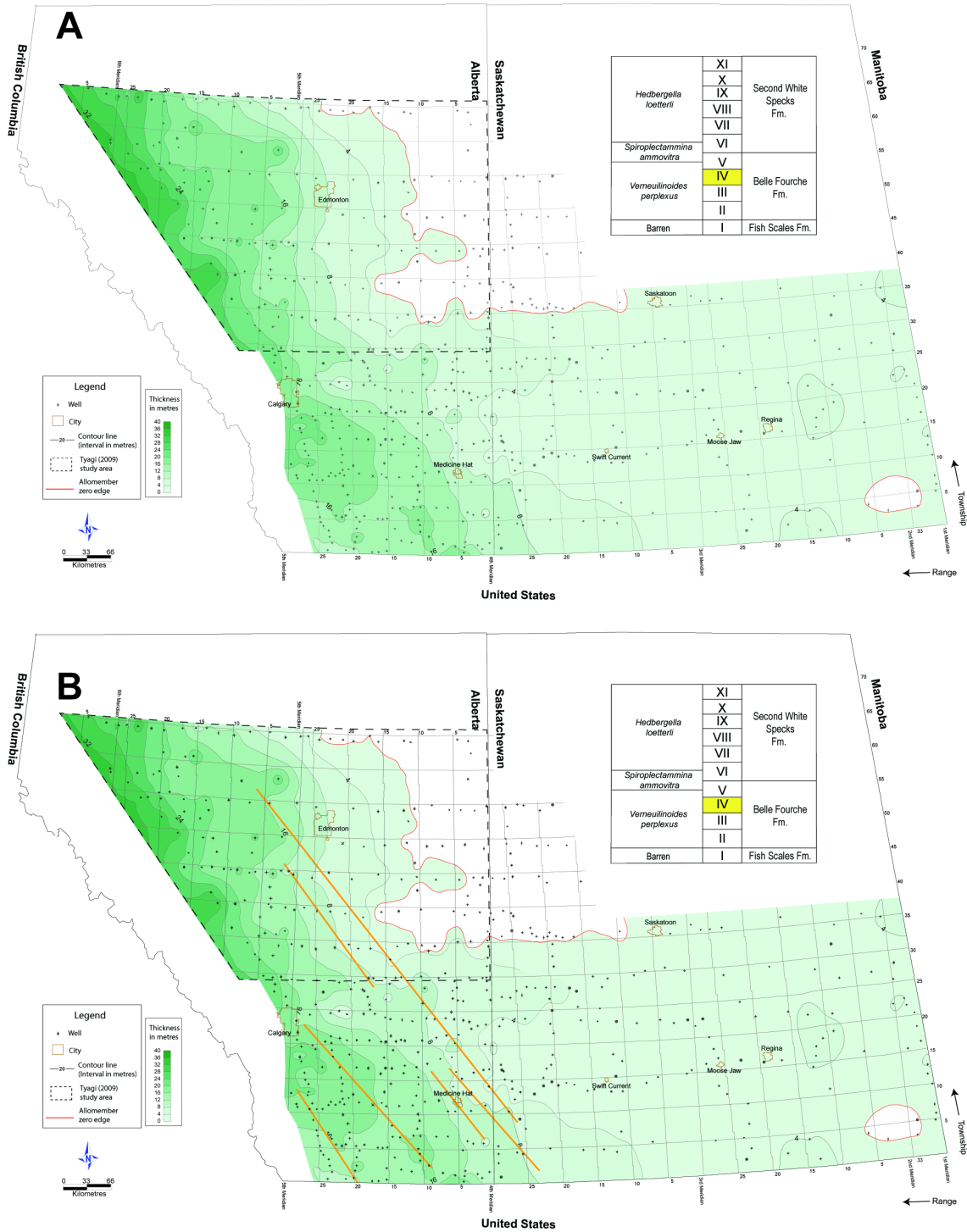


Figure 5:25: (A) Isopach map of allomember IV. (B) Isopach map with structural features overlay. Lineaments (Lyatski et al. 2005) = solid orange lines.

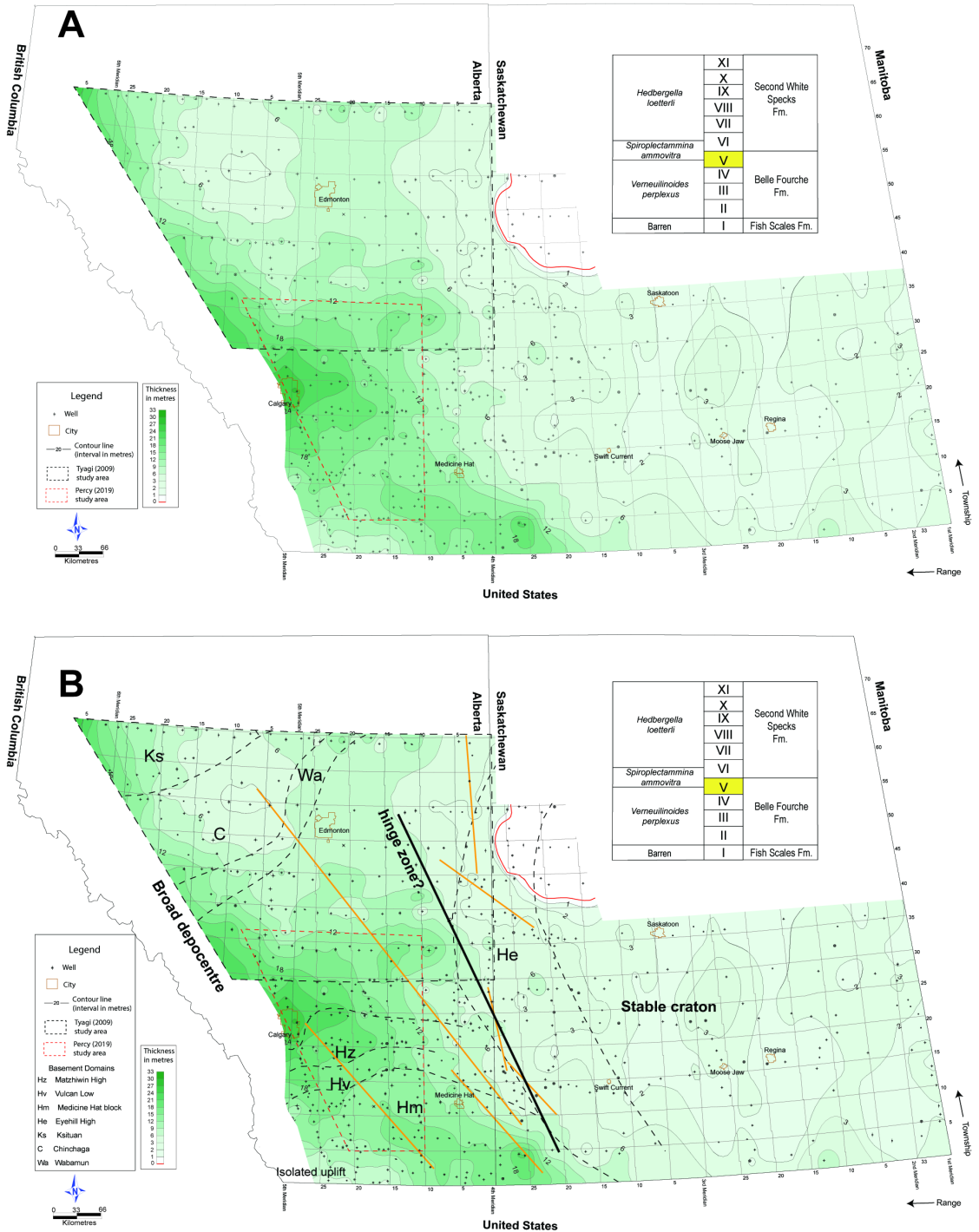


Figure 5:26: (A) Isopach map of allomember V. (B) Isopach map with structural features overlay. Basement domains (Ross et al., 1994) = black dashed lines. Lineaments (Lyatski et al. 2005) = solid orange lines.

Wabamun (W) basement domains in northwestern Alberta could reflect differential subsidence that occurred in response to tectonic loading to the west, whereby the domains underwent uplift, a slow rate of subsidence, or did not subside at all (Tyagi, 2009). Isolated thinning in the southwest corner of Alberta suggests that the adjacent, northwest-southeast thickening pattern may reflect a backbulge instead of a foredeep depozone and the thin deposit of allomember V to the east into Saskatchewan defines the stable craton. This potential backbulge depozone could extend northward, between range 1W5 and 10W4 (six metre contour), indicating the thinning above the Chinchaga domain represents a forebulge region that became uplifted in response to a tectonic load west of the study area. However, this explanation is speculative at best because of limited well control in southwest Alberta and not knowing if subsidence was influenced by movement along the Bow Island Arch.

5.3.1.6 Allomember VI

Allomember VI is sheet-like across the basin, showing progressive lapout on to the forebulge unconformity in northeastern Alberta (Tyagi, 2009) and evidence of localized erosion in west-central Saskatchewan (Figures 5.27). The northwest-southeast subsidence pattern alignment with basement lineaments in Alberta becomes more prominent in allomember VI compared to allomember V (Figure 5.27B).

5.3.1.7 Allomember VII

Allomember VII exhibits a strongly wedge-shaped geometry in northwestern Alberta that becomes more sheet-like to the east. This corresponds to tectonic loading creating an arcuate depocentre in the west and progressive lapout onto the forebulge region (Tyagi, 2009) (Figure 5.28).

5.3.1.8 Allomember VIII

Tectonic loading along the strike of the deformation front produced a broad, arcuate depocentre in west-central to northwestern Alberta (Figure 5.29), possibly enhancing uplift to the east and producing a forebulge (Tyagi, 2009). The wedge-shape geometry of allomember VIII is pronounced in west-central Alberta, but becomes more subtle in the

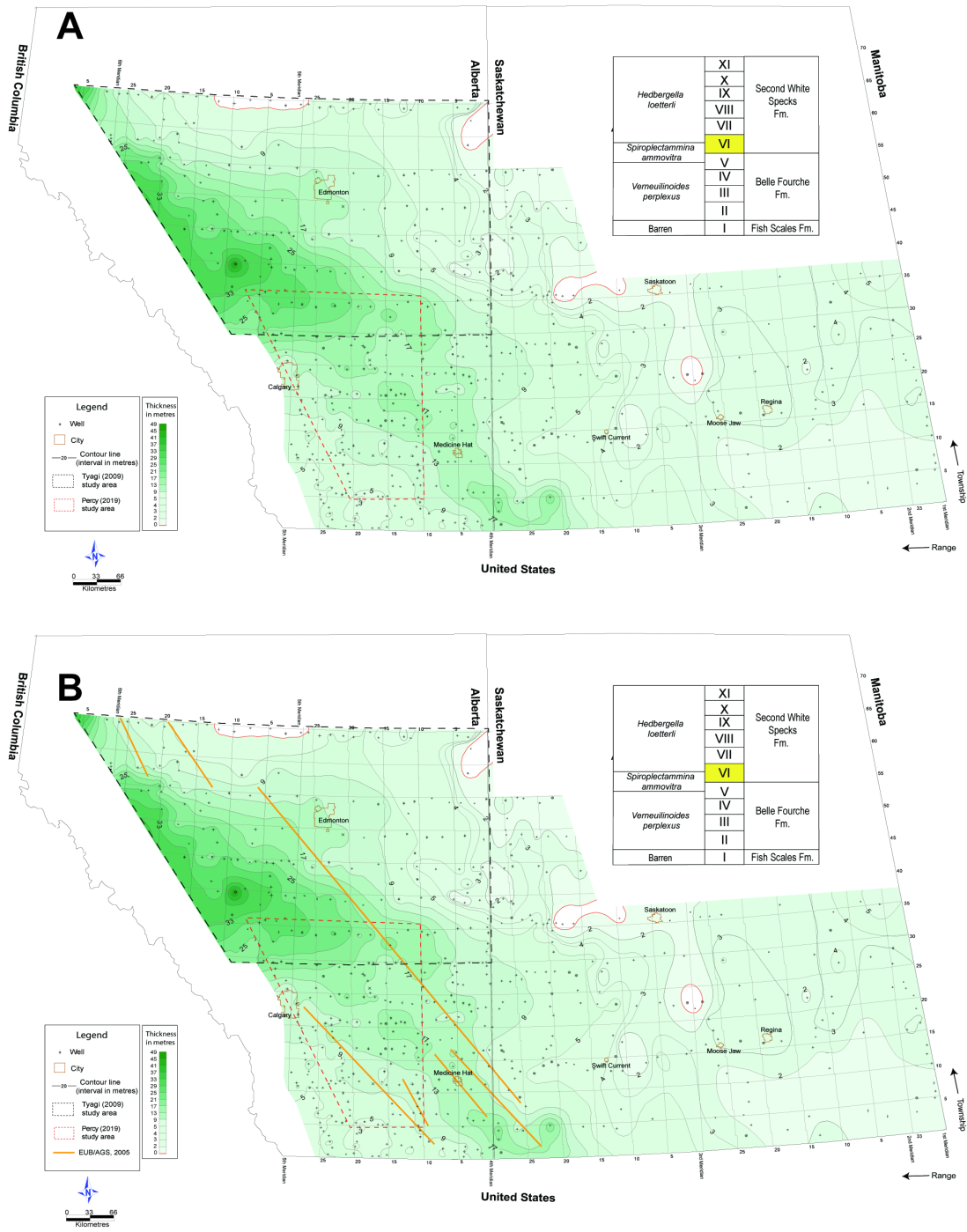


Figure 5:27: (A) Isopach map of allomember VI. (B) Isopach map with structural features overlay. Lineaments (Lyatski et al. 2005) = solid orange lines.

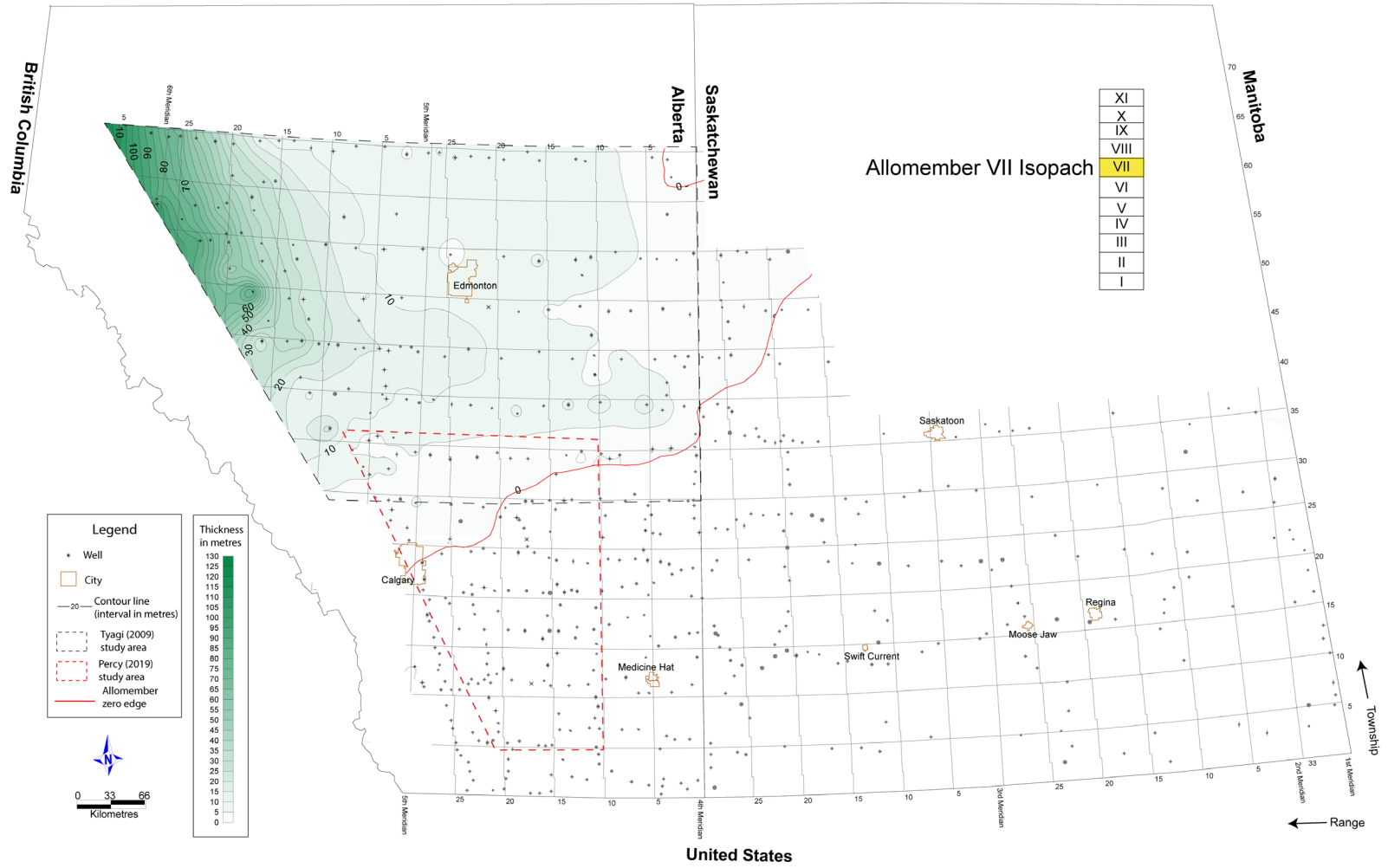
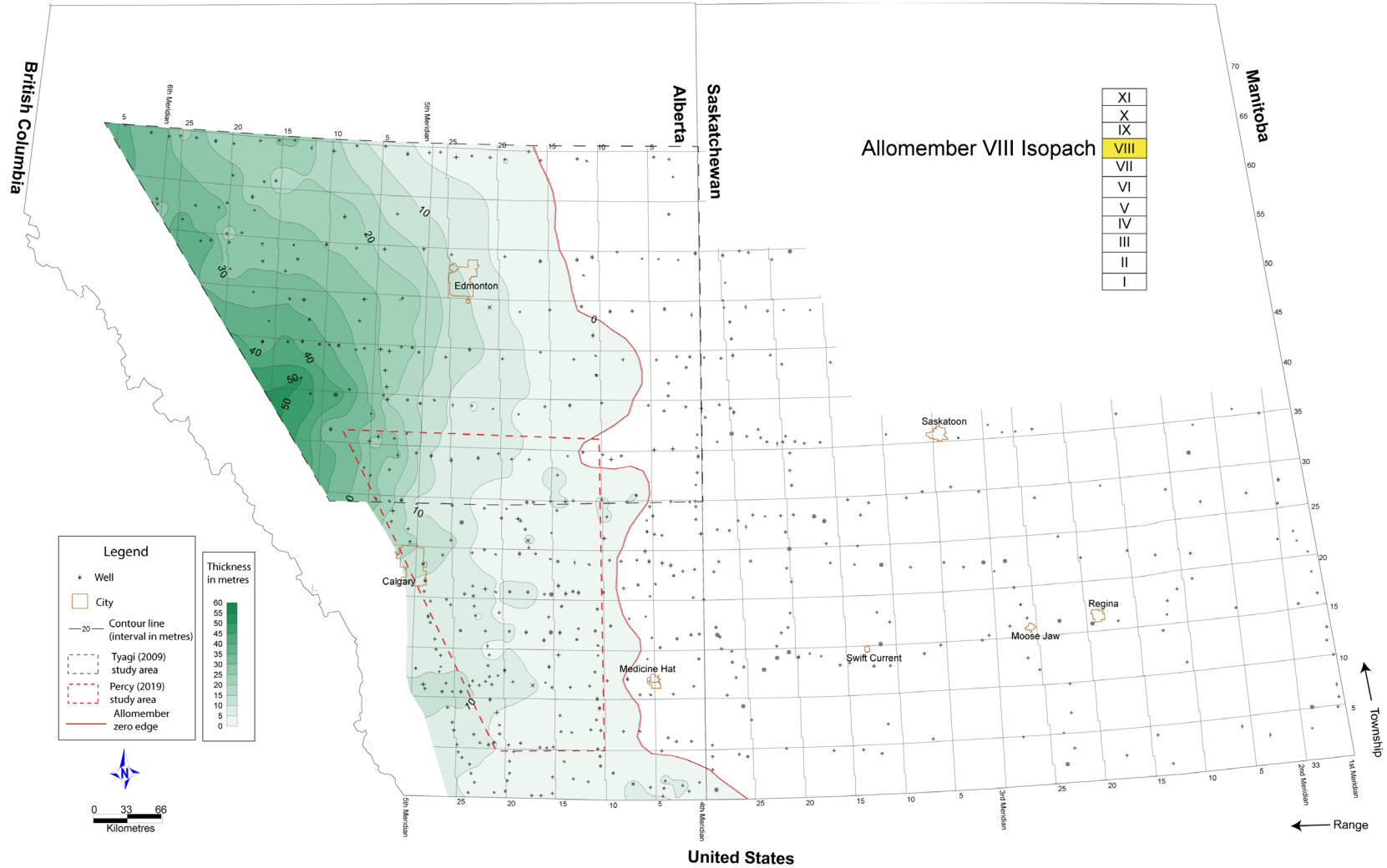


Figure 5:28: Isopach map of allomember VII.



5:29: Isopach map of allomember VIII.

south. Progressive eastward onlap onto the forebulge region is non-erosional (Tyagi, 2009).

5.3.1.9 Allomember IX

The isopach map of allomember IX shows a northwest-thickening wedge in northwestern Alberta and an isolated, arcuate depocentre in west-central Alberta west of range 5 and between townships 30 and 35 (Figure 5.30). The basement domain overlay illustrates a possible relationship between differential subsidence that may have occurred between the domains and the observed variability in the thickness of allomember IX. The allomember laps out on to the forebulge region that uplifted in response to tectonic loading.

5.3.1.10 Allomember X

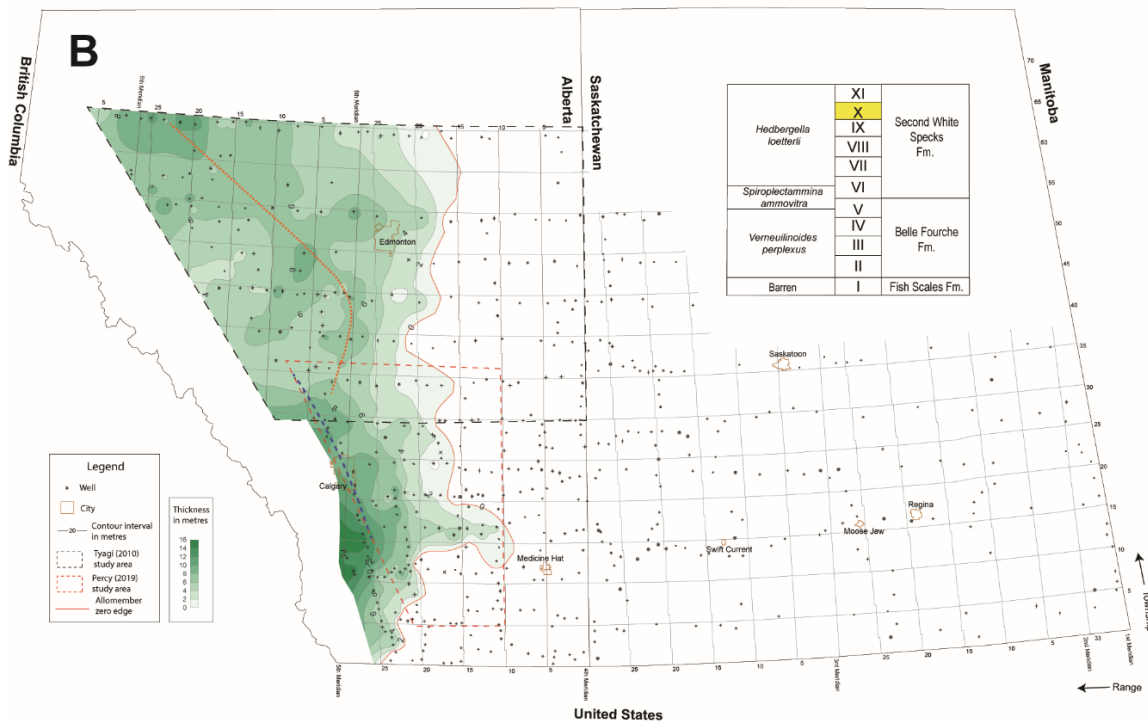
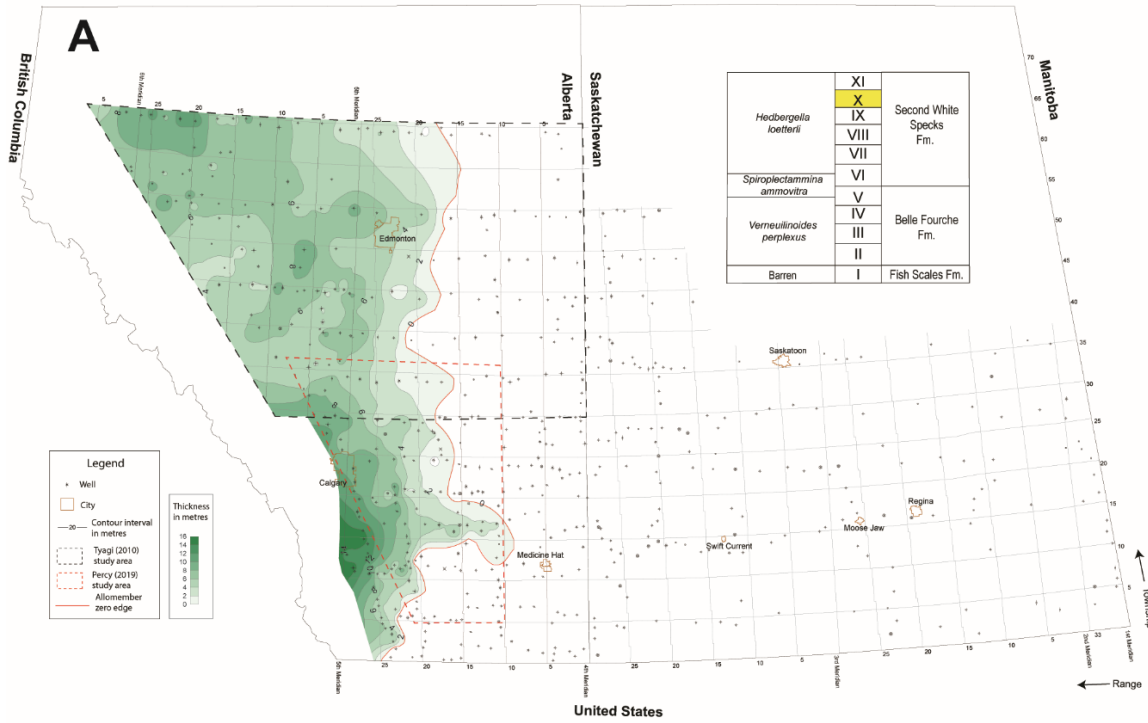
Two depozones are shown in the isopach map for allomember X. An along strike, linear thickness trend runs northwest to southeast, parallel to the Thrust Belt (orange dashed line; Figure 5.31) and an arcuate depocentre in southwestern Alberta between range 25W4 and 1W5. The linear thickness trend is interpreted as a subtle, flexural response to tectonic loading. No relationship is apparent with the linear thickness trend and basement domains in the region. In contrast to allomember IX, the principal depocentre swung to the southwestern corner of Alberta, suggesting the location of thrusting and the loci of subsidence had laterally shifted (Plint et al., 2012). A correlation between tectonic flexure and the Lochend hinge zone (blue dashed line) could be interpreted based on the hinge running nearly parallel to the arching contours of the arcuate depocentre.

5.3.1.11 Allomember XI

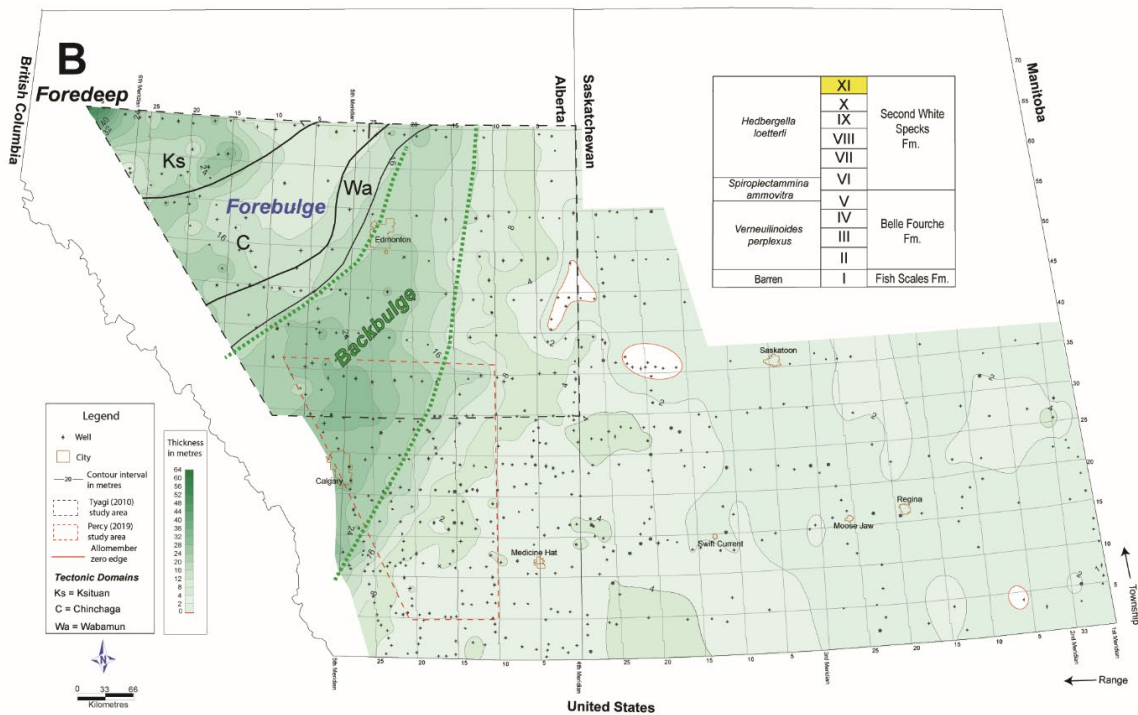
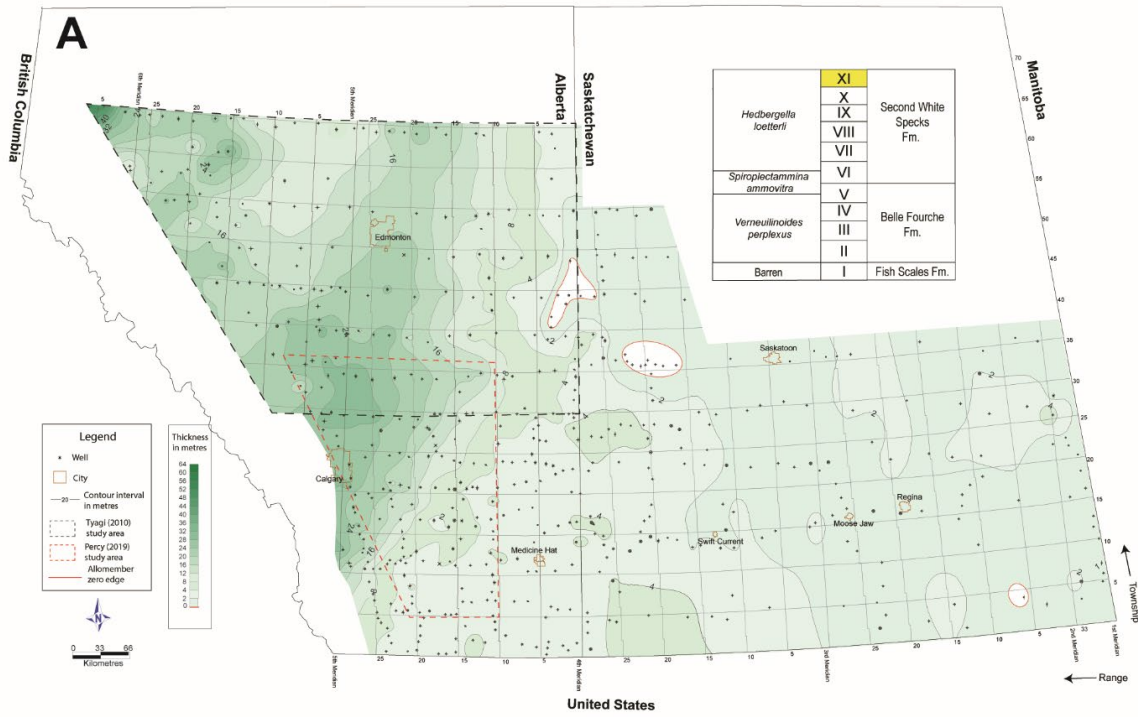
The isopach map of allomember XI shows thickening in the northwest corner of the study area and a northeast-southwest thickening that cuts across northeastern to west-central Alberta (Figure 5.32). The two depocentres are divided by a thin deposit of allomember XI. The region of thinning is interpreted as a forebulge region and the basement domain overlay in Figure 5.32B shows the area correlates to possible uplift of the Chinchaga domain. The depocentre east of the assumed forebulge would reflect the backbulge



Figure 5:30: (A) Isopach map of allomember IX. (B) Isopach map with structural features overlay. Basement domains (Ross et al., 1994) = black dashed lines.



5:31: (A) Isopach map of allomember X. (B) Isopach map with structural features overlay. Lochend hinge zone = blue dashed line. Axis of subtle thickness high = orange dashed line.



5:32: (A) Isopach map of allomember XI. (B) Isopach map with structural features overlay. Basement domains (Ross et al., 1994) = solid black lines. Interpreted backbulge region = green dashed line.

depozone (green dashed line; Figure 5.32B) and the stable craton underlies the broad, tabular geometry in eastern Alberta and across Saskatchewan.

Chapter 6

6 Sediment distribution and paleogeographic history of the Upper Cretaceous Colorado Group

Lithology distribution maps permit reconstruction of basin evolution and a better understanding of the interplay between sedimentation and subsidence that occurred during deposition of the interval studied here. The lithology maps presented in this chapter are based on the lithofacies listed in Table 4.3 and show the percentage breakdown of lithofacies in each allomember. These maps collectively depict the paleogeographic evolution of the Western Interior Seaway (WIS) from the Early Cenomanian to Middle Turonian. Summary lithology maps were constructed for each allomember to show general sediment dispersion trends and to aid in the interpretation of paleogeographic changes recorded in the study interval. The summary map for each allomember shows which lithology has a concentration of 50 percent or greater. In cases where none of the calculated lithology contours are over 50 percent, the highest percentage lithology is represented in the summary map. Regions of less well control are marked on the summary lithology maps with a hatched pattern.

6.1 Albian-Cenomanian

6.1.1 Allomember I

The lithology distribution pattern for allomember I (Figures 6.1 and 6.2) illustrates an overall broad areal distribution of quartz-rich, heterolithic sandstone and mudstone across the study area. Local concentrations of calcareous mudstone occur throughout Alberta and into western Saskatchewan, with the greatest proportion occurring in west-central Alberta. The highest percentage of sandstone is observed in a slightly northwest-southeast trend in western Saskatchewan, and a north-south-trending deposit in southeastern Saskatchewan. Localized sandstone deposits of less than 15 percent are mapped in northwestern and south-central Alberta. Mudstone percentages are highest near the eastern margin of the calcareous mudstone deposit in central Alberta and in isolated pockets found scattered in the study area.

Allomember I - Base of fish scales (BFS) to Fish Scales Upper (FSU)

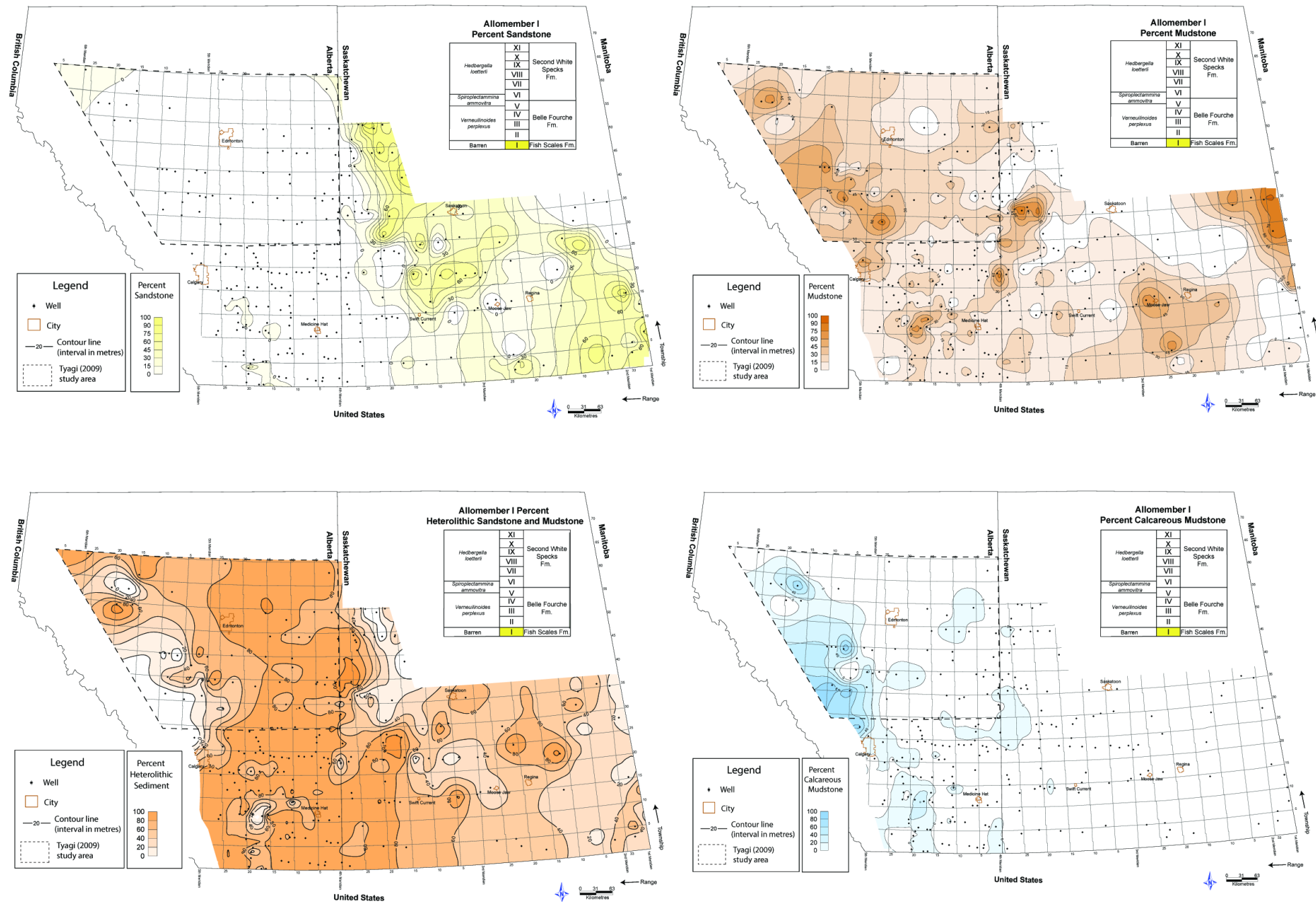


Figure 6:1: Allomember I percent lithology maps.

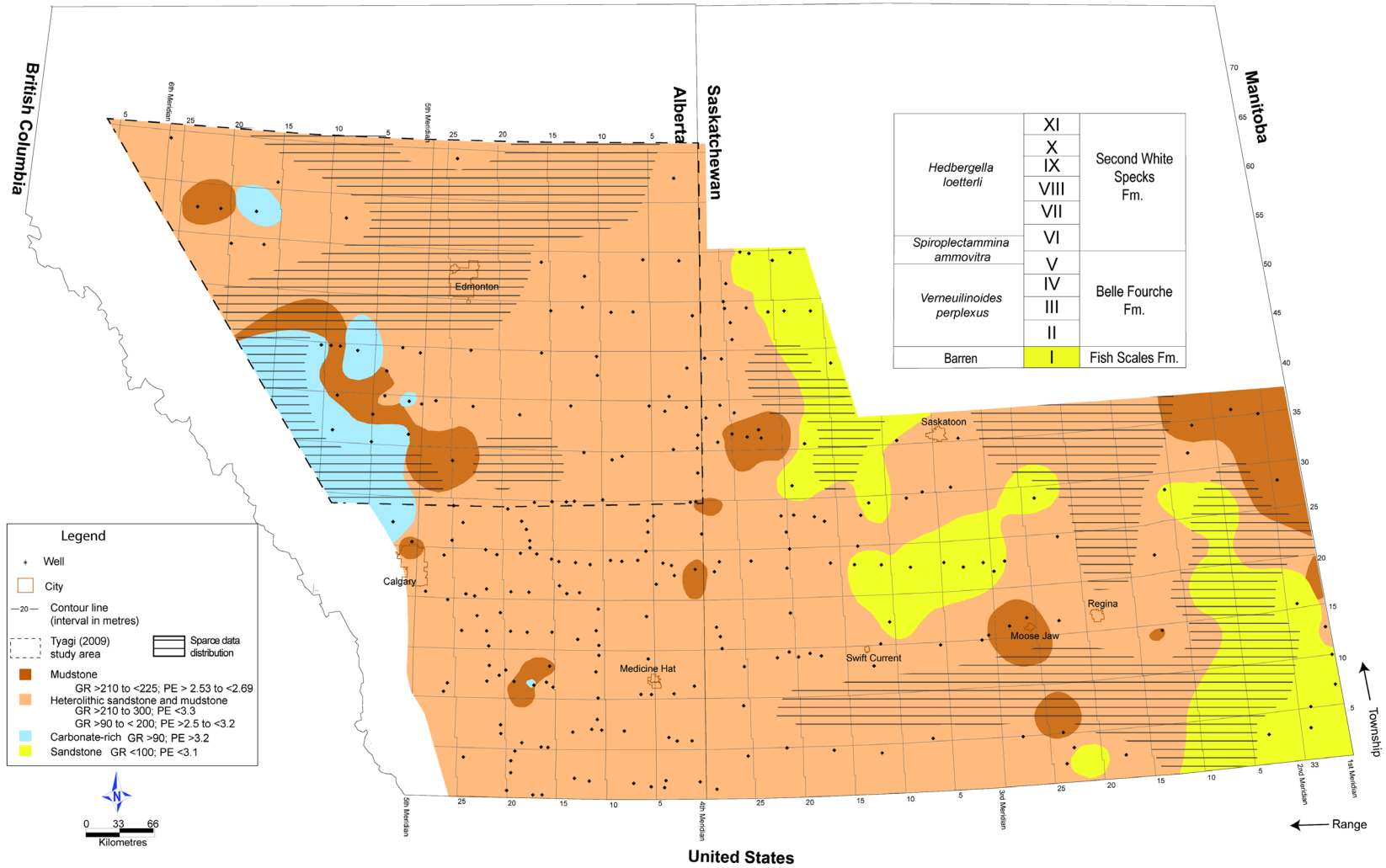


Figure 6:2: Allomember I percent lithology summary map.

Interpretation

The broad distribution pattern of heterolithic sandstone and mudstone in allomember I supports the interpretation of Roca (2007) that this succession of Lower Colorado Group strata was deposited on a low- gradient ramp in water no more than ~ 30 metres deep, where sedimentation at the sea floor was frequently influenced by storms (section 3.5.3). The extensive spread of heterolithic material across the northwest-southeast thickening trend in western Alberta in southern Saskatchewan suggests that increases in accommodation related to subsidence did not exceed the sedimentation rate. This would have maintained the low gradient ramp, allowing fine-grained, storm-deposited sediment to blanket the sea floor in those areas. Sandstone deposits in Saskatchewan appear to align with allomember thinning, suggesting either decreased accommodation due to uplift or a change in eustasy or a decrease in the amount of sediment delivered from its source area. The localized deposition of calcareous mudstones and mudstones in west-central Alberta occurs adjacent to the Lochend hinge zone, suggesting that the basinward transport of sediment was reduced and/or that water column conditions became more favourable for primary productivity.

6.2 Cenomanian

6.2.1 Allomember II

The allomember II lithology pattern (Figures 6.3 and 6.4) depicts a broad distribution of mudstone, with a patch of calcareous mudstone in west central Alberta and a north-south trending deposit of heterolithic sandstone and mudstone in western Saskatchewan.

Interpretation

The lithology patterns appear mostly independent of the uplift and differential subsidence patterns represented in the allomember II isopach. Calcareous mudstones linked to decreased clastic input and higher productivity overlie an area of thinner allomember II, while sandstone and storm-influenced heterolithic sandstone and mudstone align with a north-south thickening trend in western Saskatchewan. Conditions favourable for calcareous mudstone deposition may have been related to an increase in accommodation linked to active flexural subsidence to the west, limited sediment transport into the basin,

Allomember II - Fish Scales Upper (FSU) to X Bentonite

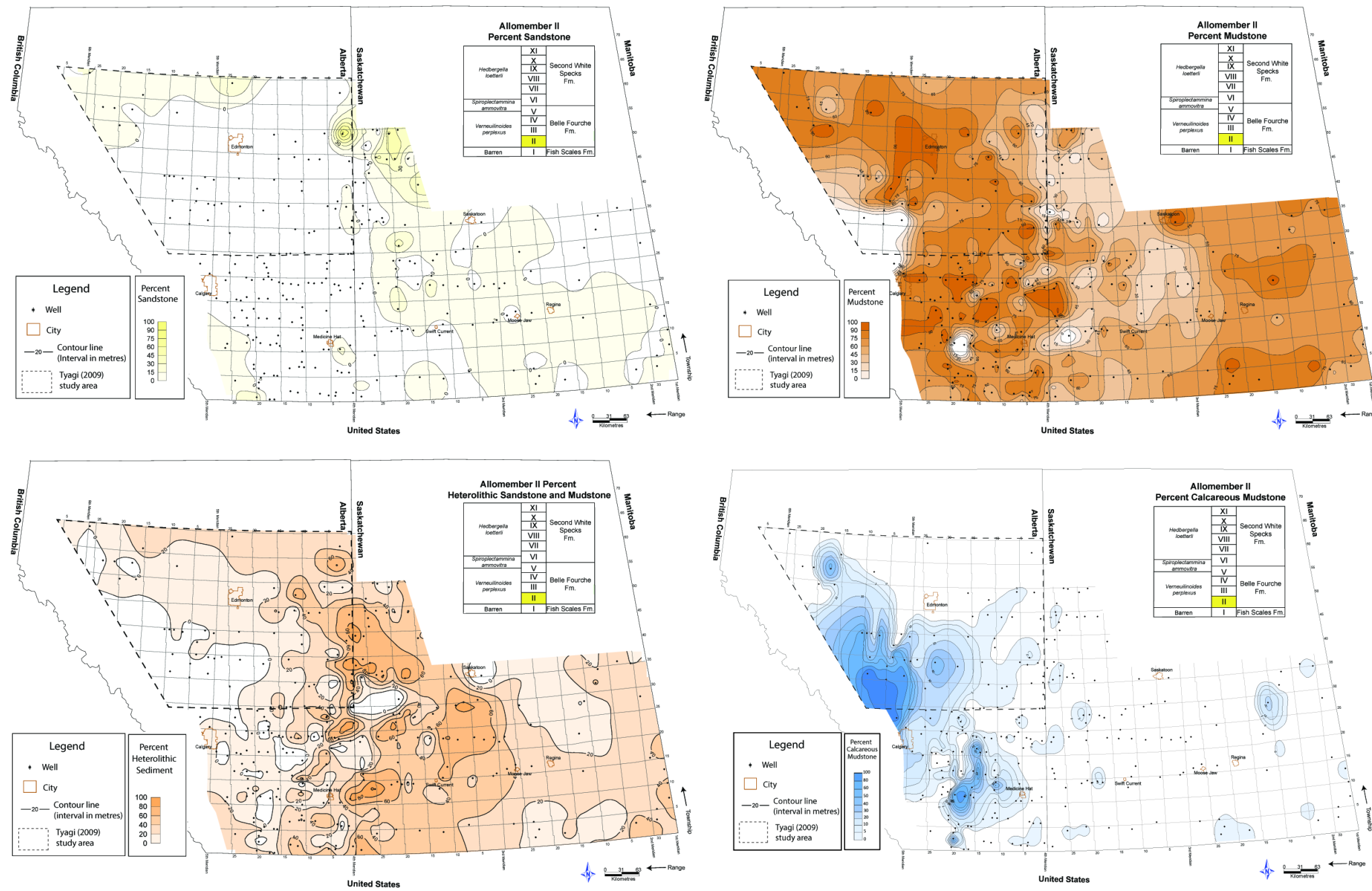


Figure 6:3: Allomember II percent lithology maps.

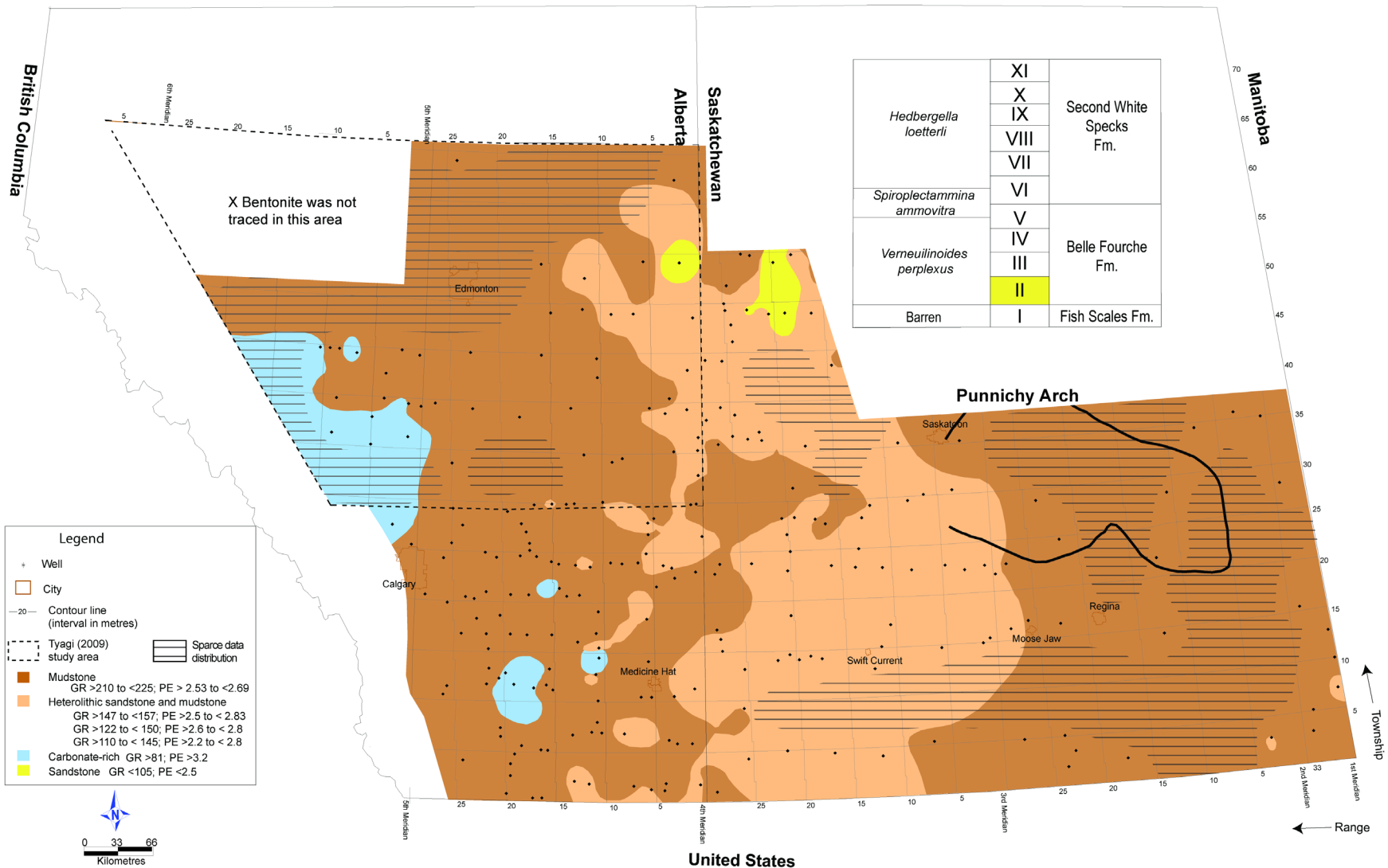


Figure 6:4: Allomember II percent lithology summary map.

and/or a eustatic sea level rise. It is interpreted here that the sedimentation rate exceeded increases in the accommodation rate due to subsidence within the Eyehill magnetic high region, allowing this area of the basin to fill and to increase the tendency for storm waves to rework the seafloor sediment. The presence of thinly bedded mudstone and lack of heterolithic sandstone and mudstone on top of the thinned isopach within the Punnichy Arch suggests that sediment was predominately deposited below storm wave base in this region.

6.2.2 Allomember III

Allomember III lithology distribution (Figures 6.5 and 6.6) continues the broad deposition of silty argillaceous mudstone as observed in allomember II. Calcareous mudstone continues to dominate in the west central area of Alberta, with higher percentages beginning to extend southeastward. Heterolithic sandstone and mudstone continues along southwestern Saskatchewan and into southeastern Alberta, with additional prominent deposits occurring in northwestern Alberta and southeastern Saskatchewan. Apart from an isolated pocket of mapped sandstone of less than 15 percent in western Saskatchewan, sandstone is confined to northwestern and northcentral Alberta and accounts for up to 30 percent of the total volume of allomember strata.

Interpretation

Heterolithic deposits in northwestern Alberta in allomember III are interpreted as offshore transition zone sediments (Figure 3.2) that were deposited basinward of the paleoshoreline mapped by Plint (2000). The fairly consistent allomember thickness and a tabular geometric shape in eastern Saskatchewan implies the sea floor had a very low gradient. Pockets of storm deposited heterolithic sandstone and mudstones in this area may reflect an increased susceptibility to events of sediment reworking relating to relative sea level oscillations. The calcareous mudstone restricted to the southwest corner of the erosion edge in eastern Alberta (red arrow, Fig. 6.6) may be the remnant of an originally broader deposit that was largely eroded during uplift after its deposition.

Allomember III - X Bentonite to Dunvegan A

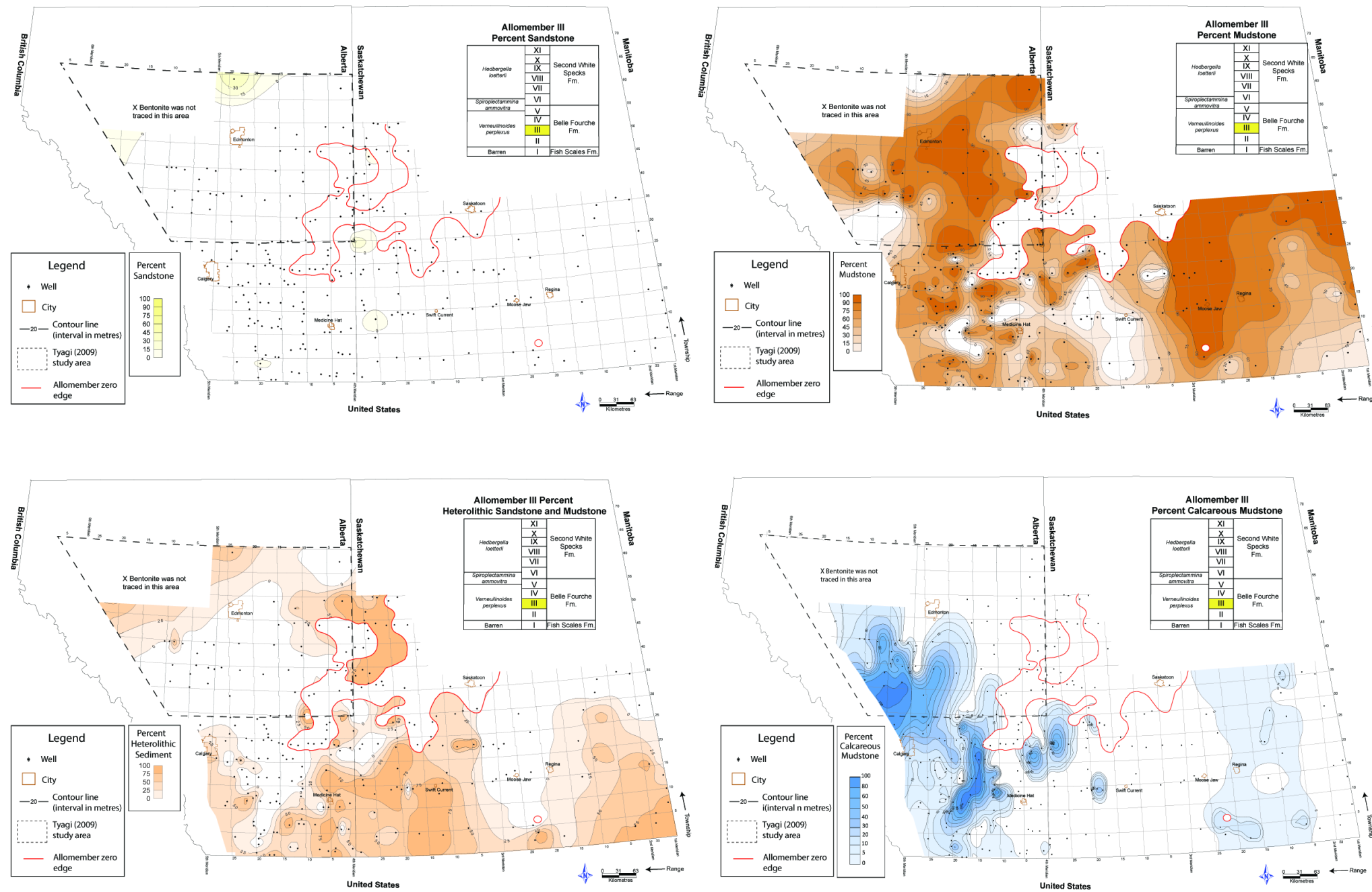


Figure 6:5: Allomember III percent lithology map.

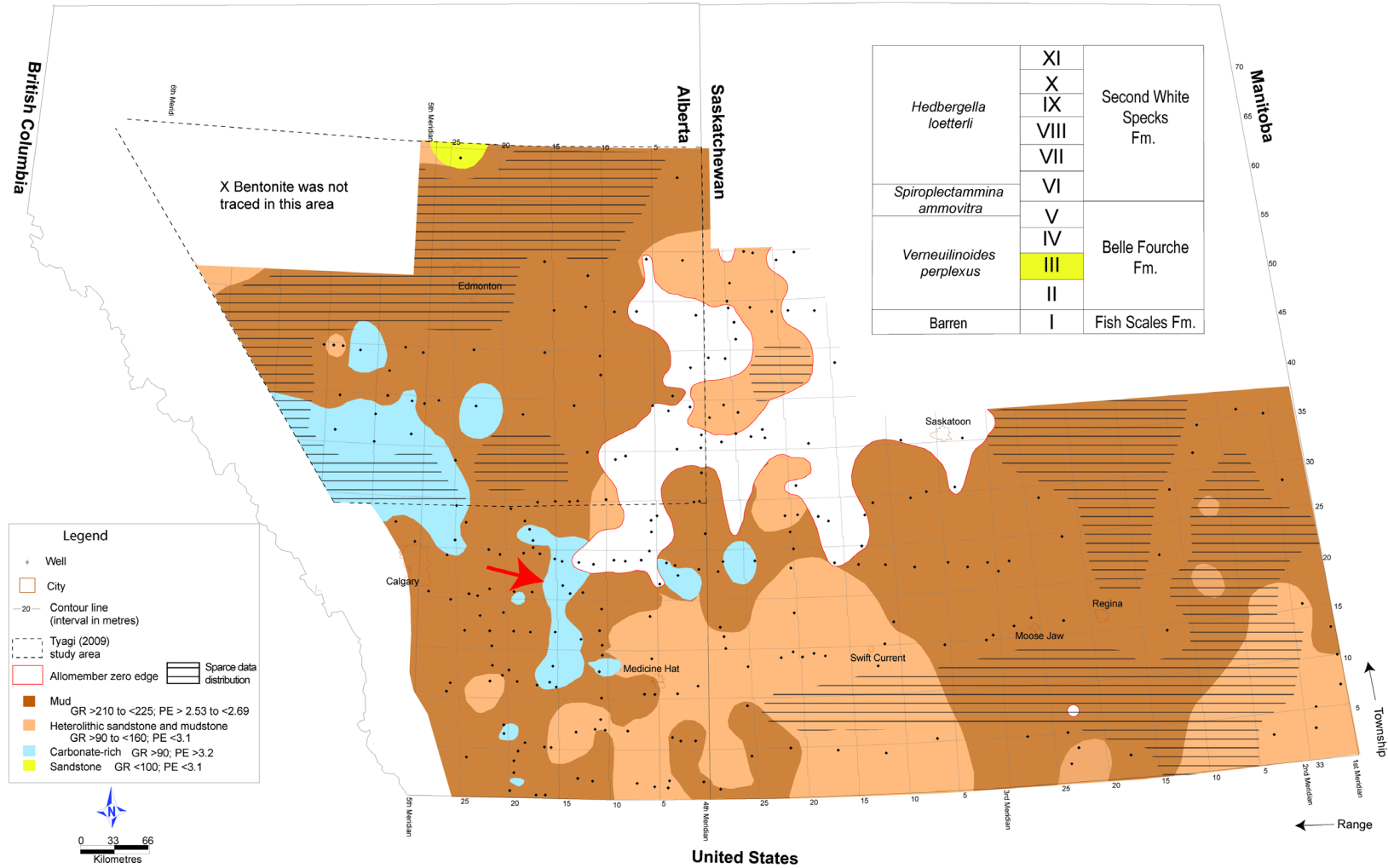


Figure 6:6: Allomember III percent lithology summary map. Red arrow = refer to text.

6.2.3 Allomember IV

The lithology distribution for allomember IV (Figures 6.7 and 6.8) shows a swath of calcareous mudstone across central Alberta and Saskatchewan that is flanked to the northwest and southeast by mudstone. Heterolithic sandstone and mudstone is present in northwestern and southwestern Alberta, with localized deposits in south-central Saskatchewan. Sandstone is confined to northwestern Alberta.

Interpretation

Calcareous mudstones are rich in calcareous foraminifera, and their abundance in the WIS increased as the sea level rose and warm, normal-salinity Tethyan water flooded northward into the seaway (Fisher et al., 1994; Eicher and Diner, 1989). The incursion of warmer, calcareous foraminifera-rich water is recorded in allomember IV by the areal expansion of calcareous mudstone across the central part of the study area. The broad areal extent of mudstone implies that deposition occurred below storm-wave base on a broad, low-gradient ramp over most of Saskatchewan.

Sediment accumulation in northwestern Alberta during this time occurred in a large, south-east opening embayment (Plint, 2000). The sand deposit restricted to northwest Alberta (Figure 6.7 and 6.8) likely represents the basinward extent of wave-reworked lowstand sandstone deposits within the embayment (Plint, 2000), and the southeast trending transition between heterolithic sandstone and mudstone, non-calcareous mudstones, and calcareous mudstone suggest a deepening of the basin toward the southeast. Plint (2019) suggested relative sea-level changes during the deposition of allomember A-X (which is time equivalent to allomember IV), were driven by cycles of high frequency eustatic rise and fall and not tectonic flexure. The heterolithic sandstone and mudstone deposits in southwestern Alberta suggest either a decrease in accommodation or the existence of a sediment input source southwest of the study area. The slight overlap between storm-wave influenced heterolithic sandstone and mudstone and a region of uplift in the southwest corner of Alberta (Figure 6.8), as well as a vague north-south deepening trend along range 20W4 (as implied by the distribution of calcareous mudstone), suggests that accommodation in this part of the study area may

Allomember IV - Dunvegan A to X transgressive

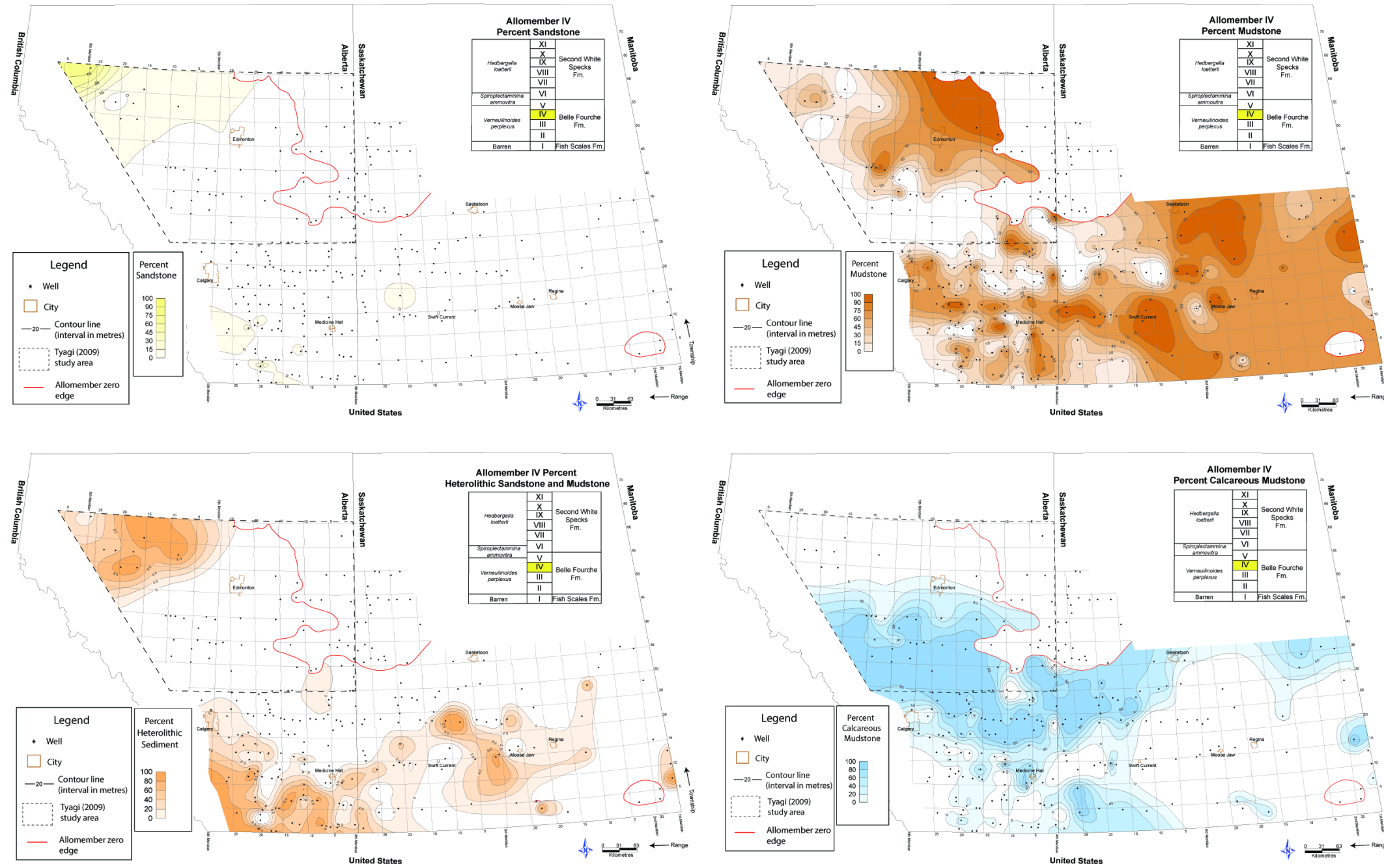


Figure 6:7: Allomember IV percent lithology maps.

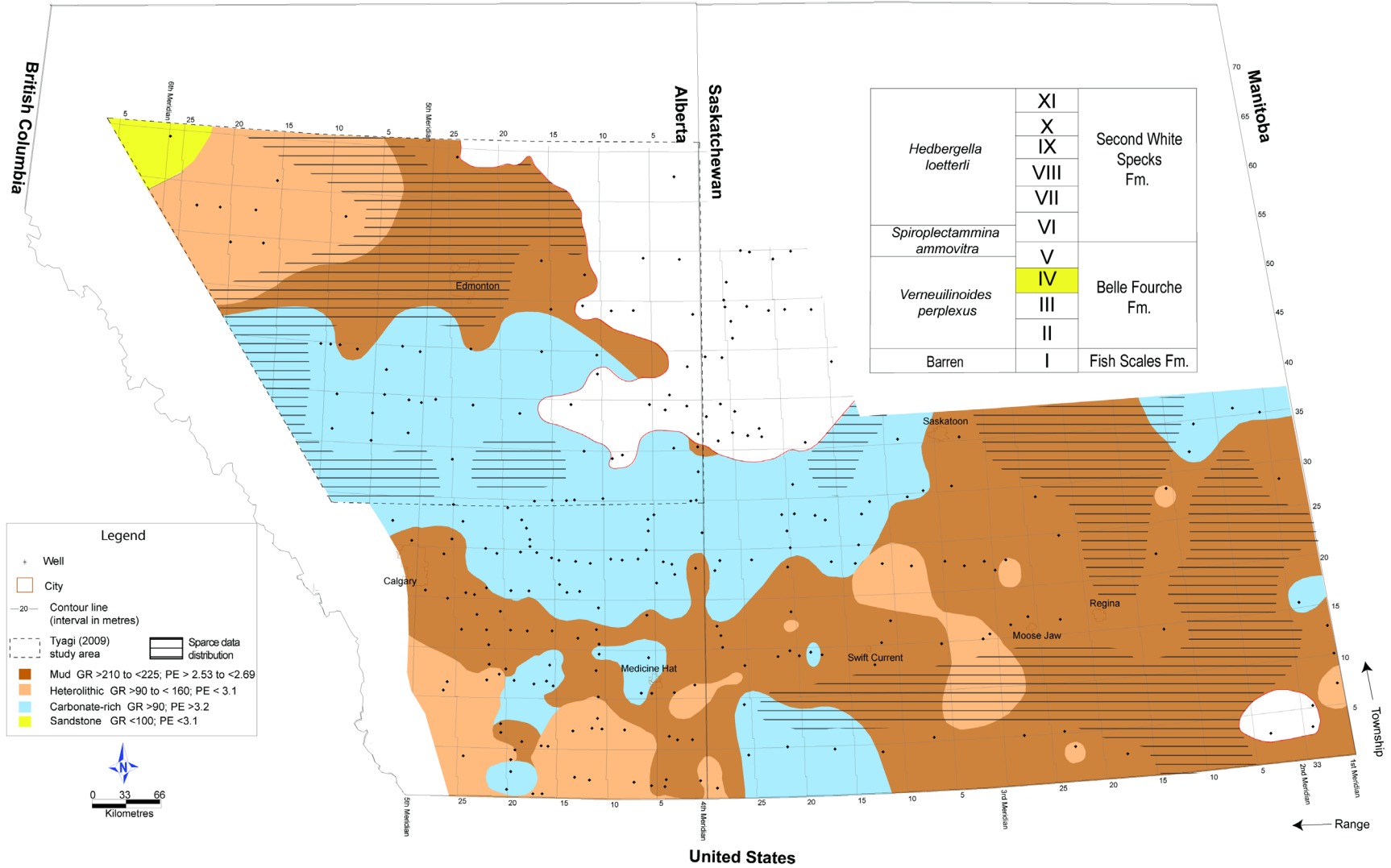


Figure 6:8: Allomember IV percent lithology summary map.

have been more strongly influenced by tectonic flexure than eustatically driven sea-level changes. The base of allomember IV coincides with the transgressive backstep on the top of Dunvegan allomember A, which corresponds with the increase in deposition of biogenic carbonate.

6.2.4 Allomember V

Allomember V shows the areal expansion of calcareous mudstone across the basin. Heterolithic sandstone and mudstone remains confined to northwestern and southwestern Alberta, with isolated pockets occurring in western Saskatchewan. The geographic distribution of mudstone is substantially reduced relative to allomember IV and confined to northeastern and southwestern Alberta, and northwestern Saskatchewan.

Interpretation

Sediment distribution patterns recorded in Late Cenomanian allomember V (Figure 6.9 and 6.10) resulted from a combination of eustatically- and tectonically driven changes to marine productivity and elastic sediment supply. Widespread deposition of calcareous mudstones across the study region reflects continued global sea level rise during the Greenhorn cycle and increased productivity as proto-Gulf of Mexico water inundated the WIS. The extensive deposit of calcareous mudstone corresponds to another backstep of the shoreline that is recorded by the X transgressive surface at the base of allomember V (Fig. 4.1). The distribution of mudstone in northwestern Saskatchewan and northeastern Alberta may have resulted from flexural uplift in the region that promoted subaerial erosion to the north, beyond the study area, and provided a fine-grained sediment source that supplied siliciclastic mud to the basin.

Heterolithic sandstones and mudstones in northwestern Alberta represent proximal offshore interbedded silts and clays that were reworked and dispersed by waves and combined flows, possibly due to a decrease in accommodation due to uplift within the Kiskatinaw domain. The distribution of these heterolithic sediments in southwestern Alberta corresponds to a region of uplift, and the implied mudstone and subsequent calcareous mudstone deposits appear to run parallel to the northwest-southwest

Allomember V - X transgressive to K1

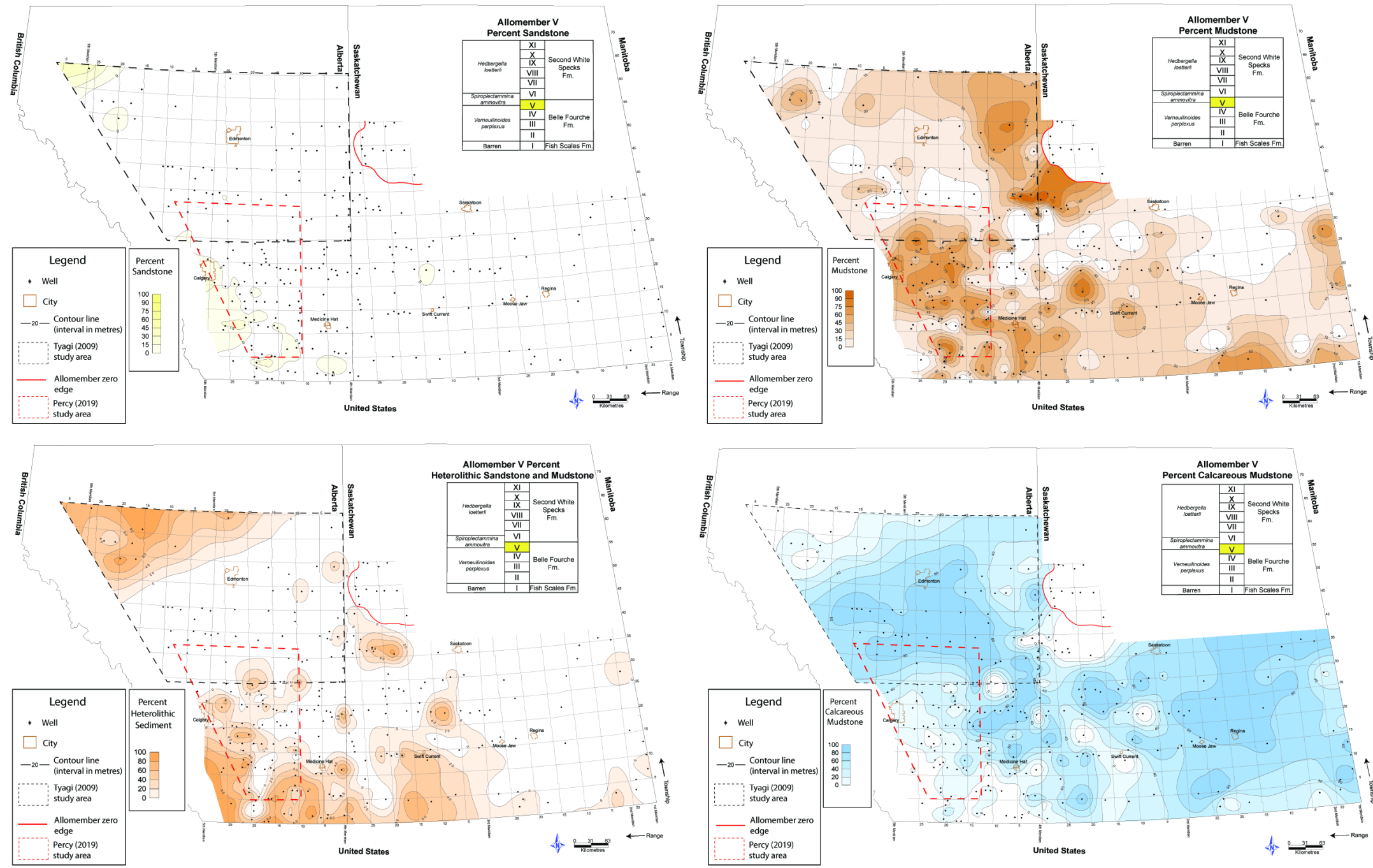


Figure 6:9: Allomember V percent lithology maps.

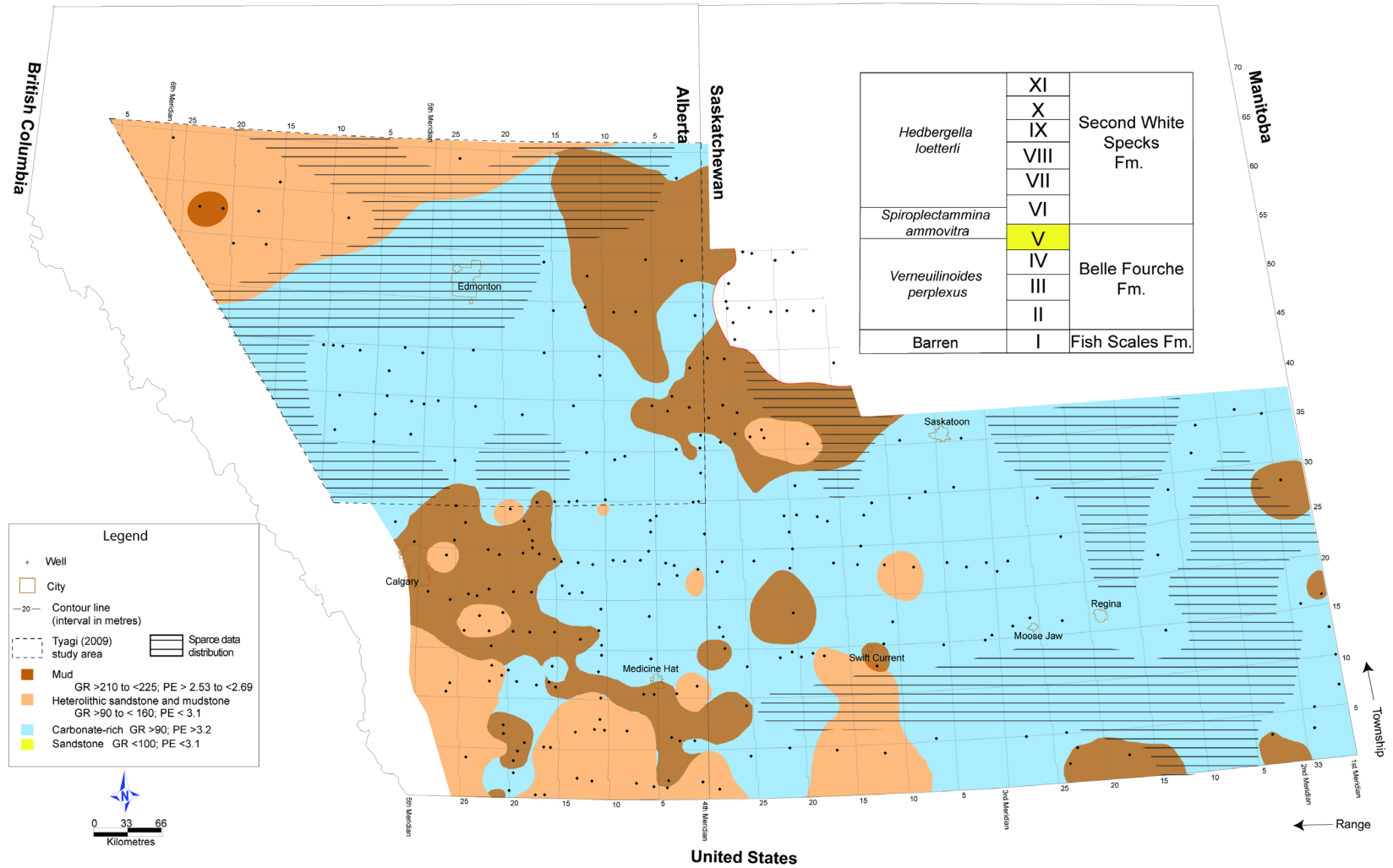


Figure 6:10: Allomember V percent lithology summary map.

thickening trend. The dominance of calcareous mudstone records a shift from more proximal to more distal offshore conditions, characterized by a decrease in non-calcareous terrigenous sediment and an increase in the calcareous remains of microplankton (e.g., foraminifera and coccoliths).

6.2.5 Allomember VI

The geographic distribution of calcareous mudstone in allomember VI (Figures 6.11 and 6.12) is more discontinuous than in allomember V. The highest areal coverage occurs in west central Alberta and eastern Saskatchewan, with localized patches occurring in northwestern Saskatchewan and southern and central Alberta.

Interpretation

The transgressive peak of the Greenhorn cycle occurred in the mid Early Turonian (Kaufmann and Caldwell, 1993), and the transition to more broadly distributed siliciclastic sediment in allomember VI compared to the preceding allomembers IV and V records a shift to a slower rate of global sea-level rise. There is no obvious correlation between lithology distribution and the northwest-southeast trending subsidence pattern, which implies lateral changes in lithology over short distances were not predominantly influenced by tectonic flexure. The patchiness of heterolithic sandstone and mudstone records sediment distribution influenced by storms on the shallow, low gradient ramp. The abrupt lithology change between calcareous and non-calcareous mudstone lithofacies on the map (Figure 6.12) could be a product of poor data resolution (large spacing between wells due to the lack of required geophysical logs) or may truly record different paleoceanographic conditions between ocean fronts produced between the Boreal and Tethyan water masses (Fisher, 1991).

Fisher et al. (1994) used foraminiferal biofacies and ocean front reconstructions to interpret that the patterns of abrupt shifting between intertonguing calcareous and non-calcareous mudstone units in the late middle through late Cenomanian Greenhorn and Belle Fourche Formations of southeastern Montana and southern Black Hills of South

Allomember VI - K1 surface to Bighorn River bentonite

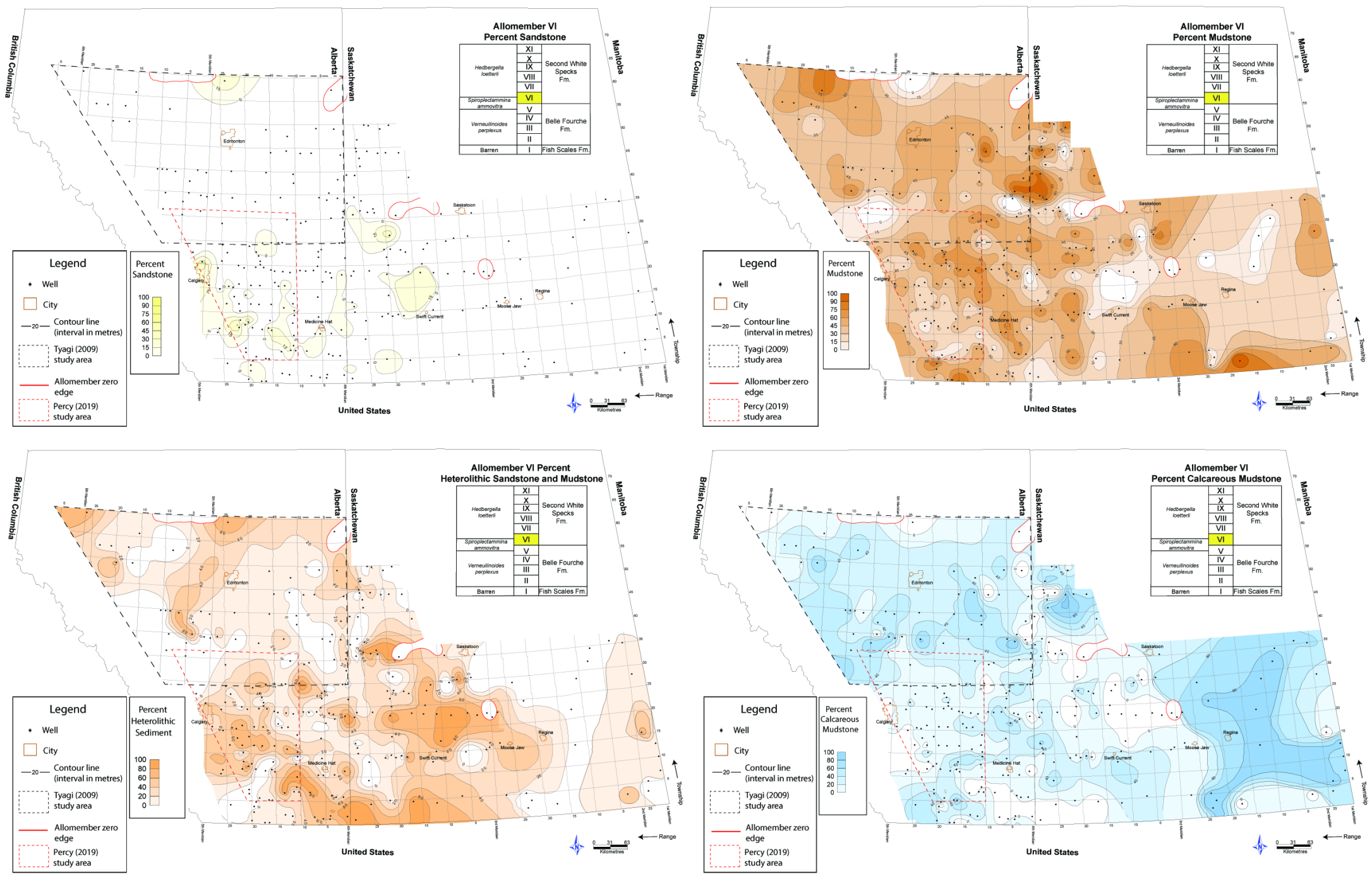


Figure 6:11: Allomember VI percent lithology maps.

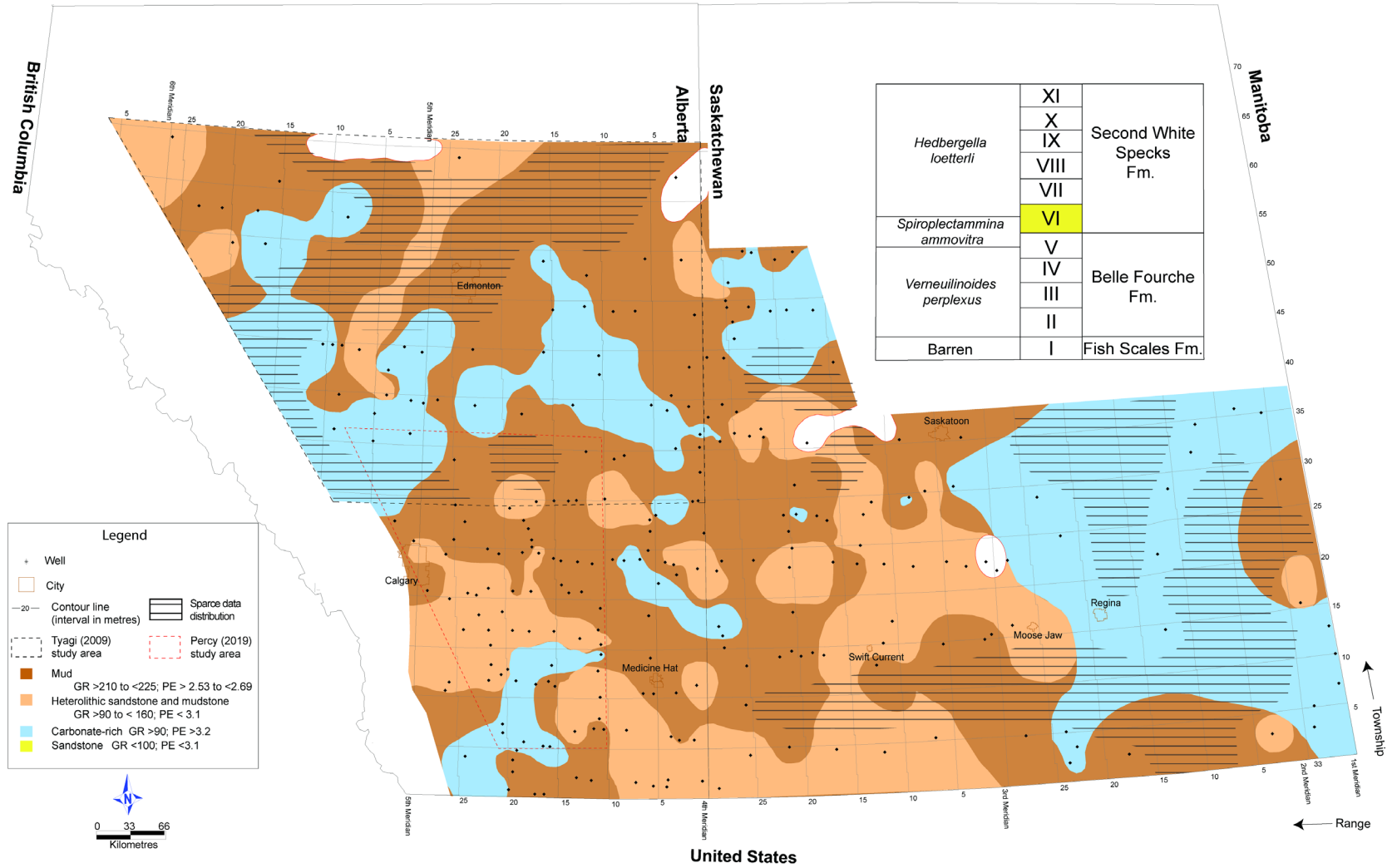


Figure 6:12: Percent lithology summary map.

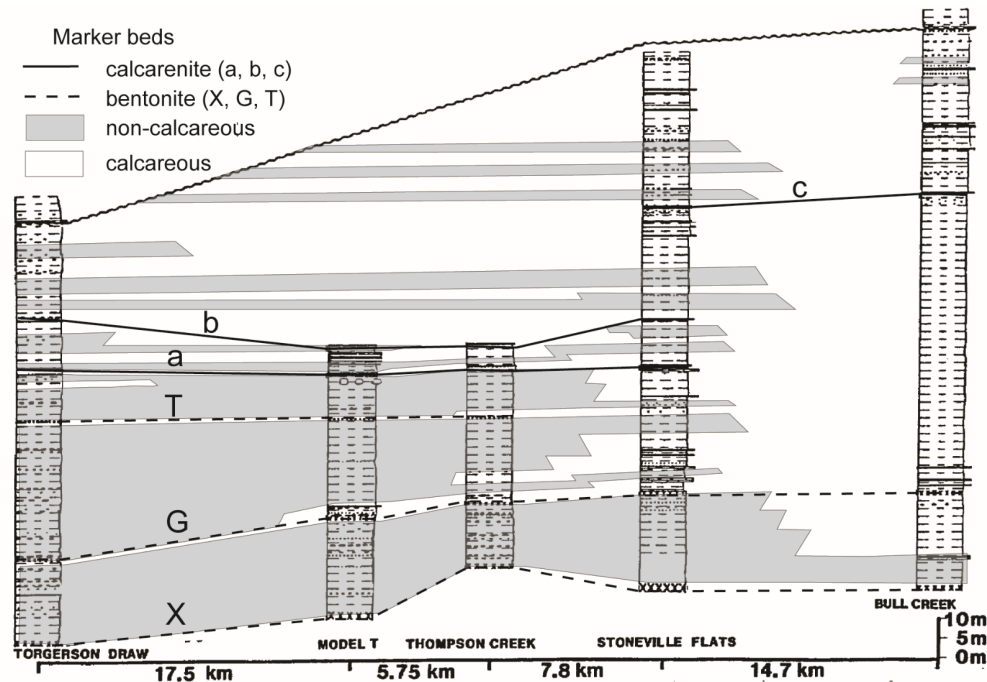


Figure 6:13: Lithofacies relationship between calcareous and non-calcareous Greenhorn Formation and Belle Fourche Formation, respectively. Sections were correlated using bentonite (X, G, T) and calcarenite (a, b, c) event marker beds. In a percentage lithofacies map, as used in this study, the lithofacies distribution would show non-calcareous mudstone at the Torgerson Draw, Model T, and Thompson Creek locations and calcareous for the Stoneville Flats and Bull Creek. Because the location on the lithofacies percentage map only shows what the predominant lithofacies is for that location, this can create areally separated patches in plan view on a map, compared to a laterally continuous, linear deposit. Illustration modified from Fisher et al. (1994).

Dakota (Figure 6.13) records the dynamics of a boundary between of two water masses of contrasting temperature and salinity. Oceanic fronts range from 10 metres to 10 kilometres in width, and their surface of maximum gradient defines changes in temperature, density and salinity (Fisher et al., 1994). Based on the foraminiferal distribution patterns, Fisher et al. (1994) deduced the orientation of the water mass boundary, or ocean front, that existed in their study area in Greenhorn/Belle Fourche time varied between southeast-sloping, vertical, and northwest-sloping (Figure 6.14).

The lack of calcareous nanoplankton implied for the upper water column of the northern part of the seaway suggests water temperatures of less than 7°C and/or salinity lower than 33 parts per thousand (ppt). Furthermore, the occurrence of only agglutinated benthic foraminifera (vs. calcareous planktonic foraminifera) implies low bottom water temperatures, salinities 30 ppt or less, and total organic 2% or greater (Fisher et al. 1994). The presence of calcareous microplankton and calcareous benthic foraminifera in the southern water mass indicates water temperatures ranging between 7 to 25°C, and salinities between 33 and 38 ppt. Differences in salinity and temperature conditions between the adjacent water masses resulted in calcareous microorganisms being ecologically excluded from northern waters (Fisher et al., 1994).

6.3 Turonian

6.3.1 Allomember VII

The same basic basic distribution pattern of calcareous mudstone in west-central Alberta observed in allomenber VI continues into allomember VII, with isolated occurrences along the border of northeastern Alberta and northwestern Saskatchewan (Figure 6.15 and Figure 6.16). Except for a localized area in northeastern Alberta, heterolithic sandstone and mudstone is more or less confined to northern Alberta and mudstone dominates the central region of Alberta.

Interpretation

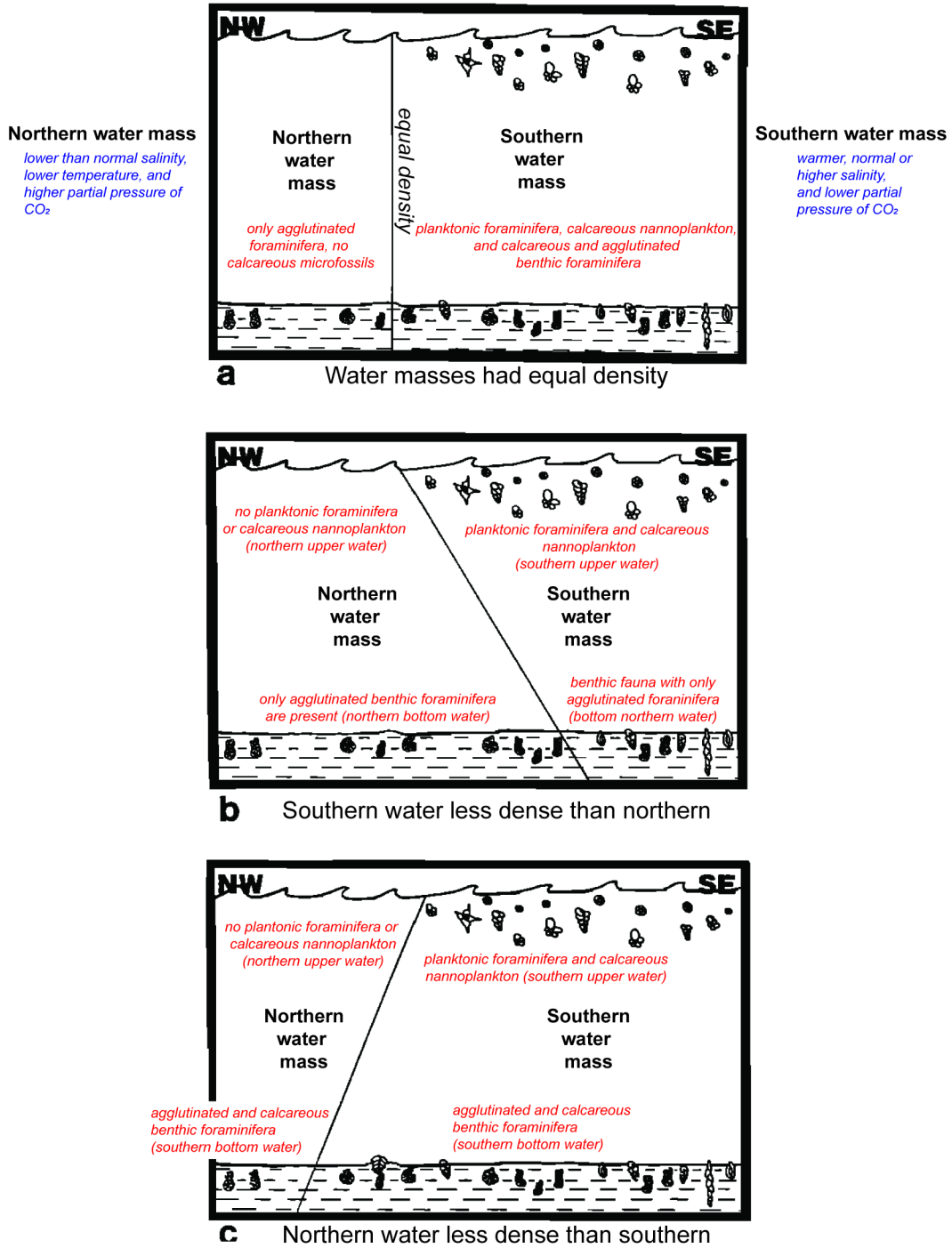


Figure 6:14: Illustration showing three hypothetical types of water mass boundaries occurring between Arctic (northern) and proto-Gulf of Mexico (southern) seaways, and the associated microfauna and microflora. Figure modified from Fisher et al. (1994).

Allomember VII - Bighorn River bentonite to regional flooding surface

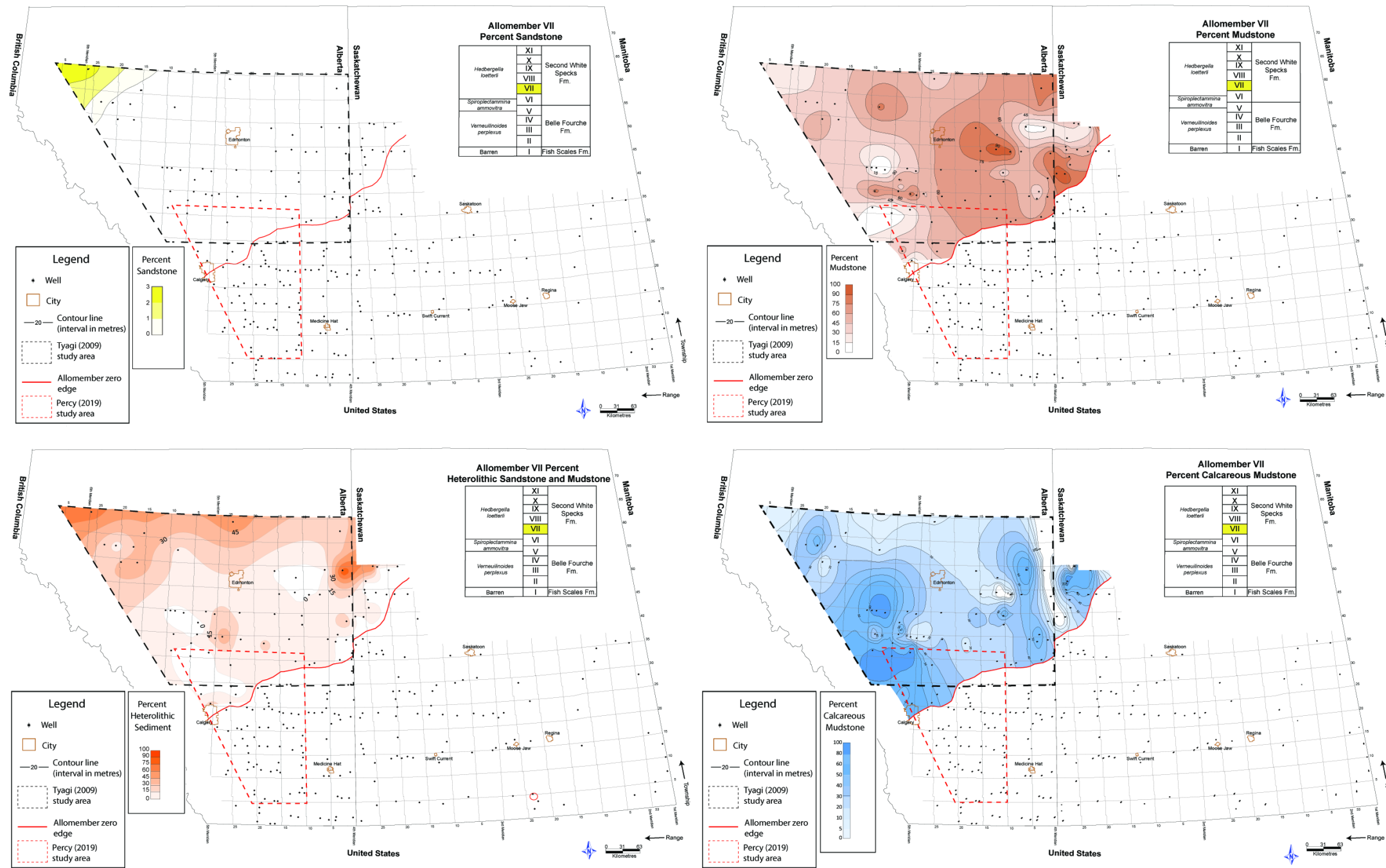


Figure 6:15: Allomember VII percent lithology maps.

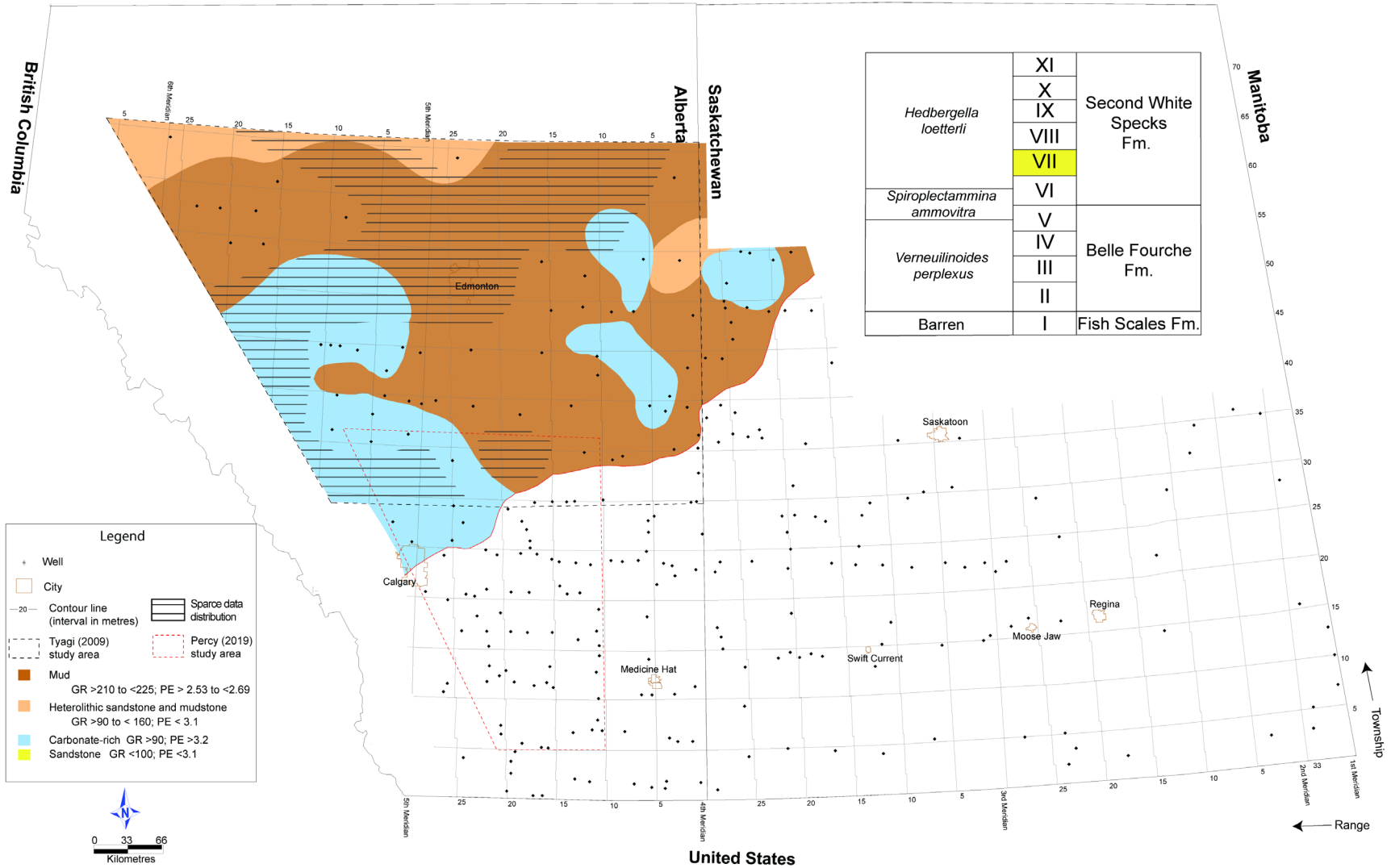


Figure 6:16: Allomember VII prevent lithology summary map.

Major tectonic loading was taking place in northwestern Alberta during allomember VII time (Varban and Plint, 2005). Northwest of the study area, Varban and Plint (2008a) noted that the vertical stacking of shoreface sandstones and a lack of clinoform development at this time points to a near-equilibrium state between rates of sediment supply and accommodation. The limited distribution of heterolithic material in northwestern Alberta and the basinward extent of the mudstone may reflect mud re-suspension by storm waves and transportation along-shelf and across-shelf via wind forced currents, resulting in mud accumulation beyond an accommodation envelope (Figure 6.17) (Varban and Plint, 2008a). The sub-aqueous mud accommodation envelope is the vertical limit to mud accumulation and is defined by ambient wave energy, sediment grain-size, and inferred water depths of no more than 20 metres deep (Varban and Plint, 2008a). Mud that accumulates above this depth becomes resuspended and exported along- and across-ramp to areas of the basin with greater accommodation (Varban and Plint, 2008a). The presence of both mudstone and calcareous mudstone in central Alberta, basinward from the paleoshoreline that was mapped to the northwest of the study area (Varban and Plint, 2008b), implies that sedimentation took place on a very shallow, nearly horizontal mud platform. In such a setting relative sea level fall of a few meters would have enabled the re-suspension of muds that, in turn, would have disrupted the accumulation of calcareous-rich sediment.

6.3.2 Allomember VIII

Lithology mapping for allomember VIII (Figures 6.18 and 6.19) shows the restriction of heterolithic siliciclastic sediment to mainly northern Alberta and discontinuous distribution of calcareous mudstone and non-calcareous mudstone in central and southwestern Alberta.

Interpretation

The broad deposition of mudstone may have resulted from the re-suspension of mud (by surface waves) in a bottom layer that underwent along-shelf and across-ramp transport caused by wind-forced currents (Varban and Plint, 2008a). The presence of heterolithic

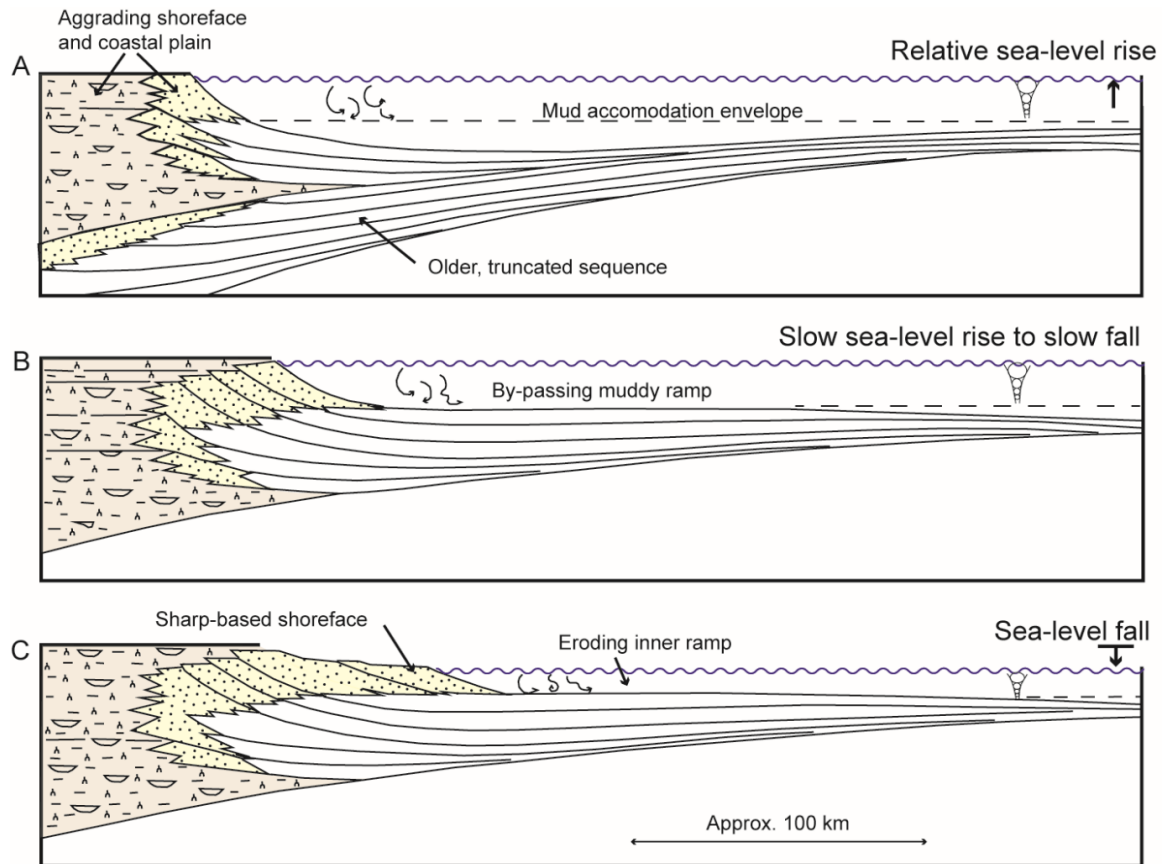


Figure 6:17: Illustration of the Kaskapau Formation mud-dominated ramp sequence (Figure modified and text summarized from Varban and Plint, 2008a). Shoreface and coastal plain deposits in image A undergo aggradation during rapid sea-level rise, limiting basinward transport of mud. During lower rate of relative sea-level rise (image B), combined flows carry muddy heterolithic deposits seaward and form a broad sub-aqueous platform. In the Kaskapau Formation, the upper surface of the platform defines the accommodation envelope and the top of each allomember mapped by Varban and Plint (2008b). The authors inferred that sediment accumulated up to the accommodation envelope, which is equivalent to the top of each of their allomembers, and excess sediment beyond that upper boundary was reworked further offshore and along-shelf. During modest relative sea-level fall (image C), a sharp-based shoreface progrades across the shallow, near-horizontal surface of the inner ramp.

Allomember VIII - Regional flooding surface to “Blue” bentonite

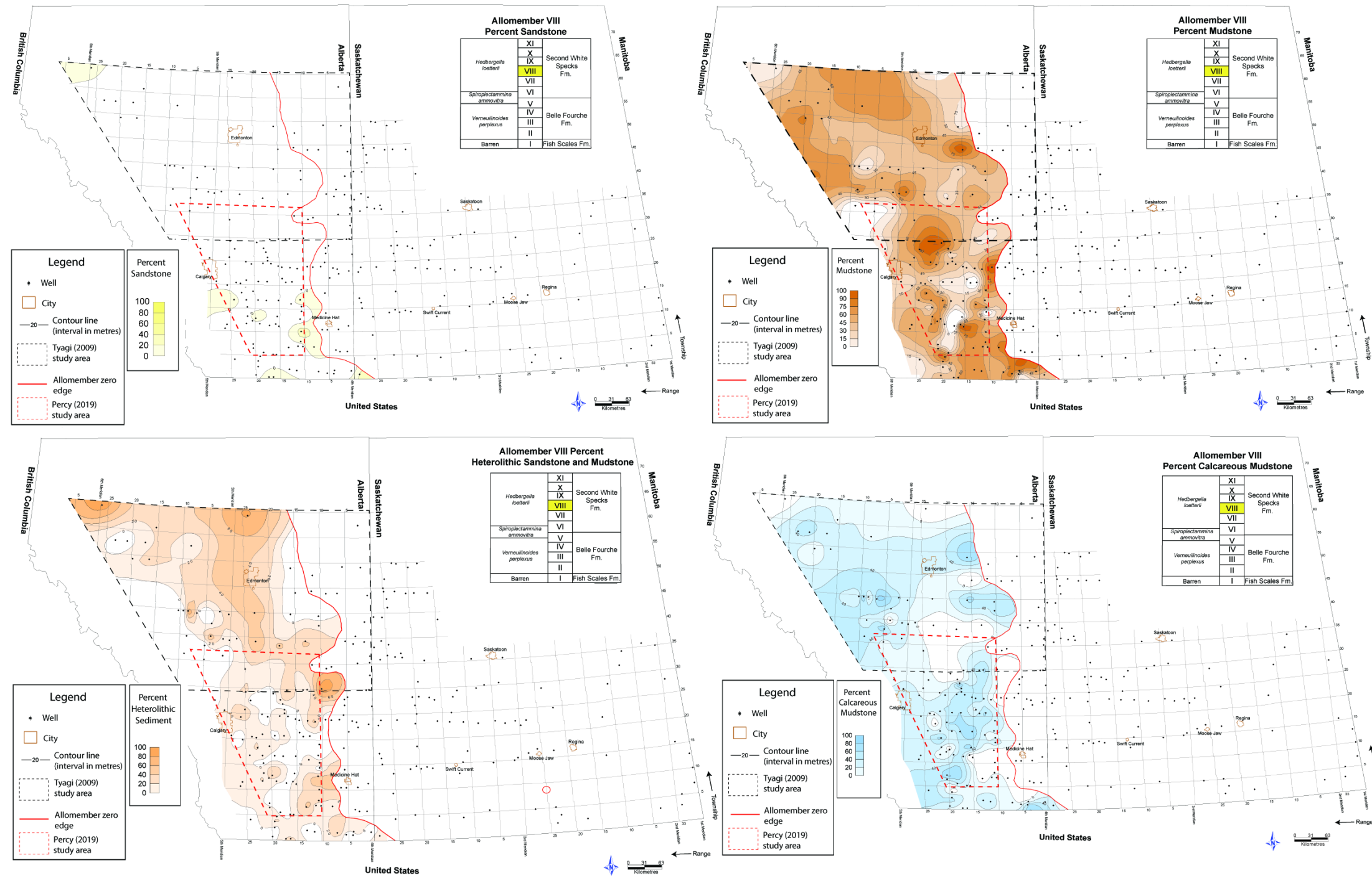


Figure 6:18: Allomember VIII percent lithology maps.

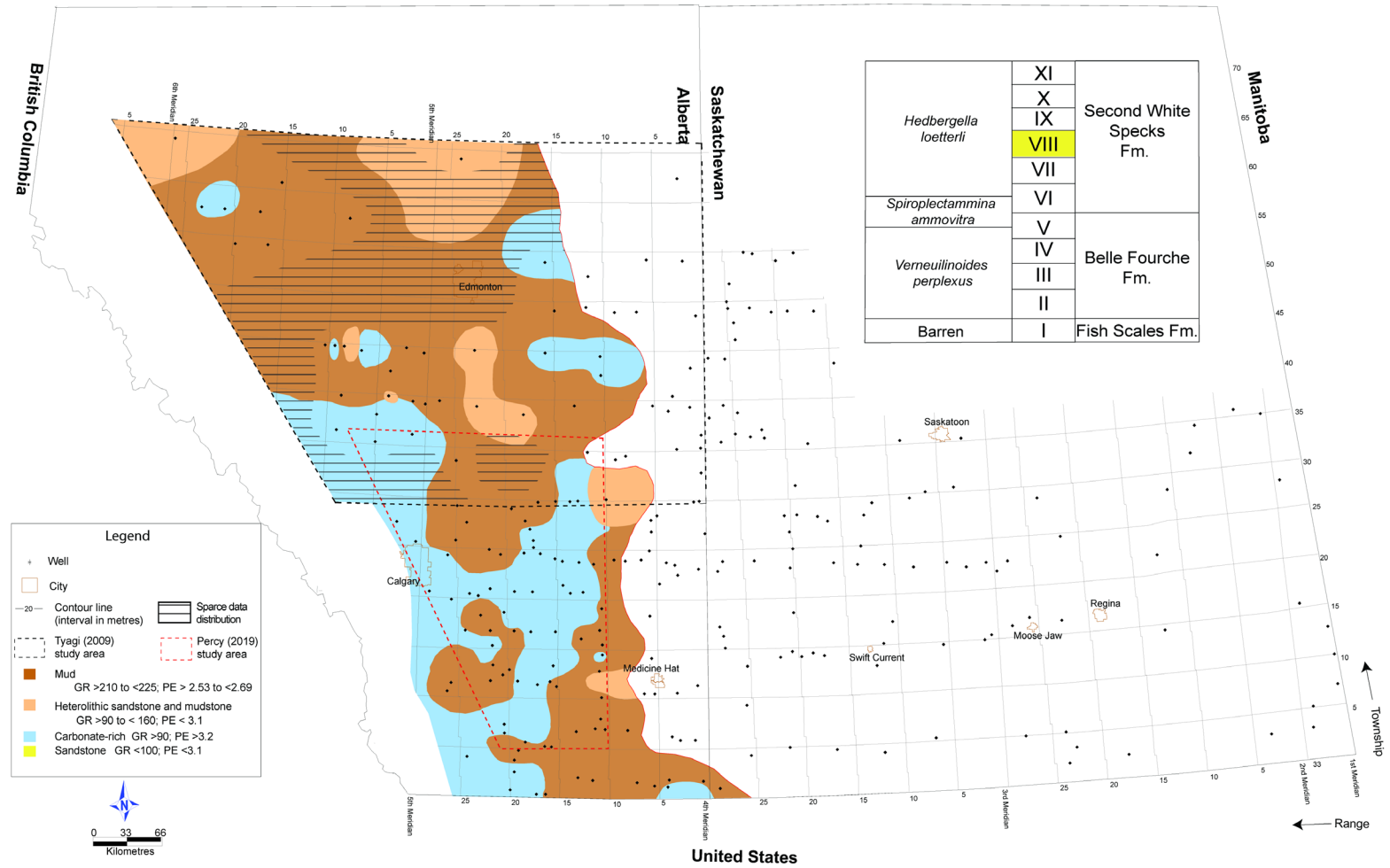


Figure 6:19: Allomember VIII percent lithology summary map.

sediment and mudstone along the southeastern edge of the erosion edge, and isolated pockets of heterolithic material in central Alberta, reflect pockets of increased quartz content and indicate locations in the basin where muddy sediment was winnowed from storm-wave events. The presence of calcareous mudstone illustrates where marine conditions favoured deposition of biogenic carbonate and the input of mud and silt sediment was limited.

6.3.3 Allomember IX

The lithology maps in Figures 6.20 and 6.21 show non-calcareous mudstone as the dominant lithology across allomember IX. Heterolithic sandstone and mudstone is observed as isolated pockets and calcareous mudstone is limited to southwestern Alberta with localized deposits in central and northwestern Alberta.

Interpretation

The distribution of heterolithic sandstone and mudstone in northern Alberta relative to allomember VIII suggests that the sea-floor in this part of the basin was subjected to frequent storm reworking, possibly in response to accommodation loss through uplift, or accommodation was filled as quickly as it was created (Varban and Plint, 2008b). Southeasterly along-shelf and across-ramp mud transport continued during this time. The overlap of calcareous mudstone and the implied depocentre between Townships 30 and 35, Ranges 05 and 10W5 suggests that the lithology change may be linked to tectonically-influenced clastic-starvation. The patches of calcareous mudstone located along Township 45 and surrounded by mudstone could reflect zones of calcareous and non-calcareous siliciclastic deposition patterns due to ocean front mixing or limited data available for log analysis (i.e. no photoelectric log available). The distribution of mudstone southeast of the depocentre may reflect redistribution of siliciclastic-dominated sediment in response to uplift.

6.3.4 Allomember X

In allomember X, there is a shift from minimal to maximal areal coverage of calcareous mudstone along the western edge of the study area, parallel to the deformation front

Allomember IX - “Blue” bentonite to regional flooding surface

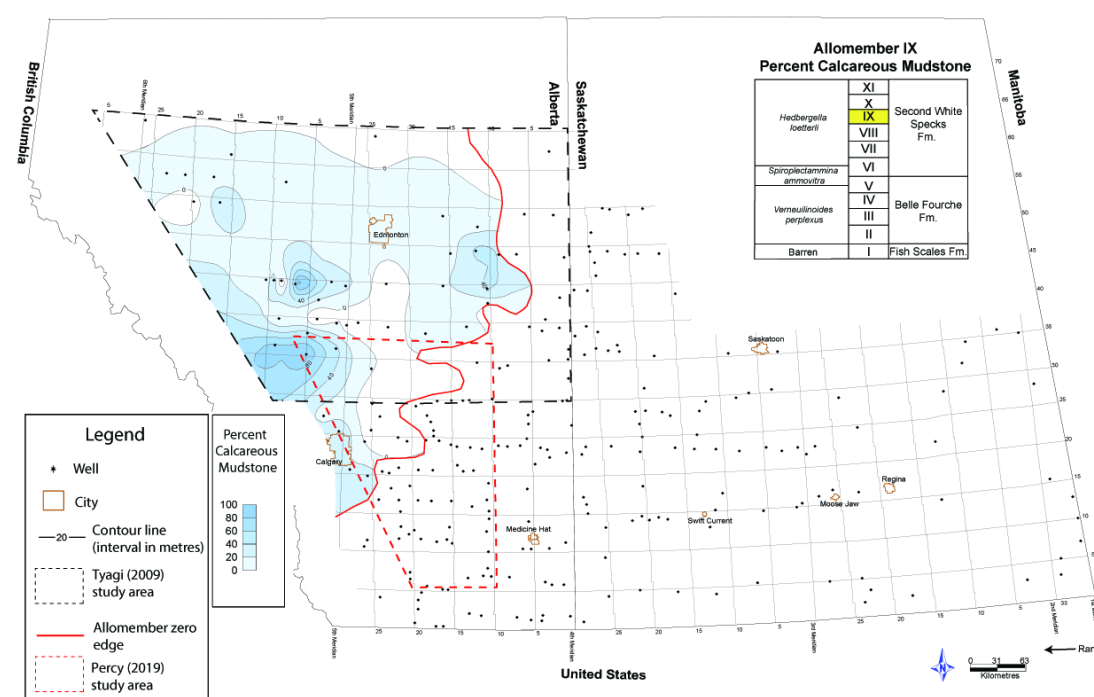
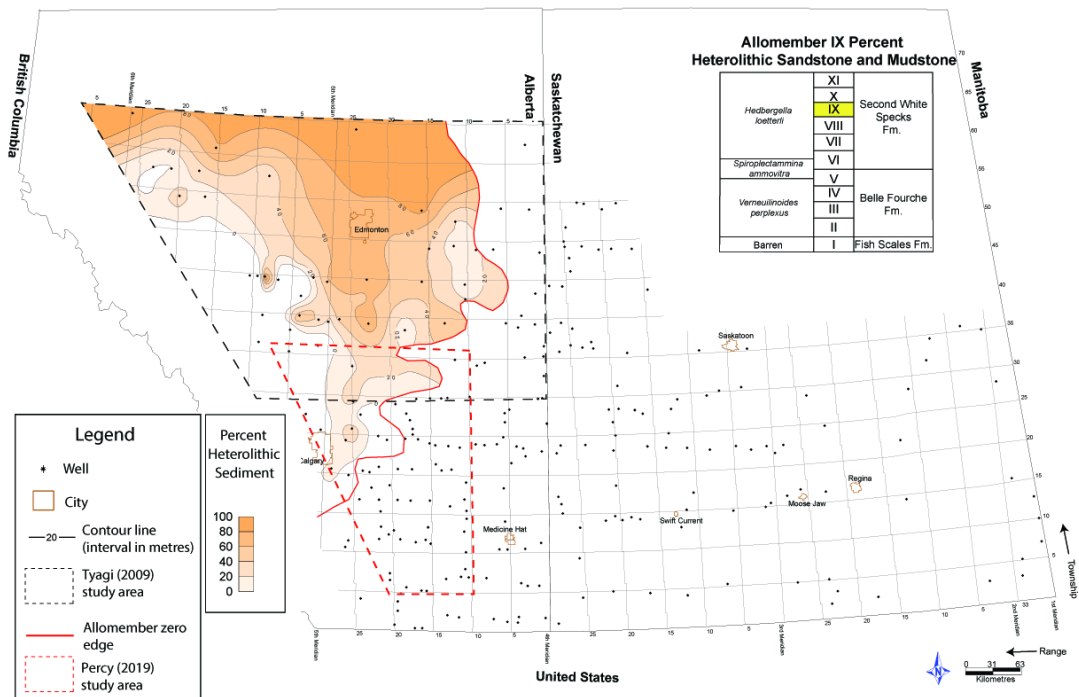
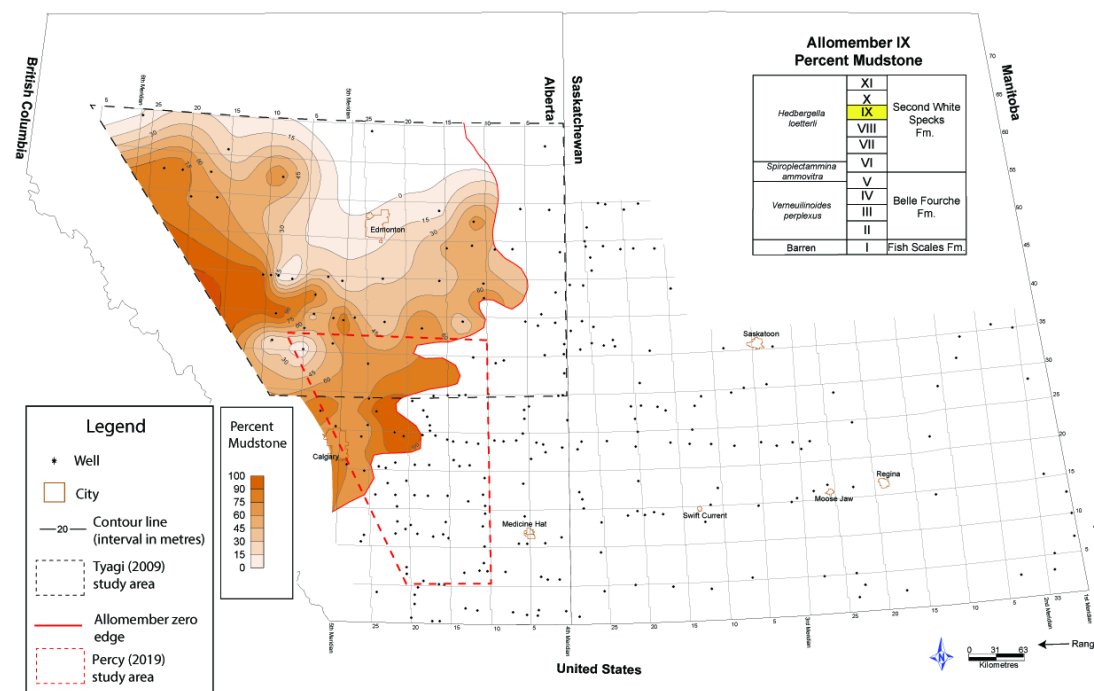


Figure 6:20: Allomember IX percent lithology maps.

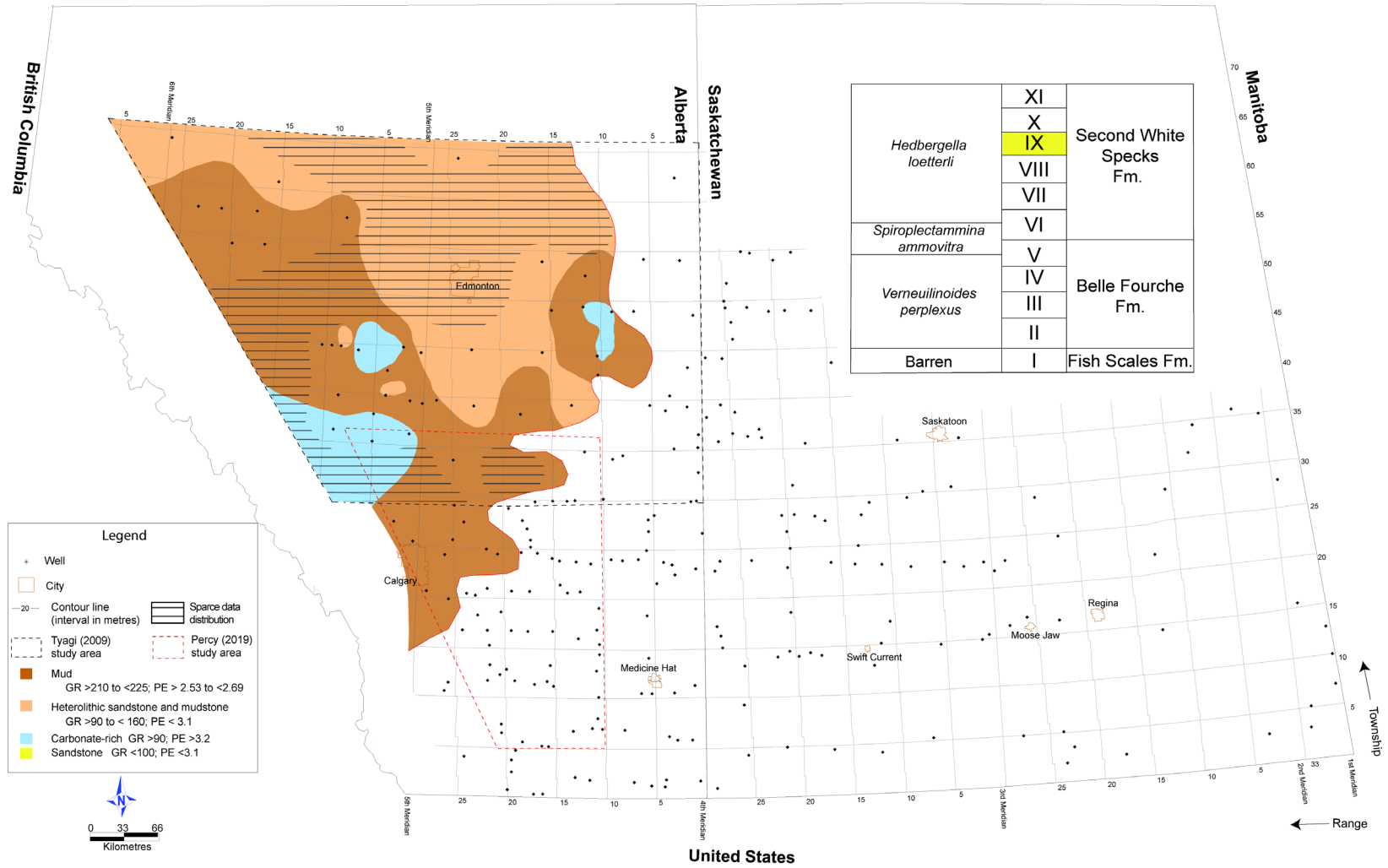


Figure 6:21: Allomember IX percent lithology summary map.

Allomember X - Regional flooding surfaces

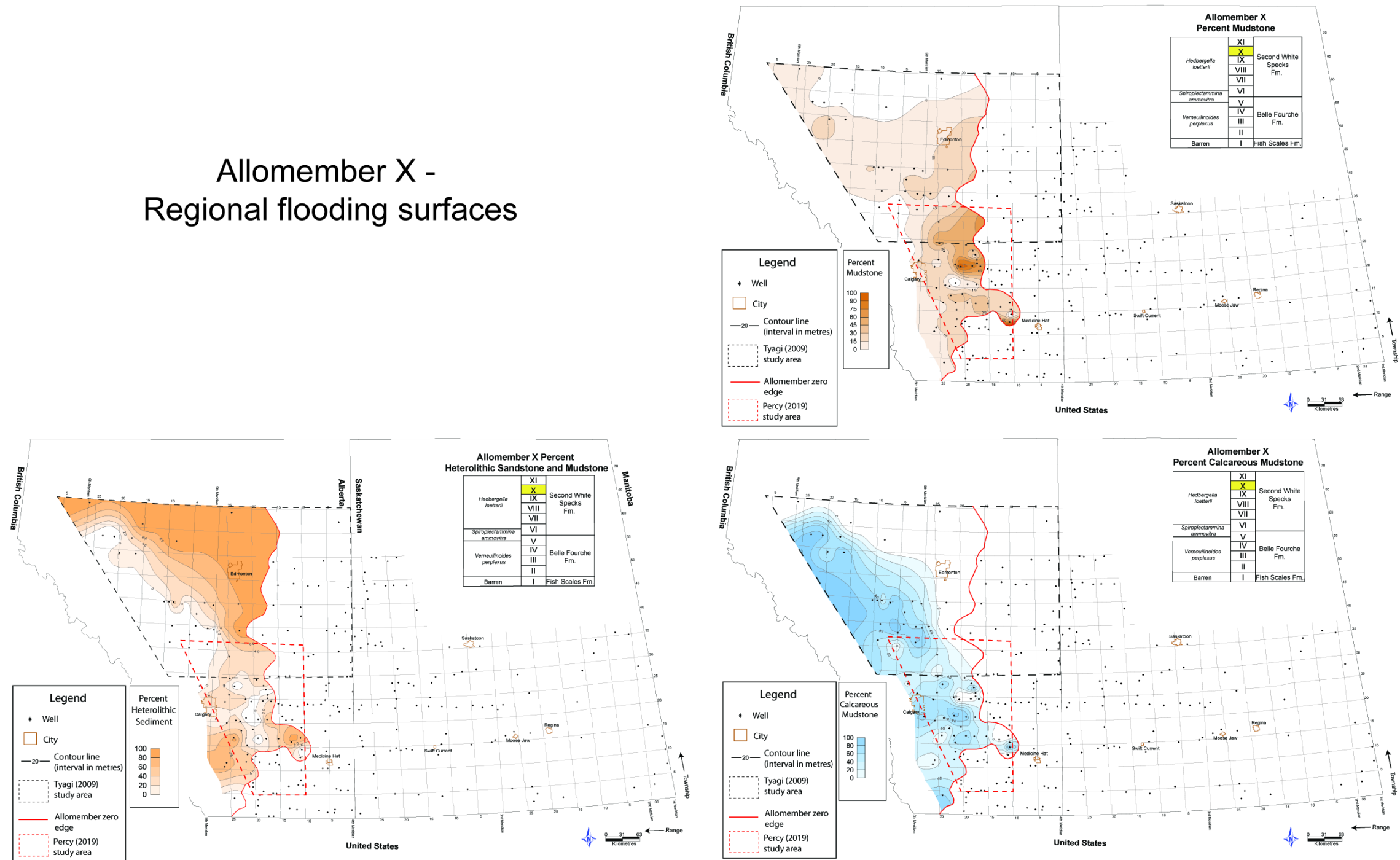


Figure 6:22: Allomember X percent lithology maps.

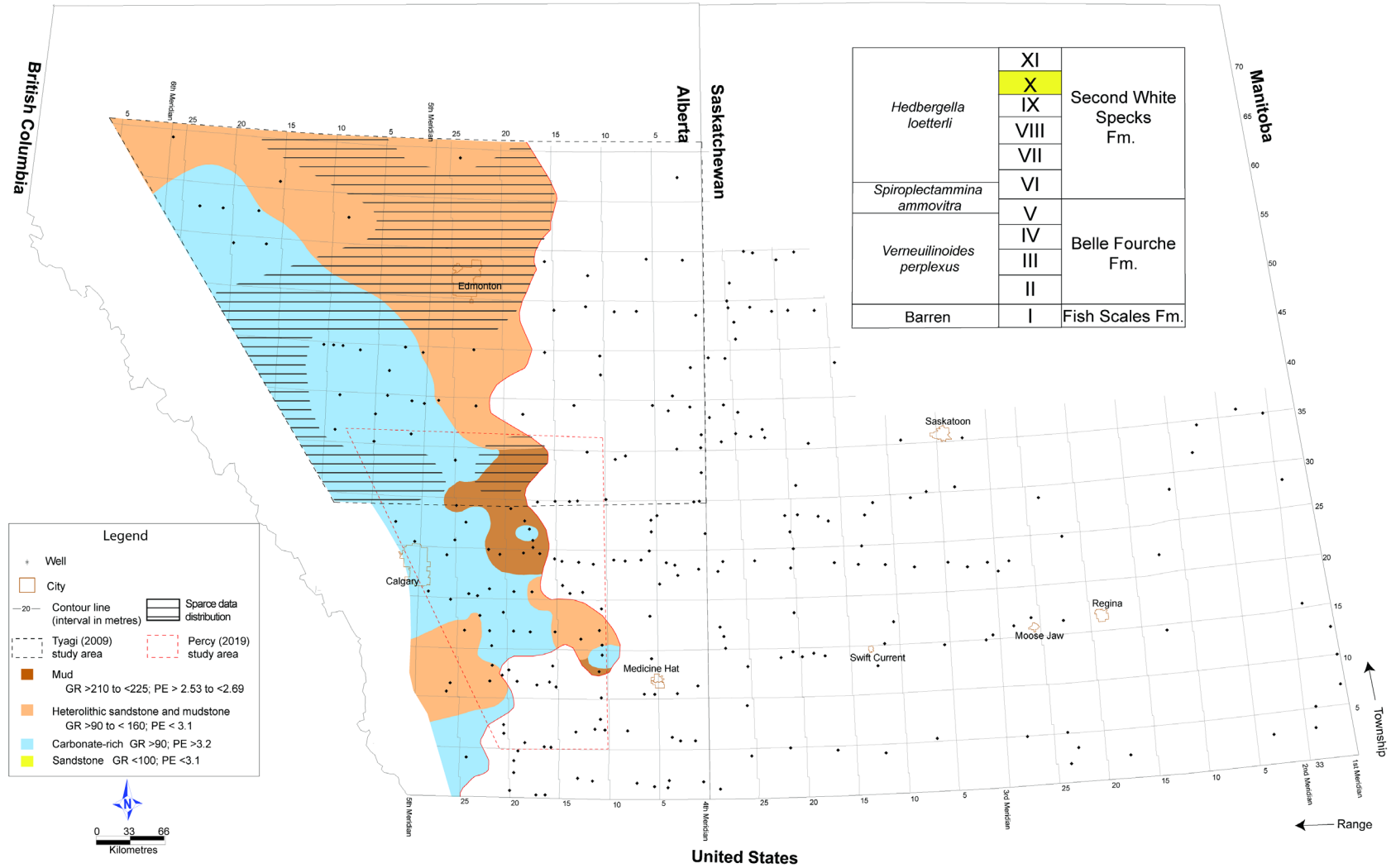


Figure 6:23: Allomember X percent lithology summary map.

(Figure 6.22 and 6.23). Heterolithic sandstone and mudstone deposits are found in three regions: In the northern and southern depocentre areas and adjacent to the northwest-southeast allomember thickening trend. An isolated patch of mudstone occurs in central Alberta, west of the zero edge.

Interpretation

The distribution of calcareous mudstone trending parallel to the deformation front implies that marine conditions favourable for primary productivity (including the proliferation of calcareous phytoplankton) was dominant during the final stage of the Greenhorn cycle. The calcareous mudstone deposit also records a time of prominent and rapid flexural subsidence in the west that prevented progradation of nearshore clastics (Varban and Plint, 2008b).

The heterolithic lithology belt running parallel to the northwest-southeast thickening trend (Figure 6.23) is located on the proximal side of an uplifted forebulge region. The large area occupied by the heterolithic deposit implies that accommodation loss through flexural uplift may have outpaced gains in accommodation through eustatically-driven sea level rise and promoted sediment reworking below storm-wave base. Heterolithic deposits overlying the two depocentres (in northwest and southwest Alberta) were dispersed seaward by combined flows during a lower rate in relative sea-level rise (Varban and Plint, 2008a), where the rate of subsidence did not exceed sedimentation rates and allowed accommodation to be filled as quickly as it was created.

6.3.5 Allomember XI

In allomember XI, calcareous mudstone is the dominant lithology across the study area, with scattered patches of non-calcareous mudstone and heterolithic sandstone and mudstone in southern Alberta and into Saskatchewan (Figures 6.24 and 6.25). A broad belt of heterolithic sandstone and mudstone in northern and central Alberta mimics the pattern observed in allomember X, with a slightly expanded western limit.

Allomember XI - Regional flooding surface to "Green" bentonite

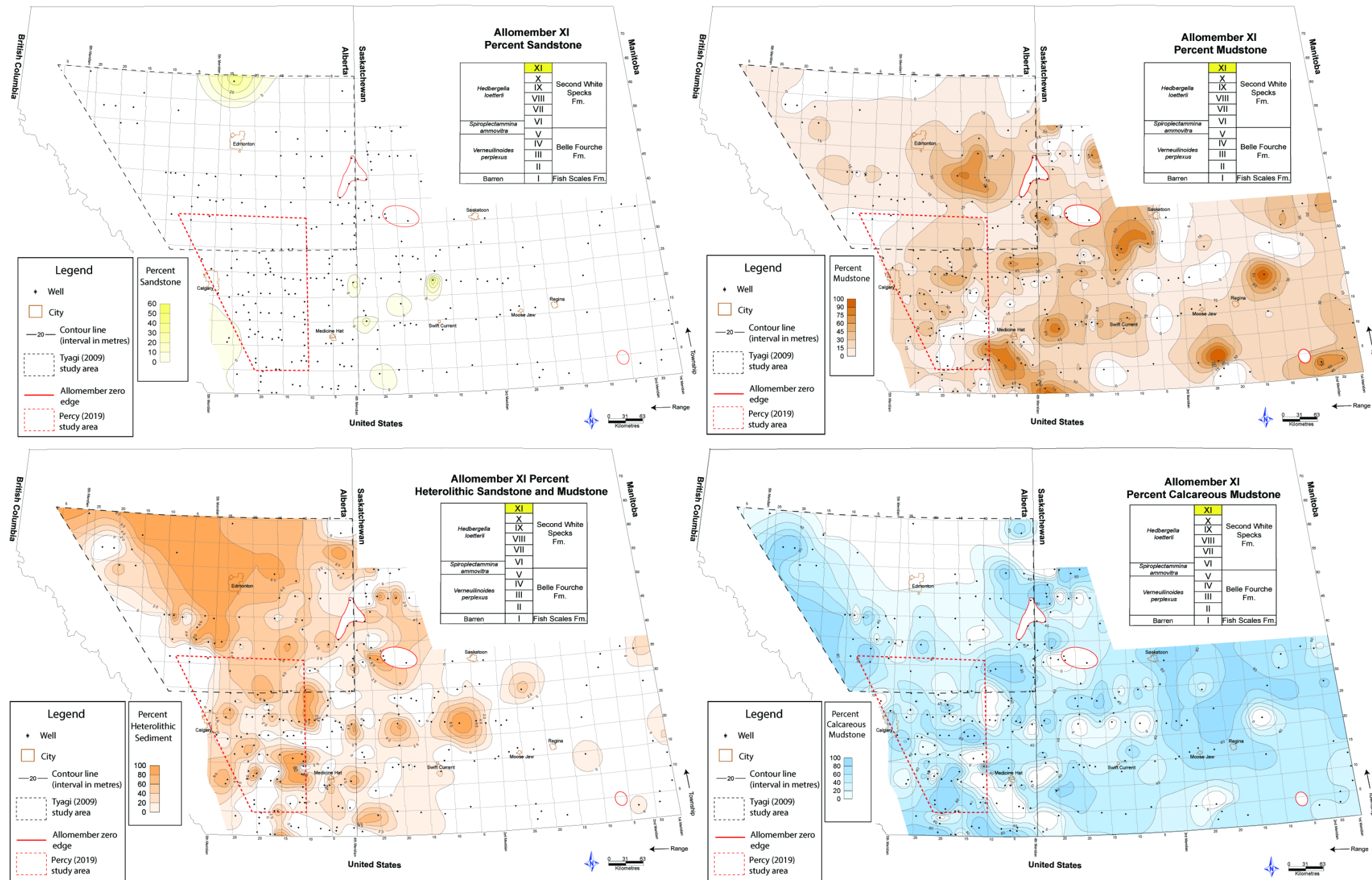


Figure 6:24: Allomember XI percent lithology maps.

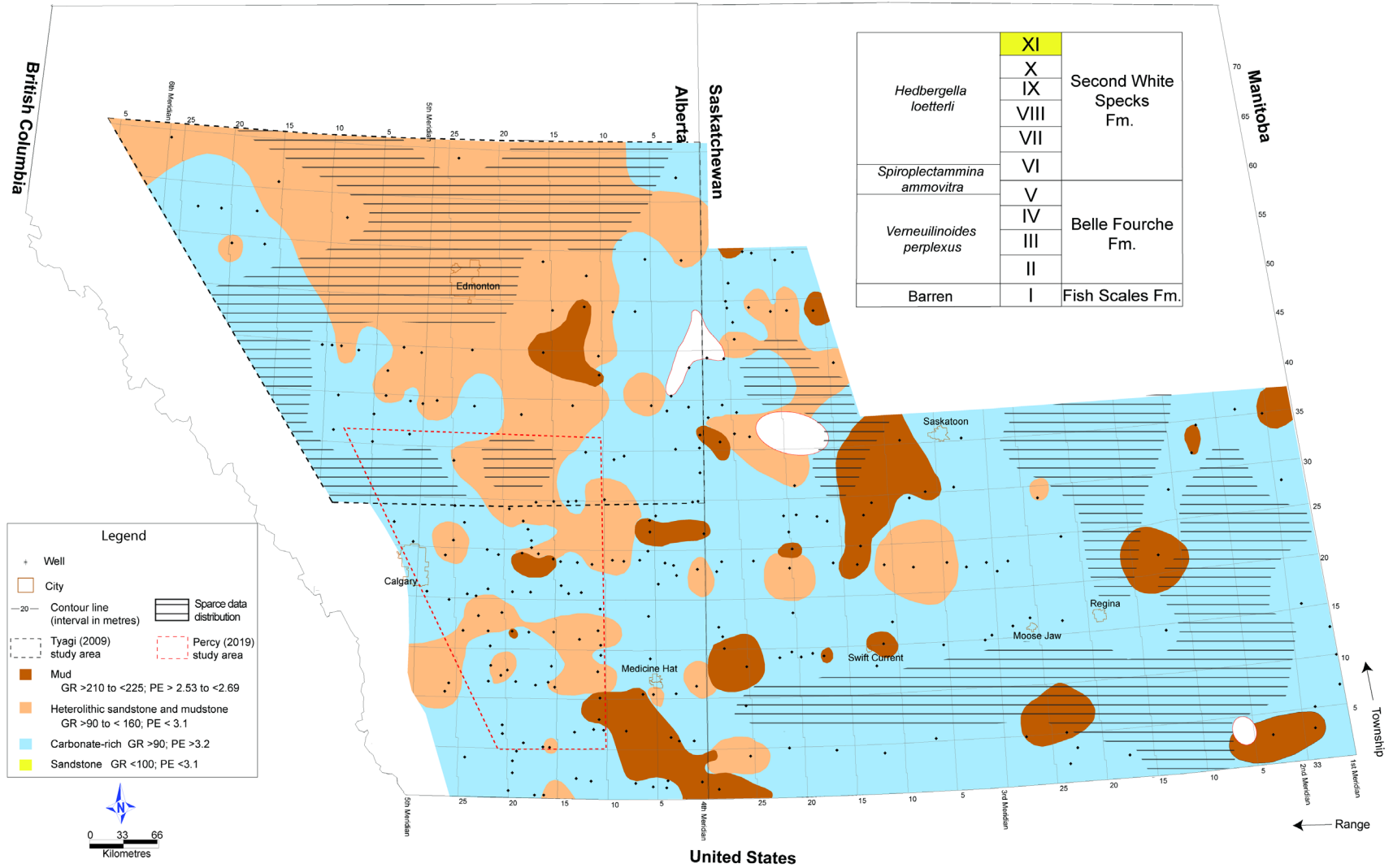


Figure 6:25: Allomember XI percent lithology summary map.

Interpretation

The calcareous mudstone and heterolithic sandstone and mudstone distribution pattern in northern and western Alberta suggests similar depositional conditions experienced in this part of the basin for allomember X. During deposition of allomembers X and XI, eastward progradation of sandstones and westward migration of offshore mudstones was rare (Varban and Plint, 2005; Varban and Plint, 2008a). The relatively stable positioning of the mudstones and shoreface sandstones mapped northwest of the study area for both allomember X and XI implies sediment supply and accommodation rates were close to equilibrium. The prominence of heterolithic sandstone and mudstone in northern to central Alberta extends in a northwest-southeast trajectory, across the northwestern depocentre that lies within the Ksituan (KS) domain and the northeastern arm of the central Alberta backbulge region. Overlap of heterolithic material and the identified depocentres suggests that any increase in accommodation related to subsidence was matched by the sedimentation rate. It also indicates that sediment was efficiently distributed geographically, enabling the continued existence of a broad, shallow ramp that fostered storm wave influence on the sea floor and the offshore transport of re-suspended sediment (Varban and Plint, 2008a). Isolated occurrences of mudstone and heterolithic sandstone and mudstone within the calcareous mudstone in Saskatchewan and southwestern Alberta indicate the mixing of water masses and preserved strata where sediment was deposited within storm wave base, respectively. Subtle changes in accommodation in Saskatchewan and southwestern Alberta likely record modest changes in relative sea-level within the stable craton region of the basin.

Chapter 7

7 Organic geochemistry data collection and evaluation methods

Rock-Eval is a laboratory-based method used to quantify and characterize organic matter in sedimentary rocks (Behar et al., 2001). It uses programmable pyrolysis to measure pyrolysis parameters (discussed in section 7.4.1) and calculate the total organic carbon, organic matter type and hydrocarbon-generative potential (thermal maturity) of petroleum source rocks. The LECO SC-444 (LECO) apparatus analyzes carbon elemental concentration in samples by induction combustion-IR detection, using the amount of expelled carbon dioxide from the combustion process to determine organic carbon content of a sample. This chapter reviews the origin and preservation factors of organic matter in marine rocks, describes data sources for the geochemical database used in this study, and summarizes logistical and data limitations associated with Rock-Eval and LECO analyses. The final section describes methods to characterize the organic geochemistry data and the methods and limitations associated with calculating the original total organic carbon.

7.1 Origin of organic matter in marine mudstones

Kerogen is organic material that is insoluble in organic solvents, water or oxidizing acids, whereas the soluble portion of organic material in organic solvents is bitumen (Bjørlykke, 2010). Strata rich in kerogen are called source rocks owing to their capability to generate and expel petroleum products when exposed to rising temperatures (with increasing depth of burial) in the subsurface. Oil is generated from kerogen when thermal conditions reach temperatures of 100-150 °C. As subsurface temperatures reach 150-180°C, the oil cracks to wet gas (containing a significant proportion of hydrocarbon compounds heavier than methane) and eventually converts to dry gas (predominantly methane) at temperatures of 150-220°C (Allen and Allen, 2005). The concentration of organic matter in source rocks is related to three main variables: supply (production), preservation, and dilution by silt, clay and/or bioclastic material (Tyson, 2001). Organic matter is produced in both terrestrial and aquatic environments, with the latter providing conditions with a greater

tendency to promote its preservation and accumulation owing to reduced rates of oxidation and microbial degradation. In marine settings, organic matter is primarily supplied by photosynthetic algae and cyanobacteria in the water column (autochthonous), by fluvial or eolian transport of terrigenous plant material (allochthonous), and/or by the reworking and re-deposition of organic matter sourced from older sedimentary rocks (Arthur and Sageman, 1994; Bjorlykke, 2010).

Primary productivity in the ocean is controlled by solar radiation and nutrient supply in the photic zone, which ranges in thickness from 100 to 200 metres in the open ocean to a few metres in turbid, nearshore waters (Pedersen and Calvert, 1990). Here, marine-based organic material is produced by phytoplankton in the water column (Pedersen and Calvert, 1990; Suter, 2006). Smaller contributions of organic matter are made by zooplankton and benthic and nektonic macrofauna (Allen and Allen, 2005). Phytoplankton that is not immediately oxidized can be eaten by zooplankton that, in turn, can be eaten by larger marine organisms. The latter ultimately excrete indigestible components as fecal pellets that further contribute to the organic matter content of sea floor sediment (Bjorlykke, 2010). In addition to sunlight (in the photic zone) and nutrient supply, the amount of marine organic matter produced in the ocean also depends on salinity and water temperature (Arthur and Sageman, 1994; Allen and Allen, 2005).

Nutrients that contribute to primary production (e.g., nitrogen, phosphorous, and iron) are supplied to the ocean via river plumes (refer to section 3.4) and/or upwelling, with the intensity of the nutrient supply largely dependent on latitude (Katz, 2005; Suter, 2006). For river-based nutrient contribution, latitude is important as stream runoff relies on the relative rates of precipitation and evaporation (Ghadeer and Macquaker, 2012; Bohacs et al., 2005; Katz, 2005). Upwelling occurs where wind-driven surface waters flowing parallel to the coastline are deflected offshore by Coriolis force (refer to section 3.2), causing deep ocean water to replace the offshore-flowing surface water (Allen and Allen, 2005). This process produces a high nutrient flux of nitrogen and phosphate that ultimately stimulates growth of phytoplankton in the photic zone (James and Lukasik, 2010). At mid-latitudes, productivity is low because upwelling is limited, and the warm

surface water is consistently separated from the cold deep waters. In contrast, equatorial regions undergo moderate, but sustained primary productivity, as surface water is driven away from the equator and upwelling ensues (Pederson and Calvert, 1990). At polar latitudes, high primary productivity rates occur in spring and summer after winter winds have mixed and fertilized surface waters, and the increased exposure time to sunlight has expanded the euphotic zone and warmed surface layers (Pederson and Calvert, 1990).

Accumulation of organic matter occurs when rates of production and preservation outweigh the rates of degradation and dilution (Fig. 7.1) (Bohacs et al., 2005).

Degradation processes include oxidation as the organic matter settles into deeper water, consumption by infauna, remineralization, and bacterial decay in the sea floor sediments (Katz, 2005). Organic matter that reaches the sea floor is either buried or resuspended by waves and/or currents (Suter, 2006). Although preservation processes vary between regions depending on productivity levels, water depth, sedimentation rates, and availability of oxidants (Pederson and Calvert, 1990), organic matter preservation is enhanced when exposure time to oxygen and heterotrophic organisms is limited (Arthur and Sageman, 2005; Katz, 2005; Burdige, 2007; Zonneveld et al, 2010).

Rapid settling of organic matter through the water column and rapid burial of organic matter at the sea floor can reduce exposure to oxygen and biological degradation. For organic-rich mud, increased settling time to the seafloor through the formation of organomineralic aggregates (OMAs) enhances organic matter preservation (Macquaker et al., 2010; Ghadeer and Macquaker, 2012). OMAs are the ancient equivalent to the “marine snow” observed in modern marine settings. The term “marine snow” refers to suspended organic-rich particulate matter in the ocean that forms, during periods of high primary production and/or phytoplankton blooms, as aggregates of organic detritus, micro-organisms, and clay minerals (Fig. 7.2) (Alldredge and Silver, 1988; Macquaker et al., 2010). OMAs are loosely held together by a combination of electrochemical attraction between grains, biologically enhanced aggregation of smaller components (i.e., phytoplankton, fecal pellets, micro-aggregates, and inorganic particles) and physical interlocking of irregularly shaped grains resulting from their random collision

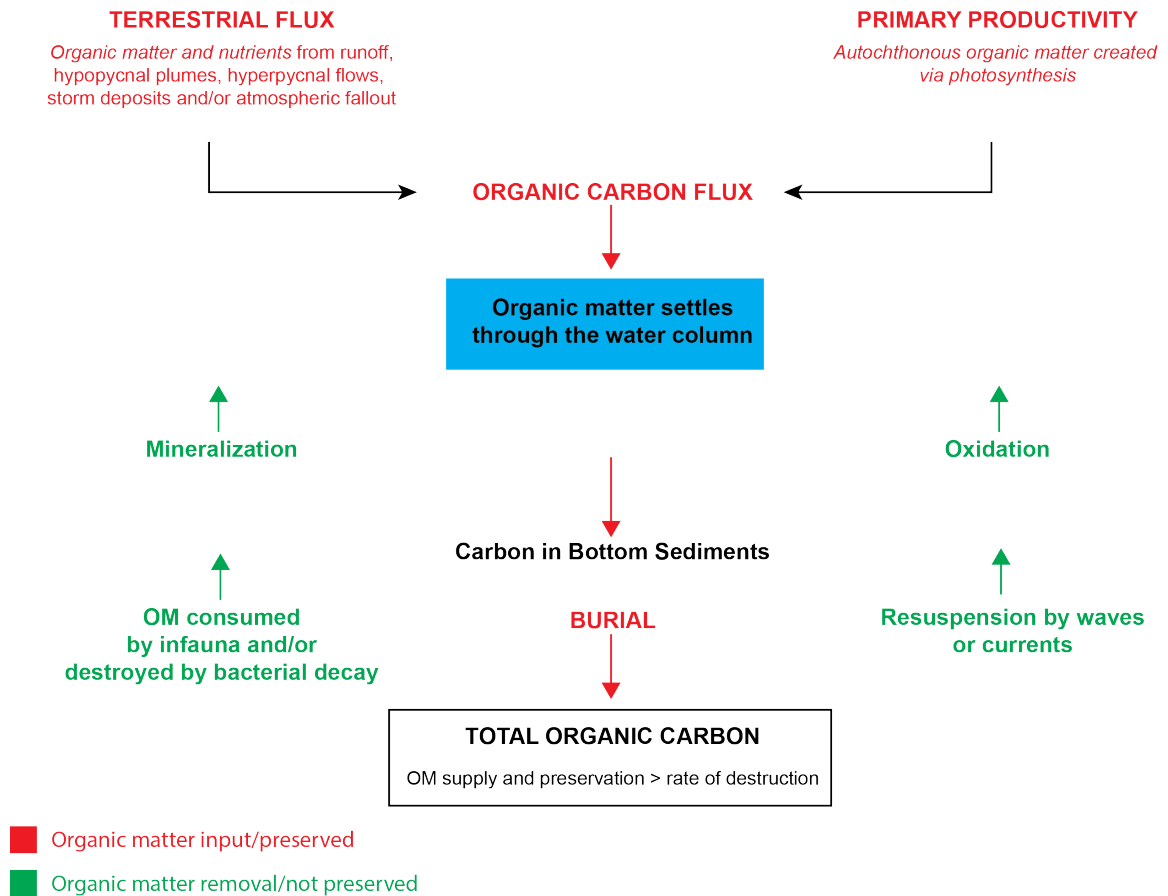


Figure 7:1: Schematic of the factors that influence production of organic carbon in marine sediments. Modified from Suter (2006).

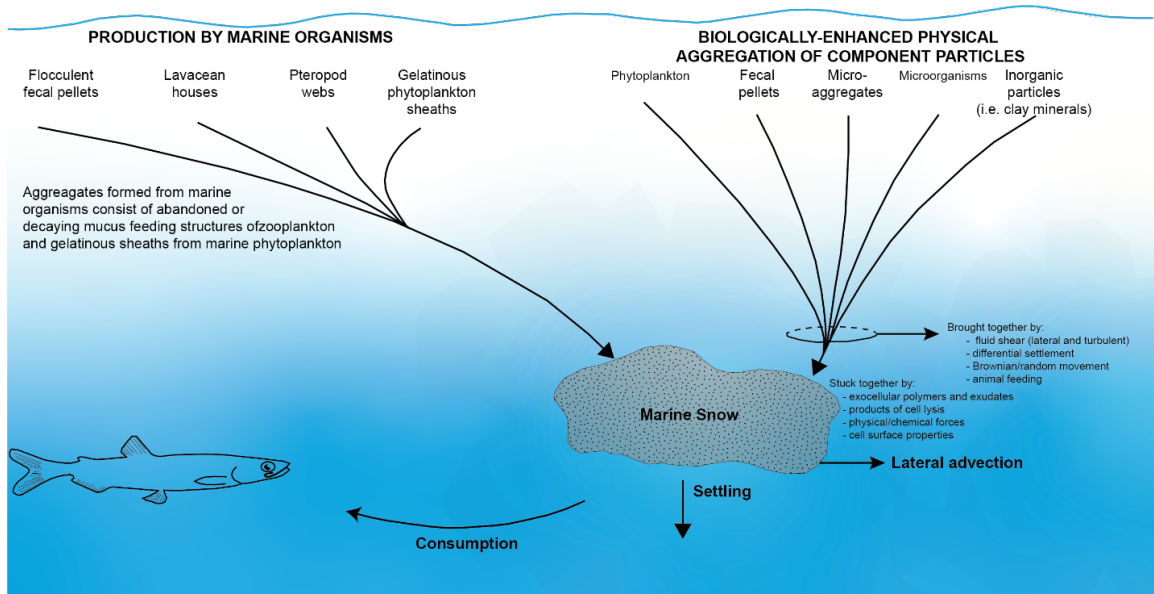


Figure 7:2: Illustration depicting the production of marine snow. Modified from Alldredge and Silver (1988).

Macquaker et al., 2010). Formation of these large composite aggregate grains ($>500\mu\text{m}$) allows the organic matter to settle rapidly through the water column to the seafloor (Fowler and Knauer, 1986; Alldredge and Silver, 1988; Simon et al., 2002), limiting its exposure to degradation processes and promoting its preservation (Buridge, 2007). In addition to increasing its settling rate, the encapsulation of reactive organic matter into OMAs provides a physical barrier and protection against chemical or biological degradation that can happen as the aggregates travel through the water column (Alldredge and Silver, 1988; Buridge, 2007).

It is generally agreed that high sedimentation rates improve organic matter burial efficiency and reduce exposure time to degradation (chemical or biologically) (Katz, 2005). Tyson (1995; 2001) recognized that to promote preservation of organic matter at the sea floor, a balance must exist between sedimentation rate and dissolved oxygen conditions. Sedimentation rates of less than 5 cm/1000 years in oxic settings reflect the best scenario for organic matter preservation, with greater sedimentation rates causing dilution (Tyson, 1995). Slow sedimentation rates in oxic settings result in minimal organic matter preservation, whereas in an anoxic setting, a slow sedimentation rate would provide protection against degradation agents and minimize dilution (Tyson, 1995). At rates $> 30\text{-}35$ cm/1000 years, the level of preservation is inevitably high regardless of the level of bottom-water dissolved oxygen (Tyson, 1995). It is noted that, even under oxygen-deficient conditions and an adequate sedimentation rate to enhance burial, the preservation of organic-carbon rich deposits at the sea floor can be diminished via physical mixing by storm-derived turbulent bottom currents or by biological mixing by macro-organisms that periodically reintroduce oxygen, nutrients, or transport organic matter between redox zones (Arthur et al., 1998; Arthur and Sageman, 2005; Zonneveld et al., 2010; Ghadeer and Macquaker, 2012).

Low-oxygen conditions in sediment porewaters and bottom-water settings play an important role in organic matter preservation. Dysoxia refers to reduced-oxygen conditions and anoxia refers to conditions characterized by dissolved oxygen contents of < 1 ml/l of dissolved oxygen, below which the abundance, size and activity of benthos is significantly reduced.

Tyson (2005) described three scenarios in which organic matter can be rapidly transferred into a permanent anoxic environment and preserved: 1) porewaters and lower water column can rapidly become anoxic due to an increasing supply of organic matter that raises the demand for oxygen (autodilution by biogenic minerals); 2) rates of sediment deposition can increase, allowing for the degradation of organic matter within the sediment and development of anoxic porewater conditions (siliciclastic dilution and greater supply of terrestrial-based organic matter); and 3) watermass stratification reduces oxygen resupply from vertical mixing to levels approaching (but not meeting) oxygen demand, causing dysoxic-anoxic conditions to extend downward into the lower water column. As dead organic matter settles out towards the sea floor, aerobic bacterial respiration degrades the material and removes oxygen from the water column. An increased rate of organic matter decay, combined with a stratified water column, would cause bottom waters to become dysoxic to anoxic and result in an oxygen minimum zone (OMZ). “Black shale” deposition associated with marine transgression and slow sedimentation rates has been attributed to the downward extension of dysoxic-anoxic conditions to the lower water column (Arthur and Sageman, 1994; Tyson, 2005; Arthur and Sageman, 2005). Arthur and Sageman (2005) have cited rising sea level (transgression) in epeiric seas and the expansion of an OMZ from the open ocean as a major control on organic matter burial. During sea level rise, reduced ventilation in the water column caused from deepening combined with water column stratification, transgressive condensation, and expanding spatial limits of anoxic water (OMZ) from the interplay between a deepening water column and decreased sedimentation rate all influenced organic matter content in the Western Interior Seaway during the Cretaceous (Arthur and Sageman, 2005).

7.2 Geochemical database

Geochemical data used in this study are obtained from two sources: rock samples collected from logged core, and public domain datasets (legacy data). Legacy information was compiled from the following reports: Beaton et al., 2009; Bloch and Leckie, 1993; Bloch et al., 1999; Fowler and Snowdon, 1998a; Fowler and Snowdon, 1998b; Snowdon, 1994a; Snowdon, 1994b; Snowdon, 1995; Snowdon and Riediger, 1995a; Snowdon and

Riediger, 1995b; Snowdon, 1996; Snowdon, 1997. Data were filtered out of the database if the samples were located outside of the stratigraphic interval being investigated and/or the total organic content (TOC) was less than 0.3%. All measured and calculated parameters from Rock Eval are considered questionable if samples have TOC values less than or equal to 0.3% (Peters, 1986). Additional limitations related to Rock Eval outputs are discussed in section 7.3.3.

7.2.1 Sample collection

Cores included in this project were selected from a public domain database of oil and gas wells for Alberta and Saskatchewan using geoSCOUT[®] software. Database search criteria identified wells cored in the Second White Specks through Fish Scales interval. Wells were selected based on the length of continuous core, quality of geophysical well logs (gamma ray, resistivity, density and neutron porosity, and photoelectric), and whether the well location filled data-gaps in areas of poor legacy geochemical data coverage. Eighteen wells were selected for evaluation based on these criteria. The longest core interval sampled for this study (100/07-19-045-06W5) is over 76 metres and the shortest (100/16-28-041-04W5) is slightly over five metres in length (Table 7.1).

A total of 408 samples were collected from cores for analysis (Table 7.1); 241 samples from the Alberta Energy Regulator Core Research Centre in Calgary, Alberta and 167 from the Saskatchewan Subsurface Geological Laboratory in Regina, Saskatchewan. Sampling constraints for wells 131/11-09-017-23W2 and 121/06-35-013-13W3 resulted in no sample collection or analysis performed, respectively. Samples were collected at 1- to-3-metre intervals, with some having greater spacing based on core sampling restrictions imposed by facility operators. Sample sizes ranged from small, thin flakes/chips to solid, disks of core. The flake/chip samples were collected from loose pieces of rock positioned within a relatively intact core, to ensure the stratigraphic location of the sample was known. Disks of core, 1 to 5 cm thick, were collected from intact core intervals, at the discretion of facility operators. A reference line was drawn on the rock sample to show top-of-core orientation when the sample size was large enough and collected from an intact piece of core. Core orientation was not applicable to this study; however, it was done to ensure the information was available if future evaluations

performed on the samples required it. Collected samples were placed in resealable, plastic storage bags and labeled with the well location (UWI), core depth, and sample number.

7.2.2 Sample preparation

Rock-Eval 6 analysis was conducted on 147 samples collected from wells 100/07-19-045-06W5, 141/07-34-035-01W2, and 111/03-22-055-25W3. Sample preparation for pyrolysis analysis required approximately one gram of the rock sample be manually crushed in an agate mortar and pestle, and ground until a uniform consistency was achieved. The pulverized sample was transferred into a 12.5 ml plastic vial and labeled accordingly. The Rock-Eval 6 analyses were performed at the Geological Survey of Canada Laboratory in Calgary, Alberta. Additional sample preparation was conducted by the laboratory technician if it was required.

TOC was determined for 258 samples from 13 wells (Table 7.1) using a LECO CS-244 dry combustion and infrared carbon analyzer. This analysis was performed at the Biotron Experimental Climate Change Research Centre at Western University, London, Ontario. Prior to submission to the Biotron laboratory, the rock samples were pulverized into a powder-consistency using a vibratory ring pulverizer, and then transferred into labelled 12.5 ml plastic vials.

7.3 Rock-Eval pyrolysis

Rock-Eval was originally developed by the Institut Français du Pétrole (IFP) (Espitalié et al., 1977) and later modified to Rock-Eval II, a system that provided more analyses per unit of time and was easier to operate (Peters, 1986). Rock-Eval 6 is the most recent version of the analytical system, its design modified to improve the measurement of temperature along the heating program and incorporating a measurement of carbon dioxide effluents to better differentiate between mineral and organic carbon (Behar et al., 2001). This study incorporates data from samples collected using both Rock-Eval II and Rock-Eval 6; therefore, a brief description of the operational differences between the two systems is discussed below.

Table 7.1: List of cores examined in this study, number of samples collected and the organic matter analysis type.

<i>Alberta (UWI)</i>	<i>Number of Samples</i>	<i>Core length (m)</i>	<i>Analysis Type</i>	<i>Saskatchewan (UWI)</i>	<i>Number of Samples</i>	<i>Core length (m)</i>	<i>Analysis Type</i>
100/14-07-036-05W5	12	7.5	LECO	141/07-34-035-01W2	53	38.35	Rock-Eval6
100/07-19-045-06W5	72	76.48	Rock-Eval6	111/03-22-055-25W3	23	18.25	Rock-Eval6
100/16-28-041-04W5	4	5.14	LECO	142/05-08-028-28W3	30	28.5	LECO
100/11-12-006-16W4	9	26.82	LECO	101/16-23-023-28W2	26	18.88	LECO
102/07-04-028-18W4	19	38.5	LECO	101/06-11-014-26W3	7	15.55	LECO
103/06-04-017-13W4	56	79	LECO	121/06-35-013-13W3	2	17	not analyzed
100/02-34-024-15W4	9	33	LECO	101/06-15-015-13W2	10	17.25	LECO
102/16-18-023-03W4	37	26.5	LECO	131/11-09-017-23W2	none	28	none
100/06-23-043-11W4	23	17.5	LECO	101/06-28-029-24W2	16	14.8	LECO

In Rock-Eval 6, the programmed heating is conducted over a temperature range of 100-850°C, compared to the 180- 600°C range used for Rock-Eval II. A higher final temperature is necessary for total thermal degradation of terrestrial-based organic matter and for a more reliable measurement of the generative capacity of the rock (Hart and Steen, 2015; Lafargue et al., 1998). Increased temperatures also reduce the risk of incomplete combustion of refractory material and allow for the determination of mineral carbon in samples (Behar et al. 2001). The reduction in the initial pyrolysis temperature to 100°C permits detailed study of free hydrocarbons that are expelled during the early heating phase of the program (Behar et al., 2001; Lafargue et al., 1998). Differences in the limitations of the two systems are presented in section 7.3.3.

Total carbon (TC) in a rock comprises both organic and inorganic material. The total organic carbon (TOC) component is biologically derived carbon composed of hydrocarbons and kerogen. Three types of organic matter — extractable, pyrolyzable and residual carbon — are measured by Rock-Eval, and represented by the S1, S2 and S4 curves, respectively (Figure 7.3). Tmax is a measured variable that represents the temperature at which the maximum amount of pyrolysate hydrocarbon (S2) is produced during the procedure and is used as a relative indicator of thermal maturity in a sample. The following section summarizes the Rock-Eval 6 pyrolysis process and introduces additional parameters produced during the procedure. Parameters calculated using outputs measured during heating are discussed in section 7.3.2.

7.3.1 Rock-Eval 6 pyrolysis

Rock-Eval 6 uses both pyrolysis and oxidation ovens to assess source rock potential (Figure 7.4). During pyrolysis, 70 mg of pulverized rock is placed in an inert atmosphere of nitrogen and gradually heated to a maximum temperature of 650°C. A flame ionization detector (FID) monitors and records the expulsion of hydrocarbons. The sample is initially pyrolyzed between 100°C and 300°C for less than five minutes, allowing free hydrocarbons present in the sample prior to pyrolysis to be released (S1 peak, Figure 7.4). As programmed heating continues at 25°C/minute up to 650°C, the thermal breakdown of

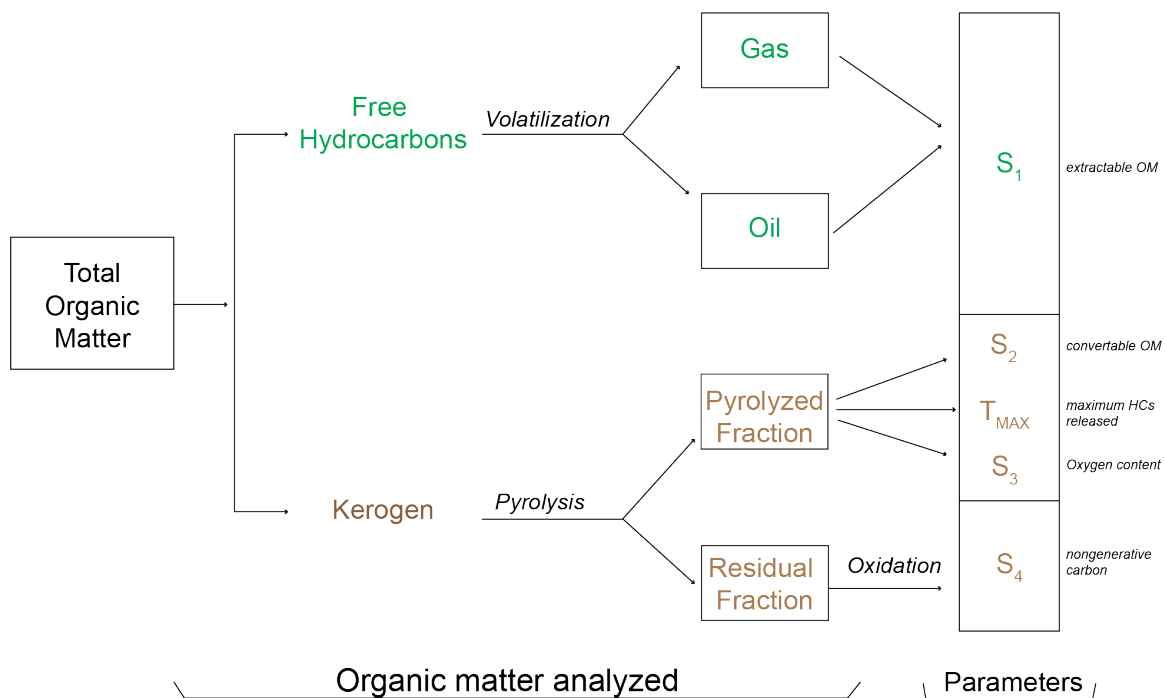


Figure 7:3: Diagram of organic matter analyzed, and the associated variables produced during Rock-Eval 6 pyrolysis. OM = organic matter. HCs = hydrocarbons. (Modified from Lafargue *et al.*, 1998).

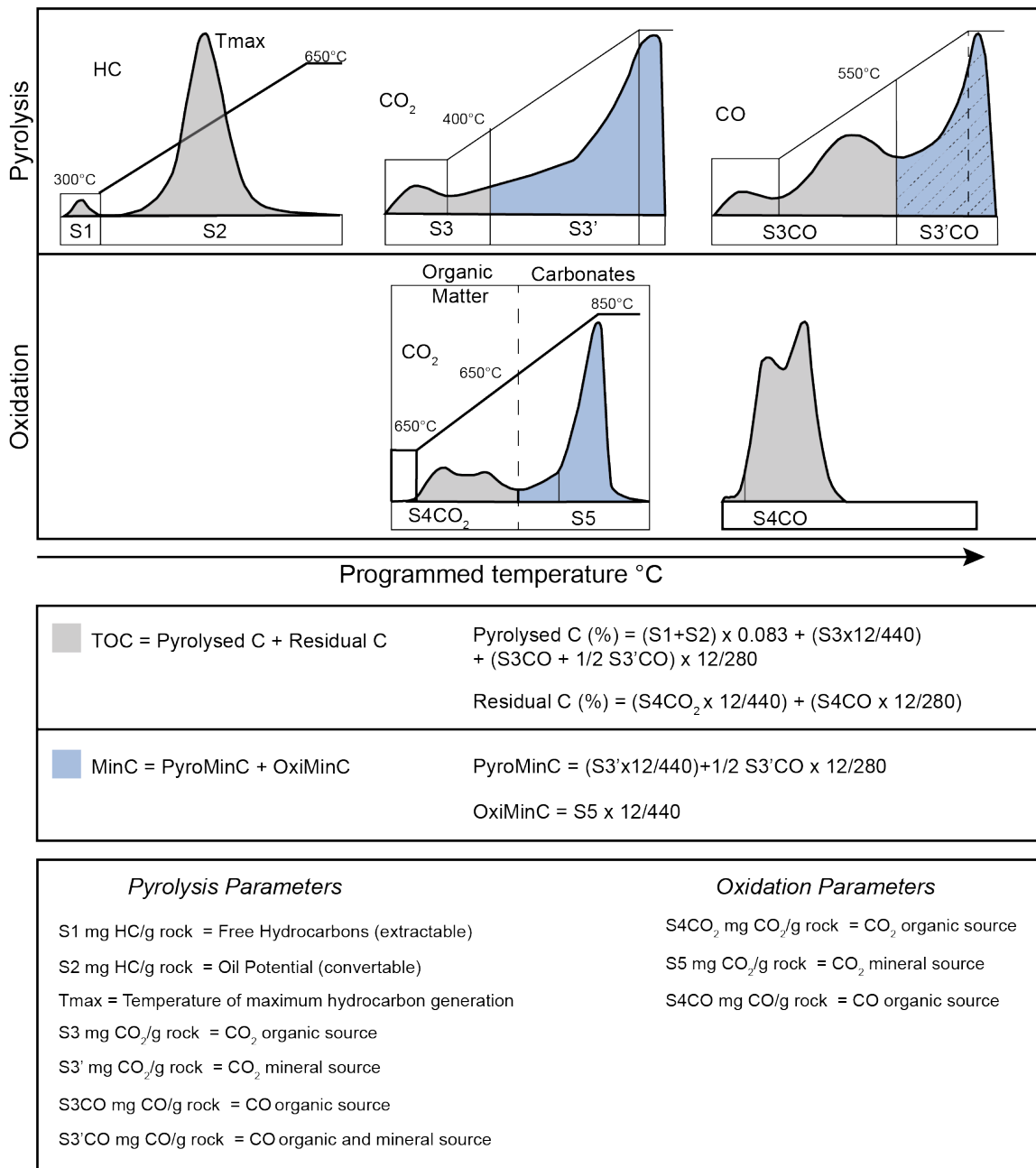


Figure 7:4: Graphic of pyrolysis and oxidation processes, illustrating the measurement and calculation of TOC and mineral carbon using a Rock-Eval 6 apparatus. Modified from Behar *et al.*, 2001.

kerogen occurs (*S2* peak). This stage represents the oil potential of the source rock. Both the *S1* and *S2* variables are measured as milligrams of hydrocarbons per gram of rock.

While the FID measures *S1* and *S2* parameters, an infrared (IR) detector continuously records CO₂ and CO production during pyrolysis (Figure 7.4): carbon dioxide (CO₂) (*S3*, *S3'*) and carbon monoxide (CO) (*S3CO*, *S3'CO*) mg CO/gram of rock. Continual measurement of CO and CO₂ provides information on mineral carbon content in the rock and possible mineral type (e.g., siderite, magnesite, calcite, or dolomite). The *S3* parameter represents organic CO₂ released between 300°C and 400°C, and *S3'* is carbonate mineral sourced CO₂ (such as magnesite and siderite) released between 400°C and 650°C. CO of organic origin, *S3CO*, is measured from initial heating to 300°C to 550°C. *S3'CO* begins at the upper temperature reached during the *S3CO* phase and terminates at 650°C, when pyrolysis is completed. *S3'CO* is CO with both organic and mineral origin and results from the reactivity of CO₂ released during thermal decomposition of carbonates in organic matter between 550°C and 650°C.

Once pyrolysis is complete, samples are placed in an inert atmosphere-filled (helium or nitrogen) combustion oven and heated from 300°C to 850°C to oxidize the remaining carbon in the sample (Figure 7.4). Outputs from oxidation are represented by the *S4CO*₂, *S5* and *S4CO* mg CO/g rock curves and are measured in mg CO₂/gram of rock. *S4CO* is CO of organic origin and is recorded from initial heating until the end of measurement at 850°C. CO₂ released during oxidation is measured in two parts: carbon of organic origin which is generated between 300°C and up to 720°C, and carbon of mineral origin (*S5*), produced from decomposition of carbonate minerals above the minimum temperature of *S4CO*₂.

7.3.2

Rock-Eval measurements and calculated parameters obtained from pyrolysis (*S1*, *S2*, *S3*, *S3'*, *S3CO*, and *S3'CO*) and oxidation (*S4CO*₂, *S5* and *S4CO*) processes are used to evaluate source rock characteristics. The explanation below briefly summarizes calculated outputs for analyzed samples as provided by the Geological Survey of Canada

Laboratory. These parameters include production index (PI), total organic carbon (TOC), hydrogen index (HI) and oxygen index (OI).

Tmax and the production index (PI) are proxies used to infer the thermal maturity of a sample. When the maximum hydrocarbons released during pyrolysis occurs at less than 435°C, the sample is deemed thermally immature, and if hydrocarbons are released at Tmax between 435°C and 475°C the sample is thermally mature. PI is the ratio $S1/(S1+S2)$ and indicates the amount of hydrocarbons already produced ($S1$) relative to the total amount the sample can produce ($S1+S2$).

The total organic carbon (TOC) is calculated using peak height measurements of pyrolysis and oxidation products: pyrolysable organic carbon (PC) and residual carbon (RC) (Figure 7.4), each measured in weight percentage (wt%). PC is calculated using hydrocarbons ($S1$ and $S2$), CO ($S3'CO$ and $S3CO$) and CO₂ ($S3$) released during pyrolysis. It is expressed as:

$$PC = \frac{\left[(S1+S2) * 0.83 + S3 * \frac{12}{44} + \left(S3CO + \frac{S3'CO}{2} \right) * \frac{12}{28} \right]}{10},$$

where 0.83 represents 83 wt% of the organic carbon in the S2 peak, no matter the organic matter type (Lafargue et al, 1998; Behar et al., 2001), 12/44 and 12/28 account for the mass of carbon in CO₂ and CO, respectively.

RC is based on outputs during the oxidation process and is equal to the addition of $S4CO_2$ and $S4CO$:

$$RC = \frac{\left(S4CO_2 * \frac{12}{44} + S4CO * \frac{12}{28} \right)}{10}$$

HI corresponds to the amount of pyrolysable organic material from $S2$ relative to TOC ($S2 \times 100/TOC$) and OI is the amount of CO₂ from $S3$ relative to TOC ($S3 \times 100/TOC$) (expressed as mg HC/g of TOC and mg CO₂ /g TOC, respectively).

7.3.3 Rock-Eval limitations

The following summarizes limitations to consider when reviewing programmed pyrolysis data from Rock-Eval (Katz, 1983; Peters, 1986; Peters and Cassa, 1994; Behar et al., 2001; Dembicki, 2009; Jarvie, 2012; Hart and Steen, 2015):

- 1) Rock-Eval analysis may produce low Tmax values when cuttings are mixed with rock from formations higher up in the drill hole or have been drilled using oil-based mud or drilling fluids with additives.
- 2) Organic-based drilling additives (e.g., walnut shells) tend to increase the HI.
- 3) High-maturity samples with less than 0.5 wt% TOC can produce a low and poorly defined S2 peak, leading to unreliable HI and Tmax values.
- 4) Samples rich in carbonate minerals release CO₂ during pyrolysis and increase S3 and OI values. Pretreating samples with acid or maintain a maximum pyrolysis temperature below 650°C may reduce the effects.
- 5) Hydrocarbon retention on mineral grains can reduce the S2 peak and HI of the sample.
- 6) Bitumen can cause suppressed Tmax values if bitumen contributes to the S2 peak.
- 7) The S1 parameter reflects the minimum estimate of free/extractable hydrocarbons because volatiles may be lost from core and cuttings during storage, and in turn impacts calculated parameters (i.e., PI).

Additional Rock-Eval II limitations:

- 1) S2 is slightly underestimated in samples processed from Rock-Eval II because thermal cracking of terrestrial organic matter is not always complete at the 600°C final heating temperature.
- 2) Tmax measurements in Rock-Eval II are lower than maximum temperature estimates in Rock-Eval 6 due to the placement of the measuring probe in the oven wall.

7.4 LECO analysis

LECO carbon analyzer is another method used for measuring total organic carbon in rock. The LECO apparatus analyzes carbon elemental concentration in samples by induction

combustion-IR detection, using the amount of expelled carbon dioxide from the combustion process to determine organic carbon content of a sample. Although it is a simpler process when compared to Rock-Eval, and only provides information on the amount of carbon in a sample, it is a reliable option for collecting information on organic matter content. The following is a summary of the procedure provided by Dr. Charles Wu, operator of the LECO carbon analyzer (LECO SC 444) at the Biotron facility.

For total carbon determination, approximately 100 mg of pulverized sample is air dried and measured into a disposable combustion crucible and further dried overnight in an oven at 60° C. When cooled to room temperature, the sample is re-weighed and the moisture (%) is calculated based on weight loss between weights before and after drying overnight. The sample is then placed in a grinder, or in a mortar and pestle, for homogenization. Once complete, the material is sieved through a 100- or 140-mesh sieve, and the portion that falls through is collected for pre-treatment.

Pre-treatment begins with wetting the sample by adding 1 – 2 mL of hydrochloric acid to one gram of rock to observe any effervescence. If detected, the sample goes through a subsequent heating and acid treatment process. Large crucibles are heated at 450° C for four hours, with their weights recorded with and without the sample. Effervescence is tested for by adding 1 mL of 5% phosphoric acid and doing so continuously until effervescence is no longer observed. The total amount of acid added is recorded. This process digests the mineral (inorganic) carbon present in the sample.

Four times the amount of distilled water relative to the amount of phosphoric acid is added to the sample. The sample is then placed on a hot plate at low heat setting for one to two minutes so the fluid can evaporate. The sample is then dried overnight at 60° C. At this stage, treated samples are weighed, ground into a fine particle size, and placed into crucibles in the desiccator. The untreated and treated sample are then run through the LECO SC 444 to assess for total organic carbon. The resulting data for both total carbon and total organic carbon are adjusted for the sample's moisture content in the air-dried samples. Inorganic carbon is calculated by subtracting the organic carbon concentration from total carbon measured in the sample.

7.4.1 LECO limitations

Data limitations regarding LECO analysis relate to the pre-treatment step used to remove carbonate mineral material from the sample (Behar, et al., 2001; Katz, 1983; Peters and Cassa, 1994). The pre-treatment for carbonates may cause part of the organic carbon to become hydrolyzed and lost in the aqueous phase, leading to possibly less reliable TOC data compared to TOC measurement collected by Rock-Eval 6. Inorganic carbon (i.e., dolomite) that is not removed from the pre-treatment process will lead to a high bias in the TOC results.

7.5 Organic geochemistry characterization

Rock-Eval pyrolysis data are presented in diagrams that provide details on thermal maturity and kerogen type. These include the pseudo-Van Krevelen diagram, which plots hydrogen/carbon (H/C) ratios against oxygen/carbon (O/C) ratios, and the HI vs Tmax (°C) diagram. The Van Krevelen plot was first developed by Van Krevelen (1961) to characterize coals and their coalification path using the principles that different organic matter components and the depositional conditions can be expressed using the global atomic composition of carbon, hydrogen, and oxygen. Tissot and Welde (1984) adapted the plot to characterize kerogen in source rocks and is commonly referred to as the pseudo-Van Krevelen diagram.

The thermal degradation of kerogen through increased burial (also termed catagenesis) is depicted on pseudo-Van Krevelen and HI vs. Tmax diagrams by the merging of the maturation paths with the plot origin (Hart and Steen, 2015). Kerogen quality can be defined using an S2 vs. present-day TOC plot. Based on where the data lie within these diagrams, kerogen can be categorized into three types: type I, type II, and type III.

Type I kerogen is generally associated with freshwater basin (e.g., lakes) source rocks that are prone to produce oil, is typical of algal material, and has high HI and low OI values (Peters and Cassa, 1994; Bjorlykke, 2010). Type II is derived from mixtures of marine-based phytoplankton, zooplankton and micro-organisms that accumulated under reducing conditions and land derived plant material (Bjorlykke, 2010). Type II is an oil prone kerogen with moderately high HI and low OI compared to types III and IV (Peters

and Cassa, 1994). Type III kerogen is characteristic of organic matter from land plants and tends to be gas-prone (Peters and Cassa, 1994; Hart and Steen, 2015). Type III has relatively low HI and high OI values. Type IV kerogen is inert (or non-generative) carbon that is characterized by extremely low HI values and low to high OI (Peters and Cassa, 1994). A combination of kerogen types, such as type I and II or type II and III, can reflect mixing of organic matter type in the natural environment.

7.5.1 Reconstruction of original total organic content

The TOC of source rocks decreases as kerogen is converted to hydrocarbons with increasing burial depth and thermal maturity (Tissot et al, 1987). This results in a difference between the present-day TOC (TOC_{pd}) and HI (HI_{pd}) values measured during RockEval pyrolysis and the original concentrations before catagenesis took place. The reduction of original TOC (TOC_0) ranges between 70% for type I kerogen, 50% for type II, and 12% for type III, suggesting present day TOC_{pd} values may be substantially lower than the TOC_0 prior to alteration by thermal maturity (Daly and Edman, 1987). Because both TOC and HI are used to characterize organic carbon type and maturity, using TOC_{pd} and HI_{pd} that have been restored to pre-thermal degradation values will more accurately represent organic carbon content variability at the time of deposition, and improve the assessment of hydrocarbon generation potential (Jarvie et al., 2012). For this study, estimating TOC_0 for thermally mature samples will better support interpretations regarding the depositional (paleoenvironmental) controls that enhance or impede organic matter production and preservation across the study area. The following sections discuss the methodology used to calculate the original TOC (TOC_0) and original HI (HI_0). The estimated HI_0 is the hydrogen index prior to the conversion of kerogen to hydrocarbons and is a required input to calculate TOC_0 .

7.5.1.1 Estimating original hydrogen index

In the literature, the HI_0 has been estimated using several different methods. A best fit line through the data on a TOC vs S2 diagram (slope HI method) is one technique that has been used to estimate HI_0 (Cornford et al, 1998). Tobey and Campbell (2016) suggest that the line should intersect the origin because as TOC approaches zero, S2 should also

approach zero as there is no TOC. Applying this approach and considering that source rock quality is not uniform throughout a sedimentary column, more than one line with different slopes would be expected to best represent HI. Jarvie et al (2012) estimated HI_0 from a frequency distribution of HI data collected from RockEval analysis of immature marine, type II source rocks, where the distribution represents probabilities that a value will be met or exceeded. For example, in the case of HI, a P90 of 350 mg HC/g TOC indicates 90% of the samples are equal or greater in value. The P50 of the distribution represents the median of the dataset and is accepted as the estimated HI_0 . Hart and Steen (2015) used maturation trend lines as guides to extrapolate HI_{pd} values back to the Y axis to estimate HI_0 . Jarvie et al (2007) developed an approach that uses a visual assessment of maceral types, where the HI_0 is computed from the total sum of their proportions.

The estimated HI_0 used in this study is an average obtained from two methods: the P50 frequency distribution of RockEval derived HI values (Jarvie et al., 2012), and the best fit line through a S2 vs. TOC diagram (Cornford et al., 1998) from a data set of immature rock samples with assigned lithofacies classification. Table 7.2 lists the estimated HI_0 for each lithofacies. Instead of using the median (P50) value of all thermally immature samples to estimate HI_0 , P50 was estimated for each of the lithofacies to constrain the HI_0 and better reflect the variability in organic-rich facies. Histograms were created for calcareous mudstone (lithofacies 3), silty argillaceous mudstone (lithofacies 5), and heterolithic sandstone and mudstone (lithofacies 2) lithofacies classifications using thermally immature sample data (Figure 7.5). None of the geochemical samples in the database were classified as sandstone, and therefore are not included in the lithofacies subdivisions for estimating HI_0 and TOC_0 .

The estimated HI_0 derived from the best fit line on a S2 vs. TOC diagram is shown in Figure 7.6. Different estimated HI_0 values are obtained when the data is divided by formation (Second White Specks, Belle Fourche, and Fish Scales) compared to lithofacies (calcareous mudstone, argillaceous mudstone, and heterolithic sandstone and mudstone) when plotted in an S2 vs. TOC diagram.

Table 7.2: Estimated HI₀ values for lithofacies classifications.

Lithofacies	S2 vs. TOC best fit line	P50 (Immature samples)	Average estimated HI ₀ from both methods
Calcareous mudstone	443	456	450
Silty argillaceous mudstone	375	295	335
Heterolithic sandstone and mudstone	192	171	182

Classifying the data in terms of lithofacies refines the estimated HI₀, showing calcareous mudstone has the greatest quality of organic matter with the highest HI value, followed by silty argillaceous mudstone and heterolithic sandstone and mudstone. Using a database of worldwide marine source rock geochemistry data, Jarvie et al (2012) stated the distribution of HI₀ values ranges between 250 to 800 mg HC/g TOC. The estimated HI₀ obtained in this study broadens the lower range of that scale to include 180 mg HC/g TOC and defines a potential range that could capture best approximations of HI₀ and reduce uncertainty.

7.5.1.2 Calculating original total organic content

Previous methods used to reconstruct TOC₀ include Rock-Eval pyrolysis data and mass balance equations (Peters et al., 2005; Jarvie et al., 2012; Chen and Jiang, 2016), calibration of gamma ray geophysical logs to core measurements of TOC (Modica and Lapierre, 2012), and petroleum system modelling (Romero-Sarmiento et al., 2013). Aviles (2021) used Chen and Jiang (2016) to estimate TOC₀ for thermally mature samples from the Second White Specks and Belle Fourche formations in west-central Alberta and suggests that using empirical formulas that simplify assumptions, such as the method proposed in Jarvie et al (2012), could lead to erroneous estimations of

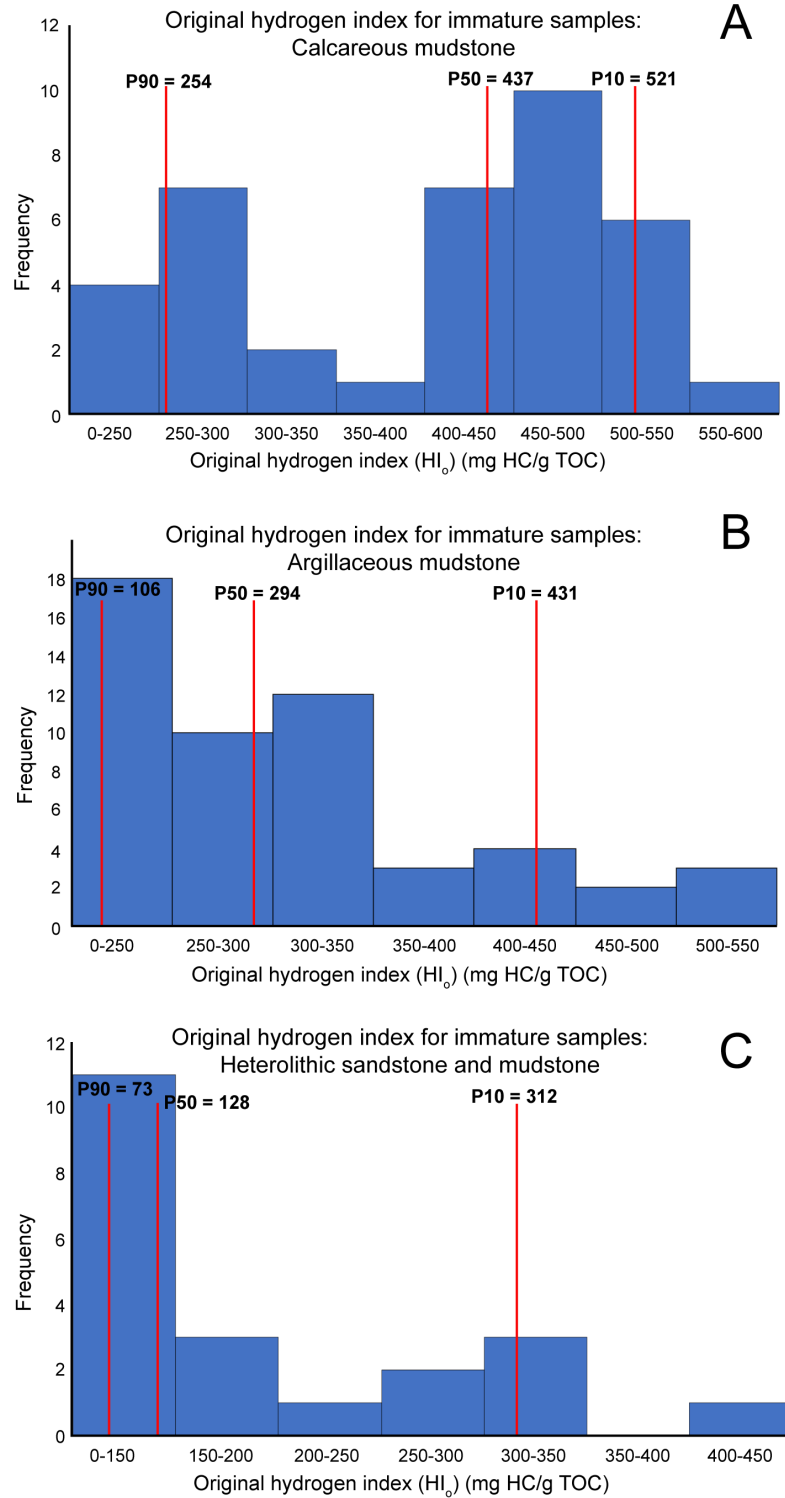


Figure 7:5: HI₀ distribution of calcareous mudstone (A), silty argillaceous mudstone (B), and heterolithic sandstone lithofacies(C) classified, thermally immature samples. Exceedance probabilities (P10, P50, and P90) denoted with a red line.

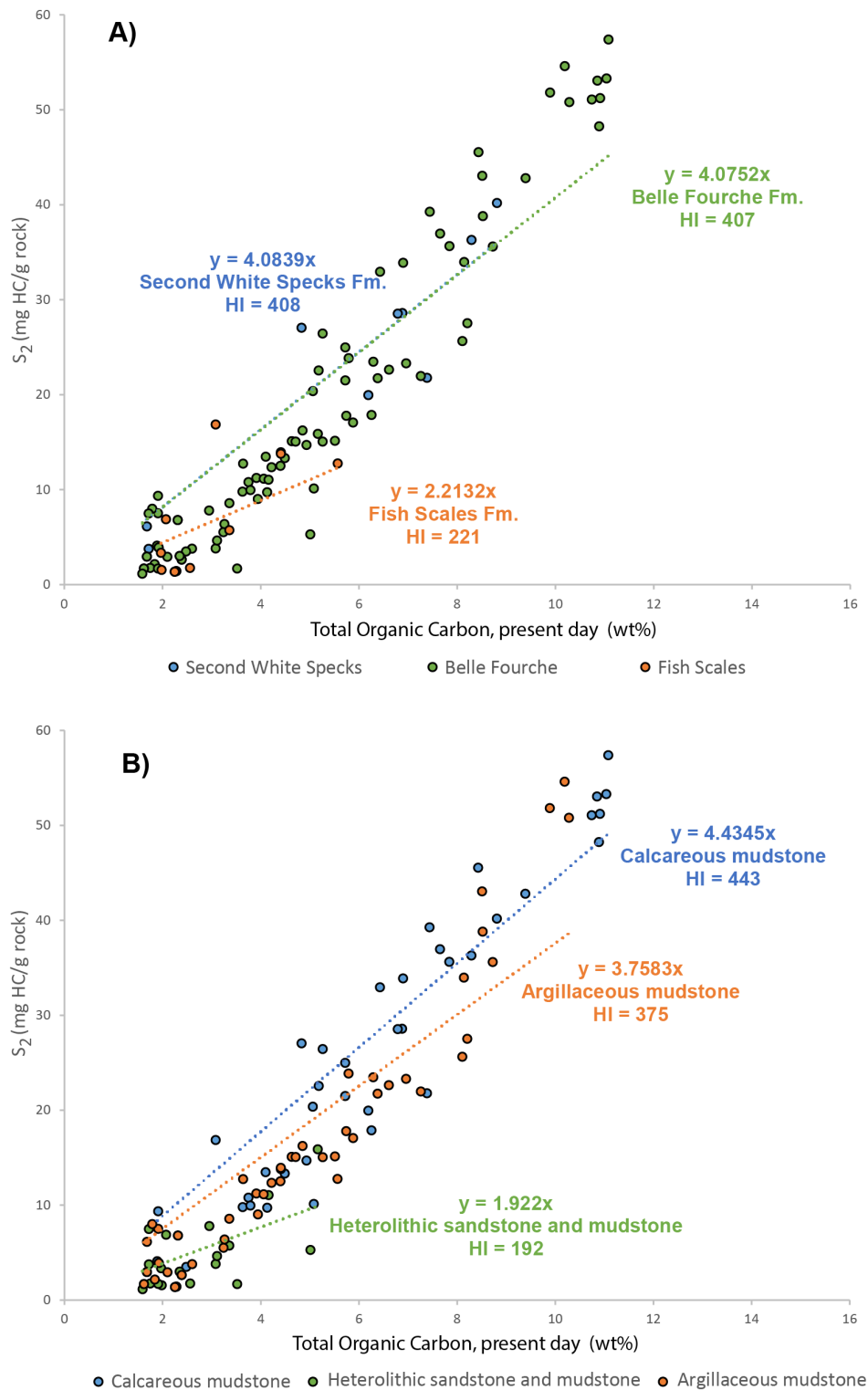


Figure 7:6: S_2 vs. TOC diagram showing estimated HI_0 when data is segregated by formation (A) and lithofacies classification (B).

hydrocarbon generation potential. However, in a study by Hart and Hofmann (2022) that investigated the importance of restoring TOC in paleoenvironmental analyses, the authors noted that regardless of the method used (Peters et al. (2005), Jarvie et al. (2012) and Modica and Lapierre (2012)), no significant differences between TOC_0 values were observed. This study estimates TOC_0 for thermally mature samples using the method proposed by Jarvie et al. (2012). The following describes the steps used to estimate TOC_0 , as outlined in Hart and Hofmann (2022).

The initial step in the method is to determine the kerogen- and bitumen-free TOC content (TOC_{bkfree}) by subtracting the percentage of organic carbon in present day S1 and S2 (OC_{S1+S2}), both mg HC/g TOC, from TOC_{pd} (wt.%). A constant of 0.085 is used to convert the mg HC/g TOC units to weight percent and assumes that hydrocarbons generated from a source rock are 85% carbon (Jarvie et al., 2012).

$$OC_{S1+S2} = (0.085 \times [S1_{pd} + S2_{pd}]) \quad (1)$$

$$TOC_{bkfree} = TOC_{pd} - OC_{S1+S2} \quad (2)$$

The next step is to calculate the non-generative organic carbon (NGOC; the weight percent of non-generative carbon present in TOC_0) using an adjusted TOC_{bkfree} that corrects for bitumen and/or oil cracking contributions to organic carbon. The constant used in this equation (0.0008) represents the reciprocal of the maximum value of HI_0 (1177), assuming the generated hydrocarbons are approximately 85% carbon.

$$NGOC = TOC_{bkfree} - (HI \times 0.0008) \quad (3)$$

The NGOC and amount of generative organic carbon originally present in TOC_0 (GOC_0) are required to estimate TOC_0 . The NGOC is estimated from HI_0 and the assumed maximum value of HI_0 :

$$GOC_0 = (HI_0/1177) \quad (4)$$

$$TOC_0 = NGOC / (1 - \%GOC_0) \quad (5)$$

7.5.1.3 Limitations to original total organic content reconstruction

Calculating TOC_0 using an estimated HI_0 cannot be precisely defined; the values obtained from the process are a best-guess scenario and require acknowledgement of the uncertainties that influence the result. Furmann et al. (2015) used the visual kerogen type percentages method of Jarvie et al. (2007) to estimate HI_0 for late Cenomanian to early Turonian aged cores from west-central Alberta. One of the cores used in that investigation is also included in this study: 100/07-19-045-06W5. Samples collected from this core are mature and predominately kerogen type II. Lithofacies represented in the samples were identified based on core descriptions provided by K. Greff, Marion (2019), and mineral carbon (wt.%) data from RockEval analysis. The estimated TOC_0 for samples from this core in Furmann et al. (2015) is 1.26 to 1.40 times higher than TOC_{pd} , compared to a more conservative range of no change to 1.26 times higher obtained from the calculation methodology used in this study. The mean estimated HI_0 for silty argillaceous mudstone (lithofacies 5), calcareous mudstone (lithofacies 3), and heterolithic sandstone and mudstone (lithofacies 2) in Furmann et al. (2015) is 393 mg HC/g TOC (max = 426, min = 331; 16 samples total), 408 mg HC/g TOC (one sample), and 399 mg HC/g TOC (max = 421, min = 376; two samples), respectively. The estimated HI_0 values applied in the current study for silty argillaceous mudstone and calcareous mudstone (335 and 450 mg HC/g TOC, respectively) are not substantially different than the mean values of Furmann et al. (2015), but there is a difference of 20 to 40% in calculated TOC_0 between the two bodies of work. The largest variance occurs in samples where this study assigned a heterolithic sandstone and mudstone lithofacies with an estimated HI_0 of 187 mg HC/g TOC and Furmann et al. (2015) had a visual assessment based estimated HI_0 of 421 mg HC/g TOC. This demonstrates a potential discrepancy in calculated TOC_0 if a core sample is classified as heterolithic sandstone and mudstone using the lithofacies methodology in this study compared to lower-resolution lithofacies assignment from logging the core. The sample by Furmann et al. (2015) may have been collected from a mudstone interbed, and that level of detail is missed when assigning lithofacies classification through a lower resolution method such as geophysical logs.

Another difference in methodology to consider is that Furmann et al. (2015) used the TOC_0 calculation proposed by Jarvie et al. (2007). The appendix of Jarvie et al. (2007) that outlines the equations used was not accessible, so a direct comparison between Jarvie et al. (2007) and Jarvie et al. (2012) cannot be completed. However, inputting the estimated HI_0 values of Furmann et al. (2015) into the Jarvie et al. (2012) equation for calculating TOC_0 reduces the percent difference to from 0 % to 21%.

Additional uncertainty that contributes to less accurate HI_0 estimates is the assumption that the organic matter type within an allomember in the study area with thermally mature marine source rocks is the same (Hart and Hoffman, 2022). To help address the uncertainty, the TOC_0 for thermally mature samples was calculated using the range of estimated HI_0 for each lithofacies and includes a higher value of 600 mg HC/g TOC for some samples where the 450 mg HC/g TOC value produced a negative TOC_0 result. The estimated HI_0 of 600 mg HC/g TOC was chosen because it remains within the proposed HI_0 range for marine shales (300 to 700 mg HC/g TOC) by Jarvie et al. (2012). The negative TOC_0 can result from an incorrect estimated HI_0 (the value being too low), or the TOC_{pd} is too low to begin with.

Chapter 8

8 Organic matter distribution in the Upper Cretaceous Colorado Group

This chapter begins by presenting organic geochemistry trends for the Upper Cretaceous Colorado Group in the Western Canada Sedimentary Basin. These results are discussed in the final section of this chapter and used to examine temporal and spatial trends related to organic matter production and preservation across the study area.

8.1 Kerogen type

Figures 8.1 through 8.3 show the pyrolysis data for the Fish Scales, Belle Fourche, and Second White Specks formations, respectively, plotted on pseudo-Van Krevelan and HI vs. Tmax diagrams. The data points are sized proportional to the TOC value for that sample (i.e., larger circle = higher TOC value) and the dataset is segregated by meridian to give spatial context to the variability in TOC.

Samples from the Fish Scales Formation plot across Type II and Type III, with some data points plotting in Type IV (Figure 8.1A and B). The highest TOC values are evident in wells from Meridian 4 (grey circles) and lie predominately within the Type II kerogen type. Fish Scales Formation samples from wells in W2 (blue circles) and W5 (yellow circles) regions also fall within the Type II category, with some data points being captured in Types III and IV. Only one data point was collected for the Fish Scales Formation in W6, the most westerly division, and it lies within the Type IV kerogen pathway. In the HI vs Tmax diagram (Figure 1B), the samples predominately maintain the Type II to Type III classification.

In the Belle Fourche Formation, kerogen type in both the pseudo-Van Krevelan and Hi vs Tmax diagrams is identified as predominantly Type II and Type II-III. Data in W1 through W5 plot within the Type II (Figure 8.2A) and Type II to Type II-III (Figure 8.2B) path. Samples from W6 (red circles) are from wells located adjacent to the deformation front in western Alberta and plot as Type III kerogen.

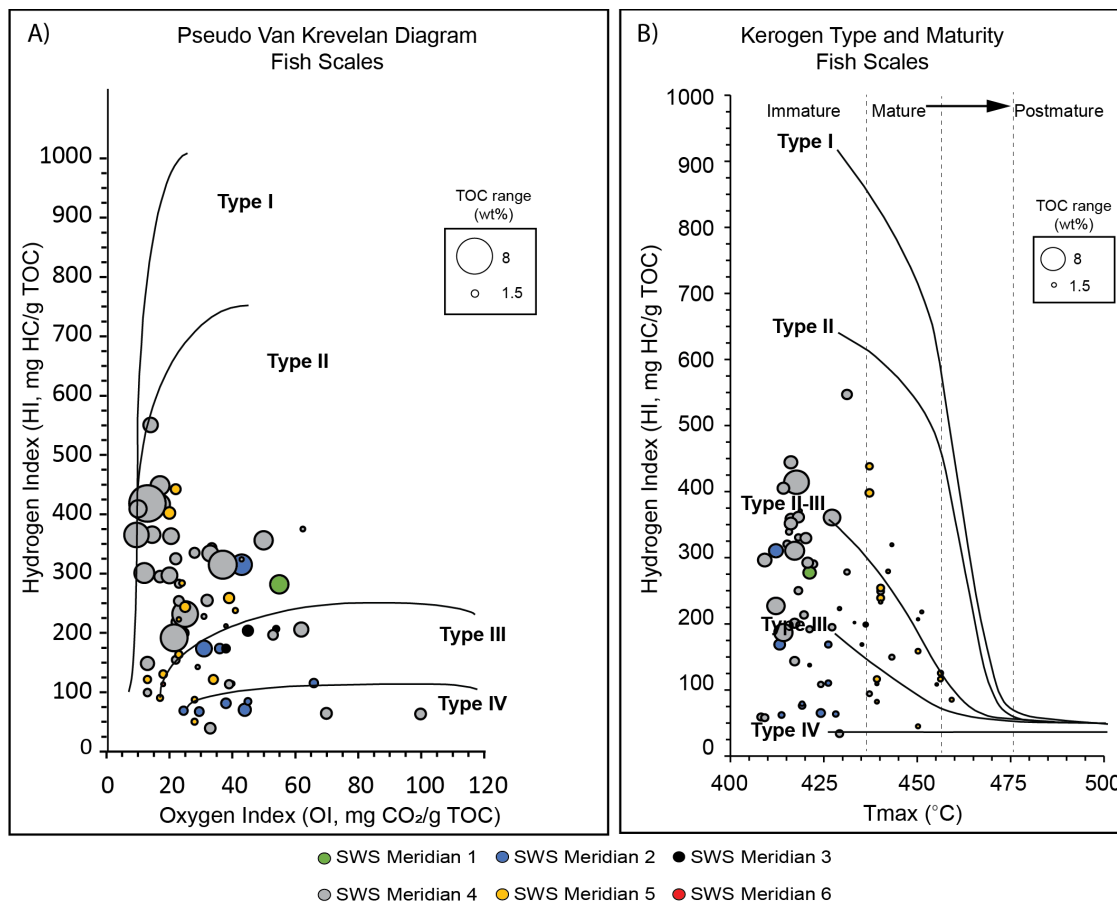


Figure 8:1: Pseudo-Van Krevelan (A) and HI vs. Tmax (B) diagrams for samples collected from the Fish Scales Formation. A) Diagram shows that the majority of data fall into Type II to Type III kerogen types and TOC (bubble size) decreases as thermal maturity increases (maturity increases as data approaches point of origin). B) Samples from W1, W2 and W3 are identified as immature, Meridian 4 data points are mainly immature with a few mature, and all samples from W5 and W6 wells plot within the mature hydrocarbon window. Similar to diagram A), the samples plot along the Type II-III classification.

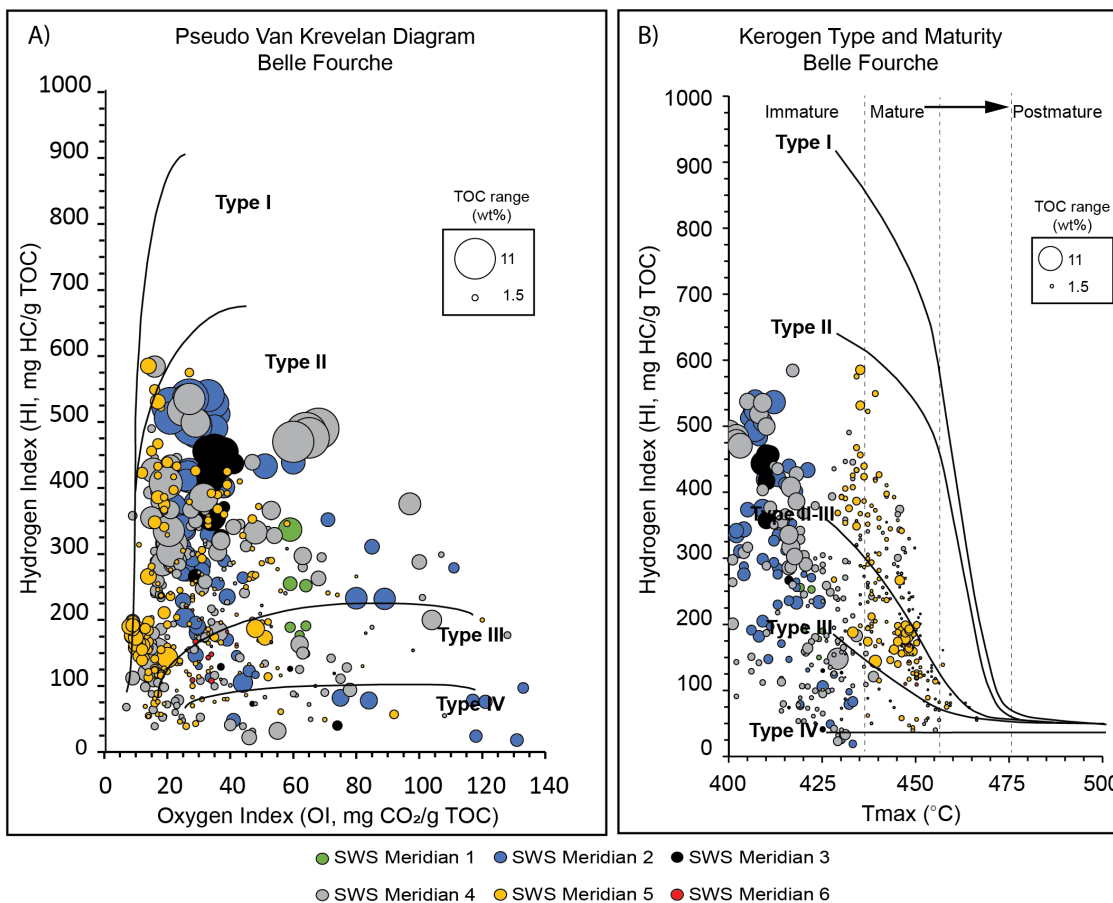


Figure 8:2: Pseudo-Van Krevelan (A) and HI vs. Tmax (B) diagrams for samples collected from the Belle Fourche Formation. A) Diagram shows that TOC (bubble size) decreases as thermal maturity increases (maturity increases as data approaches point of origin). The samples lie within the Type II, III, and IV classification, but majority of the data is Type II. B) Immature samples are from wells located in W1, W2, W3 and W4 and mature data is largely from wells in W5 and W6. Much of the data is Type II-III to Type III kerogen.

The Second White Specks Formation samples plotted in Figures 8.3A and 8.3B from wells in W2, W4 and W5 imply they are primarily marine Type II and Type II-III kerogen. All samples from wells in W6 are Type III, with some samples from W3, W4 and W5.

Figure 8.4 shows pseudo-Van Krevelan (refer to section 7.5) and HI vs. Tmax diagrams with the data segregated by lithofacies (calcareous mudstone, silty argillaceous mudstone, and heterolithic sandstone and mudstone) identified in Chapter 7. Only the data with lithofacies information available are shown in the figure. Comparison of the data according to lithofacies shows that the kerogen type in calcareous mudstone (green circles) is dominantly Type II to Type II-III and silty argillaceous mudstone (blue circles) is Type II to Type II-III, with some amounts of Type III. The heterolithic sandstone and mudstone samples are identified as Type II to Type III on the pseudo-Van Krevelan diagram and Type II-III to Type III on the HI vs. Tmax diagram.

8.2 Thermal maturity

The Colorado Group rocks within the study area are thermally immature to thermally mature. The Tmax distribution in Figure 8.5 originates from Tmax values estimated in this study and legacy data obtained from the public domain (refer to Chapter 7), representing the mean Tmax value from the Fish Scales, Belle Fourche, and Second White Specks formations. The thermally immature samples used in this study come from wells west of the 435°C Tmax contour (thick black line; Figure 8.5) and lie within a mean Tmax of 400°C to 435°C. In thermally mature samples, the mean Tmax range between 435°C and 450°C. Tmax is typically highest along the deformation front and decreases towards the east, with localized variability occurring across the study area. In the pseudo-Van Krevelan diagrams (Figures 8.1A, 8.2A, and 8.3A) samples from W4 and W5 plot both close and far away from the point of origin (indicating mature and immature, respectively), while the W6 samples are all mature. The samples collected from wells in W1, W2 and W3 are thermally immature. These maturity trends are also observed in the corresponding HI vs. Tmax diagrams (Figures 8.1B, 8.2B, and 8.3B).

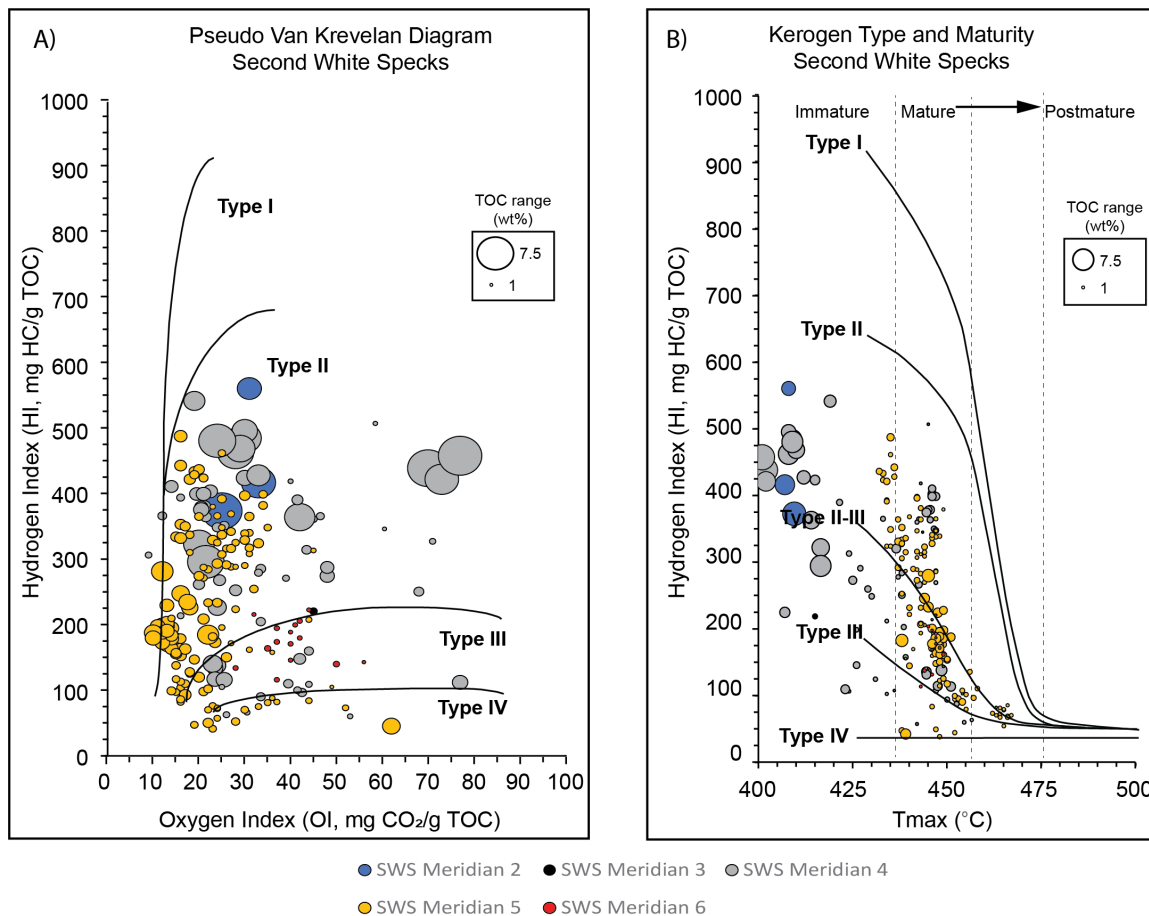


Figure 8:3: Pseudo-Van Krevelan (A) and HI vs. Tmax (B) diagrams for samples collected from the Second White Specks Formation. Similar to the Fish Scales and Belle Fourche formations, the pseudo-Van Krevelan diagram (A) shows that TOC (bubble size) decreases as thermal maturity increases (maturity increases as data approaches point of origin). The samples are predominantly Type II, with some scatter in the Types III and IV domain. In diagram B), the immature samples have higher TOC and are from wells located in W2, W3 and W4. Samples from Meridian 5 are mostly mature with some immature data points, with all W6 data points plotting as mature.

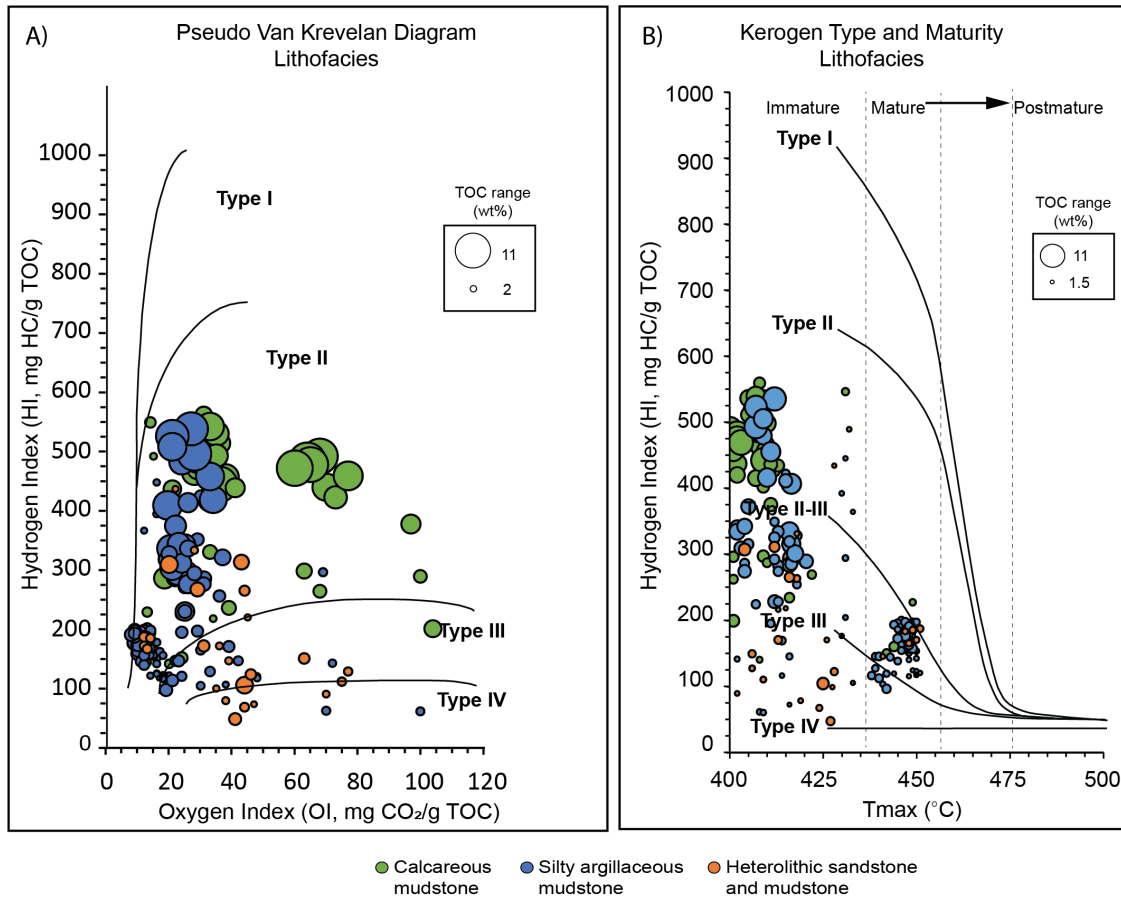


Figure 8:4: Pseudo-Van Krevelan (A) and HI vs. Tmax (B) diagrams showing data segregated by lithofacies classification. Core samples from calcareous mudstone and silty argillaceous mudstone lithofacies are Type II to Type II-III kerogen and samples in both plots are dominantly immature with some scatter of data suggesting increased thermal maturity. Samples with a heterolithic sandstone and mudstone classification are Type II to Type III, with higher occurrences of Type III and IV than of Type II.

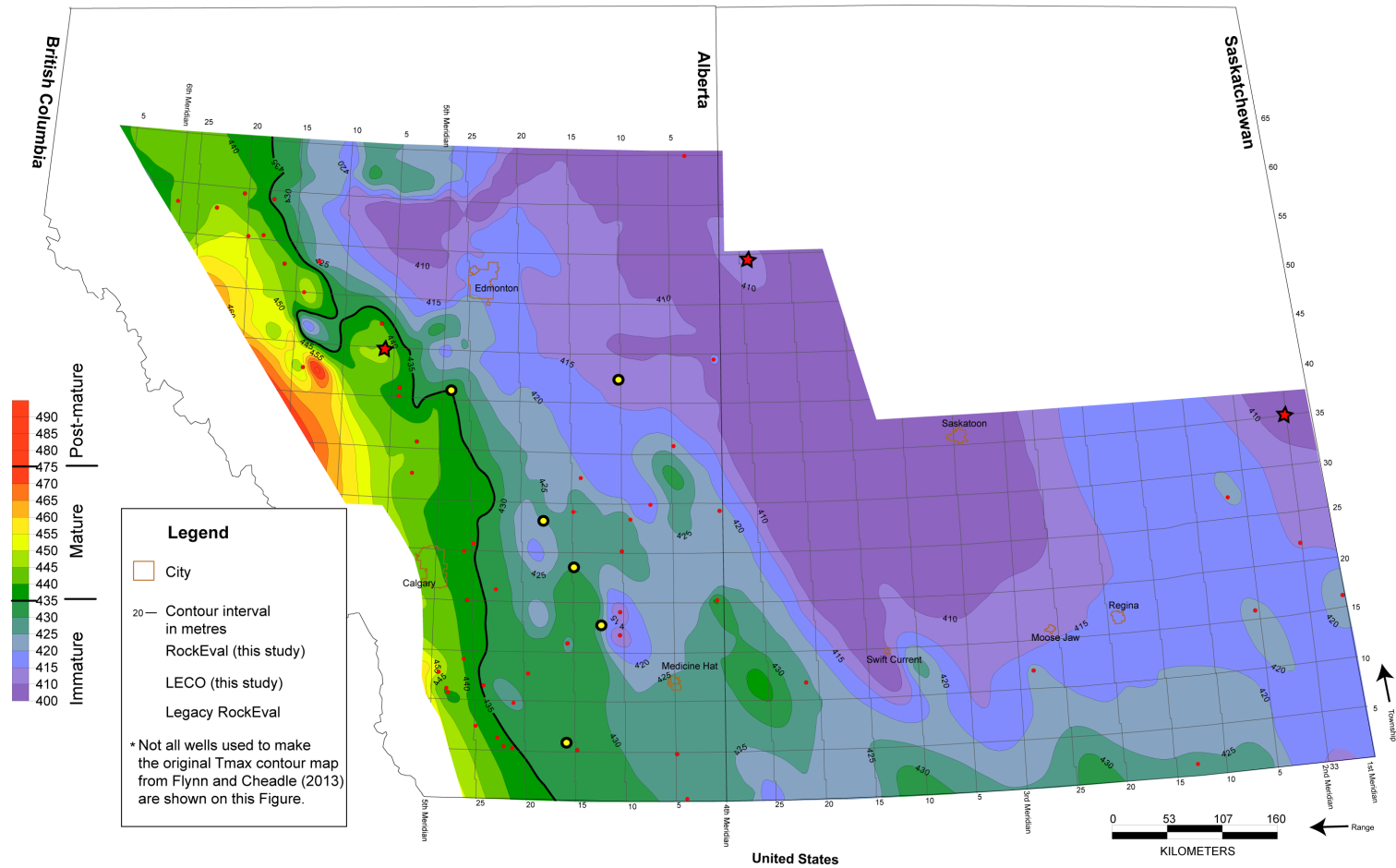


Figure 8:5: Mean thermal maturity map for the Fish Scales, Belle Fourche, and Second White Specks formations of the Upper Cretaceous Colorado Group. Modified from Flynn and Cheadle (2013).

8.3 Kerogen quality

The quality of a source rock is determined from its organic matter richness (TOC) and the quality of that organic matter, which is related to its hydrogen content (the S2 or HI of that sample). Organic matter richness is characterized as poor, fair, good, very good, or excellent, based on geochemical parameters (Table 8.1). A rock sample with TOC of less than 1 wt.% ranks fair to poor, 1-2 wt.% is good, between 2-4 wt.% is very good and greater than 4 wt.% is excellent (Peters and Cassa, 1994). Based on these parameters, the organic matter richness of Colorado Group strata varies from fair to excellent.

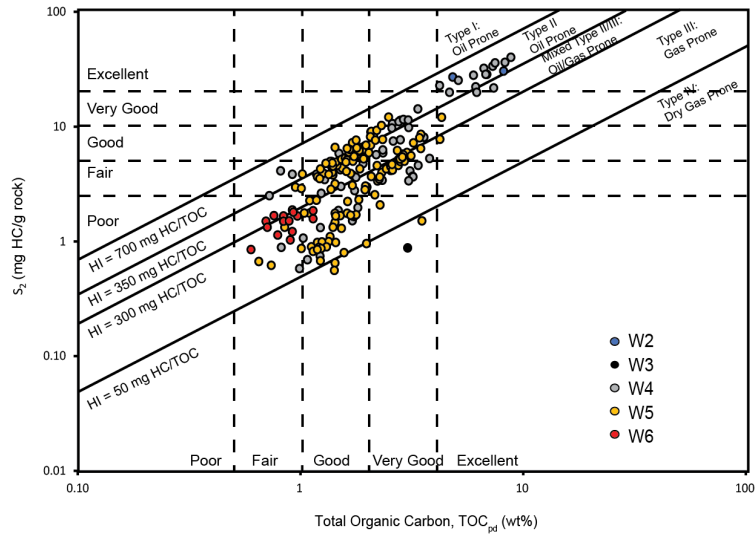
Table 8.1: Geochemical parameters indicating source rock quality. Modified from Peters and Casa (1994).

Petroleum Potential	TOC (wt.%)	Rock-Eval pyrolysis	
		S1	S2
Poor	0 – 0.5	0 – 0.5	0 – 2.5
Fair	0.5 - 1	0.5 - 1	2.5 - 5
Good	1 - 2	1 - 2	5 - 10
Very Good	2 - 4	2 - 4	10 - 20
Excellent	> 4	> 4	> 20

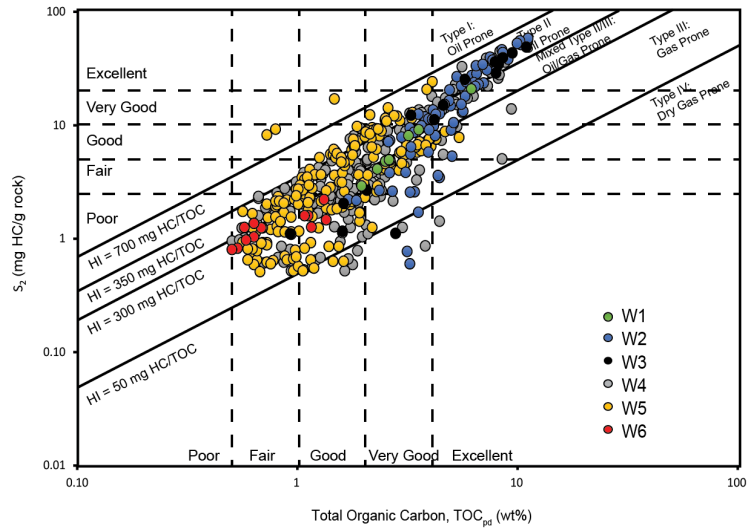
Dividing all geochemical data used in this study by formation, the average TOC from samples collected from the Fish Scales Formation is 2.43 wt.%, with data ranging between 0.63 and 7.96 wt.%. The highest and lowest TOC values in the Belle Fourche Formation samples are 13.03 wt.% and 0.5 wt.% respectively, with a mean of 2.97 wt.%. The mean TOC for the Second White Specks is 2.67 wt.%, with samples ranging between 0.6 to 9.32 wt. %.

Organizing the geochemical dataset by lithofacies, the average TOC for calcareous mudstone, silty argillaceous mudstone, and heterolithic sandstone and mudstone is 5 wt.%, 4.12 wt.%, and 2.64 wt.%, respectively.

A) Second White Specks: S₂ vs TOC



B) Belle Fourche: S₂ vs TOC



C) Fish Scales: S₂ vs TOC

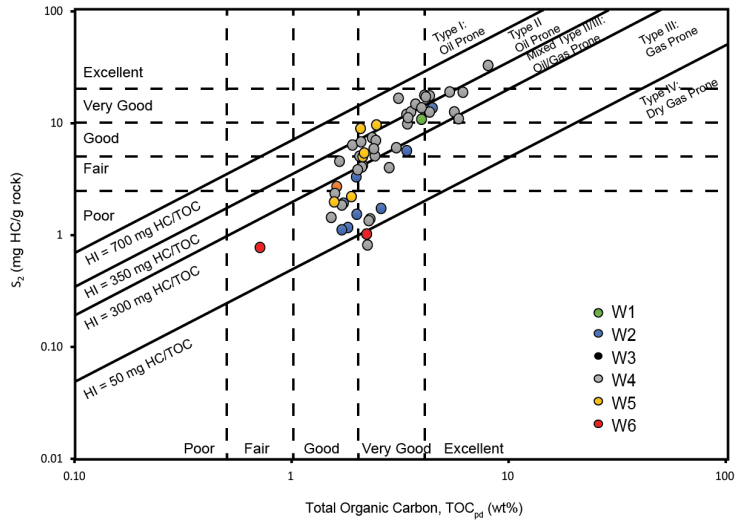


Figure 8:6: S2 vs TOC diagrams for the Second White Specks (A), Belle Fourche (B), and Fish Scales (C) formations. The diagrams show that source rock quality in the formations ranges between poor and excellent generation potential and fair to excellent organic matter richness.

8.3.1 S2 vs TOC

Figure 8.6 shows S2 vs. TOC diagrams for the Fish Scales, Belle Fourche, and Second White Specks formations. The data points are colour coded according to the meridian closest to the location where the sample was taken from. The data trend suggests the samples have poor to excellent generation potential (S2 parameter) and fair to excellent organic matter richness (TOC). In general, samples from W2, W3, and W4 have the best generation potential and organic matter content, with some scatter to poorer quality in the Belle Fourche Formation W3 data. Poorer quality source rock appears in samples from W6, with a mixture of fair to very good quality in W5 data points.

The S2 vs TOC diagram for lithofacies classified data (Figure 8.7) demonstrates that the best generation potential occurs in calcareous mudstone and silty argillaceous mudstones, and lower potential and organic matter richness relates to samples of heterolithic sandstone and mudstone material.

8.4 Total organic content

The original total organic content (TOC_0) values for thermally mature samples ($>435^{\circ}C$ T_{max}) was restored using Jarvie et al (2012) and estimated original hydrogen index (HI_0) (refer to Chapter 7). After filtering the data and excluding wells with $TOC < 1.5$ wt.%, $T_{max} < 400^{\circ}C$, and $S2 < 0.5$ (Chen and Jiang, 2015), eight samples were removed from the 218 thermally mature dataset. Using the estimated HI_0 range of 600, 450, 335, and 182 mg HC/g TOC, the estimated TOC_0 values of the samples ranged between 0.53 and 1.67 times greater than TOC_{pd} . The average TOC_0 value per allomember alongside the estimated HI_0 used is shown in Table 8.2.

Average TOC (wt. %) per allomember and meridian is presented in Table 8.2. Reviewing the data from oldest (allomember I) to youngest (allomember XI) gives an indication of variable organic matter content up through the stratigraphic column of the study interval, and the east to west division of the data, spanning W1 to W6, provides spatial context to the dataset. The average TOC content across the study area ranges from 0.56 to 7.89 wt.%, with the lowest values occurring in the western limit of the study area (meridian W6) and highest in in the east (W3 and W2). Reviewing the average TOC

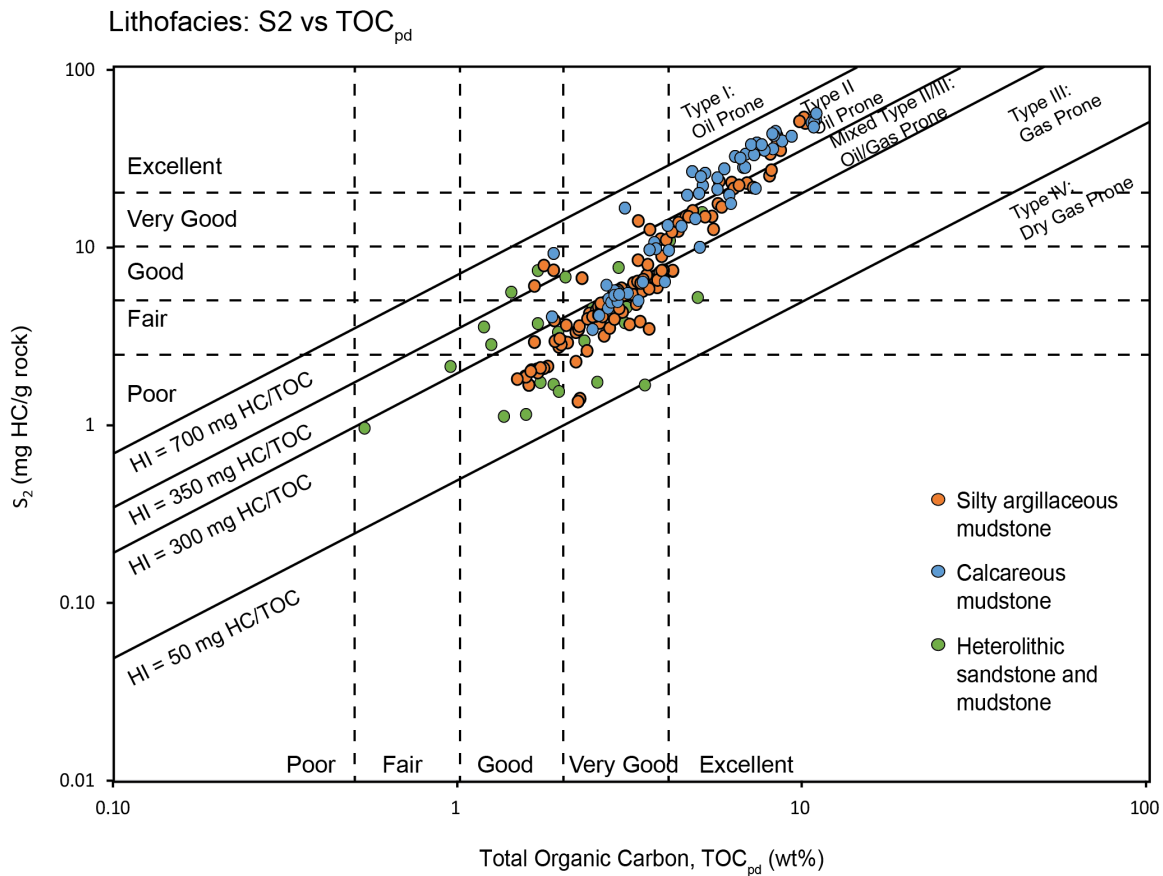



Figure 8:7: S₂ vs TOC diagram showing source rock generation potential and organic matter richness for data with corresponding lithofacies classification data. The trends show that the best source rock generation potential (S₂) and organic matter richness (TOC) occurs in calcareous mudstones and silty argillaceous mudstones. No samples from sandstone (Lithofacies 1) or foraminifera- and coccolith-rich packstone-grainstone (Lithofacies 4) intervals in the cores had accompanying TOC data

Table 8.2: Average total organic content per allomember and meridian to illustrate data variation stratigraphically and spatially. The bolded average values include all TOC data with the initial filter added (TOC values <0.5, Tmax <400, and S2<0). The mean restored TOC data shown in italics have been filtered to remove TOC<1.5, as per Chen and Jiang (2015). HI₀ = estimated hydrogen index value used to estimate TOC₀

Meridian	Average total organic content per allomember											HI ₀
	Oldest  Youngest											
	I	II	III	IV	V	VI	VII	VIII	IX	X	XI	
W1	3.93	2.57	3.17	*	6.12	*	**	**	**	**	*	
W2	2.32	4.22	5.45	7.89	6.20	6.53	**	**	**	**	6.63	
W3	2.37	3.11	3.38	4.82	5.66	4.35	**	**	**	**	2.38	
W4	3.12	2.63	3.77	3.29	2.35	4.59	*	3.77	3.10	1.60	3.98	HI₀
	<i>3.19</i>	<i>2.78</i>	***	***	<i>2.71</i>	<i>4.96</i>	*	<i>4.34</i>	<i>3.71</i>	<i>1.80</i>	***	600
	<i>3.18</i>	<i>2.75</i>	***	***	<i>2.68</i>	<i>4.93</i>	*	<i>4.18</i>	<i>3.33</i>	<i>1.64</i>	***	450
	<i>3.17</i>	<i>2.73</i>	***	***	<i>2.66</i>	<i>4.92</i>	*	<i>4.09</i>	<i>3.13</i>	<i>1.56</i>	***	335
W5	3.16	2.71	***	***	2.65	4.90	*	4.01	2.94	1.48	***	182
	1.48	1.20	1.74	2.01	2.50	2.11	2.16	1.80	1.68	1.59	1.28	HI₀
	<i>2.08</i>	<i>2.23</i>	<i>3.71</i>	<i>3.63</i>	<i>3.61</i>	<i>2.73</i>	<i>2.79</i>	<i>2.49</i>	<i>2.39</i>	<i>2.38</i>	<i>2.37</i>	600
	<i>1.91</i>	<i>2.14</i>	<i>3.15</i>	<i>3.12</i>	<i>3.10</i>	<i>2.38</i>	<i>2.43</i>	<i>2.17</i>	<i>2.09</i>	<i>2.30</i>	<i>2.07</i>	450
W6***	<i>1.82</i>	<i>2.09</i>	<i>2.86</i>	<i>2.86</i>	<i>2.83</i>	<i>2.20</i>	<i>2.24</i>	<i>2.01</i>	<i>1.93</i>	<i>2.27</i>	<i>1.92</i>	335
	<i>1.73</i>	<i>2.04</i>	<i>2.57</i>	<i>2.60</i>	<i>2.57</i>	2.03	2.05	<i>1.85</i>	<i>1.78</i>	<i>2.23</i>	<i>1.77</i>	182
W6***	1.45	0.56	*	0.88	1.33	1.11	0.92	0.67	0.85	0.70	*	

* No data

** Beyond zero edge

*** Thermally mature data filtered out (removed TOC <1.5, TMax <400, S2<0.5)

stratigraphically upsection, the values gradually increase from allomember I (oldest) to allomember XI (youngest), with some variations where TOC begins to decrease after allomember VI.

8.4.1 Variation of total organic content in lithofacies

The average TOC was calculated for calcareous mudstone, silty argillaceous mudstone, and heterolithic sandstone and mudstone lithofacies (Table 8.3). Calcareous mudstone has the highest average TOC, followed by silty argillaceous mudstone and heterolithic sandstone and mudstone. Figures 8.8, 8.9, and 8.10 show examples of calcareous mudstone, silty argillaceous mudstone, and heterolithic sandstone and mudstone lithofacies in core with samples locations and the reported TOC value.

Table 8.3: Average total organic content per lithofacies. The lithofacies classification is sourced from core and geophysical log.

Lithofacies Classification	Total Organic Content		
	Average	Maximum value	Minimum value
Calcareous mudstone	5.83	13.03	1.76
Silty argillaceous mudstone	3.59	10.28	1.14
Heterolithic sandstone and mudstone	2.70	6.37	0.54

Figures 8.11 and 8.12 are north-south (NS 1 to NS 1') and west-east (WE-1 to WE-1') summary cross sections, respectively, that illustrate TOC changes through the Colorado Group strata and across the basin. Cross section NS 1 – NS 1' (Figure 8.11) includes three wells with thermally mature TOC data that have been restored to TOC₀. Only one well in the thermally mature dataset has associated lithofacies information obtained from core, 100/07-19-045-06W5. The other wells in the cross section were illustrated alongside closely located (5-8 km) adjacent wells that had lithofacies classification assigned using the geophysical well log data method. Both cross sections show TOC values greater than 2 wt.% (the estimated cutoff for very good kerogen quality) are

UWI: 103 06 04 017 13W4

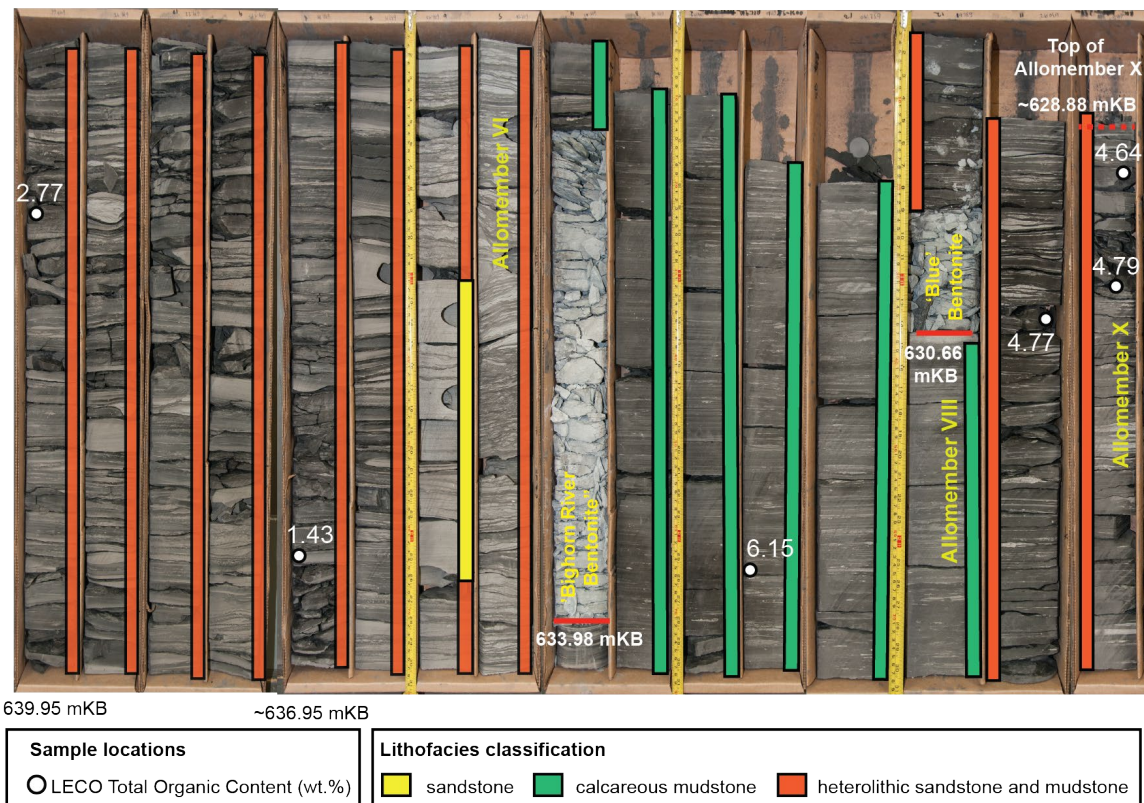
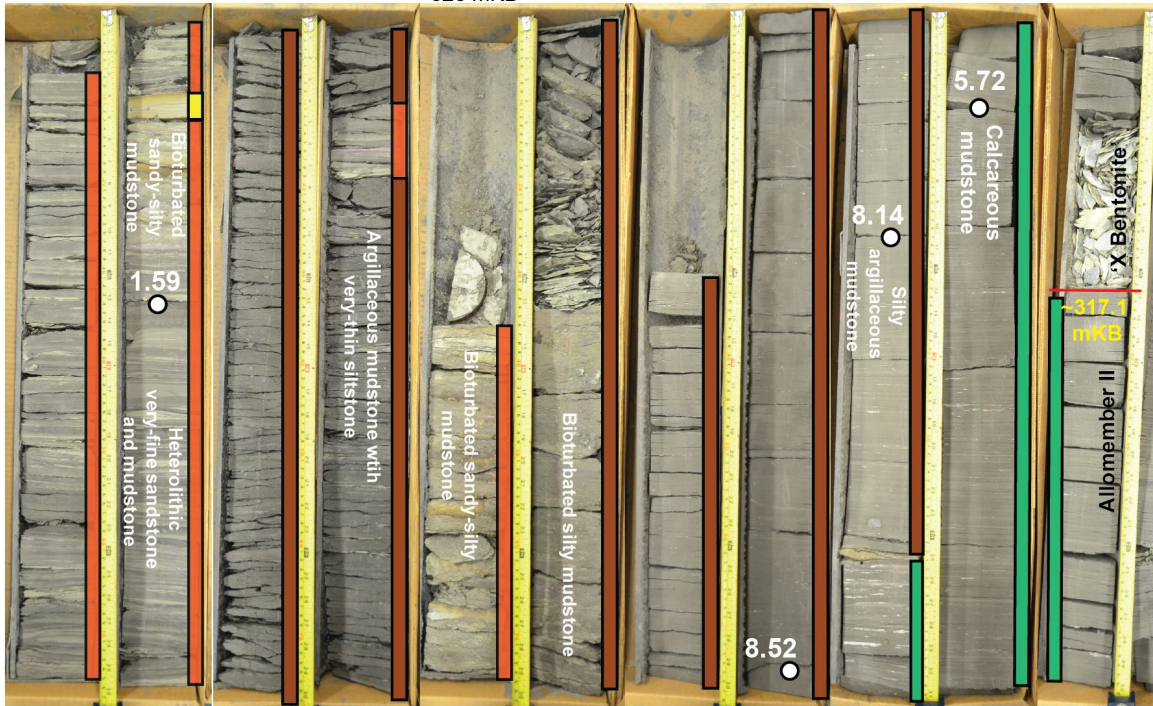


Figure 8:8: Core photo of 103/06-04-017-13W4 showing sandstone, calcareous mudstone and heterolithic sandstone and mudstone in allomembers VI, VIII and XI and TOC values obtained from samples. The TOC is lowest in heterolithic sandstone and mudstone and highest in calcareous mudstone. The increase in TOC that occurs in samples within allomember X compared to the samples in allomember VI may be associated with a relative decrease in quartz content, demonstrating a link between TOC preservation and changes in mineral content.

UWI: 111 03 22 055 25W3

~ 320 mKB



~323.4 mKB

Sample locations	Lithofacies classification		
○ LECO Total Organic Content	■ sandstone	■ calcareous mudstone	■ heterolithic sandstone and mudstone

Figure 8:9: Core photo of 111/03-2-055-25W3 showing TOC results for samples collected from heterolithic sandstone and mudstone, silty argillaceous mudstone, and calcareous mudstone in allomember II. The highest TOC values are from silty argillaceous mudstone and calcareous mudstone samples.

UWI: 141 07 34 035 01W2



Figure 8:10: Core photo of TOC results from samples collected from silty argillaceous mudstone and calcareous mudstone in well 141/07-34-035-01W2 and TOC results. The TOC varies between 4.10 and 11.08 wt.%.

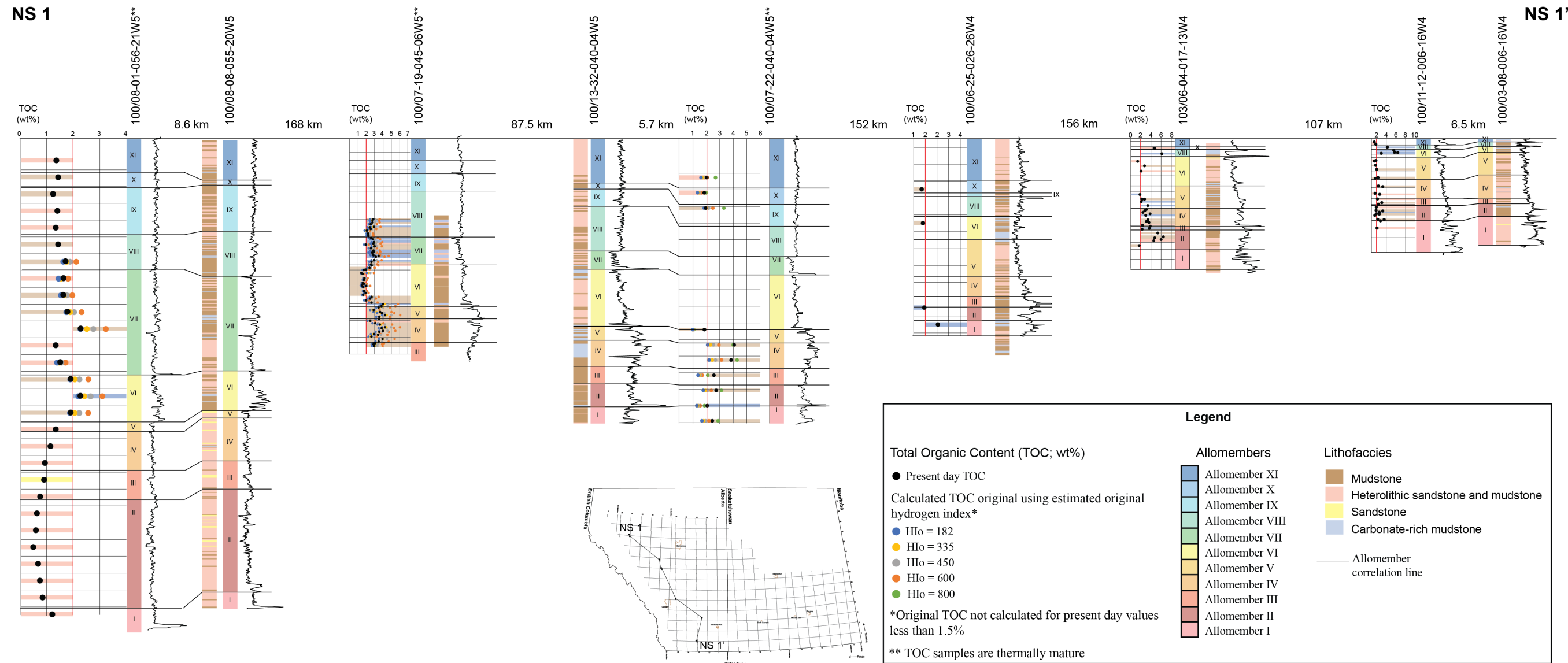


Figure 8:11: North-south summary cross section showing total organic content and corresponding lithofacies classification. Thermally mature samples greater than the 1.5 wt.% cutoff criteria were restored to original total organic content. An estimated HI₀ of 800 was used for some samples in 100/07-22-040-04W where the TOC_{pd} remained higher than the estimated TOC₀ when using estimated HI₀ values 600, 450, 335 and 182. Data from all wells except for 100/07-19-045-06W5, where the core was logged and sampled in this study, were correlated to the adjacent well to designate a lithofacies classification. The red line at 2 wt.% indicates the total organic content cutoff for very good generation potential. The lithofacies classification in 100/07-19-045-01W6 is interpreted from core logged by K. Greff (date unknown) and Marion (2019). It is possible that the interpreted lithofacies that came from those descriptions did not match entirely and the material contained more sandstone than described. This could explain the distinct shift to lower TOC values within the middle to upper strata of allomember VI.

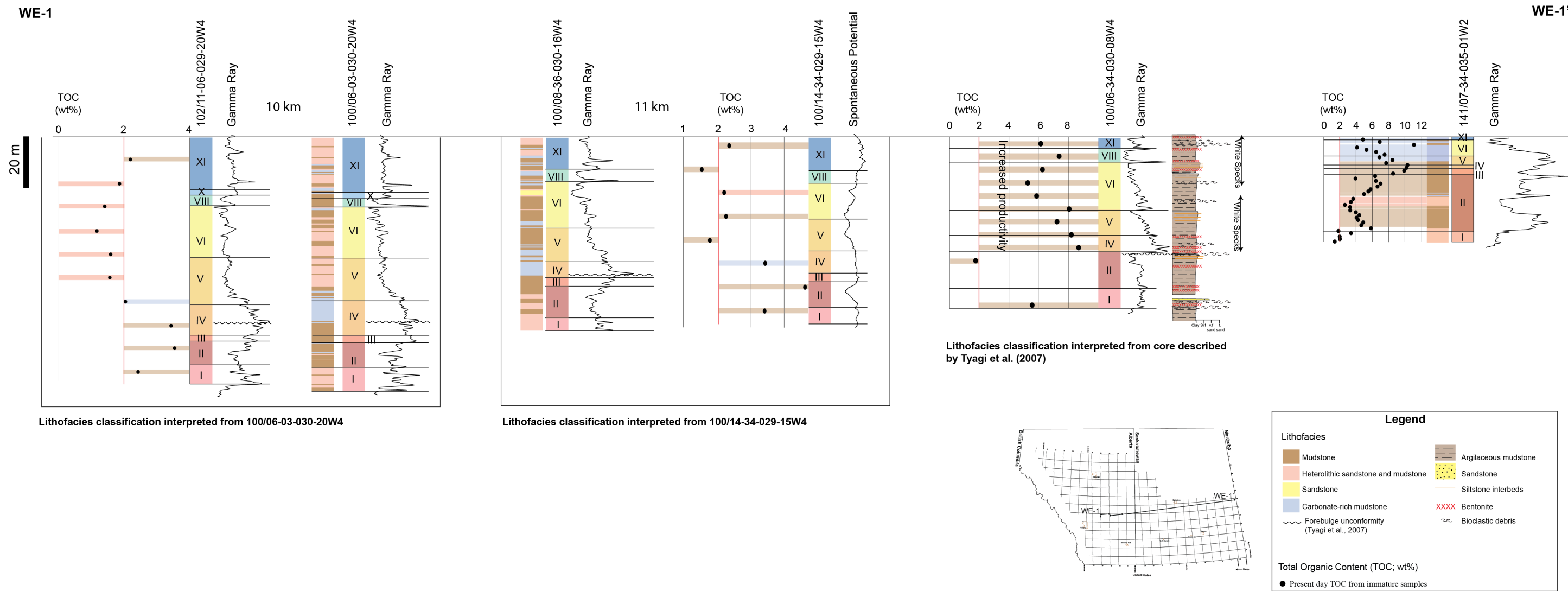


Figure 8:12: West to east summary cross section showing total organic content data with corresponding lithofacies classification. Data from 102/11-06-029-20W4 and 100/14-34-029-15W4 were correlated to 100/06-03-030-20W4 and 100/08-36-030-16W4, respectively, to assign lithofacies classifications to the samples. Well 141/07-34-035-01W2 was logged and sampled for this study. The red line at 2 wt.% indicates the total organic content cutoff for very good generation potential.

commonly associated with silty argillaceous mudstones and calcareous mudstones. Some samples in silty argillaceous material have TOC values less than the 2 wt.% cutoff, and vice versa for heterolithic sandstone and mudstone. Data trends from north to south (Figure 8.11) show allomembers I through V becoming increasingly muddy and organic-rich toward the southern limit of the cross section (100/11-12-006-16W4). Increasing proportion of calcareous mudstone occurrences in strata shallower than allomember VI corresponds to a sharp rise in TOC. In the WE-1 to WE-1' cross section (Figure 8.12), the TOC between allomembers V and XI increases in wells towards the east as the lithofacies become muddier.

8.5 Organic matter distribution in the Blackstone Alloformation

Enhanced primary productivity during Cenomanian-Turonian is linked to the inflow of warm nutrient-rich water from the Tethyan Sea (proto-Gulf of Mexico) and the development of bottom water anoxia. Evidence of this incursion is evident in the allomember lithology percentage maps as the distribution of calcareous mudstone expands geographically across the basin. In lithology maps that show a complex distribution pattern of isolated calcareous mudstone and non-calcareous argillaceous mudstone deposits intermixed with siliciclastic sediment (Chapter 6), sedimentation was also influenced by variable influx of siliciclastic sediment supply and/or redistribution of sediment by storms. The complexity in sedimentation and TOC results presented in this chapter support the interpretation that organic matter enrichment is largely related to changes in organic matter preservation potential.

Consideration of the TOC data presented above in conjunction with subsidence history and lithology distribution demonstrates that geographical and temporal distribution of organic matter was influenced by allogenic controls that altered the balance of dilution and preservation processes (i.e., development of organo-mineralic aggregates (OMAs) and sedimentation/burial rates) across the basin. The discussion below examines the relationship between observed TOC trends and sedimentation trends related to tectonism

and eustasy. Organic matter distribution is not discussed for allomembers IX and X due to limited availability of TOC data for these intervals.

In a regional study on multi-scale sedimentological heterogeneity in the Belle Fourche and Second White Specks formations in southern Alberta, Percy (2019) concluded that organic matter accumulation occurred where OMAs were subject to traction transport processes and became concentrated under low sedimentation rates as storm waves and currents reworked the seafloor sediment. The lack of persistent bottom water anoxia during the OAEII event, as suggested by a low-diversity ichnofauna and inoceramid bivalves (Schroder-Adams et al., 1996), suggests that the preservation of organic matter was favoured by the episodic and rapid burial of organic-rich sediments (Percy, 2019).

The TOC data collected for this study shows that organic-rich sediment is enhanced in thinly bedded silty argillaceous mudstone (Lithofacies 5) and very thinly bedded, carbonaceous, calcareous-argillaceous mudstone (Lithofacies 3) deposits. The organic-rich material (calcareous pellets and OMAs) was transported and deposited as bedload and concentrated within the millimetre-scale planar-parallel laminated silty mudstone (Lithofacies 5) and millimetre-scale, planar-parallel to discontinuous wavy laminated calcareous mudstone (Lithofacies 3). In the heterolithic sandstone and mudstone (Lithofacies 2), organic matter is generally poorly preserved in the sandstone interbeds due to dilution from siliciclastic input and/or oxygenation of bottom waters (as suggested by a strong degree of bioturbation). This is also the case for Lithofacies 1 (Fine-grained sandstone with thinly bedded and weakly bioturbated mudstone). It is noted that organic matter preservation could occur in the mudstone interbeds of Lithofacies 2 (i.e., well 102/11-06-029-20W4, Figure 8.12), as OMAs were reworked and concentrated under fair-weather conditions, with intermittent storms promoting rapid burial and thus enhancing organic matter preservation (Percy, 2019). However, the variability in the thickness of mudstone interbeds within Lithofacies 2 would not make the heterolithic lithofacies a favorable target for self-sourcing carbonaceous reservoirs.

Variations in mineral content viewed alongside TOC data provide insight on the relationship between the mapped lithofacies and organic matter preservation. In Figure

UWI: 141/07-34-035-01W2

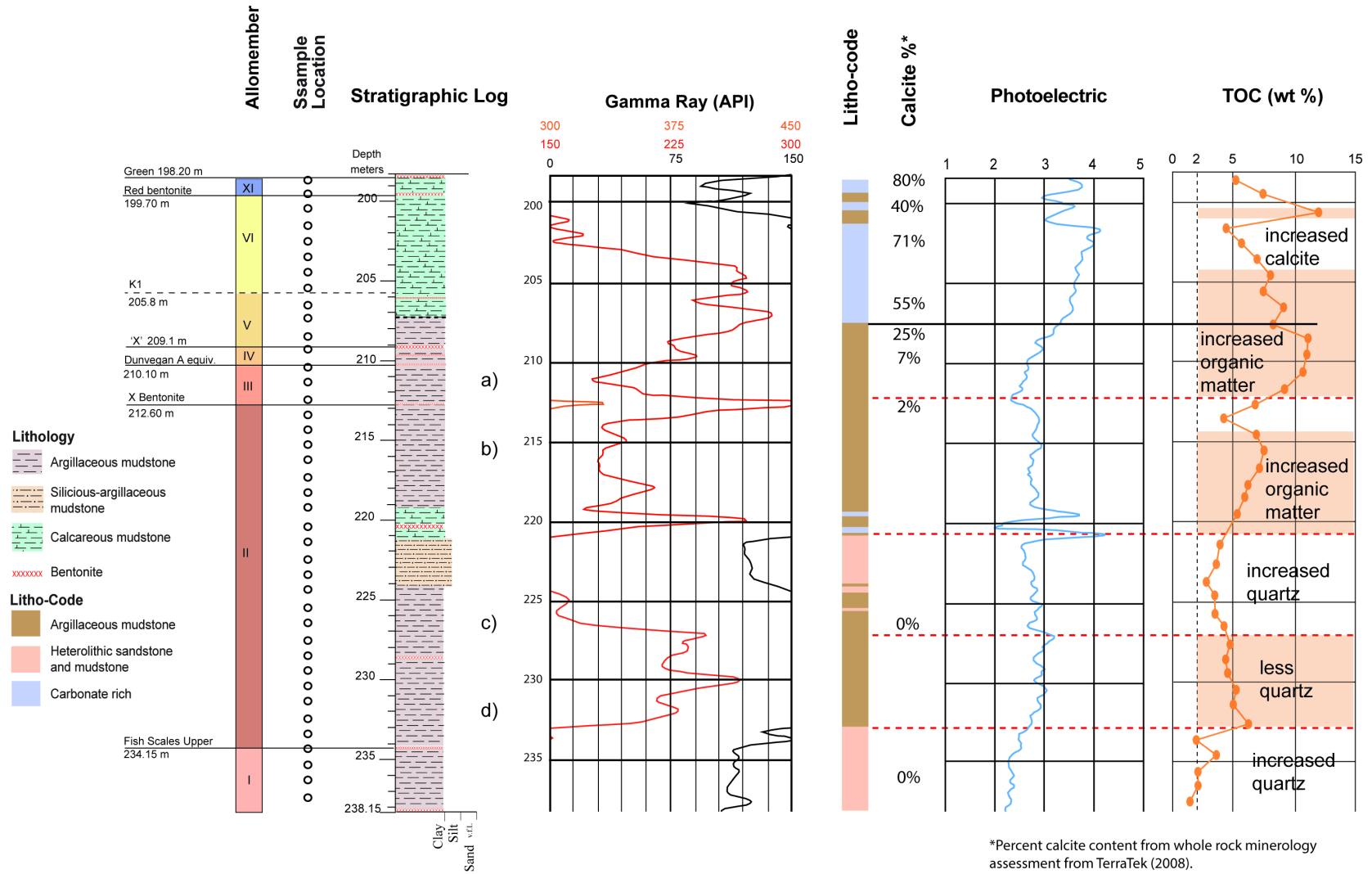


Figure 8:13: Stratigraphic log and lithofacies classification alongside geophysical well log and TOC data. Note that within the argillaceous mudstone intervals, TOC increases with decreasing quartz content. Also, within calcareous mudstone, TOC increases with decreasing calcite content.

8.13, bulk mineralogy (obtained from TeraTek, 2008) is shown alongside lithofacies and TOC data. It suggests TOC becomes diluted as the calcite content increases above 55 wt.%. The lowest TOC value from calcareous mudstone in allomember VI corresponds to a calcite content of 71 wt.%. The high biogenic carbonate production (i.e., foraminifera and coccolithophores) diluted the TOC content (Mohebati, 2016) as clay content was too low to produce OMAs and preserve organic-rich material (Hart, 2016). A decrease in calcite content to 40 wt.% corresponds to an increase in TOC to over 10 wt.%.

Total organic preservation during deposition of allomember I was low across the basin due to sedimentation processes related to deposition of siliciclastic-rich heterolithic sandstone and mudstone on a broad, low gradient ramp, with geographically isolated pockets of sandstone in northwestern and southeastern Saskatchewan. It is interpreted here that organic matter preservation was hindered during this time due to the increased supply of siliciclastics into the basin from the uplifted regions in northwestern and southeastern Saskatchewan.

During the middle Cenomanian (allomembers II through V), as the Greenhorn marine transgression caused a relative sea level in the basin, argillaceous mudstone and calcareous mudstone became the dominant lithologies. Overall, increased primary production associated with the inflow of nutrient-rich waters from the Tethyan Sea and increased deposition of siliciclastic mudstone and calcareous mudstone promoted conditions favorable for OMA development. With the possible exception of the north-south constrained deposit of heterolithic sandstone and mudstone in western Saskatchewan, the differential subsidence occurring during deposition of allomember II did not appear to negatively influence organic matter preservation. The decreasing abundance of heterolithic deposits over time suggests that sediment deposition occurred predominantly below storm-wave base, thus maintaining the low oxygen conditions that would have limited the degradation of organic matter and would have ultimately promoted organic matter preservation. Diminished organic matter content in southwestern Alberta during deposition of allomember V may be related to the dilution of organic matter content by siliciclastics. Alternatively, this could have also been

accomplished by intermittent oxic bottom water conditions resulting from decreased accommodation associated with localized tectonic uplift in the furthest southwest corner of the study area.

As discussed in section 6.3.1, the complex depositional pattern observed for allomember VI can be explained as a consequence of the mixing of two water masses with contrasting temperature and salinity. This reasoning, combined with implied subsidence patterns, may help explain heterogeneity in organic matter distribution across the basin during the lower Turonian. The northwest-southeast subsidence pattern recorded in the deposition of allomember VI may have enhanced conditions favourable to organic matter enrichment by possibly restricting the basinward delivery of siliciclastic sediment from the northwest (outside the study area) and limiting dilution by terrigenous material. Deepening would have also sustained sedimentation below storm-wave base and maintained dysoxic to anoxic bottom water conditions. The co-occurrence of heterolithic sandstone and mudstone, calcareous mudstone and argillaceous mudstone suggest that sedimentation at the sea floor remained susceptible to reworking in the distal offshore setting of the low gradient ramp. This would have produced localized areas of poorer organic matter preservation.

Organic matter distribution during deposition of allomembers VII and VIII was influenced by: 1) limited basinward transport of terrigenous material as a result of active subsidence in the northwest, and 2) depositional condensation related to along-shelf and across-ramp transport of mud on a low gradient ramp, respectively. OMAs that formed in the water column rapidly settled and were transported on the seafloor by storm-generated geostrophic flows (Varban and Plint, 2008a).

During the deposition of allomember XI, sedimentation rate was approximately equal to accommodation rate, permitting the deposition of storm-influenced heterolithic sandstone and mudstone over broad areas of the basin. Although no TOC data is available for allomember XI in wells containing calcareous mudstone in western Alberta, organic matter preservation is expected to have been enhanced in that region. Trapping of siliciclastic material in the west would have reduced organic matter dilution and oxic

degradation of organic matter from sedimentation within storm-wave base would have been low. As described for allomember VI, the mixing of water masses may have complicated the observed organic matter distribution, leading to uncertainties in the true geographic limits of potential organic-rich, thermally mature deposits within this allomember. At the most distal offshore position in eastern Saskatchewan, TOC values varied based on the amount of calcite. As shown in Figure 8.13, a calcite content of 80 wt.% in allomember XI corresponds to a drop in TOC, suggesting the organic matter became diluted from high carbonate production.

Chapter 9

9 Conclusions

This thesis investigated the relationship between basin evolution, sedimentary processes, and organic matter distribution in the Blackstone Alloformation of the Upper Cretaceous Colorado Group. Results from this work contribute to the understanding of how foreland basin dynamics and eustasy influenced the distribution and preservation of organic matter. The integration of well logs with lithofacies observations and organic geochemistry data on a basinwide scale is a methodology that can be used in other formations in a foreland basin setting, to help predict lithofacies trends in areas where core information is lacking.

The objectives outlined in Chapter 1 were required to test the hypothesis that depositional conditions essential for the accumulation of organic matter across the Western Canada Foreland Basin during deposition of the Blackstone Alloformation are inherently linked to basin-scale allogenic processes. Integration of results from these objectives demonstrates that: 1) organic matter enrichment is influenced by the changing sedimentary processes that occurred in response to dynamic tectonism and eustasy, and 2) organic matter distribution can be predicted by upscaling lithofacies data to basin scale.

The objectives and corresponding findings of this thesis are summarized below in point form.

9.1 Objectives and results

9.1.1 Objective 1: Constructing a basinwide allostratigraphic framework

Objective 1 was to construct a basinwide allostratigraphic framework for the Blackstone Alloformation to reveal stratal architecture and changes in subsidence patterns.

- A basinwide allostratigraphic framework linking the previous studies of Tyagi et al (2007) and Tyagi (2009) was developed for the Blackstone Alloformation in

the Western Canada Foreland Basin. The framework consists of 15 north-south and 12 west-east cross section lines constructed using geophysical wireline log data from 574 wells. Drillcore from 18 wells were logged to tie marine flooding surfaces and regionally correlative bentonites identified in Tyagi et al. (2007) and Tyagi (2009) across the basin, from western Alberta to the Saskatchewan-Manitoba border. This work divided the Blackstone Alloformation into eleven allomembers (I through XI).

- The study interval is bound by the base of Fish Scales Marker at the bottom and a regionally extensive bentonite informally named the “Green” bentonite. Variable expressions of allomember bounding surfaces demonstrate that sedimentation on a low gradient shallow marine ramp was influenced by subtle changes in accommodation. For example, the regional disconformity surface at the top of allomember V, known as the K1 surface, is observed in core as a condensed, erosional, or flooding surface at different locations in the basin. Its variable expression suggests regional and localized changes in sediment supply and accommodation. The Bighorn River bentonite is observed in cores from the proximal and distal setting of the basin, becoming eroded as a result of tectonic uplift within the forebulge region.
- Stratal geometries in the basin are wedge-shaped adjacent to the deformation front in western Alberta, transitioning to tabular-shaped eastward towards the stable craton (Manitoba). The westward thickening of allomembers is interpreted to reflect continued subsidence from tectonic loading in the fold-and-thrust belt. A prominent forebulge region was mapped in allomembers III to IV, and VII to IX. Changes in the positions of flexure-generated depocentres recorded in the allomembers are interpreted to have been responses to the shifting locations of active thrusting.
- Isopach mapping revealed shifts in the locations of depocentres during Cenomanian-Turonian time. In allomembers I, II, and III a depocentre is dominant in northwest Alberta, then shifts to broad subsidence that runs along the

western limit of Alberta in allomember IV. A northwest-southeast trending subsidence pattern in southern Alberta is observed in allomember V and VI. This was followed by increased loading in the fold and thrust belt during allomember VII through IX, promoting the development of a prominent forebulge that was accompanied by the erosion of strata deposited earlier in the distal basin. The backbulge depozone records sediment deposition on the stable craton region and is not easily identified in most allomember isopach maps. A proximal depozone basinward of a region of uplift in allomember XI is interpreted as a backbulge, its proximity to the deformation front suggesting a narrow zone of high-amplitude flexure during this time.

- Basement structures likely influenced allomember thickness as sediment was deposited over reactivated basement terranes. Allomember I and II thinned over a possibly uplifted Punnichy Arch in response to subsidence in the Williston Basin. Reactivation of the Coburg syncline in southwestern Saskatchewan produced slight thickening in allomembers II and III. The northwest-southeast thickening trend observed in isopach maps for allomembers IV, V, and VI are parallel to mapped basement lineaments. It is considered that this subsidence pattern could represent either a backbulge depozone with a foredeep positioned to the west of the study area, or differential subsidence in the foredeep that had responded to non-uniform movement on basement terranes.

9.1.2 Objective 2: Map lithology distribution across the basin

Objective 2 was to map lithology distribution across the basin using geophysical well log data in conjunction with recurring lithofacies defined from core. These maps were used to reveal sedimentation patterns and determine if they are linked to specific depozones in the Western Canada Foreland Basin.

- Five lithofacies are defined in the study area based on observations made from drillcore. These include sandstone (Lithofacies 1), thinly bedded heterolithic sandstone and mudstone (Lithofacies 2), very thinly bedded, carbonaceous, calcareous-argillaceous mudstone (Lithofacies 3), foraminifera- and coccolith-

rich packstone-grainstone (Lithofacies 4), and thinly bedded, silty argillaceous mudstone (Lithofacies 5). These lithofacies record deposition in proximal offshore (inner shelf/offshore transition zone) to distal offshore settings on a low-gradient, shallow marine ramp. Three lithofacies successions are recognized and record the proximal and distal expression of gradational transgressive-regressive successions deposited on this ramp. Upward-shallowing in the most shore-proximal position in the study area is recorded by the upward transition from siliciclastic mudstone into heterolithic sandstone and mudstone, and ultimately sandstone. Silty argillaceous mudstone records the proximal and distal offshore expression of regression whereas transgression is recorded in the distal offshore by the appearance of calcareous mudstone and pelagic carbonates.

- Four lithology categories used to create lithology distribution maps were identified based on the lithofacies observed in core. The maps represent the percentage of each lithology: mudstone (Lithofacies 5), heterolithic sandstone and mudstone (Lithofacies 2), sandstone (Lithofacies 1), and carbonate-rich sediment (Lithofacies 3 and 4). Sediment distribution patterns suggest sedimentation during deposition of the Blackstone Alloformation was influenced by tectonic flexure and eustacy. Siliciclastic sediment input to the basin was predominantly sourced from northwestern Alberta throughout the Cenomanian-Turonian. Incursion of sandstone in northwest and southeast Saskatchewan during deposition of allomember I could reflect a sediment source exists in those regions beyond the study area. Influence of the Greenhorn transgression on sedimentation is evident by the increasing geographic distribution of calcareous mudstone over time.
- Localized patches of mudstone and heterolithic sandstone and mudstone within basinwide coverage of calcareous mudstone record sedimentation influenced by storms on the low gradient ramp in a shallow marine setting. The abrupt lithologic change was also influenced by laterally shifting ocean fronts where water masses of different temperature, density, and salinity became mixed.

9.1.3 Objective 3: Link programmed pyrolysis data to basin lithology distribution

Objective 3 was to link programmed pyrolysis data obtained from Rock-Eval and LECO analyses to basin lithology distribution to investigate how allogenic drivers influence organic matter preservation.

- Organic geochemical parameter data was obtained from programmed pyrolysis (Rock-Eval and LECO). Samples collected from the study interval are kerogen type II and type II-III. Thermally mature samples were obtained predominantly from wells located west of Meridian 5 (W5), with the highest Tmax occurring adjacent to the deformation front. Thermally immature data characterize wells located in Meridian 1 through 4 (W1 to W4).
- The total organic content (TOC) ranges between <1% to 13.03%, with the highest value occurring within the Belle Fourche Formation. Calcareous mudstone and silty argillaceous mudstone (equivalent to Lithofacies 3 and Lithofacies 5, respectively) contain the highest wt.% TOC, followed by heterolithic sandstone and mudstone. Calcareous mudstone samples from wells located in W2, W3, and W4 have the best hydrocarbon generation potential.
- Organic matter preservation in the Blackstone Alloformation is greatest in Lithofacies 3 (calcareous mudstone) and Lithofacies 5 (silty argillaceous mudstone) where depositional conditions favoured the transport and concentration of calcareous pellets and organo-mineralic aggregates (OMAs) within thin laminae. The dilution of organic matter that led poor preservation resulted from siliciclastic input from tectonic uplift regions and/or high biogenic carbonate production where the clay content was too low for OMA development. Preservation of organic-rich material was hindered in the sandstone beds of the heterolithic sandstone and mudstone deposits in regions where the sea floor was susceptible to intermittent oxygenation of bottom waters from storm-based sediment reworking. Rising sea level during the Greenhorn marine transgression combined with active tectonic loading in western Alberta enabled accumulation

of organic matter by promoting primary productivity, maintained dysoxic to anoxic bottom water conditions, and limited the basinward transport of siliciclastics (reducing dilution).

9.2 Acknowledgement of limitations of this study

The acknowledged limitations in this study are as follows:

1. Correlation work completed for this thesis depended on the availability and quality of geophysical logs. Greater distances between well locations did occur in areas of low well density. This may have caused erroneous interpretations on the lateral continuity of allomember surfaces in north-central Saskatchewan where erosion and/or non-deposition of Colorado Group strata is expected to be greatest.
2. Reduced availability of photoelectric logs limits the accuracy of mapping regional lithologic trends. Although the maps produced in this study represent the approximate extents of lithologic boundaries, the overall distribution patterns observed would not change the regional interpretation presented herein.

9.3 Future work

Opportunities for future work include the following:

- Chronostratigraphic control in this stratigraphic framework can be improved by dating the basinwide bentonites observed and correlated in this research. The location of the dated bentonites in Ridgley et al. (2001) is unclear, therefore correlation into their work did not provide clarity on ages of the mapped bentonites of the current study. Gathering age dates for the basinwide mapped bentonites of this study would be beneficial to understanding the amount of erosion or non-deposition that occurred in the WCFB during Cenomanian-Turonian time.
- Further improvements to this framework could be achieved through incorporating petrographic data, quantitative mineralogy, and increasing the well density in regions of the study area that have undergone increased drilling activity that is

beyond the historical oil and gas exploration footprint (i.e., southwestern, and northcentral Saskatchewan).

- Domestic and global interest in rare earth element (REE) exploration is driven by growing demand for products in which REEs are widely used. The presence of REE in organic-rich shale has been reported, and our understanding of the controls on REE distribution within shale is poorly understood. Utilizing the chronostratigraphic framework in this study in conjunction with REE exploration in organic-rich Colorado Group shales could help establish an association between paleogeographic conditions required for REE enrichment.

References

- Aigner, T. and Reineck, H.E. 1982. Proximal trends in modern storm sands from the Helgoland Bight (North Sea) and their implication for basin analysis. *Senckenb. Maritima* **14**: pp. 183-215.
- Aizarani, J. 2023. Shale gas and tight oil plays production in the U.S. 1999-2050. Statista. Available from <https://www.statista.com/statistics/183740/shale-gas-production-in-the-united-states-since-1999/> [accessed April 21, 2022].
- Allredge, A.L., and Silver, M.W. 1988. Characteristics, dynamics and significance of marine snow. *Prog. Oceanogr.* **20**: pp. 41-82.
- Allen P. A, Allen J.R., 2005, Basin analysis: principles and application to petroleum play assessment, 3rd ed. Wiley-Blackwell, Oxford.
- Angiel, P. J. 2013. Allostratigraphy, sedimentology and paleogeography of the Cretaceous Upper Fort St. John Group (Upper Albian-Lower Cenomanian) in Northeastern British Columbia. Unpublished Ph.D. thesis. University of Western Ontario, London, Ontario, 403p.
- Aplin, A.C., and Macquaker, J.H.S., 2011, Mudstone diversity: Origin and implications for source, seal, and reservoir properties in petroleum systems: American Association of Petroleum Geologists, v. 95, no. 12, p. 2031 – 2059.
- Aplin, A.C, Fleet, A.J, and Macquaker, J.H. 1999. Muds and mudstones: Physical and fluid-flow properties. Geological Society, London, Special Publications **158**(1), pp. 1-8.
- Arnott, R.W. and Southard, J.B. 1990. Exploratory flow-duct experiments on combined-flow bed configurations and some implications for interpreting storm-event stratification. *Journal of Sedimentary Research* **60**(2): pp. 211-219.
- Arthur, M.A., Dean, W.E., Laarkamp, K. 1998. Organic carbon accumulation and preservation in surface sediments on the Peru margin. *Chemical geology* **152**: pp. 273-286.
- Arthur, M.A., W.E. Dean, and S.O. Schlanger. 1985. Variations in the global carbon cycle during the Cretaceous related to climate, volcanism, and changes in atmospheric CO₂. *The carbon cycle and atmospheric CO₂: natural variations Archean to present* **22**, pp. 504-529.
- Arthur, M.A., and Sageman, B. 1994. Marine black shales: Depositional mechanisms and environments of ancient deposits: *Annual Review of Earth and Planetary Sciences* **22**, pp. 499-551.

- Arthur M.A., and Sageman, B., 2004, Sea-level control on source-rock development: Perspectives from the Holocene Black Sea, the Mid-Cretaceous Western Interior Basin of North America, and the Late Devonian Appalachian Basin. In: Harris NB (ed) *The deposition of organic-carbon-rich sediments: models, mechanisms, and consequences*. SEPM (Society for Sedimentary Geology), pp 35–58.
- Asquith G., and Krygowski, D., 2006, Basic well log analysis. AAPG Methods in Exploration Series, No. 16, Second Edi. American Association of Petroleum Geologists Bloch et al., 1993.
- Aviles, M. A. 2021. Organic geochemistry, organic petrography and basin modelling of the Upper Cretaceous Second White Specks and Upper Belle Fourche alloformations in the Western Canada Foreland Basin. Ph.D. thesis. Department of Earth Science. The University of Western Ontario, London, Ontario.
- Baihly, J., Altman, R., Malpani, R. and Lou, F. 2010. Shale gas production decline trend comparison over time and basins. *In* SPE Annual Technical Conference and Exhibition. One Petro.
- Barker, I.R., Davis, W.J., Moser, D.E., Kamo, S.L., and Plint, A.G. 2011. High-precision U-Pb zircon ID-TIMS dating of two regionally extensive bentonites: Cenomanian Stage, Western Canada Foreland basin. *Canadian Journal of Earth Sciences* **48** (2): pp. 543-556.
- Beaton, A.P., Pawlowicz, J.G., Anderson, S.D.A., and Rokosh, C.D. 2009. Rock Eval, total organic carbon, adsorption isotherms and organic petrography of the Colorado Group: Shale gas data release. ERCB/AGS Open File Report, 2008-11. 94p.
- Beaumont, C., 1981, Foreland basins. *Geophysics Journal International* **65**: pp. 291–329.
- Beaumont, C., Quinlan, G.M., and Stockmal, G.S. 1993. The evolution of the Western Interior Basin: Causes, consequences and unsolved problems. *In* *Evolution of the Western Interior Basin*. Edited by Caldwell, W.G.E. and Kauffman, E.G. GAC Special Paper **39**: pp. 97-117.
- Behar, F., Beaumont, V., De HL, Penteadó, B. 2001. Rock-Eval 6 Technology: Performances and Developments. *Oil Gas Sci. Technol. – Rev IFP* **56**: pp. 111-134.
- Berner, R.A. 1970. Sedimentary pyrite formation. *American Journal of Science* **268**: pp. 1-23.
- Berner, R.A. 1984. Sedimentary pyrite formation: An update. *Geochemica et Cosmochimica Acta* **48**: pp. 605-615.

- Bjorlykke, K. 2010. Petroleum geoscience: From sedimentary environments to rock physics. 1st edn. Springer Berlin Heidelberg.
- Blakey, R.C. 2014. Paleogeography and paleotectonics of the Western Interior Seaway, Jurassic-Cretaceous of North America. *Search and Discovery*. **30392**: ppl 1-72.
- Bloch, J.D. and Leckie, D.A. 1993. Rock-Eval data of the Cretaceous Colorado Group, Western Canada Sedimentary Basin. Geological Survey of Canada, Open File 2676, 22p, Calgary.
- Bloch, J. D., Schroder-Adams, C., Leckie, D. A., Craig, J. & McIntyre, D. J., 1999, Sedimentology, micropaleontology, geochemistry and hydrocarbon potential of shale from the Cretaceous lower Colorado Group in Western Canada, *Geological Survey of Canada Bulletin* 531, 185 p.
- Bloch, J., Schroder-Adams, C., Leckie, D. A., McIntyre, D. J., Craig, J. & Stainland, M. 1993. Revised stratigraphy of the lower Colorado Group (Albian to Turonian), Western Canada. *Bull. CSPG* 41(3), 325-348.
- Bhattacharya, J.P. 1989. Allostratigraphy and river- and wave-dominated deltaic sediments of the Upper Cretaceous (Cenomanian) Dunvegan Formation, Alberta. Unpublished Ph.D. thesis, McMaster University, Hamilton, Ontario, 588 p.
- Bhattacharya, J.P. 1993. The expression and interpretation of marine flooding surface and erosional surfaces in core; Examples from the Upper Cretaceous Dunvegan Formation, Alberta foreland basin, Canada. *In* Sequence stratigraphy and facies associations. *Edited by* H.W. Posamentier, C.P. Summerhayes, B.U. Haq and G.P. Allen. International Association of Sedimentologists **18**, pp. 125-160.
- Bhattacharya, J.P., and MacEachern, J.A., 2009, Hyperpycnal rivers and prodeltaic shelves in the Cretaceous seaway of North America: *Journal of Sedimentary Research*, v. 79, p. 184-209.
- Bhattacharya, J. P and Posamentier, H. W. 1994. Chapter 25. Sequence stratigraphy and allostratigraphic applications in the Alberta Foreland Basin. In: *Geological Atlas of the Western Canada Sedimentary Basin* (edited by Mossop, G.D. & Shetson, I.). CSPG, Available from <https://ags.aer.ca/reports/atlas-western-canada-sedimentary-basin> [accessed July 6, 2022].
- Bhattacharya, J.P. and Walker, R.G. 1991. Allostratigraphic subdivision of the Upper Cretaceous Dunvegan, Shaftsbury and Kaskapau formations in the northwestern Alberta subsurface. *Bulletin of Canadian Petroleum Geology*, **39**, pp. 145-164.
- Bennett, R.H., O'Brien, N.R., and Hulbert, M.H. 1991. Determinants of clay and shale microfabric signatures: Processes and mechanisms. *In* *Microstructure of Fine-*

Grained Sediments: From Mud to Shale. *Edited by* Bennett, R.H., Bryant, W.R. and Hulbert, M.H. New York, Springer-Verlag, pp. 5-32.

Boggs, Jr. S. and Boggs, S. 2009. Petrology of Sedimentary Rocks. Cambridge university press.

Bohacs, K.M., Grabowski, G.J.J., Carroll, A.R., Mankiewicz, P.J., MiskellGerhardt, K.J., Schwalbach, J.R., Wegner, M.B., and Simo, J.A. 2005. Production, destruction, and dilution: The many paths to source-rock development. *In* The Deposition of Organic-Carbon-Rich Sediments: Models, Mechanisms, and Consequences. *Edited by* Harris, N.B. SEPM Special Publication **82**: pp. 61-101.

Bond, G. C. & Kominz, M. A. 1984. Construction of tectonic subsidence curves for the early Paleozoic miogeocline, southern Canadian Rocky Mountains: Implications for subsidence mechanisms, age of breakup, and crustal thinning *GSA Bulletin* **95**, 155-173.

Burdige, D.J. 2007. Preservation of organic matter in marine sediments: Controls, mechanisms, and an imbalance in sediment organic carbon budgets? *Chemical Reviews* **107**: pp. 467-485.

Burgess, P. M. & Moresi, L. N. 1999. Modelling rates and distribution of subsidence due to dynamic topography over subducting slabs: is it possible to identify dynamic topography from ancient strata. *Basin Research* **11**, 305-314.

Caldwell, W.G.E. 1984. Early Cretaceous transgressions and regressions in the southern interior plains. *In* The Mesozoic of Middle North America. *Edited by* Stott, D.F. and Glass, D.J. CSPG Memoir **9**: pp. 173-203.

Caldwell, W.G.E., North, B.R., Stelck, C.R., and J.H, W. 1978. A foraminiferal zonal scheme for the Cretaceous System in the Interior Plains of Canada. *In*: Western and Arctic Canadian Biostratigraphy. *Edited by* C.R. Stelck, and B.D.E. Chatterton. Geological Association of Canada, Special Paper. pp. 495-575.

Caldwell, W.G.E., Diner, R., Eicher, D.L., Fowler, S.P, North, B.R., Stelck, C.R. and von Holt Wilhelm, L. 1993. Foraminiferal biostratigraphy of the Cretaceous marine cyclothem. *In*: *Evolution of the Western Interior Basin*. (Edited by W.G.E. Caldwell and E.G. Kauffman. Geological Association of Canada. Special Paper.

Campbell, C.V. 1967. Lamina, laminaset, bed and bedset. *Sedimentology* **8**: 7-26.

Cant, D.J. and Stockmal, G.S. 1989. The Alberta Foreland Basin: Relationship between stratigraphy and Cordilleran terrane-accretion events. *Canadian Journal of Earth Science* **26** pp. 1964-1975.

- Catuneanu, O. 2002. Sequence stratigraphy of clastic systems: concepts, merits, and pitfalls. *Journal of African Earth Sciences* **35**(1): pp. 1-43.
- Catuneanu, O. 2004. Basement control on flexural profiles and distribution of foreland facies: the Dwyka Group of the Karoo Basin. *Geology* **32**(6): pp. 517-520.
- Cattaneo, A., Trincardi, F., Asioli, A, and Correggiari, A. 2007. The western Adriatic shelf clinoform: energy-limited bottomset. *Continental Shelf Research*, v. 27. pp. 506-525.
- Cheadle, B.A. 2011. Systemic reservoir characterization of organic-rich mudstones. Presented at CSPG GeoConvention, Calgary, Alberta, 9-11 May 2011.
- Chamberlain, C.P., Jan, M.Q., Zietler, P.K. 1989. A petrologic record of the collision between the Kohistan Island-Arc and Indian Plate, northwest Himalaya. In: *Tectonics of the Western Himalayas*. (Edited by L.L. Malinconico and R.J. Lillie. *Geol. Soc. Am. Spec. Paper*, 232, 23-32.
- Chen, Z. and Jiang, C. 2016. A revised method for organic porosity estimation in shale reservoirs using Rock-Eval data: Example from Duvernay Formation in the Western Canada Sedimentary Basin. *American Association of Petroleum Geologists Bulletin* **100**: pp. 405-422.
- Chiles, J.P. and Delfiner, P. 2012. *Geostatistics: modelling spatial uncertainty*. New Jersey, John Wiley & Sons. 731p.
- Christopher, J.E and Yurkowski, M. 2005. The Upper Cretaceous (Turonian) Second White Specks Formation of eastern Saskatchewan; *In* Summary of Investigations 2005, Volume 1, Saskatchewan Geological Survey, Sask. Industry Resources, Misc. Rep. 2005-4.1. 12p.
- Christopher, J.E., Yurkowski, M., Nicolas, M., and Bamburak, J. 2006. The Cenomanian-Santonian Colorado Formations of Eastern Southern Saskatchewan and Southwestern Manitoba. *In*: Saskatchewan and Northern Plains Oil and Gas Symposium 2006, *Edited by* Gilboy, C.F. and Whittaker, S.G., Saskatchewan Geological Society Special Publication 19, pp. 299-318.
- Clifton, H.E. 2006. A reexamination of facies models for clastic shorelines. *In* Facies Models Revisited. *Edited by* Posamentier, H.W. and Walker, R.G. Society of Economic Paleontologists and Mineralogists, Special Publication **84**: pp. 293-338.
- Cobban, W.A., Walaszczyk, I., Obradovich, J., and McKinney, K.C. 2006. A USGS Zonal table for the Upper Cretaceous Middle Cenomanian-Maastrichtian of the Western Interior of the United States based on Ammonites, Inoceramids, and Radiometric ages. USGS Open File Report No. 1250, 46p.

- Cornford, C., Gardner, P., Burgess, C. 1998. Geochemical truths in large data sets. I: Geochemical screening data. *Organic Geochemistry* **29**: pp. 519-530.
- Dalrymple, R.W. 2010. Introduction to Siliciclastic Facies Models. *In* *Facies Models 4*. Edited by James, N.P. and Dalrymple, R.W. Geological Association of Canada. pp. 59-72.
- Daly, A.R. and Edman, J.D. 1987. Loss of organic carbon from source rocks during thermal maturation. *American Association of Petroleum Geologists Bulletin* **71**(5): pp. 546.
- DeCelles PG, Giles KA (1996) Foreland basin systems. *Basin Res* 8:105–123.
- Dembicki, H. 2009. Three common source rock evaluations errors made by geologists during prospect or play appraisals. *American Association of Petroleum Geologists Bulletin* **93**: pp. 341-356.
- Dickinson WR (1974) Plate Tectonics and Sedimentation. In: *Special Publications of SEPM (SP22)*. pp 1–27.
- Didyk, B.M, Simoneit, B.R.T., Brassell, S.T., and Eglinton, G. 1978. Organic geochemical indicators of paleoenvironmental conditions of sedimentation. *Nature* **272**(5650), pp. 216-222.
- Dionne, D., Schroder-Adams, C.J., and Cumbaa, S.L. 2016. Foraminiferal response to ecological perturbations along the eastern margin of the Canadian Western Interior Seaway, Cenomanian-Turonian interval. *Journal of Foraminiferal Research* **46**(2): pp. 124-148.
- Duke, W.L. 1990. Geostrophic circulation of shallow marine turbidity currents? The dilemma of paleoflow patterns in storm-influenced prograding shoreline systems. *Journal of Sedimentary Petrology* **60**: pp. 870-883.
- Duke, W.L, Arnott, R.W.C. and Cheel, R.J. 1991. Shelf sandstones and hummocky cross-stratification: new insights on a stormy debate. *Geology* **19**(6): pp. 625-628.
- Dunham, R.J. 1962. Classification of carbonate rocks according to depositional texture. *American Association of Petroleum Geologists*. **1**: 108-121.
- Eicher, D.L., and Diner, R. 1985. Foraminifera as indicators of water mass in the Cretaceous Greenhorn Sea, Western Interior. *In* *Fine-grained Deposits and Biofacies of the Cretaceous Western Interior Seaway: Evidence of Cyclic Sedimentary Processes*. Edited by Pratt, L.M., Kauffman, E.G., and Zelt, F.B. SEPM Field Trip Guide. Vol. 4. Soc. Econ. Paleont. Mineralol., Tulsa, OK.

- Elder, W.P. 1988. Geometry of Upper Cretaceous bentonite beds: Implications about volcanic source areas and paleowind patterns, western interior, United States. *Geology* **16**: pp. 835-838.
- Elderbak, K., and Leckie, M.R. 2016. Paleocirculation and foraminiferal assemblages of the Cenomanian-Turonian Bridge Creek Limestone bedding couplets: Productivity vs. dilution during OAE2. *Cretaceous Research* **60**, pp. 52-77.
- Ellis, D.V. and Singer, J.M. 2008. *Well logging for Earth Scientists*. Springer, Dordrecht, 692p.
- Ericksen, M.C., and Slingerland, R.L. 1990. Numerical simulations of tidal and wind-driven circulation in the Cretaceous interior seaway of North America. *Geological Society of American Bulletin* **102**, pp 1499-1516.
- Espitalie, J., Madec, M., Tissot, B., Mennig, J.J., and Leplat, P. 1977. Source rock characterization method for petroleum exploration. *Proceedings of the 9th Offshore Technology Conference* **3** (2935): pp. 439-444.
- Fisher, C.G. 1991. Calcareous nannofossil and foraminifera definition of an oceanic front in the Greenhorn Sea (Late Middle through late Cenomanian), northern Black Hills, Montana and Wyoming: Paleooceanographic implications. Unpublished Ph.D. University of Colorado, Boulder, Colorado.
- Fisher, C.G., Hay, W.W., and Eicher, D.L. 1994. Ocean front in the Greenhorn Sea (late middle through late Cenomanian). *Paleoceanography* **9**(6): pp. 879-892.
- Fleming, B. P. & Jordan, T. E. 1990. Stratigraphic modeling of foreland basins: interpreting thrust deformation and lithosphere rheology. *Geology* **18**,430-434.
- Flynn, J.A. and Cheadle, B.A. 2013. Development of an allostratigraphic framework for the Cretaceous Colorado Group: Implications for discrete petroleum system development in mudstones. *In* Summar of Investigations 2012, Volume 1. Saskatchewan Geological Survey. Ministry of the Economy, Misc. Rep. 2013-4.1, Paper A-4. 19p.
- Fowler, M.G. and Snowdon, L.R. 1998a. Rock-Eval/TOC data for nine west-central Alberta Wells (TWPS. 58-59, RGEs. 18W5-12W6). Geological Survey of Canada, Open File 3591, 74p. Calgary.
- Fowler, M.G. and Snowdon, L.R. 1998b. Rock-Eval/TOC data for eight central Alberta wells (TWPS. 35-50, RGEs. 6-21W5). Geological Survey of Canada, Open File 3590, 75p, Calgary.

- Frank, M.C. 2006. Coal distribution in the Upper Cretaceous (Campanian) Belly River Group of southwest Saskatchewan. Saskatchewan Industry and Resources. Open File Report 2005-33.
- Furmann, A., Mastalerz, M., Brassel, S.C. et al. 2015. Organic matter geochemistry and petrography of Late Cretaceous (Cenomanian-Turonian) organic-rich shales from the Belle Fourche and Second White Specks formations, west-central Alberta, Canada. *Organic Geochemistry* **85**: 102-120.
- Gale, A. S., Hardenbol, J., Hathway, B., Kennedy, W. J., Young, J. R. & Phansalkar, V. 2002. Global correlation of Cenomanian (Upper Cretaceous) sequences: evidence for Milankovitch control on sea level. *Geology* 30(4), 291-294.
- Gilboy, C.F. 1988. Geology and natural gas production of the Upper Cretaceous Second White-Speckled Shale, southwestern Saskatchewan. *In* Summary of Investigations 1988. Saskatchewan Geological Survey, Saskatchewan Energy and Mines.
- Ghadeer, S.G. and Macquaker, J.H.S. 2012. The role of event beds in the preservation of organic carbon in fine-grained sediments: Analysis of the sedimentological processes operating during deposition of the Whitby Mudstone Formation (Toarcian, Lower Jurassic) preserved in northeast England, *Marine and Petroleum Geology* **35**(1): pp. 309-320.
- Glover, P.W.J. 2000. Formation Evaluation: MSc. Petroleum Geology course notes. Department of Geology and Petroleum Geology, University of Aberdeen, UK. Available from https://homepages.see.leeds.ac.uk/~earpwjg/PG_EN/CD%20Contents/GGL-66565%20Petrophysics%20English/ [accessed April 17, 2023].
- Gluyas, J. and Swarbrick, R. 2003. *Petroleum Geoscience*. Blackwheel Science Ltd., Oxford, 349p.
- Grabowski, R.C. Droppo, I.G. and Wharton, G. Erodibility of cohesive sediment: The importance of sediment properties. *Earth Science Reviews* **105**(3-4): pp 101-120.
- Hart, B.S. 1990. The stratigraphy and sedimentology of the Upper Cretaceous Cardium Formation in Northwestern Alberta and adjacent British Columbia. Unpublished Ph.D. thesis, University of Western Ontario, London, Ontario, 503p.
- Hart, B.S. 2016. Marine mudstone source rocks in epicontinental basins: Development of a conceptual facies model and application to Cenomanian/Turonian mudstones of the Cretaceous Western Interior Seaway. *Hydrocarbon Source Rocks in Unconventional Plays, Rocky Mountain Region*: Rocky Mountain Association of Geologists, Special Publication, pp. 364-421.

- Hart, B.S. and Hofmann, M.H. 2022. Revisiting paleoenvironmental analysis and interpretations of organic-rich deposits: The importance of TOC corrections. *Organic Geochemistry* **170**.
- Hart, B.S. and Steen, A.S. 2015. Programmed pyrolysis (Rock-Eval) data and shale paleoenvironmental analyses: A review. *Interpretation* **3**(1).
- Haq, B.U. 2014. Cretaceous eustasy revisited. *Global and Planetary Change*. 113, pp. 44-58.
- Haq, B.U., Hardenbol, J., and Vail, P.R. 1987. Chronology of fluctuating sea levels since the Triassic. *Science*, 235, pp. 1156-1167.
- Hay, M.J. 2006. Stratigraphy, sedimentology, and paleogeography of the upper Dunvegan Formation, mid-Cenomanian, Alberta, Canada: Interactions between deltaic sedimentation, flexural tectonics and eustasy. Unpublished M.Sc. thesis, University of Western Ontario, London, Ontario, 197p.
- Hay, W.H. and Floegel, S. 2012. New thoughts about the Cretaceous climate and oceans. *Earth Science Reviews*, **115**: pp. 262-272.
- Hay, M.J. and Plint, A.G. 2009. An allostratigraphic framework for a retrogradational delta complex: the uppermost Dunvegan Formation (Cenomanian) in subsurface and outcrop, Alberta and British Columbia. *Bulletin of Canadian Petroleum Geology*, **57**(3): pp. 323-349.
- Hay, M.J. and Plint, A.G. 2020. High-frequency sequences within a retrogradational deltaic succession: Upper Cenomanian Dunvegan Formation, Western Canada Foreland Basin. *The Depositional Record.*, **6**, pp. 524-551.
- Hay, W.H. Eicher, D.L., and Diner, R. 1993. Physical oceanography and water masses in the Cretaceous Western Interior Seaway. In: *Evolution of the Western Interior Basin*. (Edited by W.G.E. Caldwell and E.G. Kauffman. Geological Association of Canada. Special Paper.
- Hill, P.S., Fox, J.M., Crockett, J.S., Curran, K.J, Friedrichs, C.T., Geyer, W.R., Milligan T.G. et al. Sediment delivery to the seabed on continental margins. Special Publication 37 of the International Association of Sedimentologists. Blackwell Publishing, Malden, MA. pp. 49-99.
- Hooper, E. 2019. Allostratigraphy and sedimentology of the Muskiki and Marshybank members of the Wapaibi Formation (Upper Cretaceous, Coniacian) in Southwestern Alberta, Canada. Ph.D. thesis, Department of Earth Sciences, The University of Western Ontario.
- Hu, Y and Plint G (2009) An allostratigraphic correlation of a mudstone-dominated, syn-tectonic wedge: the Puskwaskau Formation (Santonian-Campanian) in outcrop and subsurface, Western Canada Foreland Basin. *Bull Can Pet Geol* 57:1-33

- Huneke, H. and Henrich, R. 2011. Pelagic sedimentation in modern and ancient oceans. *Developments in Sedimentology*. **63**: pp. 215-351.
- Jarvie, D.M. 2012. Shale Resource Systems for Oil and Gas Part 1 – Shale-gas Resource Systems. *Shale Reserv Resour. 21st century*. American Association of Petroleum Geologists Mem. **97**: pp. 69-87.
- Jarvie, D.M., Hill, R.J., Ruble, T.E., and Pollastro, R.M. 2007. Unconventional shale-gas systems: The Mississippian Barnett Shale of north-central Texas as one model for thermogenic shale-gas assessment. *American Association of Petroleum Geologists Bulletin* **91**: 475-499.
- Jiang, P. 2013. Pore morphometrics and thermal evolution of organic-matter microporosity, Colorado Group, Western Canada Foreland Basin. M.Sc. thesis. Department of Earth Sciences, The University of Western Ontario, London, Ontario.
- Jeletzky, J.A. 1968. Macrofossil zones of the marine Cretaceous of the Western of Canada and their correlation with the zones and stages of Europe and Western Interior of the United States. *Geological Survey of Canada Paper* 67-72, 66p.
- Jordan T (1981) Thrust Loads and Foreland Basin Evolution, Cretaceous, Western United States. *Am Assoc Pet Geol Bull* 65:2506–2520.
- Jordan, T. E. 1995. Retroarc foreland basins. In: *Tectonics of sedimentary basins* (edited by Busby, C. J. & Ingersoll, R. V.). Blackwell Science, 331-362.
- Katz, B.J. 1983. Limitations of ‘Rock-Eval’ pyrolysis for typing organic matter. *Organic Geochemistry* **4**: 195-199.
- Katz, B.J. 2005. Controlling factors on source rock development – A review of productivity, preservation and sedimentation rate. *In* The deposition of organic-carbon-rich sediments: Models, mechanisms, and consequences. Society for Sedimentary Geology Special Publication **82**, Tulsa, Oklahoma, p 282.
- Kaufmann, E.G. 1977. Geological and biological overview: Western Interior Cretaceous Basin: Cretaceous facies, faunas, and paleoenvironments across the Western Interior Basin. *Mountain Geologist* **14** (3): pp. 75-99.
- Kauffman, E.G. 1984. Paleobiogeography and evolutionary response dynamic in the Cretaceous Western Interior Seaway of North America. *In*: Jurassic-Cretaceous Bioclimatology and Paleogeography of North American. *Edited by*: G.E.G. Westerman. Geological Association of Canada, Special Paper. Pp. 273-306.

- Kauffman, E.G., and Caldwell WE (1993) The Western Interior Basin in Space and Time. In: Caldwell WE, Kauffman EG (eds) Evolution of the Western Interior Basin. Geological Association of Canada, Special paper 39, pp 1–30.
- Kauffman, E.G., Sageman, B.B., Kirkland, J.I., Elder, W.P. Harries, P.J., and Villamil, T. 1993. Molluscan biostratigraphy of the Cretaceous Western Interior Basin, North American. *In: Evolution of the Western Interior Basin. Edited by W.G.E. Caldwell and E.G. Kauffman. Geological Association of Canada. Special Paper. pp. 397-434.*
- Kennedy, W.J. and Garrison, R.E. 1975. Morphology and genesis of nodular chalks and hardgrounds in the Upper Cretaceous of southern England. *Sedimentology* **22**: pp. 311-386.
- Kent, D.M. and Christopher, J.E. 1994 Geological history of the Williston Basin and Sweetgrass Arch. *In Geological Atlas of the Western Canada Sedimentary Basin. Canadian Society of Petroleum Geologists and Alberta Research Council, pp 421-430.*
- Komar, P.D. 1976. Beach processes and sedimentation: Prentice Hall, 429p.
- Konitzer, S.F., Davies, S.J., Stephenson, M.H., and Leng, M.J. 2014. Depositional controls on mudstone lithofacies in a basinal setting: Implications for the delivery of sedimentary organic matter. *Journal of Sedimentary Research* **84**: pp. 198-214.
- Kreis, L.K., Ashton, K.E., and Maxeiner, R.O. 2000. Interpretive geophysical maps of Saskatchewan; Saskatchewan Energy Mines, Open File Rep. 2000-2.
- Kreis, L.K., Haidl, F.M., Nimergeers, A.R., and Ashton, K.E., Maxeiner, R.O., and Coolican, J. 2004. Lower Paleozoic map series – Saskatchewan. Saskatchewan Industry and Resources, Misc. Report 2004-8. 56p.
- Kreitner, M.A. 2002. Sedimentology, stratigraphy and paleogeography of the Lower Kaskapau Formation, Upper Cretaceous (Cenomanian), northwest Alberta and northeast British Columbia. Unpublished M.Sc. thesis, University of Western Ontario, London, Ontario, 209p.
- Kreitner, M.A., and Plint, A.G. 2006. Allostratigraphy and paleogeography of the Upper Cenomanian, Lower Kaskapau Formation in subsurface and outcrop, Alberta and British Columbia. *Bulletin of Canadian Petroleum Geology* **54**: pp. 147-174.
- Krygowski, D.A. 2003. Guide to petrophysical interpretation. Austin, Texas, USA, 136p.
- Kuiper, K.F., Deino, A. Hilgen, F.J., Krijgsman, W., Renne, P.R., and Wijbrans, J.R. 2008. Synchronizing rock clocks of earth history. *Science* **320**(5875), pp. 500-504.

- Kuuskraa, V., Stevens, S.H., and Moodhe, K.D. 2013. Technically recoverable shale oil and shale gas resources: An assessment of 137 shale formations in 41 countries outside the United States. US Energy Information Administration, US Department of Energy. 76p.
- Lafargue, E., Marquis, F., Pillot, D. 1998. Rock-Eval 6 applications in hydrocarbon exploration, production, and soil contamination studies. *Rev l'Institut Francais de Petrole* **53**: pp. 421-437.
- Lazar, O.R., Bohacs, K.M., Macquaker, J.H.S., Schieber, J., and Demko, T.M. 2015. Capturing key attributes of fine-grained sedimentary rocks in outcrops, cores, and thin sections: Nomenclature and description guidelines. *Journal of Sedimentary Research* **85**, pp. 230-246.
- Leckie, D.A and Smith, D. 1992. Regional Setting, Evolution, and Depositional Cycles of the Western Canada Foreland Basin: Chapter 1. *In American Association of Petroleum Geologists Memoir* **55**: Foreland Basins and Fold Belts. AAPG Special Volumes, pp 9–46.
- Leckie, D.A., Bhattacharya, J.P., Bloch, J.D., Gilboy, C.F., Norris, B., Plint, A.G., Gilders, M., Holmstrom, G., Krause, F.F., Reinson, F.E. Safton, D., Sawicki, J., and Sawicki, O. 1994. Cretaceous Colorado/Alberta Group of the Western Canada Sedimentary Basin. *In: Geological Atlas of the Western Canada Sedimentary Basin. Edited by: G.D. Mossop and I. Shetsen. Canadian Society of Petroleum Geologists and the Alberta Research Council.*
- Loutit, T.S., Hardenbol, J., Vail, P.R., and Baum, G.R. 1988, Condensed sections: The key to age-dating and correlation of continental margin sequences, in Wilgus, C.K., Hastings, B.S., Kendall, C.G. St.C., Ross, C.A., and Van Wagoner, J.C., eds., *Sea Level Changes – An Integrated Approach: Tulsa, Oklahoma, Society of Economic Paleontologists and Mineralogists, Special Publication 42*, p. 183-213.
- Lyatski, H.V., Pana, D.I., and Grobe, M. 2005. Basement structure in central and southern Alberta: insights from gravity and magnetic maps. Alberta Energy and Utilities Board, EUB/AGS Special Report. 76p.
- MacEachern, J.A., Pemberton, S.G, Gingras, M.K., and Bann, K.L. 2010. Ichnology and Facies Models. *In Facies Models 4. Edited by James, N.P. and Dalrymple, R.W. Geological Association of Canada.* pp. 19-58.
- MacEachern, J.A., Bann, K.L., Pemberton, S.G., and Gingras, M.K. 2007. The ichnofacies paradigm: High-resolution paleoenvironmental interpretation of the rock record. *In Applied Ichnology. Edited by: MacEachern, J.A., Bann, K.L., Gingras, M.K., Pemberton, S.G. SEPM Short Course Notes* **52**: pp. 27-64.

- Macquaker, J.H.S. and Bohacs, K.M. 2007. On the accumulation of mud. *Science* **318**(5857): pp. 1734-1735.
- Macquaker, J.H.S. and Gawthorpe, R.L. 1993. Mudstone lithologies in the Kimmeridge Clay Formation, Wessex Basin, Southern England: Implications for the origin and controls on the distribution of mudstones. *Journal of Sedimentary Petrology* **63**(6): pp. 1129-1143.
- Macquaker, J.H.S., Taylor, K.G., and Gawthorpe, R.L. 2007. High-resolution analyses of mudstones: Implications for paleoenvironmental and sequence stratigraphic interpretations of offshore ancient mud-dominated successions. *Journal of Sedimentary Research* **77**: pp. 324-339.
- Macquaker, J.H.S., Bentley, S.J., and Bohacs, K.M. 2010a. Wave-enhanced sediment gravity flows and mud dispersal across continental shelves: Reappraising sediment transport processes operating in ancient mudstone successions. *Geology* **38**: pp. 947-950.
- Macquaker, J.H.S., Keller, M.A., and Davies, S.J. 2010b. Algal blooms and “marine snow”: Mechanisms that enhance preservation of organic carbon in ancient fine-grained sediments. *Journal of Sedimentary Research* **80**: pp. 934-942.
- Macquaker, J.H.S., Taylor, K.G., Keller, M.A., and Polya, D. 2014. Compositional controls on early diagenetic pathways in fine-grained sedimentary rocks: Implications for predicting unconventional reservoir attributes of mudstones. *American Association of Petroleum Geologists* **93**(3): pp. 587-603.
- Macquaker, J.H.S., Taylor, K.G., Young, T.P., and Curtis, C.D. 1996. Sedimentological and geochemical controls on ooidal ironstones and ‘bone-bed’ formation and some comments on their sequence-stratigraphical significance. *In* *Sequence Stratigraphy in British Geology*. Edited by Hesselbo, S.P. and Parkinson, D.N., Special Publication Geological Society **103**: pp. 97-107.
- McAnally, W.H. and Mehta, A.J. 2001. Collisional aggregation of fine estuarial sediment. *In* *Proceedings in Marine Science*, v.3., pp. 19-39.
- McLean, J.R. 1971. Stratigraphy of the Upper Cretaceous Judith River Formation in the Canadian Great Plains. Saskatchewan Research Council, Geology Division. Report No. 11. 96p.
- McNeil, D.H. and Caldwell, W.G.E. 1974. The *Ostrea beloiti* beds – A Cenomanian time-stratigraphic unit in the western Interior of Canada and the United States. *In* Geological Society of America General Meeting, Geological Society of America, Abstracts with Programs, **6**(7), pp. 867.

- McNeil, D.H. and Caldwell, W.G.E. 1981. Cretaceous rocks and their foraminifera in the Manitoba Escarpment, Geological Association of Canada, Special Paper 21.
- Marion, K. 2019. Integrating petrophysics and allostratigraphy to find sweet spots in the Upper Cretaceous Belle Fourche and Second White Specks alloformations, West-Central Alberta, Canada. Ph.D. thesis, Department of Earth Sciences, The University of Western Ontario, London, Ontario.
- Miall, A.D. 2010. The geology of stratigraphic sequences. Second ed. Springer-Verlag. Berlin, Germany. 514 p.
- Middleton, G.V. 2003. Flame structure. *In* Encyclopedia of Sediments and Sedimentary Rocks. *Edited by* Middleton, G.V., Church, M.J., Coniglio, M., Hardie, L.A., and Longstaffe, F.J., Dordrecht, Kluwer Academic Publishers, pp. 281-282.
- Mitrovica, J. X., Beaumont, C. & Jarvis, G. T. 1989. Tilting of continental interiors by the dynamical effects of subduction. *Tectonics* **8**(5): 1079-1094.
- Modica, C.L. and Lapierre, S.G. 2012. Estimation of kerogen porosity in source rocks as a function of thermal transformation: Example of the Mowry Shale in the Powder River Basin of Wyoming. *American Association of Petroleum Geologists* **96**: pp. 87-108.
- Mohebati, S. 2016. Organic, inorganic geochemistry and sedimentology of the Second White Specks Formation, eastern margin of the Western Interior Seaway. Ph.D. thesis. Department of Earth Science, University of Calgary, Calgary, Alberta.
- Moore, R.C. 1949. Meaning of facies. *In* Sedimentary Facies in Geological History: GSA Memoirs. *Edited by* Longwell, C.R., Moore R.C., McKee, E.D., Muller, S.W., Spieker, E.M., and Wood, H.E. pp. 1-34.
- Mulder, T. and Syvitski, J.P.M. 1995. Turbidity currents generated at river mouths during exceptional discharges to the world oceans. *The Journal of Geology* **103**(3): 285-299.
- Myrow, P.M. 1992a. Pot and gutter casts from the Chapel Island Formation, southeast Newfoundland. *Journal of Sedimentary Research* **62**: pp. 992-1007.
- Myrow, P.M. 1992b. Bypass-zone tempestite facies model and proximity trends for an ancient muddy shoreline and shelf. *Journal of Sedimentary Petrology* **62**: pp. 99-115.
- Myrow, P.M. and Southard, J.B. 1996. Tempestite deposition. *Journal of Sedimentary Research* **66**: pp. 875-887.

- National Resources Canada, 2020. Exploration and Production of Shale and Tight Resources. Available from <https://natural-resources.canada.ca/energy/energy-sources-distribution/natural-gas/shale-tight-resources-canada/exploration-and-production-shale-and-tight-resources/17677> [accessed April 21, 2023].
- Nichols, G. 2009. Sedimentology and Stratigraphy. John Wiley & Sons. 419 p.
- Nielsen, K.S., Schroder-Adams, C.J., Leckie, D.A. 2003. A new stratigraphic framework for the Upper Colorado Group (Cretaceous) in southern Alberta and southwestern Saskatchewan, Canada. *Bulletin of Canadian Petroleum Geology* **51**: 304-346.
- Nittrouer, C.A. and Wright, L.D. 1994. Transport of particles across continental shelves. *Review of Geophysics* **32**: pp. 85-113.
- Nittrouer, C.A., Austin, J.A., Field, M.E., Kravitz, J.H., Syvitski, J., and Wiberg, P.L. 2007. Write a Rosetta Stone: insights into continental-margin sedimentary processes and strata. Special Publication 37 of the International Association of Sedimentologists. Blackwell Publishing, Malden, MA. pp 1-48.
- North American Commission on Stratigraphic Nomenclature [NACSN], 2005, North American Stratigraphic Code: American Association of Petroleum Geologists Bulletin, **89**: pp. 1547-1591.
- Obermajer, M., Stewart, K.R., and Dewing, K. Geological and geochemical data from the Canadian Arctic Islands. Part II: Rock Eval/TOC data. Open File 5459, 27p.
- Obradovich, J.D. 1993. A Cretaceous time scale. *In* The Cretaceous system in the Western Interior of North America. *Edited by* W.G.E. Caldwell and E.G. Kauffman. Geological Association of Canada. pp. 303-331.
- Ohkouchi, N., Kuroda, J., and Taira, A. 2015. The origin of Cretaceous black shales: A change in the surface ocean ecosystem and its triggers. *Proc. Jpn. Acad. Ser. B* **91**.
- Pang, M. & Nummedal, D. 1995. Flexural subsidence and basement tectonics of the Cretaceous Western Interior basin, United States. *Geology* **23**(2): pp. 173-176.
- Passey, Q.R., Bohacs, K.M, Esch, W.L., Klimentidis, R., and Sinha, S. 2010. From oil-prone source rock to gas-producing shale reservoir – geologic and petrophysical characterization of unconventional shale-gas reservoirs. Presented at CPS/SPE International Oil and Gas Conference and Exhibition, Beijing, China, 8-10 June 2010.
- Pederson, T.F. and Calvert, S.E. 1990. Anoxia vs. Productivity: What controls the formation of organic-carbon-rich sediments and sedimentary rocks? *American Association of Petroleum Geologists Bulletin* **74**: pp. 454-466.

- Peper, T. 1993. Quantitative subsidence analysis of the Western Canada Foreland basin with implications for short-term facies changes. *Tectonophysics*, **226**: pp. 301-318.
- Percy, E.L. 2019. Depositional processes and characterization of multi-scale heterogeneity of an organic-rich mudstone, Second White Specks Formation, SW Alberta. Ph.D. thesis. Department of Earth Science. University of Calgary, Calgary, Alberta.
- Peters, K.E. 1986. Guidelines for evaluating petroleum source rocks using programmed pyrolysis. *American Association of Petroleum Geologists* **70**: pp. 318-329.
- Peters, K.E. and Cassa, M.R. 1994. Applied source rock geochemistry. *In* Memoir 60: The petroleum system – from source to trap. American Association of Petroleum Geologists Special Volumes, pp. 93-120.
- Plint, A.G. 1991. High-frequency relative sea level oscillations in Upper Cretaceous shelf clastics of the Alberta Foreland Basin: Evidence for a Milankovitch- scale glacio-eustatic control? *In* Sedimentation, Tectonics, and Eustasy. *Edited by* D.I.M. Macdonald. International Association of Sedimentologists, Special Publication **12**: pp. 409-428.
- Plint, A.G. 1996. Marine and non-marine systems tracts and fourth-order sequences in the Early-Middle Cenomanian Dunvegan Alloformation, northeastern British Columbia, Canada. *In* High resolution sequence stratigraphy: Innovations and applications. *Edited by* J.A. Howell and J.F. Aitken. Geological Society Special Publication, **104**: pp. 159-191.
- Plint, A.G. 2000. Sequence stratigraphy and paleogeography of a Cenomanian deltaic complex: the Dunvegan and lower Kaskapau formations in subsurface and outcrop, Alberta and British Columbia, Canada. *Bulletin of Canadian Petroleum Geology* **48**(1): pp. 43-79.
- Plint, A.G. 2014. Mud dispersal across a Cretaceous prodelta: Storm-generated, wave-enhanced sediment gravity flows inferred from mudstone microtexture and microfacies. *Sedimentology* **61**: pp. 609-647.
- Plint, A.G. 2010. Wave- and storm-dominated shoreline and shallow-marine systems. *In* Facies Models. 4th ed. *Edited by* N.P. James and R.W. Dalrymple. Geological Association of Canada, St. John's, Newfoundland. pp. 167-200.
- Plint, A.G. 2019. Anatomy of a late Cenomanian transgressive shelf system: The influence of high-frequency eustasy and crustal flexure on stratigraphy and paleogeography, basal Kaskapau Formation, Western Canada Foreland Basin. *Bulletin of Canadian Petroleum Geology* **67**(1): pp. 1-46.

- Plint, A.G. and Kreitner, M.A. 2019. High-frequency sequences, paleogeography and syn-depositional tectonism on a shallow clastic ramp: Doe Creek and Pouce Coupe members of the Late Cenomanian Kaskapau Formation, Western Canada Foreland Basin. *Bulletin of Canadian Petroleum Geology*, **67**(2): pp. 1-46.
- Plint, A.G., and Nummedal, D. 2000. The falling stage systems tract: Recognition and importance in sequence stratigraphic analysis. *In* Sedimentary responses to forced regressions. *Edited by* D. Hunt and R.L.G. Gawthorpe. Geological Society of London Special Publication No. 172. pp. 1-17.
- Plint, A.G. and Ulicny, D. 1999. Sequence Stratigraphy: Emphasizing clastic deposits. Notes for a short course in Sequence Stratigraphy. Prague, Czech Republic. 176p.
- Plint, A.G. and Wadsworth, J.A. 2006. Delta-plain paleodrainage patterns reflect small-scale fault movement and subtle forebulge uplift: Upper Cretaceous Dunvegan Formation, Western Canada Foreland Basin. *Society for Sedimentary Geology, Special Publication No. 85*: pp. 219-237.
- Plint, A.G., Eyles, N., Eyles, C.H., and Walker, R.G. 1992. Controls of sea level change. *In* Facies models: response to sea level change. *Edited by* R.G. Walker and N.P. James. Geological Association of Canada, St. John's, Newfoundland. pp. 15-25.
- Plint, A.G., Hart, B.S., and Donaldson, S. 1993. Lithospheric flexure as a control on stratal geometry and facies distribution in Upper Cretaceous rocks of the Alberta foreland basin. *Basin Research* **5**: pp. 69-77.
- Plint, A.G., Macquaker, J.H.S., and Varban, B.L. 2012. Bedload transport of mud across a wide, storm-influenced ramp: Cenomanian-Turonian Kaskapau Formation, western Canada foreland basin. *Journal of Sedimentary Research* **82**: pp. 801-822.
- Plint, A.G., Tyagi, A., Hay, M.J., Varban, B.L., Zhang, H., and Roca, X. 2009. Clinoforms, paleobathymetry, and mud dispersal across the Western Canada Cretaceous Foreland Basin: Evidence from the Cenomanian Dunvegan Formation and contiguous strata. *Journal of Sedimentary Research* **79**: pp. 144-161.
- Plint, A.G., Tyagi, A., McCausland, P., Krawetz, J., Zhang, H., Roca, X., Varban, B.L., Hu, Y.G., Kreitner, M., and Hay, M.J. 2012b. Dynamic relationship between subsidence, sedimentation, and unconformities in mid-Cretaceous, shallow marine strata of the Western Canada Foreland Basin: links to Cordilleran tectonics. *In* Tectonics of Sedimentary Basins: Recent advances. *Edited by* C. Busby and A. Azor. Blackwell Publishing Ltd.
- Podruski, J.A. 1988. Contrasting the character of the Peace River and Sweetgrass Arches, Western Canada Sedimentary Basin. *Geoscience Canada* **15**: 94-97.

- Potter, P.E., Maynard, J.B., and Pryor, W.A. 1980. *The Sedimentology of Shale*. New York, Springer-Verlag, 313p.
- Porter, J. W., Price, R. A. & McCrossan, R. G. 1982. The Western Canada Sedimentary Basin. *Phil. Trans. R. Soc. London A* **305**: pp. 169-191.
- Potter, P.E., Maynard, J.B., and Depetris, P.J. 2005. *Mud and Mudstones: Introduction and overview*: New York, Springer, 297p.
- Posamentier, H.W., and Allen, G.P., 1999, *Siliciclastic Sequence Stratigraphy—Concepts and Applications: SEPM, Concepts in Sedimentology and Paleontology*, **7**: 210 p
- Posamentier, H.W., and Vail, P.R. 1988. Eustatic control on clastic deposition. II. Sequence and system tracts models. *In Sea Level Changes - An Integrated Approach. Edited by C.K. Wilgus and B.S. Hastings, et al. SEPM Special Publication.* pp. 125-154.
- Posamentier, H.W., Jervey, M.T., and Vail, P.R. 1988. Eustatic controls on clastic deposition. I. Conceptual framework. *In Sea Level Changes - An Integrated Approach. Edited by C.K. Wilgus, B.S. Hastings, C.G.St.C. Kendall, H.W. Posamentier, C.A. Ross, J.C. Van Wagoner. SEPM Special Publication.* pp.125-154.
- Price, R. 1973. Large-scale gravitational flow of supracrustal rocks, southern Canadian Rockies. *In: De Jong, K.A. and Scholten, R. (eds.) Gravity and tectonics.* Wiley, New York. 491-502.
- Price R. (1994) Cordilleran Tectonic and the Evolution of the Western Canada Sedimentary Basin. *In: Mossop G., Shetsen I (eds) Atlas of the Western Canada Sedimentary Basin.* Canadian Society of Petroleum Geologists and Alberta Research Council, pp 13–24.
- Prokoph, A., Villeneuve, M.E., Agterberg, F.P., and Rachold, V. 2001. Geochronology and calibration of global Milankovitch cyclicity at the Cenomanian-Turonian boundary. *Geology* **29**(6): pp. 523-526.
- Prokoph, A., Babalola, L.O., El Bilali, H., Olagoke, S., and Rachold, V. 2013. Cenomanian-Turonian carbon isotope stratigraphy of the Western Canada Sedimentary Basin. *Cretaceous Research* **44**: pp. 39-53.
- Pryor, W.A. Biogenic sedimentation and alteration of argillaceous sediments in shallow marine environments. *Geological Society of America Bulletin* **86**(9): pp. 1244-1254.

- Quinlan, G. M. & Beaumont, C. 1984. Appalachian thrusting, lithospheric flexure, and the Paleozoic stratigraphy of the Eastern Interior of North America. *Can. J. Earth Sci* 21, 973-996.
- Reading, H.G. 2001. Clastic facies models, a personal perspective. *Bulletin of the Geological Society of Denmark* 48: pp. 101-115.
- Reading, H.G. and Levell, B.K. 1986. Controls on the sedimentary rock record. *In Sedimentary Environments: Processes, Facies and Stratigraphy. Edited by Reading, H.G.* John Wiley & Sons. pp. 5-36.
- Ridgley, J.L. and Gilboy, C.F. 2001. Lithofacies architecture of the Upper Cretaceous Belle Fourche Formation, Saskatchewan, Alberta, and Montana – Its relationship to sites of shallow biogenic gas production. *In: Summary of Investigations 2001, 1*, Saskatchewan Geological Survey, Sask. Energy Mines, Misc. Rep. 2001-4-1.
- Ridgley, J.L., McNeil, D.H., Gilboy, C.F., Condon, S.M., and Obradovich, J. 2001. Structural and stratigraphic controls on sites of shallow biogenic gas accumulations in the Upper Cretaceous Belle Fourche and Second White Specks-Greenhorn Formations in Southern Montana. *In: Gas in the Rockies. Edited by Anderson, D., Robinson, J.W., Estes-Jackson, J.E., and Coalson, E.B.* The Mountain Association of Geologists, Denver, Colorado, pp. 241-270.
- Roca, X. 2007. Tectonic and eustatic controls on the allostratigraphy and depositional environments of the Lower Colorado Group (Upper Albian), Central Foothills and adjacent Plains of Alberta, Western Canada foreland basin (Unpublished Ph.D. thesis): University of Western Ontario, London, Ontario, 323p.
- Roca, X., Rylaarsdam, J.R., Zhang, H., Varban, B.L., Sislak, C.F., Bastedo, K, and Plint, A.G. 2008. Regional allostratigraphic correlation of Upper Albian to Lower Cenomanian foreland basin strata in the Rocky Mountain Foothills and adjacent subsurface of Alberta and British Columbia: A genetic framework for a Lower Colorado allogroup. *Bulletin of Canadian Petroleum Geology* 56: p. 259-299.
- Romero-Sarmiento, M.F., Ducros, M., and Carpentier, B. et al. 2013. Quantitative evaluation of TOC, organic porosity and gas retention distribution in a gas shale play using petroleum system modeling: Application to the Mississippian Barnett Shale. *Marine Petroleum Geologists* 45: pp. 315-330.
- Ross, G.M., Villeneuve, M.E., Parrish, R.R. and Bowring, S.A. 1991. Geophysics and geochronology of the crystalline basement of the Alberta Basin, Western Canada. *Canadian Journal of Earth Sciences*. 28: pp. 512-522.
- Ross, G.M., Broome, J., and Miles, W. 1994. Potential fields and basement structure – Western Canada Sedimentary Basin. *In Geological Atlas of the Western Canada Sedimentary Basin. Edited by Mossop, G. and Shetsen, I.* pp. 335-352.

- Royden, L.H. 1993. The tectonic expression slab pull at continent convergent boundaries. *Tectonics*, vol. 12, no. 2, pp. 303-325.
- Sageman, B.B., Rich, J., Arthur, M.A., Birchfield, G.E., and Dean, W.E. 1997. Evidence for Milankovitch periodicities in Cenomanian-Turonian lithologic and geochemical cycles, Western Interior U.S.A. *Journal of Sedimentary Research* **67**(2): pp. 286-302.
- Sageman B. B., Rich J., Arthur M. A., Dean W. E., Savrda C. E. & Bralower T. J. 1998. Multiple Milankovitch cycles in the Bridge Creek Limestone (Cenomanian-Turonian), Western Interior Basin. In: *Stratigraphy and paleoenvironments of the Cretaceous Western Interior Seaway, USA* (edited by W. E. Dean & M. A. Arthur). SEPM concepts in sedimentology and paleontology No. 6, 153-171.
- Schieber, J. 1998. Deposition of mudstones and shales: Overview, problems and challenges. *In Shales and mudstones, Volume 1: Basin studies, sedimentology and paleontology. Edited by Schieber, J., Zimmerle, W. and Sethi, P.S.* Stuttgart, Schweizerbart'sche Verlagsbuchhandlung, pp. 131-146.
- Schieber, J. 2016. Mud re-distribution in epicontental basins – Exploring likely processes. *Marine and Petroleum Geology* **71**: pp. 119-133.
- Schieber, J. and Southard, J. 2009. Bedload transport of mud by floccule ripples – direct observation of ripple migration processes and their implications. *Geology* **37**: pp. 843-846.
- Schieber, J., Southard, J., and Thaisen, K. 2007. Accretion of mudstone beds from migrating floccule ripples. *Science* **318**: pp. 1760-1763.
- Schröder-Adams C.J. 2014. The Cretaceous Polar and Western Interior seas: paleoenvironmental history and paleoceanographic linkages. *Sedimentary Geology* **301**: pp. 26–40. <https://doi.org/10.1016/J.SEDGEO.2013.12.003>
- Schröder-Adams C.J, Leckie D.A, Bloch J.D. 1996. Paleoenvironmental changes in the Cretaceous (Albian to Turonian) Colorado Group of western Canada: microfossil, sedimentological and geochemical evidence. *Cretaceous Res.* **17**: pp. 311–365. <https://doi.org/10.1006/CRES.1996.0022>
- Schröder-Adams C.J., Cumbaa, S.L, Bloch, J.D., Leckie, D.A., Craig, J., El-Dein, S.A.S., Simons, D.J. H.A.E., and Kenig, F. 2001. Late Cretaceous (Cenomanian to Campanian) paleoenvironmental history of the Eastern Canadian margin of the Western Interior Seaway: Bonebeds and anoxic events. *Palaeogeography, Palaeoclimatology, Palaeoecology* **170**: pp. 261-289.
- Schultz, S.K., MacEachern, J.A., and Gibson, H.D. 2019. Late Mesozoic reactivation of Precambrian basement structures and their resulting effects on the sequence

stratigraphic architecture of the Viking Formation of east-central Alberta, Canada. *Lithosphere* **11**: 308-321.

SEPM STRATA, 2021. Relative sea level rise. Society for Sedimentary Geology.

Available from

<http://www.sepmstrata.org/Terminology.aspx?id=relative%20sea%20level%20rise> [accessed April 24, 2023].

SEPM STRATA, 2023. Lithofacies. Society for Sedimentary Geology. Available from

<http://www.sepmstrata.org/Terminology.aspx?id=lithofacies#:~:text=Example%20of%20lithofacies%20include%20wackestones,approach%20is%20lithostratigraphic%20or%20allostratigraphic.> [accessed April 21, 2023].

Shank, J.A. 2012. Sedimentology and allostratigraphy of the Cardium Formation (Turonian-Coniacian) in southern Alberta and equivalent strata in northern Montana. Unpublished Ph.D. The University of Western Ontario, London, Ontario.

Slatt, R.M. and O'Brian, N.R. 2011. Pore types in the Barnett and Woodford gas shales: Contribution to understanding gas storage and migration pathways in fine-grained rocks. *American Association of Petroleum Geologists* **95**(12): pp. 2017-2030.

Slingerland, R., Kump, L.R., Arthur M.A. et al. 1996. Estuarine circulation in the Turonian Western Interior seaway of North America. *Geological Society of America Bulletin* **108**: pp. 941-952.

Snedden, J.W. and Nummedal, D. 1991. Origin and geometry of storm-dominated sand beds in modern sediments of the Texas continental shelf. *In Shelf Sands and Sandstone Bodies: International Association of Sedimentologists, Special Publication* **14**: pp. 283-308.

Snowdon, L.R. 1994a. Rock-Eval/TOC data for 13 south-central Alberta wells (Townships 36-59, Ranges 3 to 21W5). Geological Survey of Canada, Open File 2935, 5p., Calgary.

Snowdon, L.R. 1995. Rock-Eval Tmax Suppression: Documentation and Amelioration. *American Association of Petroleum Geologists* **79**(9): pp. 1337-1348.

Snowdon, L.R. 1996. Rock-Eval/TOC data for 12 southeast Alberta wells. Geological Survey of Canada. Open File 3240, 69p, Calgary.

Snowdon, L.R. 1997. Rock-Eval/TOC data for six Alberta Foothills wells (Townships 23 to 27 and Ranges 5W5 to 7W5). Geological Survey of Canada, Open File 3493, 59p., Calgary.

- Snowdon, L.R. and Riediger, C.L. 1995a. Rock-Eval/TOC data for 10 eastern Alberta wells (Townships 25 to 33 and Ranges 1 to 10W4). Geological Survey of Canada, Open File 2989, 45p. Calgary.
- Snowdon, L.R. and Riediger, C.L. 1995b. Rock-Eval/TOC data for 19 southern Alberta wells (Townships 7 to 41 and Ranges 15W4 to 3W5). Geological Survey of Canada, Open File 2990, 126p. Calgary.
- Stelck, C.R. and Wall, J.H. 1954. Kaskapau Foraminifera from the Peace River area of western Canada. Research Council of Alberta, Report no. 68, 38p.
- Stelck, C.R., Wall, J., and Wetter, R.E. 1958. Part I – Lower Cenomanian foraminifera from Peace River Area, Western Canada. Research Council of Alberta Geological Division Bulletin **2**: pp. 1-35.
- Stott, D.F., 1963. The Cretaceous Alberta Group and equivalent rocks, Rocky Mountain Foothills, Alberta. Geological Survey of Canada, Bulletin **132**, 133p.
- Stott, D.F., 1982. Lower Cretaceous Fort St. John Group and Upper Cretaceous Dunvegan Formation of the Foothills and Plains of Alberta, British Columbia, District Mackenzie and Yukon Territory. Geological Survey of Canada Bulletin **328**.
- Stott, D.F., 1984. Cretaceous sequences of the foothills of the Canadian Rocky Mountains. *In* The Mesozoic of Middle North America. *Edited by* Stott, D.F. and Glass, D.J. CSPG Memoir **9**, pp. 85-107.
- Suter, J.R. 2006. Facies models revisited: Clastic shelves. *In* Facies Models Revisited. *Edited by* Posamentier, H.W. and Walker, R.G. Society of Economic Paleontologists and Mineralogists, Special Publication **84**: pp. 339-397.
- Synnott, D.P., Dewing, K., Sanei, H., et al. 2017. Influence of refractory organic matter on source rock hydrocarbon potential: A case study from the Second White Specks and Belle Fourche formations, Alberta, Canada. *Marine Petroleum Geology* **85**: 220-232.
- Syvitski, P.M. 1991. Principles, methods, and application of particle size analysis. Cambridge: Cambridge University Press,
- Syvitski, P.M. 2003. Sediment fluxes and rates of sedimentation. *In* Encyclopedia of Sediments and Sedimentary Rocks. *Edited by* Middleton, G.V., Church, M.J., Coniglio, M., Hardie, L.A. and Longstaffe, F.J. Dordrecht, Kluwer Academic Publishers, pp. 600-605.
- Syvitski, J.P.M, Asprey, K.W., Clattenburg, D.A., and Hodge, G.D. 1985. The prodelta environment of a fjord: Suspended particle dynamics. *Sedimentology* **32**(1): pp. 83-107.

- Taylor, A.M. and Goldring, R. 1993. Description and analysis of bioturbation and ichnofabric. *Geological Society of London, Journal*, **150**, pp. 141-148.
- Taylor, K.G. and Macquaker, J.H.S. 2011. Iron minerals in marine sediments record chemical environments. *Elements*, **7**, pp. 113-118.
- Taylor K.G. and Macquaker J.H.S. 2014. Diagenetic alterations in a silt- and clay-rich mudstone succession: an example from the Upper Cretaceous Mancos Shale of Utah, USA. *Clay Miner* **49**: pp. 213–227.
- TerraTek, 2008. Integrated tight rock analysis – Hunt Arabella 7-34-35-1W2. Hunt Oil Company of Canada, Inc., Calgary, Alberta, 117p.
- Tissot, B.P., Pelet, R., and Ungerer, P. 1987. Thermal history of sedimentary basins, maturation indices and kinetics of oil and gas generation. *American Association of Petroleum Geologists Bulletin* **71**: 1445-1466.
- Traykovski, P., Geyer, W.R., Irish, J.D., and Lynch, J.F. 2000. The role of wave-induced density-driven fluid mud flows for cross-shelf transport on the Eel River continental shelf. *Continental Shelf Research*, v. 20, pp. 2113-2140.
- Tu, Q., Schröder-Adams C.J., Craig, J. 2007. A New Lithostratigraphic Framework for the Cretaceous Colorado Group in the Cold Lake Heavy Oil Area, East-Central Alberta, Canada. *Nat Resour Res* **16**: pp. 17–30.
- Tyagi, A. 2009. Sedimentology and high-resolution stratigraphy of the Upper Cretaceous (Late Albian to Middle Turonian) Blackstone Formation, Western Interior Basin, Alberta, Canada. Ph.D. thesis, Department of Earth Sciences, The University of Western Ontario, London, Ontario.
- Tyagi, A., Plint, A.G., and McNeil, D.H. 2007. Correlation of physical surfaces, bentonites, and biozones in the Cretaceous Colorado Group from the Alberta Foothills to southwest Saskatchewan, and a revision of the Belle Fourche - Second White Specks formational boundary. *Canadian Journal of Earth Sciences* **44**: pp. 871-888.
- Tyson, R.V. 1995. Abundance of organic matter in sediments: TOC, hydrodynamic equivalence, dilution and flux effects. *In Sedimentary organic matter. Edited by Tyson, R.V. Springer, Dordrecht*, pp. 81-118.
- Tyson, R.V. 2000. Palynofacies prediction of distance from sediment source: A case study from the Upper Cretaceous of the Pyrenees. *Geology* **28**(6): pp. 569-571.
- Tyson, R.V. 2001. Sedimentation rate, dilution, preservation, and total organic carbon: some results of a modeling study. *Org. Geochem.* **32**: pp. 333-339.
- Tyson R.V. 2005. The “productivity versus preservation” controversy: cause, flaws, and resolution. *In The deposition of organic-carbon-rich sediments: models*,

mechanisms, and consequences. *Edited by Harris, N.* Society for Sedimentary Geology Special Publication 82, Tulsa, Oklahoma, p 282

USGS, 1997. Introduction to potential fields: Gravity. United States Geological Survey. Available from <https://pubs.usgs.gov/fs/fs-0239-95/fs-0239-95.pdf> [accessed April 25, 2023].

United States Energy Information Administration, 2011. North American Shale Plays. Available from https://www.eia.gov/maps/images/lower-48/northamer_gas.pdf [accessed April 21, 2023].

Vail, P.R., Todd, R.G., and Sangree, J.B. 1977. Seismic stratigraphy and global changes of sea level, Part 5: Chronostratigraphic significance of seismic reflections. *In* Seismic stratigraphy - applications to hydrocarbon exploration. *Edited by C.E. Payton.* American Association of Petroleum Geologists. pp. 99-116.

Van Krevelen, D.W. 1961. Coal. Elsevier, New York.

Van Wagoner, J.C., Posamentier, H.W., Mitchum, R.M.J., Sarg, J.F., Loutit, T.S., and Hardenbol, J. 1988. An overview of sequence stratigraphy and key definitions. *In* Sea level change - an integrated approach: Society of Economic Paleontologists and Mineralogists, Special Publication 42. *Edited by C.K. Wilgus and B.S. Hastings, et al.* pp. 39-45.

Varban, B.L. 2004. Sedimentology and stratigraphy of the Cenomanian-Turonian Kaskapau Formation, northeast British Columbia and northwest Alberta. Unpublished thesis, The University of Western Ontario, London, Ontario, 451p.

Varban B.L. and Plint A.G. 2005. Allostratigraphy of the Kaskapau Formation (Cenomanian-Turonian) in the subsurface and outcrop: NE British Columbia and NW Alberta, Western Canada Foreland Basin. *Bull Can Pet Geology.* **53** pp. 357–389.

Varban, B. L. & Plint, A.G. 2008a. Sequence stacking patterns in the Western Canada foredeep: influence of tectonics, sediment loading and eustasy on the deposition of the Upper Cretaceous Kaskapau and Cardium formations. *Sedimentology* **55** pp. 395-421.

Varban, B.L. and Plint, A.G. 2008b. Palaeoenvironments, palaeogeography, and physiography of a large, shallow, muddy ramp: Late Cenomanian-Turonian Kaskapau Formation, Western Canada foreland basin. *Sedimentology* **55** pp. 201–233.

Warren, P.S., and Stelck, C.R. 1958. Part II. Lower Cenomanian Ammonoidea and Pelycypoda from Peace River Area, Western Canada. *Research Council of Alberta Bulletin* **2** pp. 36-51.

- Waschbush, P.J. and Royden, L.H. 1992. Spatial and temporal evolution of foredeep basins: Lateral strength variations and inelastic yielding in continental lithosphere. *Basin Research* **4** pp.179-196.
- Webster R, and Oliver, M.A., 2007, *Geostatistics for Environmental Scientists*, 2nd edition: John Wiley and Sons, Ltd., 332 p.
- Williams, G.D., and Burk, C.F., 1964. Chapter 12 on Upper Cretaceous. *In: The Geological History of Western Canada. Edited by R.G. McCrossan and R.P. Glaister. Alberta Society of Petroleum Geologists.* pp. 169-189.
- Wright, L.D. and Friedrichs, C.T. 2006. Gravity-driven sediment transport on continental shelves: A status report. *Continental Shelf Research* **68**: pp. 2092-2107.
- Wright G, McMechan M., and Potter D., 1994, Structure and architecture of the Western Canada Sedimentary Basin. *In Geological Atlas of the Western Canada Sedimentary Basin. Canadian Society of Petroleum Geologists and Alberta Research Council,* pp 25–40.
- Wright, L.D., Friedrichs, C.T., Kim, S.C., and Scully, M.E. 2001. Effects of ambient currents and waves on gravity-driven sediment transport on continental shelves. *Marine Geology*, v. 175. Pp. 25-45.
- Zaitlin, B.A., Warren, M.J., Potocki, D., Rosenthal, L., and Boyd, R. 2002. Depositional styles in a low accommodation foreland basin setting: An example from the Basal Quartz (Lower Cretaceous), southern Alberta. *Bulletin of Canadian Petroleum Geology* **50**: pp. 31-72.
- Zajac, N.A. 2016. Depositional processes and facies variability in organic-rich mudstones of the Colorado Group, west-central Alberta, Canada. M.Sc. thesis, Department of Geosciences, University of Calgary, Calgary, Alberta.
- Zonneveld, K.A.F., Versteegh, G.J.M., Kasten, S., Eglinton, T.I., Emeis, K.C., Huguert, C., Koch, B.P., de Lange, G.J., Middleburg, J.J., Mollenhauer, G., Prahal, F.G., Rethemeyer, J., and Wakeman, S.G. 2010. Selective preservation of organic matter in marine environments: Processes and impact on the sedimentary record. *Biogeosciences* **7**: pp. 483-511.

Curriculum Vitae

Name: Jessica Flynn

Post-secondary Education and Degrees:

Brock University
St. Catherines, Ontario, Canada
2000-2003 B.Sc.
Honours Geology and Physical Geography

University of Brighton
Brighton, Ontario, United Kingdom
2006-2007 M.Sc.
Applied Geology

The University of Western Ontario
London, Ontario, Canada
2010-2023 Ph.D.
Geology

Honours and Awards:

Robert and Ruth Lumsden Graduate Award in Science
University of Western Ontario
2013, 2014

Graduate Thesis Research Award
University of Western Ontario
2012

Grants-in-Aid
American Association of Petroleum Geologists
2012

Student Industry Field Trip
Canadian Society of Petroleum Geologists
2003

Peter Peach Memorial Award
Brock University
2002

Related Work Experience

Wellsite Geologist
RPS Energy
Calgary, Alberta, Canada
2009-2011

Graduate Teaching and Research Assistant
The University of Western Ontario
London, Ontario, Canada
2010-2014, 2018

Quality Assurance Geologist
Oil, Gas and Salt Resource Library
London, Ontario, Canada
2014-2015

Senior Research Geologist
Saskatchewan Geological Survey
Regina, Saskatchewan, Canada
2015-Present

Publications/Presentations:

Flynn, J. (2023) Preliminary investigation into rare earth elements of the organic-rich Upper Cretaceous Colorado Group shales, East-central Saskatchewan *in* Summary of Investigations: Sask. Geol. Survey, Sask. Ministry of Energy and Resources.

Flynn, J. (2022) Basinal and sedimentological controls on organic matter preservation and distribution in distal mudrocks of the Upper Cretaceous Colorado Group. (Oral presentation). CSPG GeoConvention Annual Conference, Calgary, Alberta, Canada.

Flynn, J. (2021) Utilizing petrophysical data to map reservoir quality sandstone within the Colony, McLaren and Wasca members of the Mannville Group, West-central Saskatchewan *in* Summary of Investigations: Sask. Geol. Survey, Sask. Ministry of Energy and Resources. <https://publications.saskatchewan.ca/#/products/113677>

Flynn, J. (2018) Reservoir characterization and controls on hydrocarbon distribution within the Colony Member, Pense Formation, Mannville Group, West-central Saskatchewan *in* Summary of Investigations: Sask. Geol. Survey, Sask. Ministry of Energy and Resources. <https://publications.saskatchewan.ca/#/products/100468>

Flynn, J.* and Cheadle, B.A. (2014) Regional allostratigraphic correlations across a foreland basin: Evidence for a tectonically- or eustatically-dominated system? (Oral presentation). CSPG GeoConvention Annual Conference, Calgary, Alberta, Canada

Flynn, J.* and Cheadle, B.A. (2013) Development of an allostratigraphic framework for the Upper Cretaceous Colorado Group: Implications for discrete petroleum system development in mudstones *in* Summary of Investigations: Sask. Geol. Survey, Sask. Ministry of Energy and Resources.

Flynn, J.* and Cheadle, B.A. (2013) Going the distance: A basinwide, high-frequency allostratigraphic framework for the Upper Cretaceous Colorado Group, Western Canada Foreland Basin (poster presentation). CSPG GeoConvention Annual Conference, Calgary, Alberta, Canada.

Flynn, J.* and Cheadle, B.A. (2012) Integration of allostratigraphy with organic geochemistry: Implications for stratigraphic and spatial distribution of organic matter in a foreland basin (poster presentation). CSPG GeoConvention Annual Conference, Calgary, Alberta, Canada